NEDO-21944
79NED81
CLASS I
JUNE 1979

MARK I CONTAINMENT PROGRAM QUARTER SCALE PLANT UNIQUE TESTS

TASK NUMBER 5.5.3, SERIES 2

VOLUME 4

GENERAL ELECTRIC

NEDO-21944
79NED81
Class I
June 1979

MARK I CONTAINMENT PROGRAM
1/4 SCALE PRESSURE SUPPRESSION POOL SWELL TEST PROGRAM: PLANT UNIQUE TESTS
TASK NUMBER 5.5.3, SERIES 2

Volume 4, Appendices B - H

This work was performed with the support of Quadrex Corporation, Nuclear Services Division, and Aerotherm Division of Acurex Corporation under contract to General Electric.

Reviewed by: John M. Humphrey
John M. Humphrey
Mark I Containment Design

Approved by:
G.E. Wade, Manager
Mark I Containment Design

Approved by:
P.W. Ianni, Manager
Containment Design

NUCLEAR ENERGY PROJECTS DIVISION • GENERAL ELECTRIC COMPANY
SAN JOSE, CALIFORNIA 95125

GENERAL ELECTRIC

DISCLAIMER OF RESPONSIBILITY

Neither the General Electric Company nor any of the contributors to this document makes any warranty or representation (express or implied) with respect to the accuracy, completeness, or usefulness of the information contained in this document or that the use of such information may not infringe privately owned rights; nor do they assume any responsibility for liability or damage of any kind which may result from the use of any of the information contained in this document.

TABLE OF CONTENTS - APPENDICES

INTRODUCTION - APPENDICES

The large quantity of data and descriptive material produced by each test series has necessitated the inclusion of a set of appendices with this report. The main report highlights data from a typical plant's tests and summarizes information of general interest. Eight Appendices have been included to present data for the remaining plants, to discuss in detail certain phenomena of particular interest, and to document areas that have received additional investigative effort. The contents of these appendices are summarized below.

Appendix A, which is a continuation of Section 3, presents the test data for the other sixteen plant configurations tested. The data in Section 3 and Appendix A are not necessarily design basis data. The Task 5.5.3-2 Plant Unique Tests were performed at conditions being evaluated for plant operation. Supplementary tests are being performed for several Mark I Utilities to evaluate alternate conditions including variations in water level, submergence, drywell/wetwell pressure differential and vent header deflector design. After a review of these data, a set of test conditions will be selected for each plant to serve as a design basis for pool swell loads.

Appendix B defines the methodology used for vent header pressure integration. The values used for the six point fits to the impact pressure transducer transients and the resulting pressure integrals are also provided.

Appendix C presents plant unique data comparisons and the results of a linear regression correlation of the plant unique test data.

Appendix D estimates the amount of pool mass that is suspended in flight during the upload.

Appendix E presents a series of still pool swell pictures for each plant configuration.

Appendix F presents the results of a measurement uncertainty analysis.

Appendix G presents the specification for vent system resistance and the methods used to meet the specification.

Appendix H presents the results of evaluations of torus window related download oscillations in the plant unique data and a description of the methods employed to remove these effects for several plants.

APPENDIX B

VENT HEADER PRESSURE INTEGRATION

Forces on the vent header are determined both by a load cell with inertial correction and by an area integration of the pressure on the vent header. This appendix presents a description of the method used to integrate vent header pressures together with the transducer pressure values used and the resulting force time history for every test. Due to the volume of material contained in this appendix, Table B-3 has been placed on microfilm and is included with this report.

B.1 Impact Symmetry

The vent header impact force was determined from an area integration of pressure measured by pressure transducers on the bottom of the vent header. During the Generic Sensitivity Pool Swell Tests (conducted during February and March 1978), several different vent header transducer patterns were included to investigate the symmetry of vent header impact pressures. The test results indicated that agreements of the impact pressure measured at symmetrical positions were generally excellent (Reference 1). Because of the vent header symmetry, the pressure transducers were installed in one quadrant for the pressure integral calculation.

B.2 Typical Data

Time-history plots of the vent header impact pressures for Monticello Tests 2 and 8 are presented in Section 3.1. Test 2 was conducted at a partial drywell/wetwell differential pressure of 7.75" H_2O and with a "T" deflector.* Test 8 was conducted without an initial drywell/wetwell differential pressure (zero ΔP) and with the "T" deflector. Similarly, typical time-history plots of the vent header impact pressures for Hatch 2, Pilgrim, Fermi 2, Duane Arnold, Nine Mile Point, Brunswick, Cooper Station, Dresden, Browns Ferry, Peach Bottom, Millstone, Oyster Creek, Hatch 1, Vermont Yankee, Fitzpatrick, and Hope Creek tests are presented in Appendix A.

B.3 Pressure Integral Calculation

The vent header impact load was measured during this test series by two methods, a load cell with acceleration and thrust corrections and an area integration of pressure measured by pressure transducers on the bottom of the vent header. This Section describes the procedure and results of the pressure integration method.

---

*Pipe with a structural "T" welded on each side.

B.3.1 Test Hardware Description

The vent headers used during the plant unique test series were specifically constructed to closely match individual utility design input. Each vent header had provision made for approximately 18 pressure transducer parts on a bottom quadrant. The layout of a typical transducer pattern is shown in Figure B-1. Not all locations were used in a single test due to transducer and recording channel limitations. The basic pressure map is created in one quadrant by 13 measurements extending out to 60° from bottom dead center.

The test matrix included 101 tests. Thirteen transducers (T1 through T13) were used in all runs. The measurement locations were slightly varied in each of the plant unique tests to obtain good impact pressure distribution pattern.

Two types of pressure transducers were used, Kulite Model CQ-140-100A and Bell & Howell Model 4-312-0001, both 0-100 psia. Mount configurations for each are shown in Figure B-2.

B.3.2 Data Reduction

Twelve (with one transducer installed on downcomer bend) or thirteen pressure locations are insufficient to yield a smooth area integral in time. Therefore, an interpolation scheme was used to create pressure histories at intermediate locations. Figure B-3 and Table B-1 illustrate the nodal scheme used. Measurements are made at numbered stations and interpolated histories are created for areas A through MM. The impact load at a given time is formed by summing the product of the pressure for that time at a given node (either a measured or interpolated function) and its corresponding area. The area used is the projection of the nodal area on the horizontal plane in order to calculate the vertical force component.

A more detailed description of the interpolation technique can be found in Reference B-1.*

Each measured pressure history is approximated by 5 line segments defined by 6 points. Examples of this approximation is shown in Figure B-4. The 6 defining points for each measurement are the input data for the integration computer program. A complete tabulation of the 6 point input data from this program is included.

B.3.3 Results and Discussion

Table B-2 presents typical input data and Table B-3** lists the 6 point approximations used for the integration program for all 101 runs. Figures B-5 through B-97 show the pressure integral results for the Plant Unique Tests (time shown is the test run time and not corrected for T_o).

B.4 Comparison of Pressure Integral and Load Cell

The vent header impact force was measured during this test series by two methods; a load cell and an area integration of pressure measured by pressure transducers on the bottom of the vent header. The time history plots of vent header force determined by spatial pressure integration and load cell corrected for the vent header inertia (mass x acceleration) are compared in Section 3.1.2 for typical Monticello test runs and in Appendix A for other plants. In general, these figures show reasonably good agreement between these two methods at peak vent header impact force and throughout the transient.

---

* B-1, W. Kennedy et al, "Rigid and Flexible Vent Header Testing in the Quarter Scale Test Facility," Acurex Corp., NEDE-24520-P, March 1978.

**Included on attached microfilm.

The acceleration corrected vent header load cell transient is not as smooth as the integrated pressure due to noise in the accelerometer and high frequency structural modes in the vent header. These effects tend to make the peak reported load cell forces higher than the peak integrated pressure force.

FIGURE B-1

TYPICAL VENT HEADER INSTRUMENTATION LOCATIONS

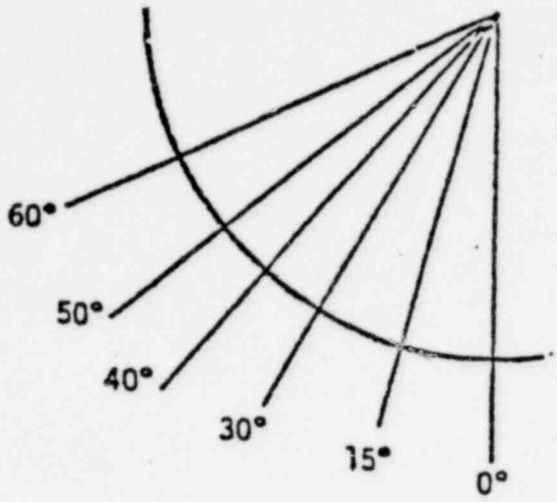

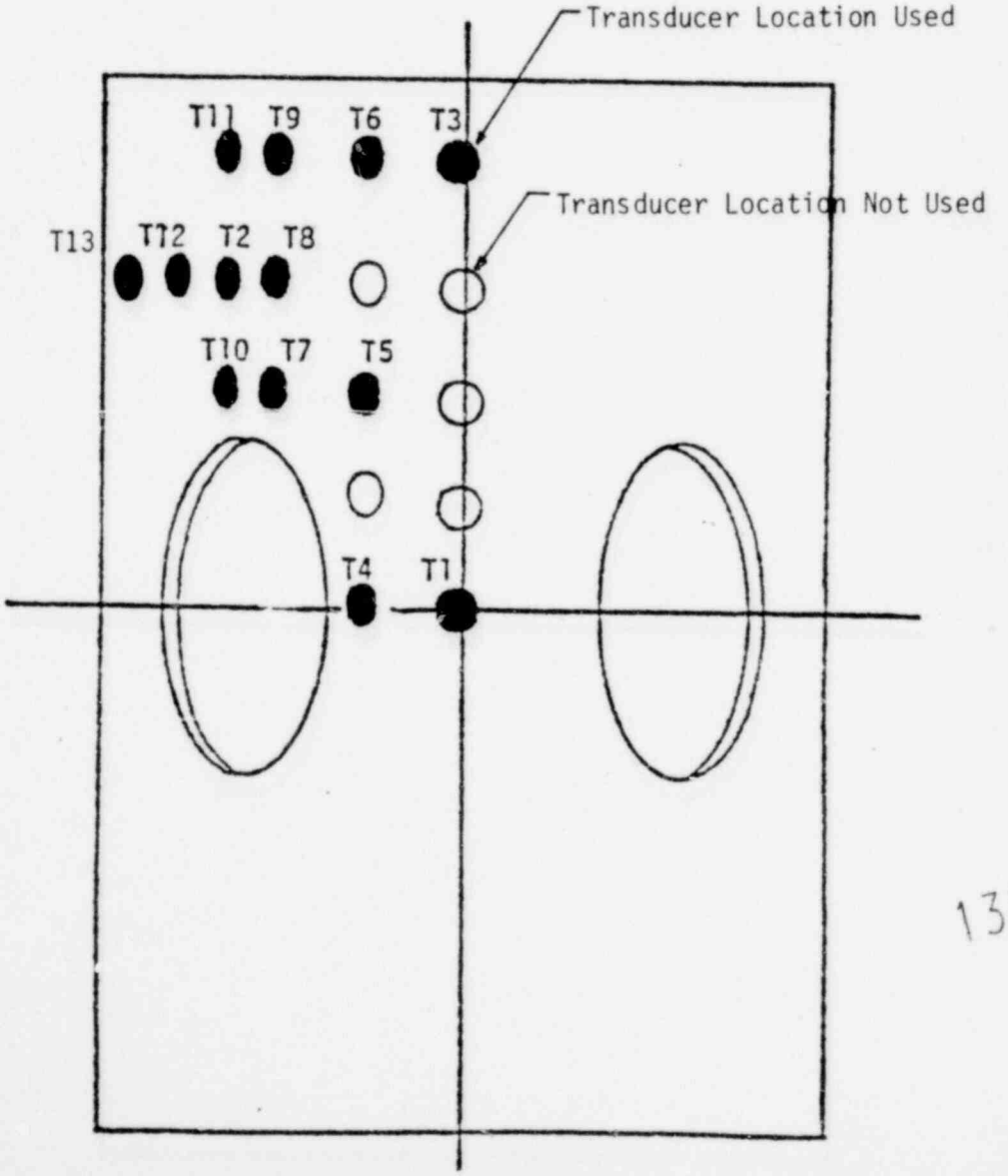

FIGURE B-2

VENT HEADER TRANSDUCER MOUNT DETAILS

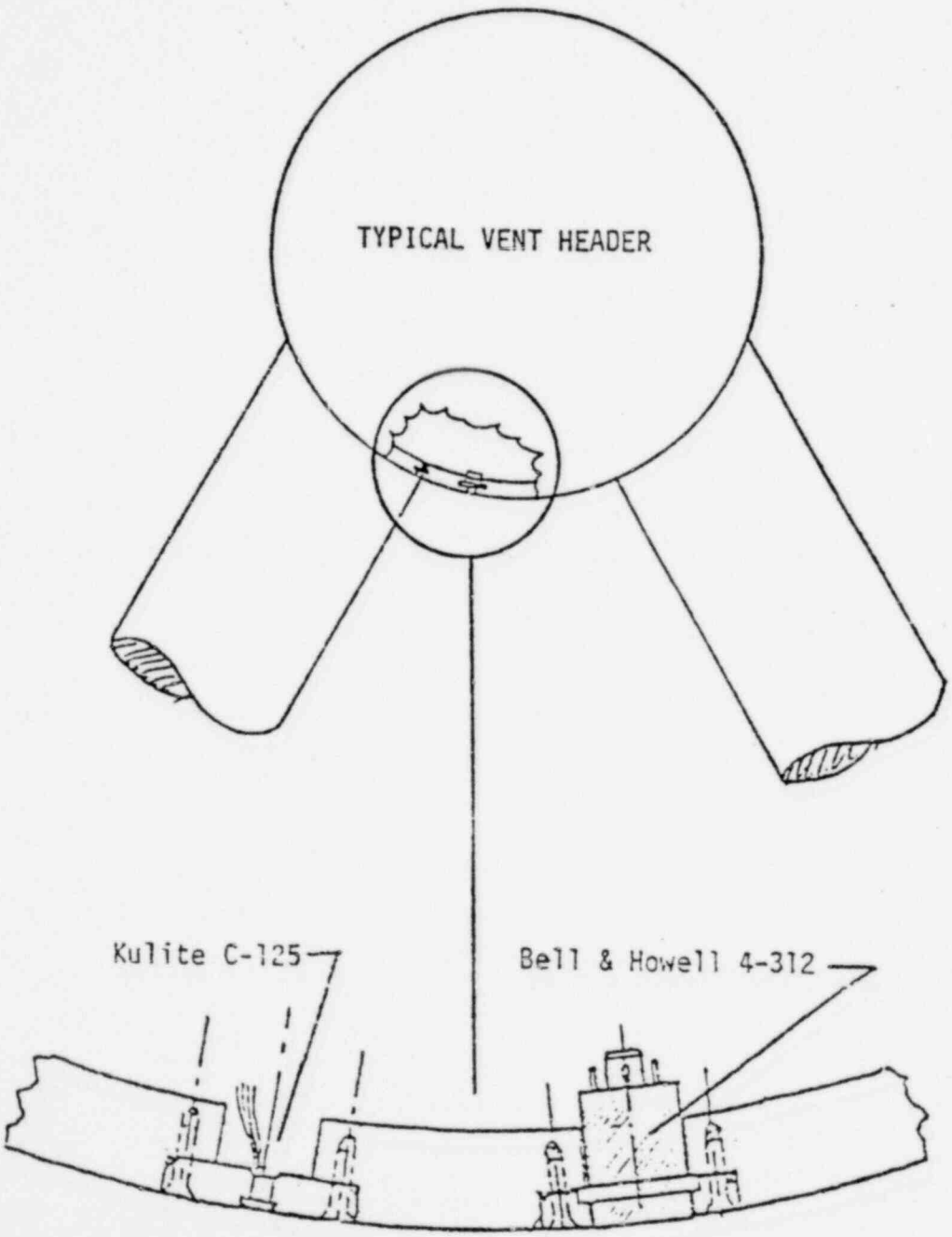

1350 360

FIGURE B-3

TYPICAL PRESSURE INTEGRAL NODAL SCHEME

VENT HEADER RADIUS = 7.5"

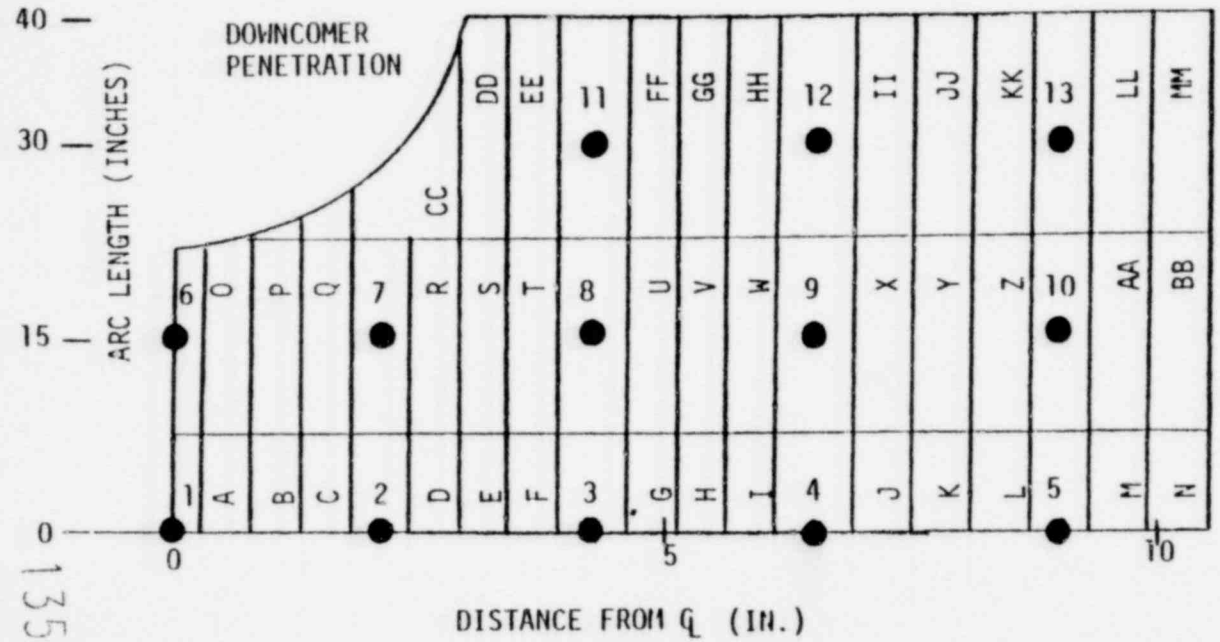

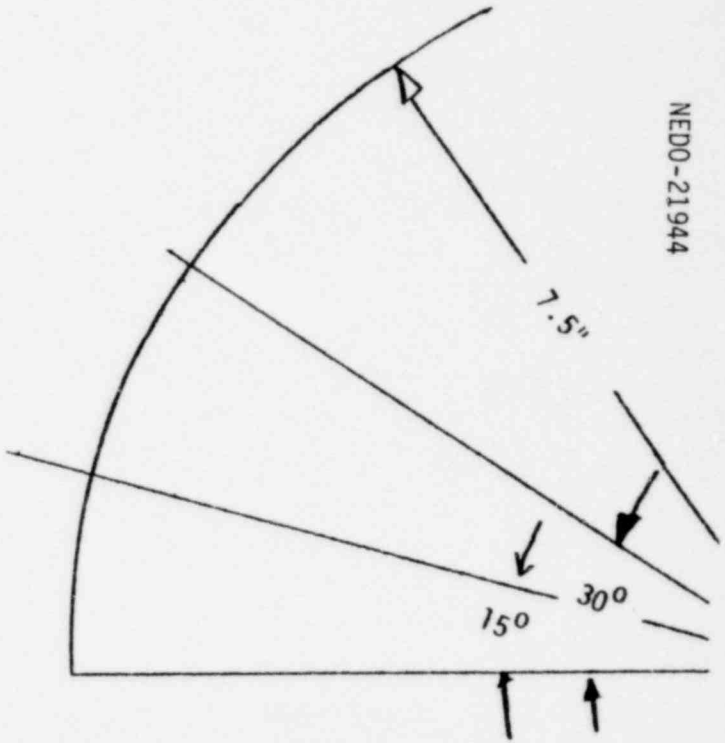

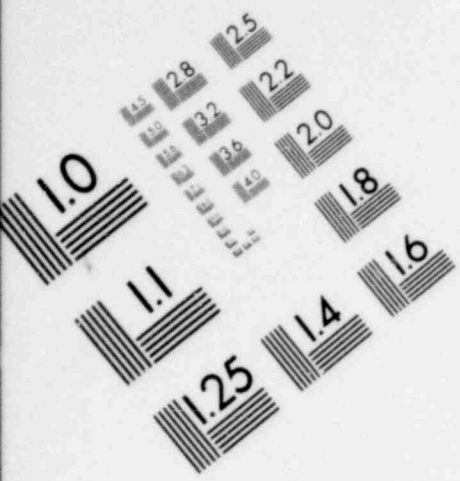

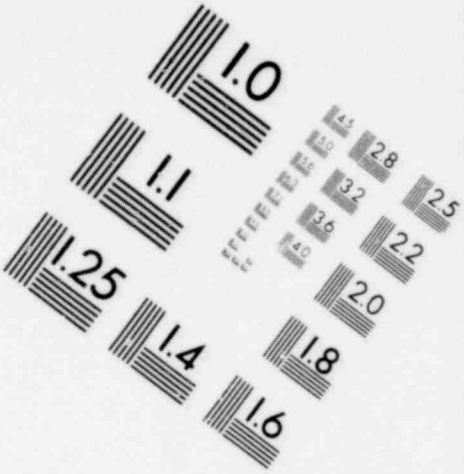

IMAGE EVALUATION TEST TARGET (MT-3)

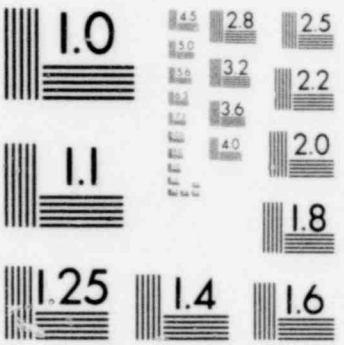

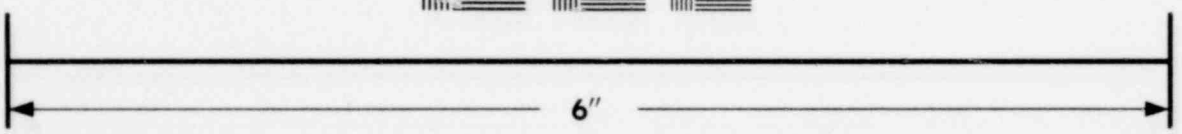

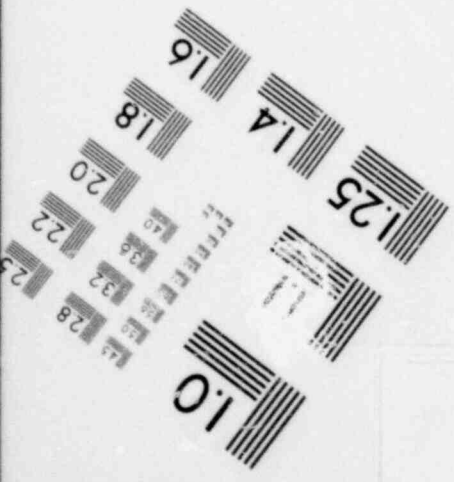

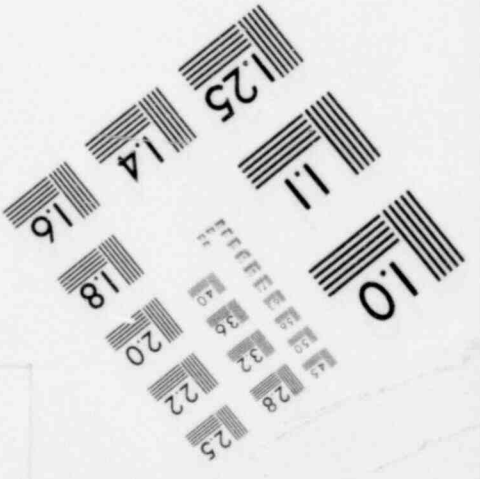

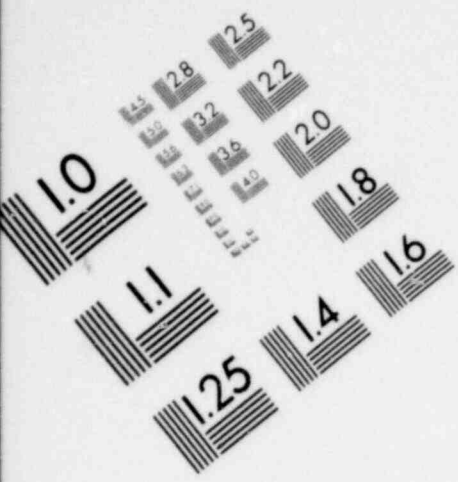

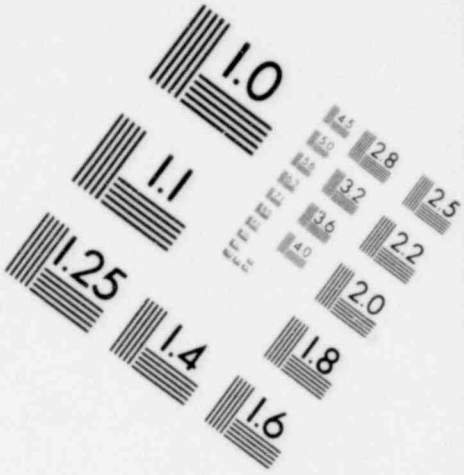

IMAGE EVALUATION TEST TARGET (MT-3)

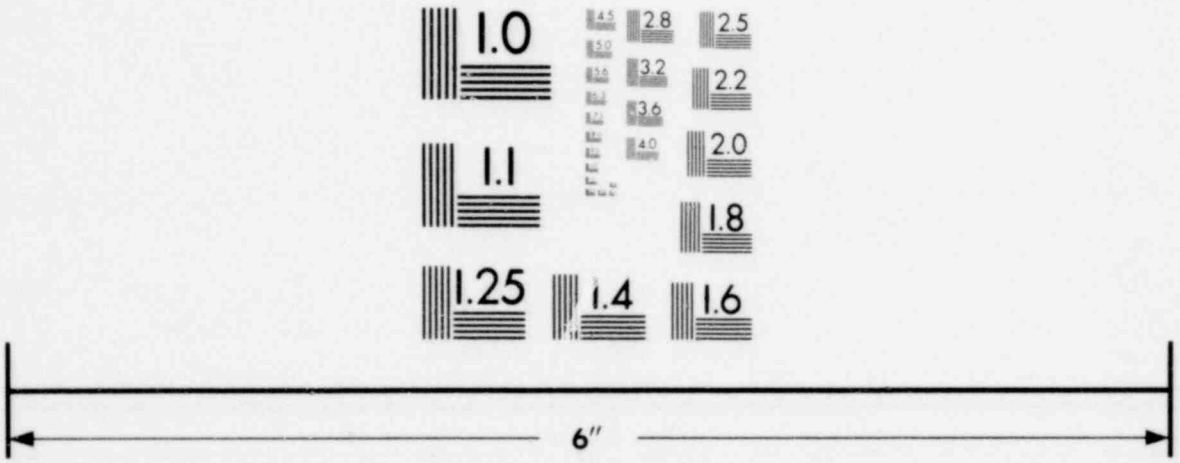

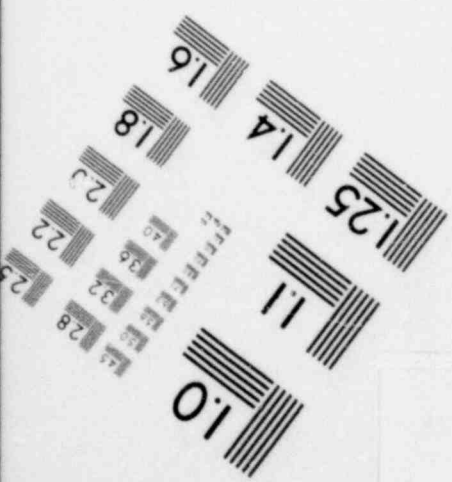

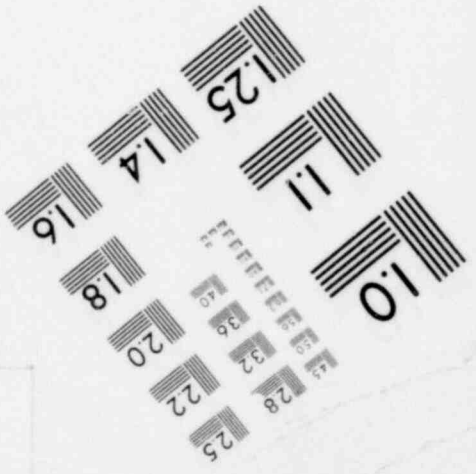

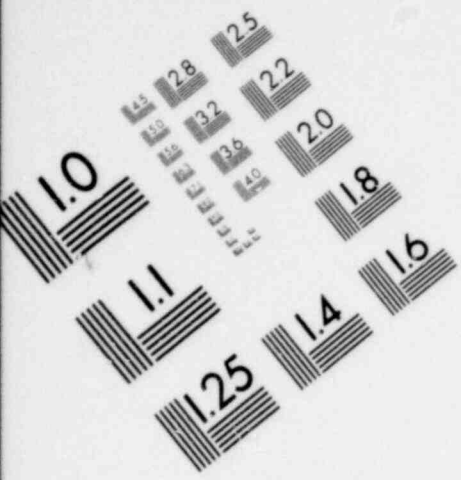

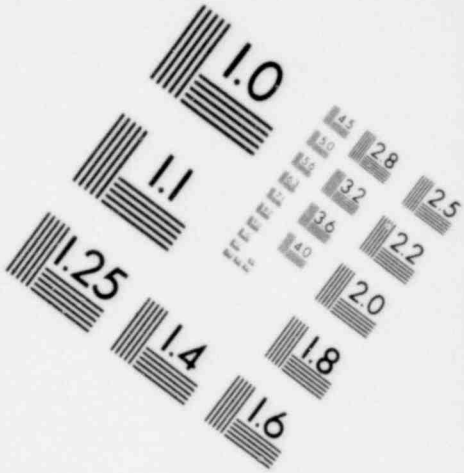

IMAGE EVALUATION TEST TARGET (MT-3)

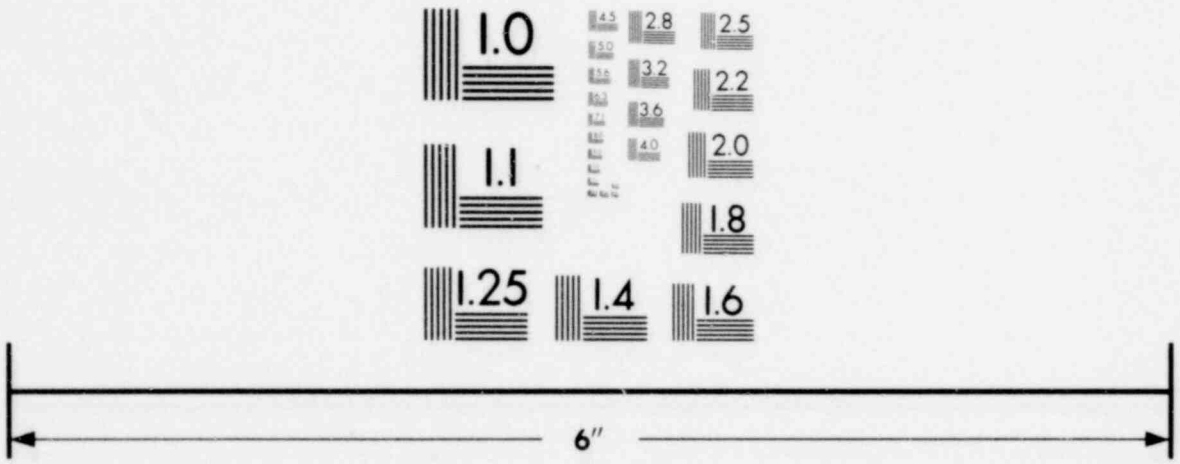

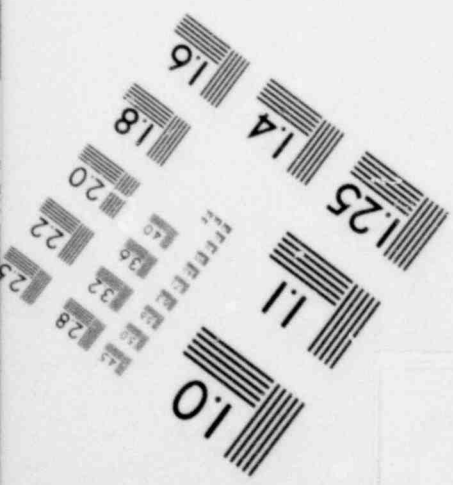

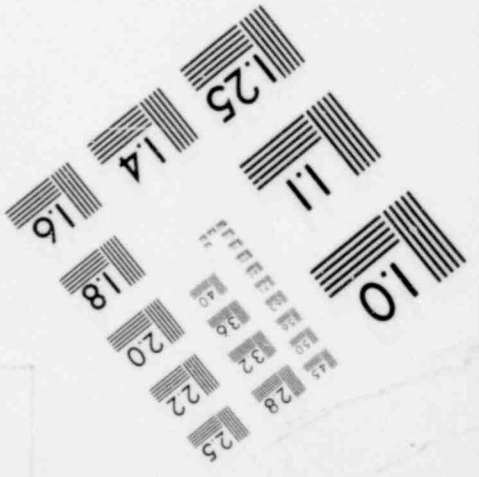

FIGURE B-4

TYPICAL SIX POINT APPROXIMATION
TO VENT HEADER IMPACT PRESSURE TRACE

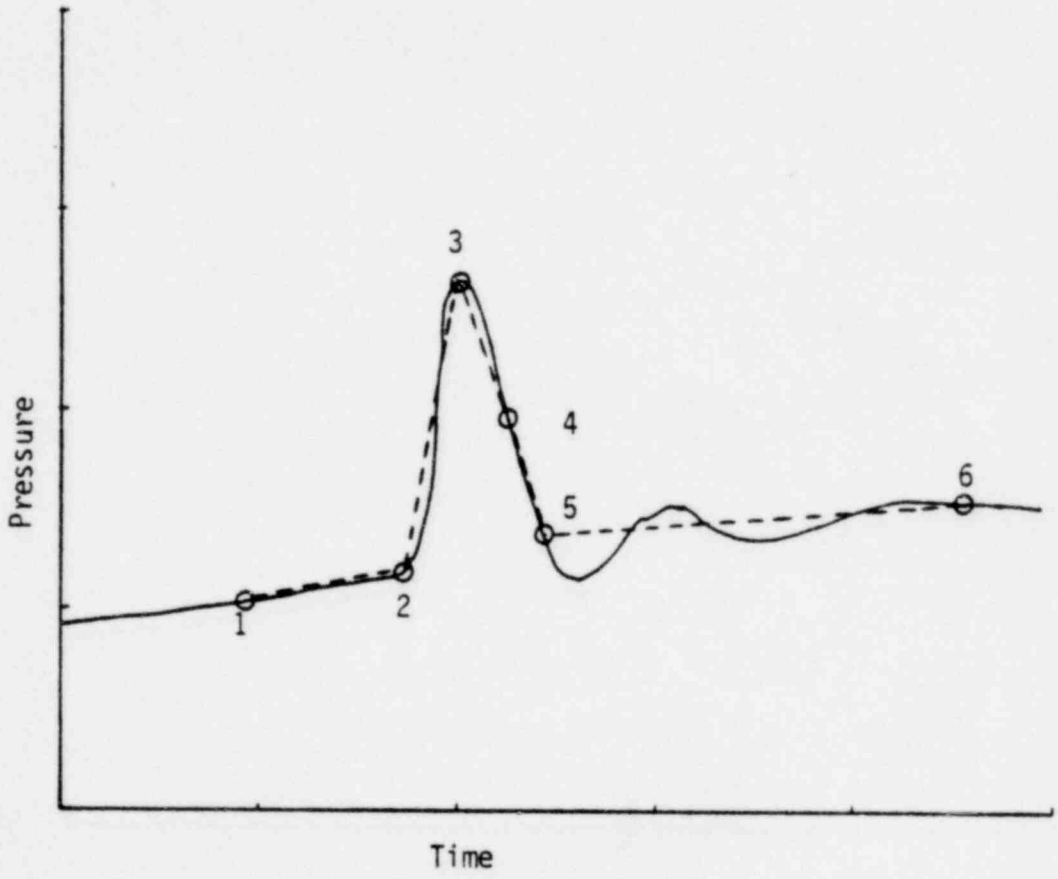

Note: Point 1 is at the earliest time of impact on any pressure transducer. All vent impact pressures are adjusted to the torus freespace pressure at that time.

1351.001

FIGURE B-5

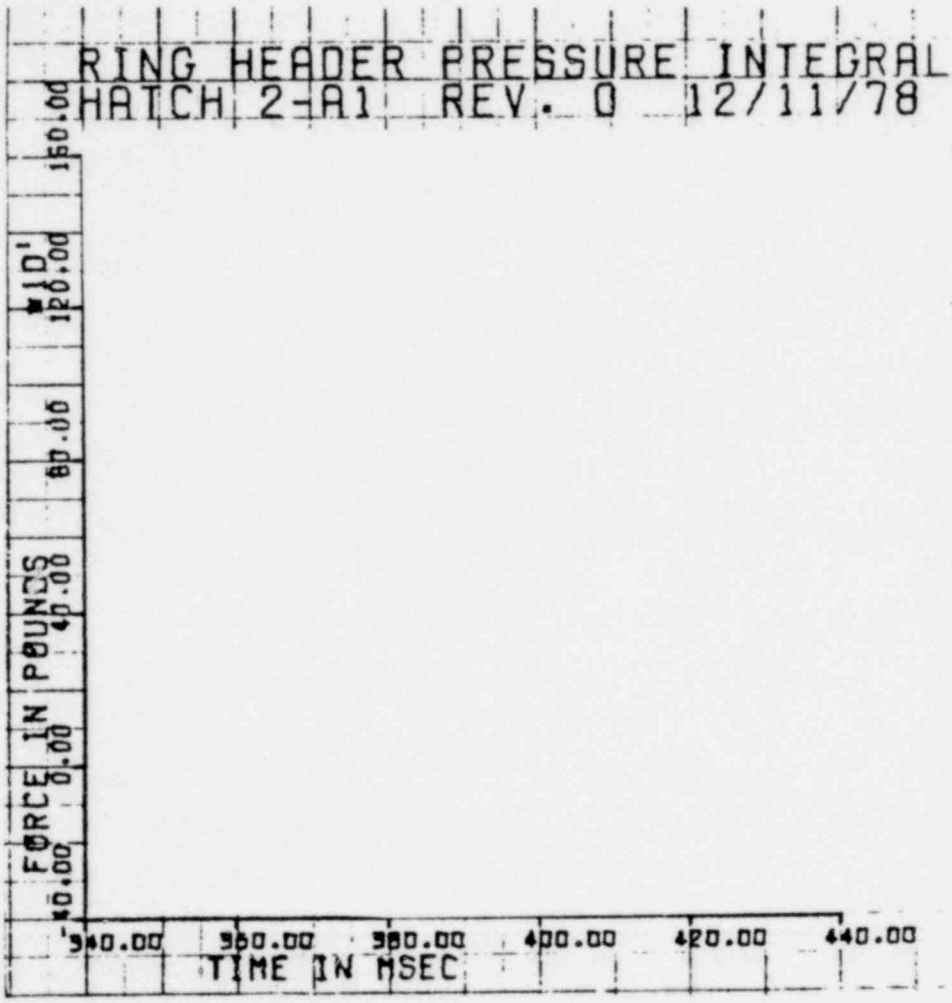

*Proprietary information deleted.

1351-002

FIGURE B-6

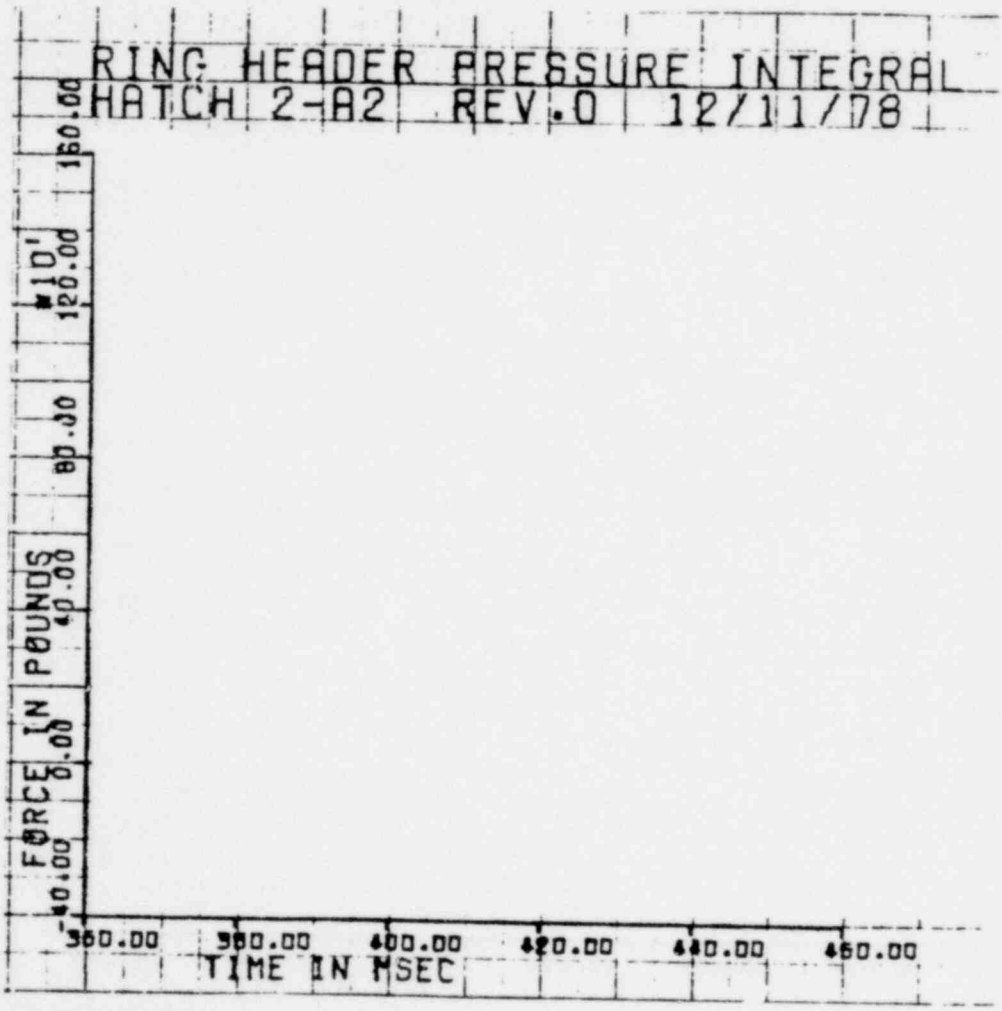

*Proprietary information deleted.

1351-003

FIGURE B-7

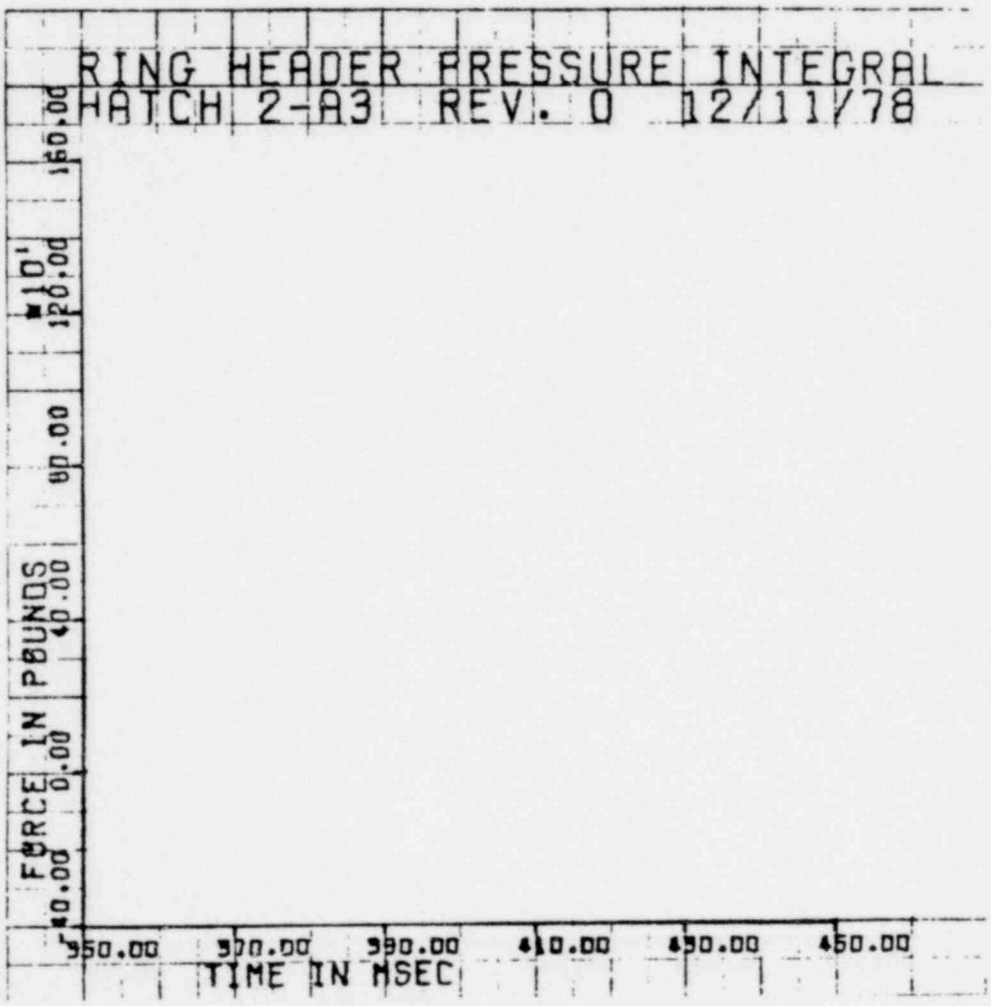

FIGURE B-8

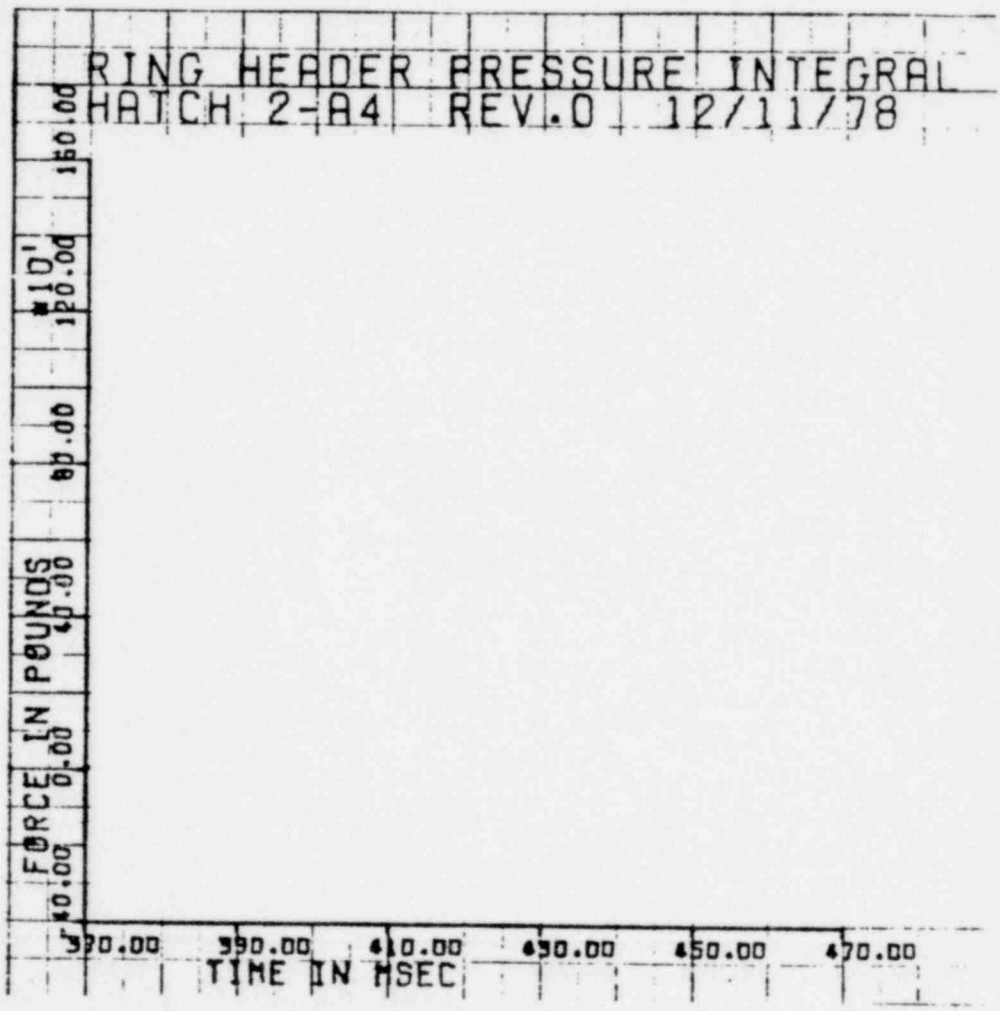

1351 005

FIGURE B-9

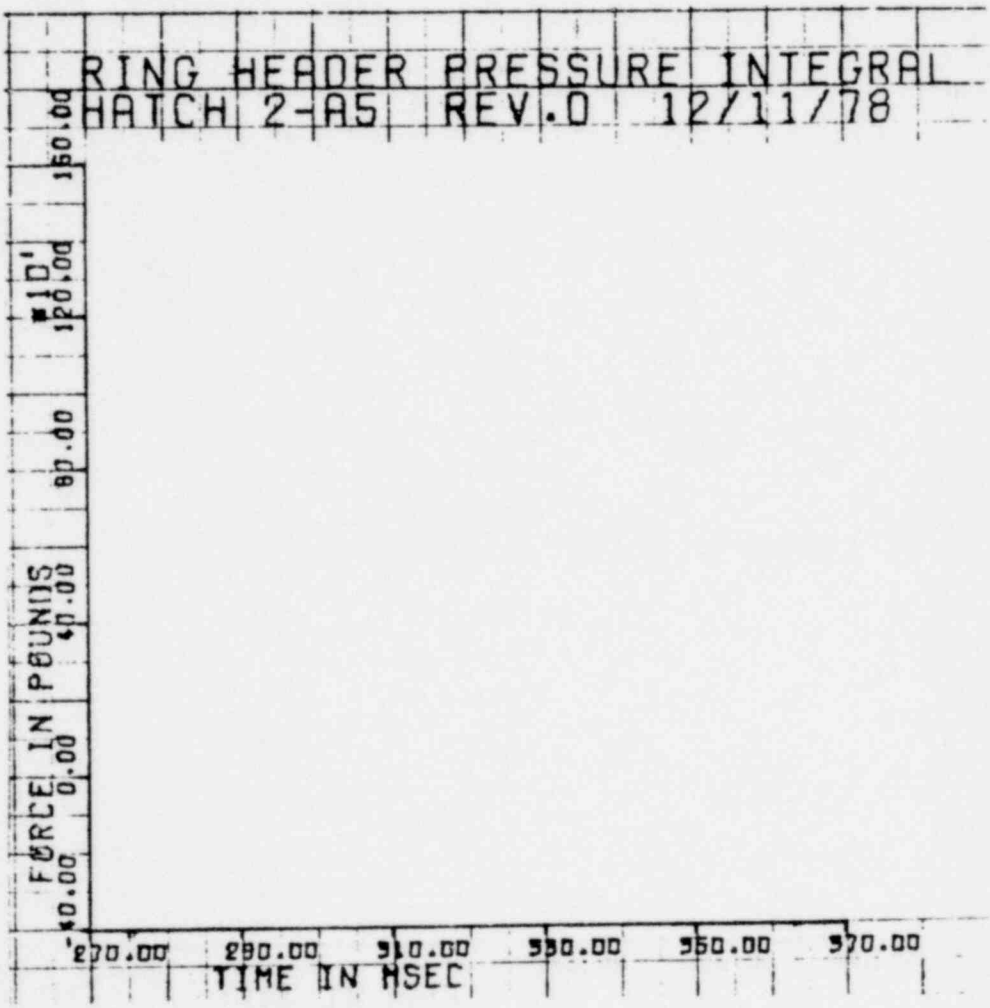

FIGURE B-10

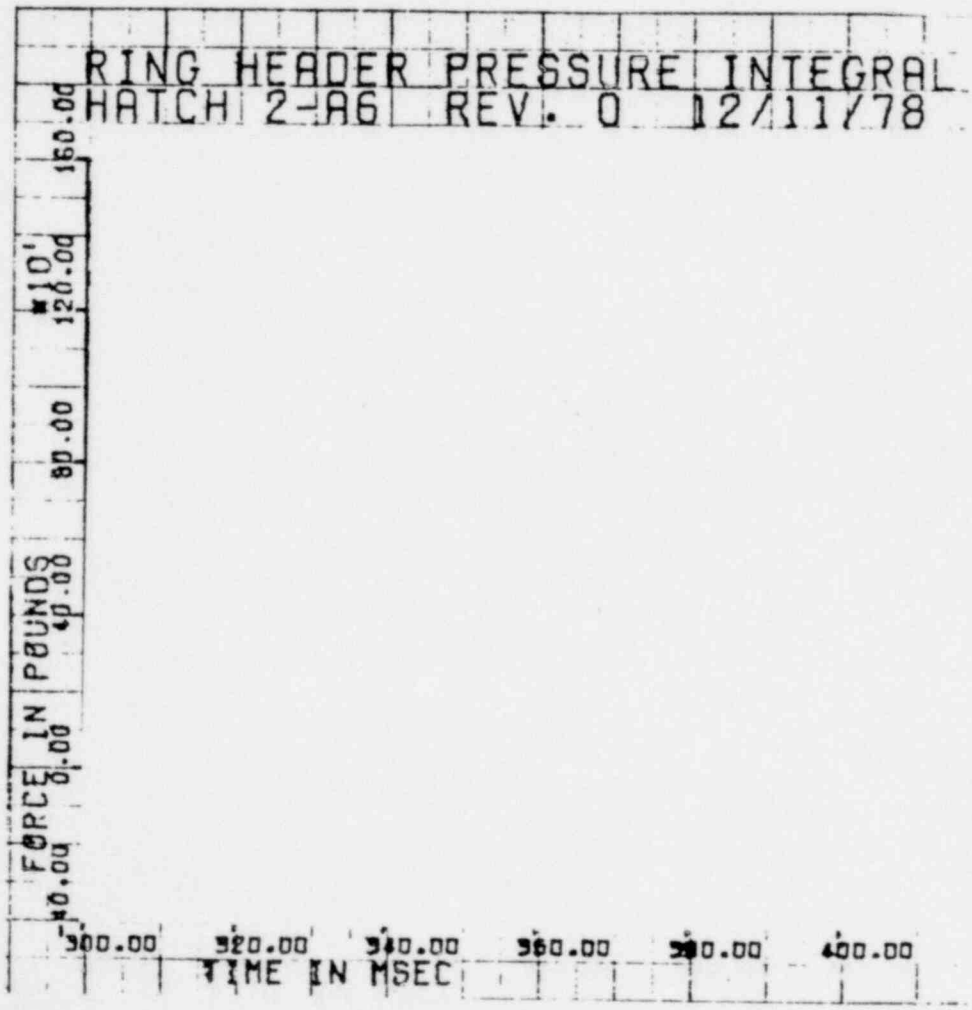

1351 007

FIGURE B-11

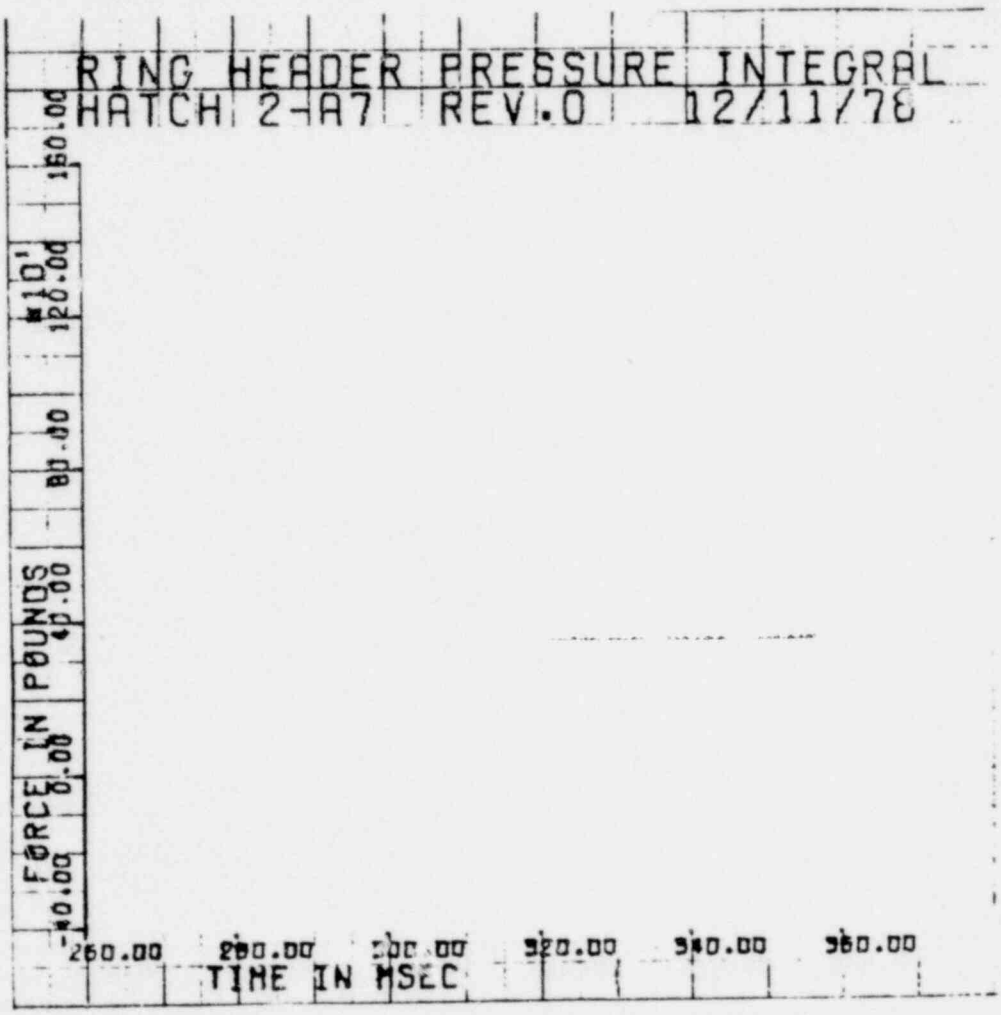

FIGURE B-12

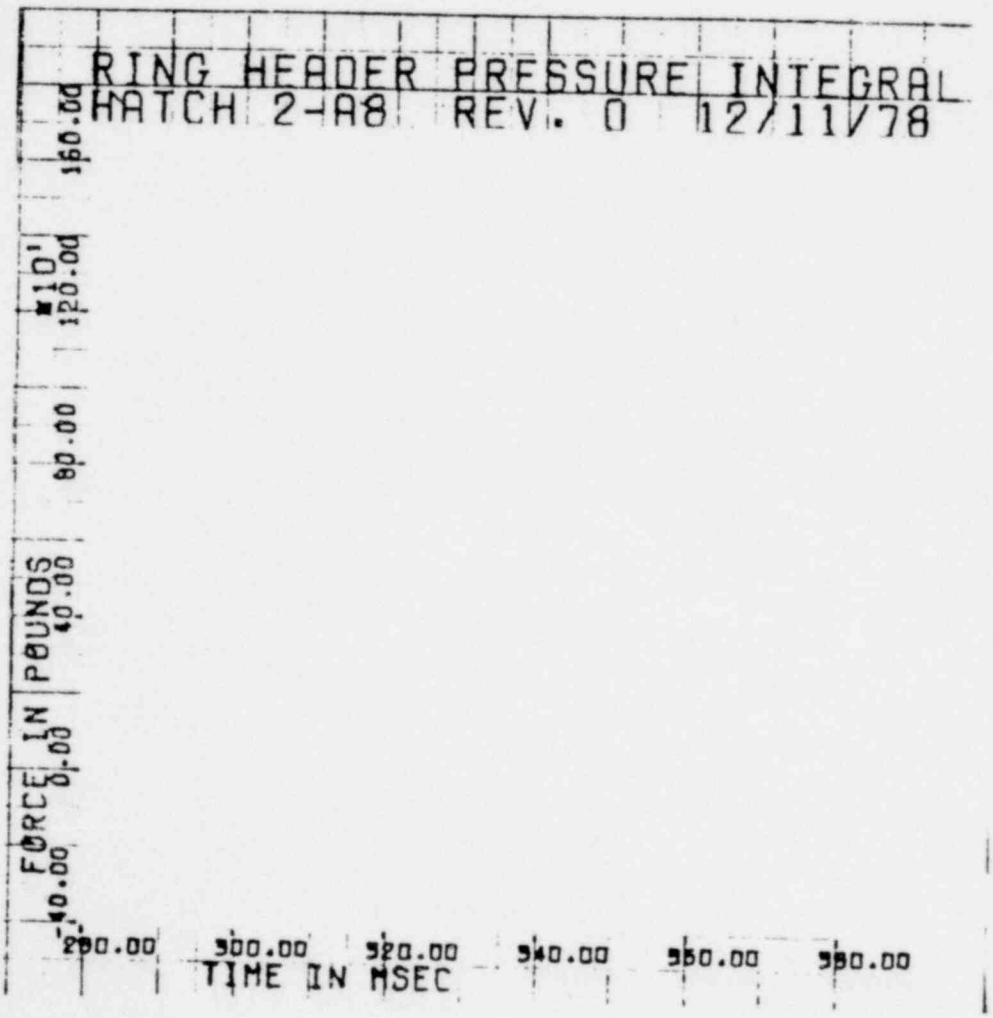

1351 009

FIGURE B-13

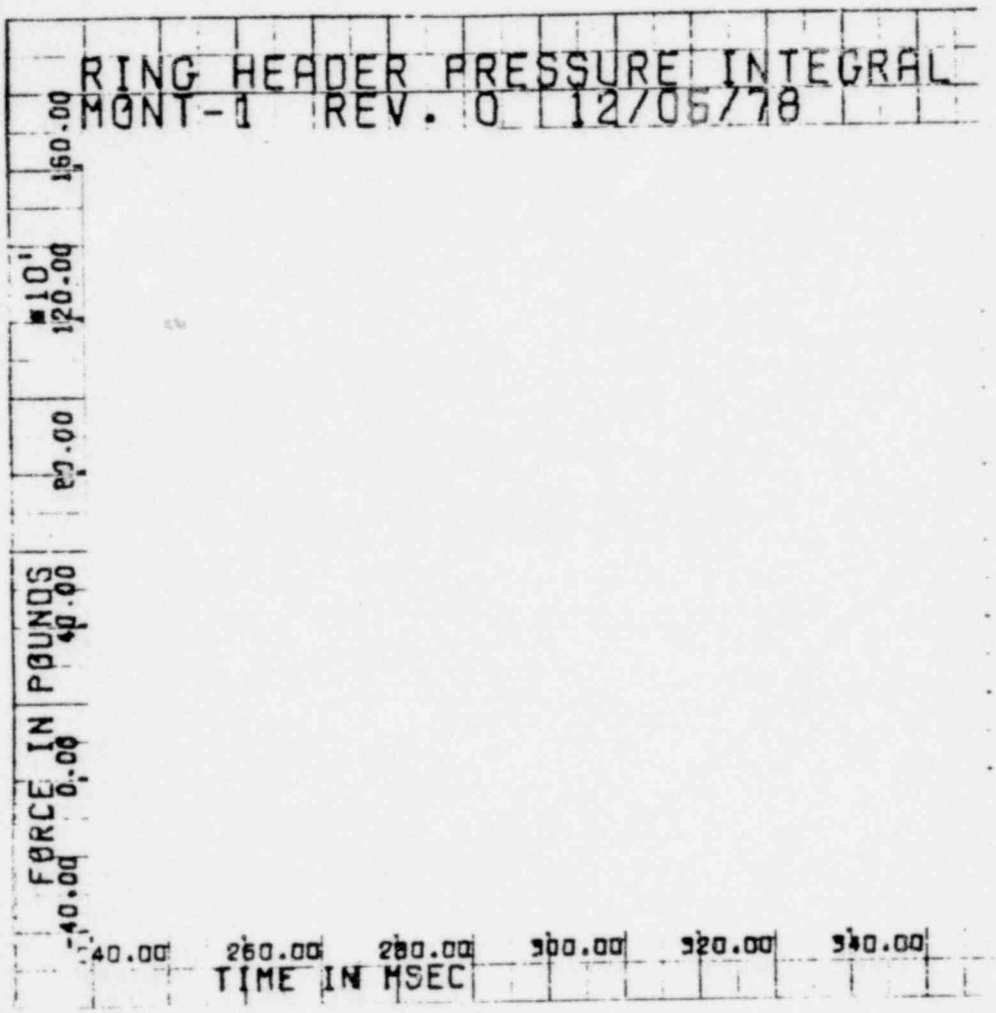

1351 010

FIGURE B-14

1351-011

FIGURE B-15

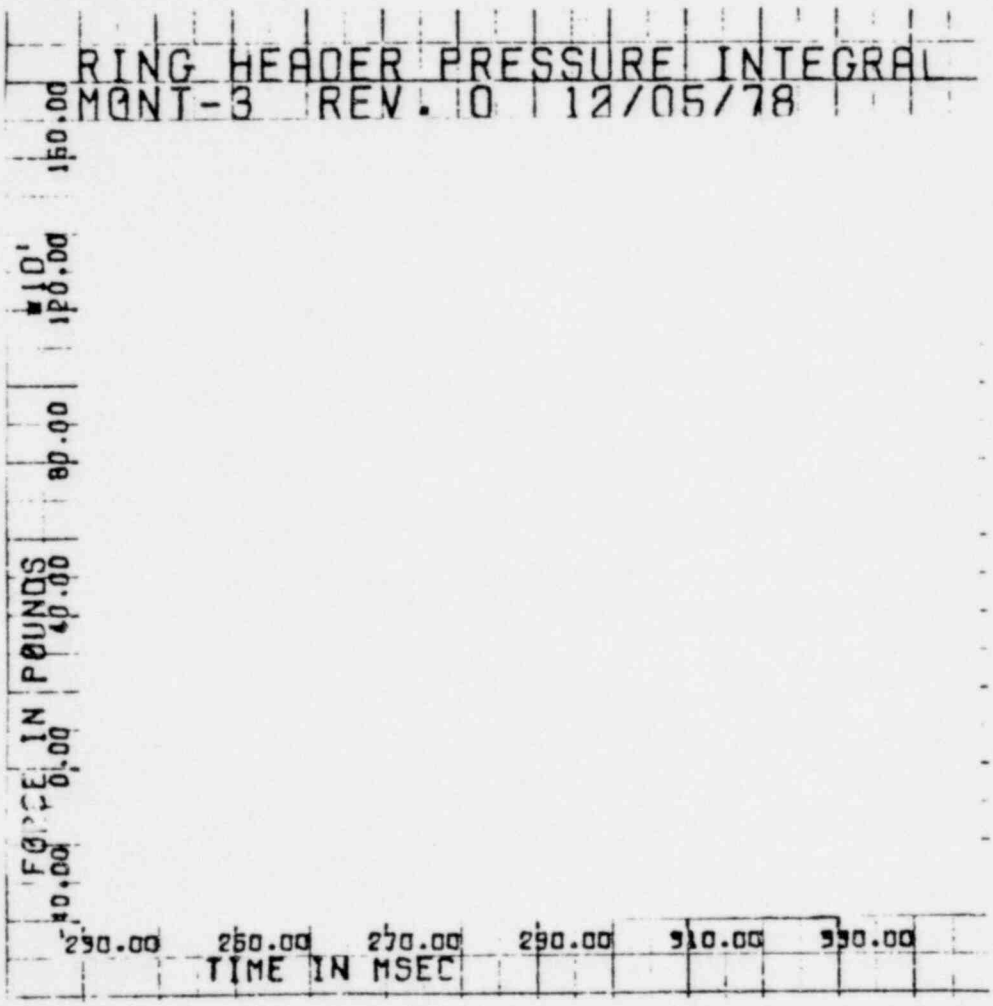

135.012

FIGURE B-16

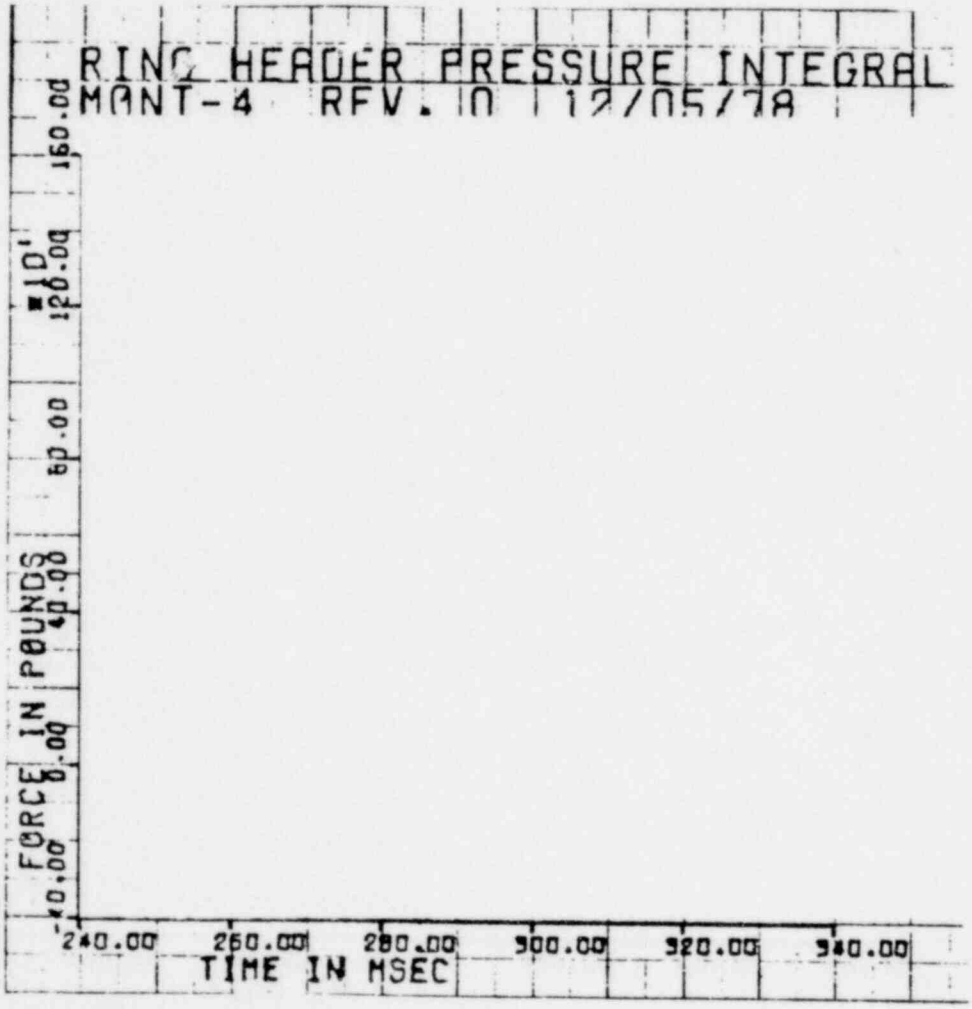

FIGURE B-17

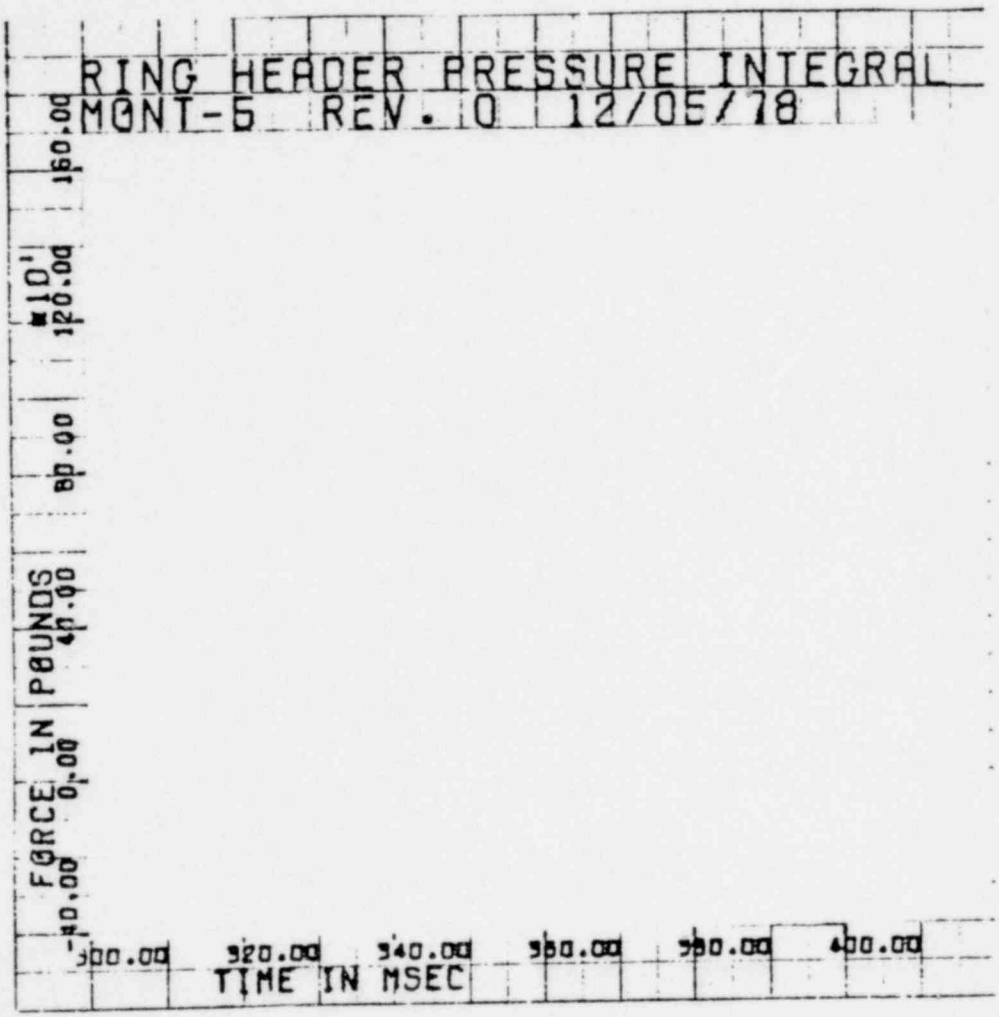

FIGURE B-18

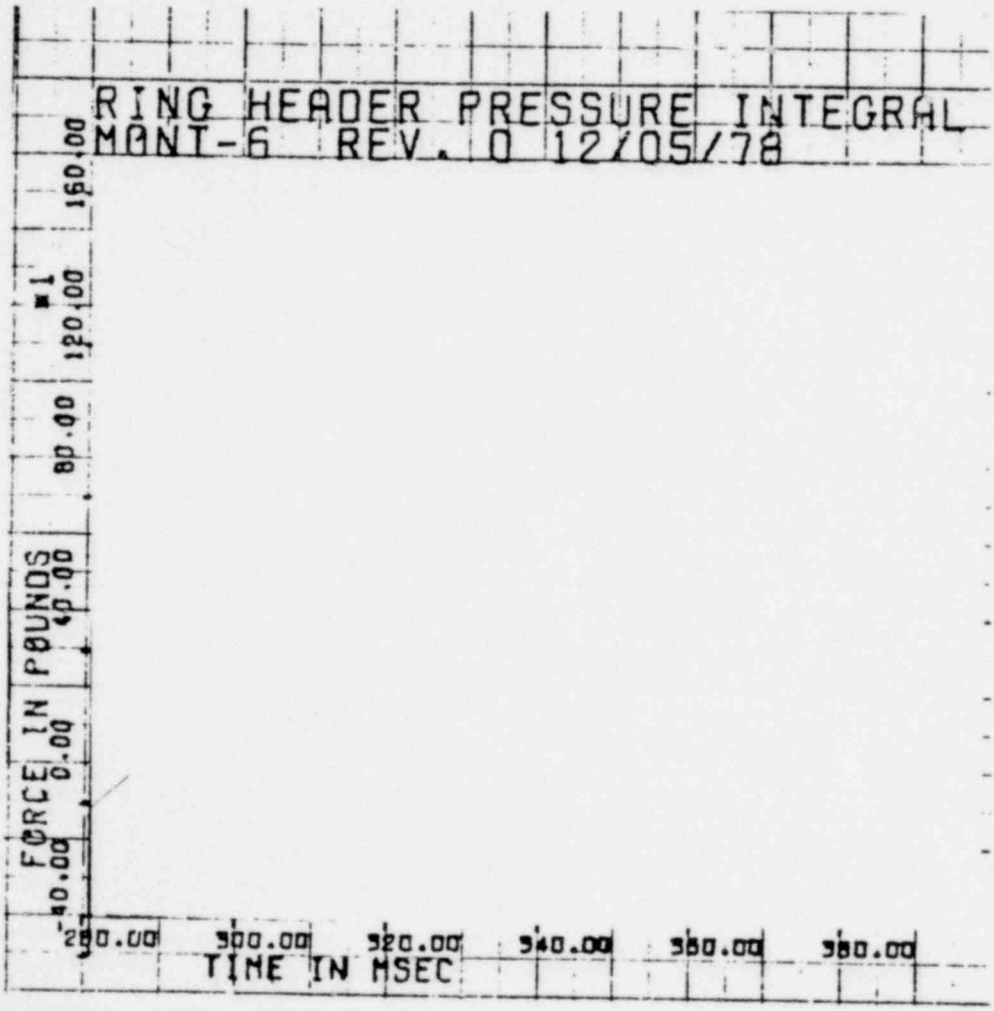

FIGURE B-19

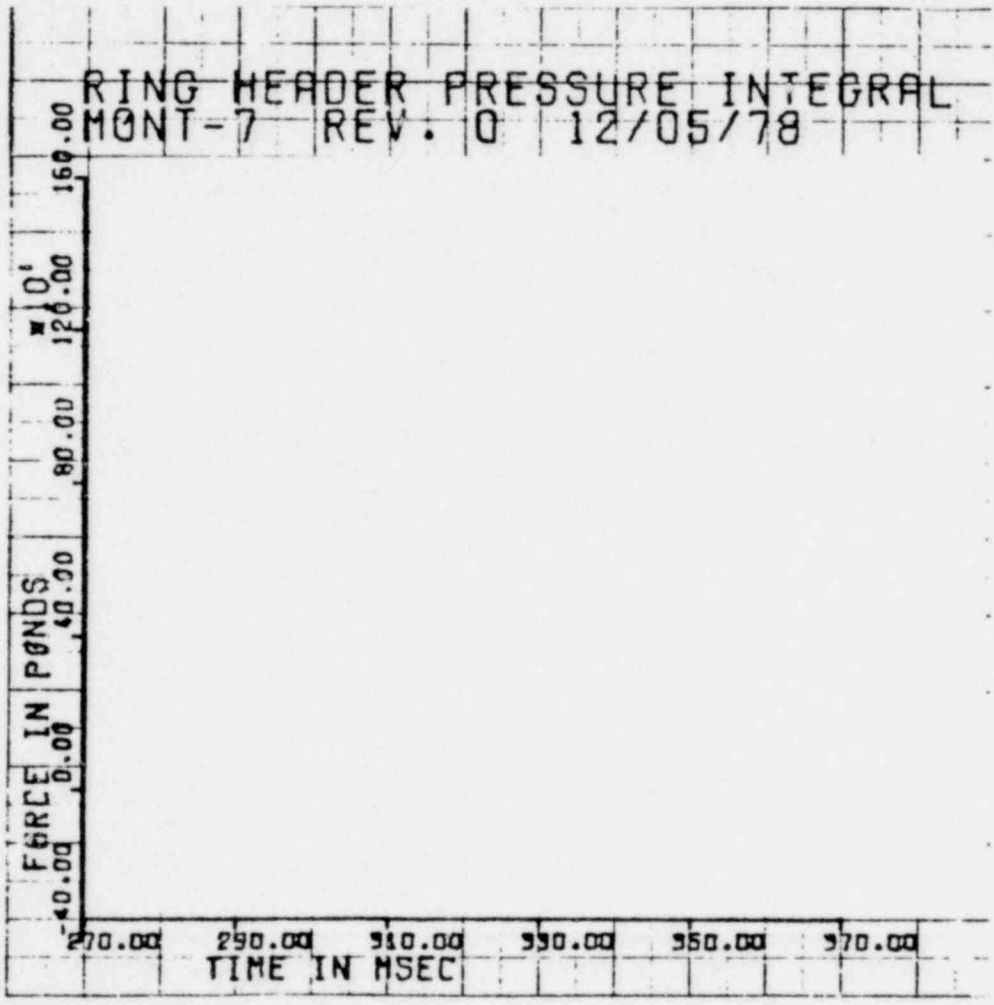

FIGURE B-20

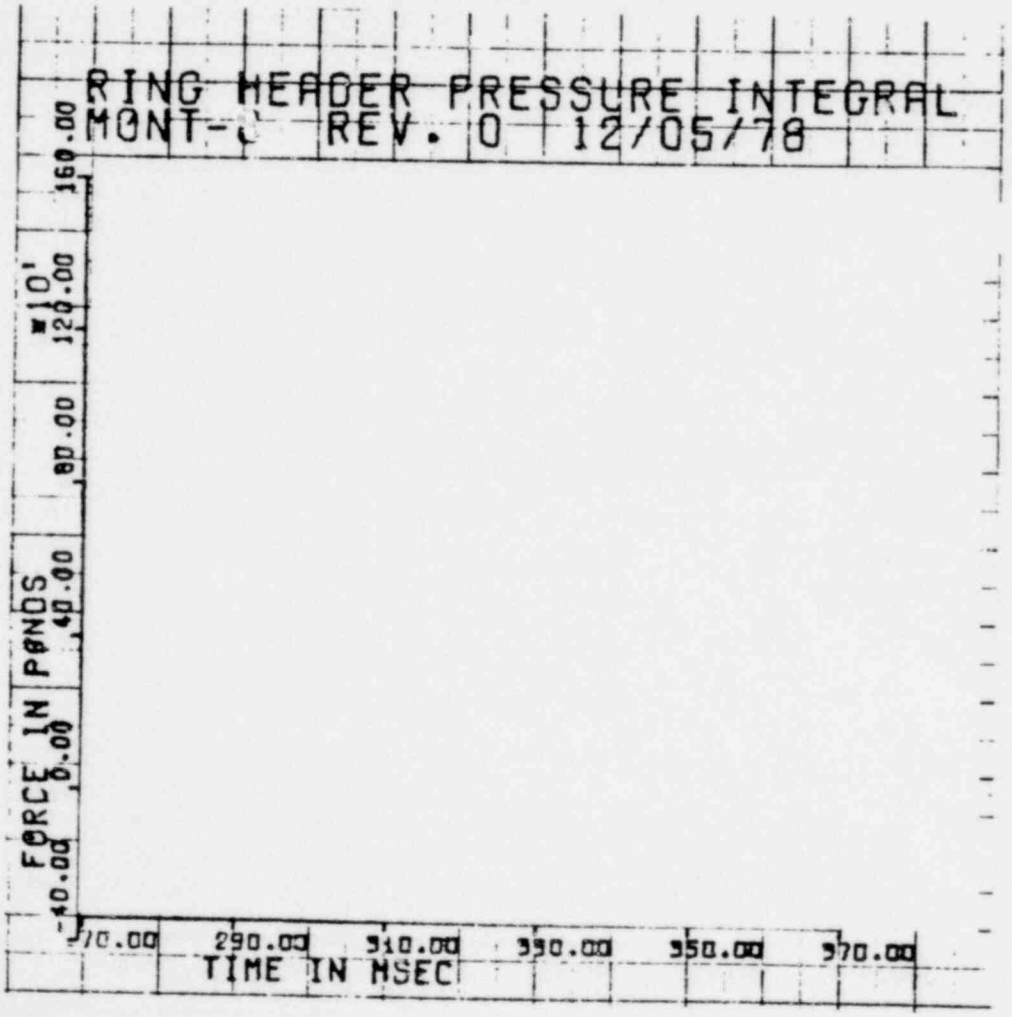

FIGURE B-21

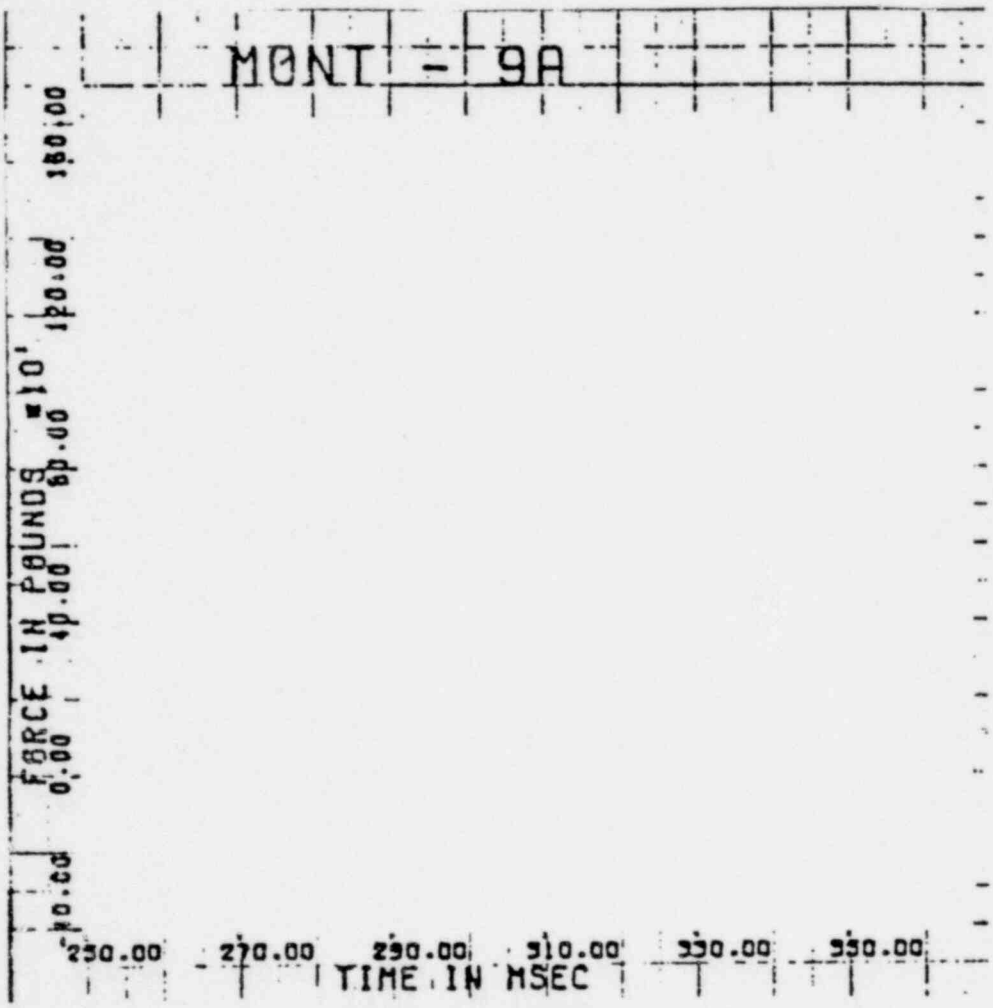

FIGURE B-22

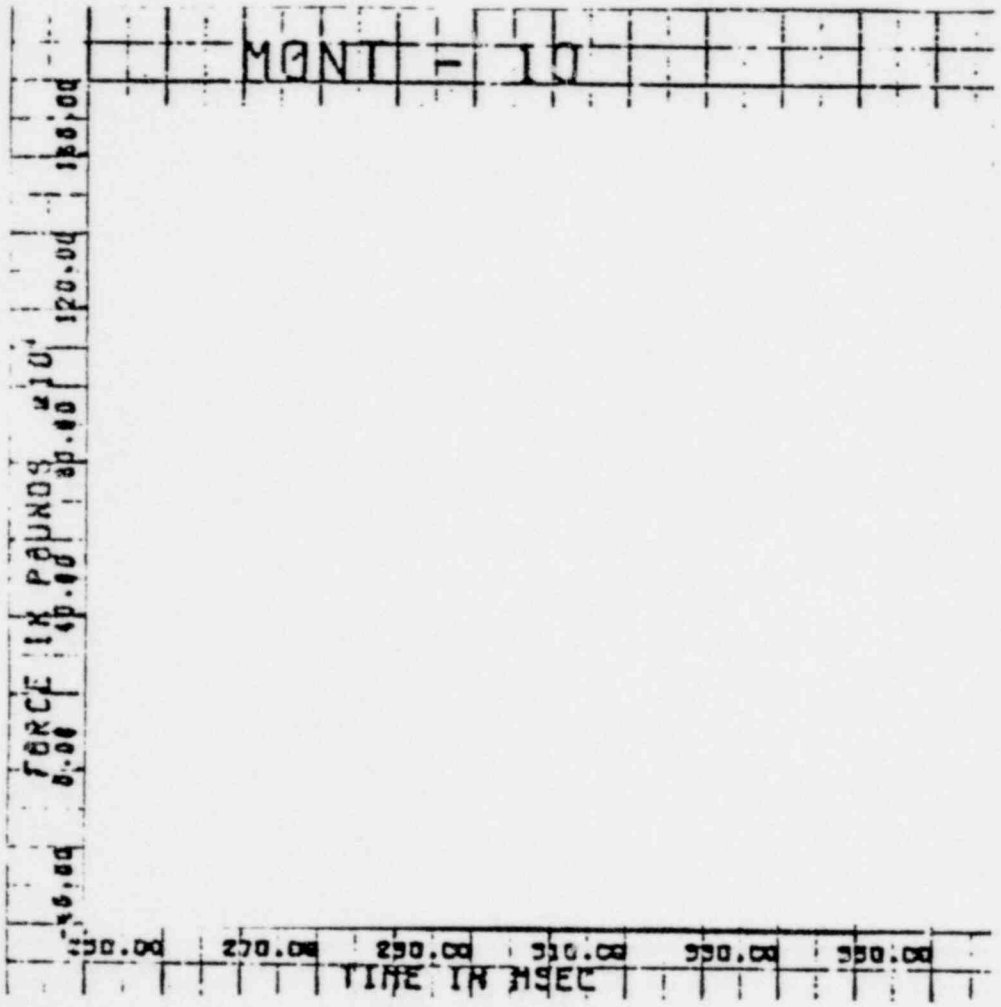

FIGURE B-23

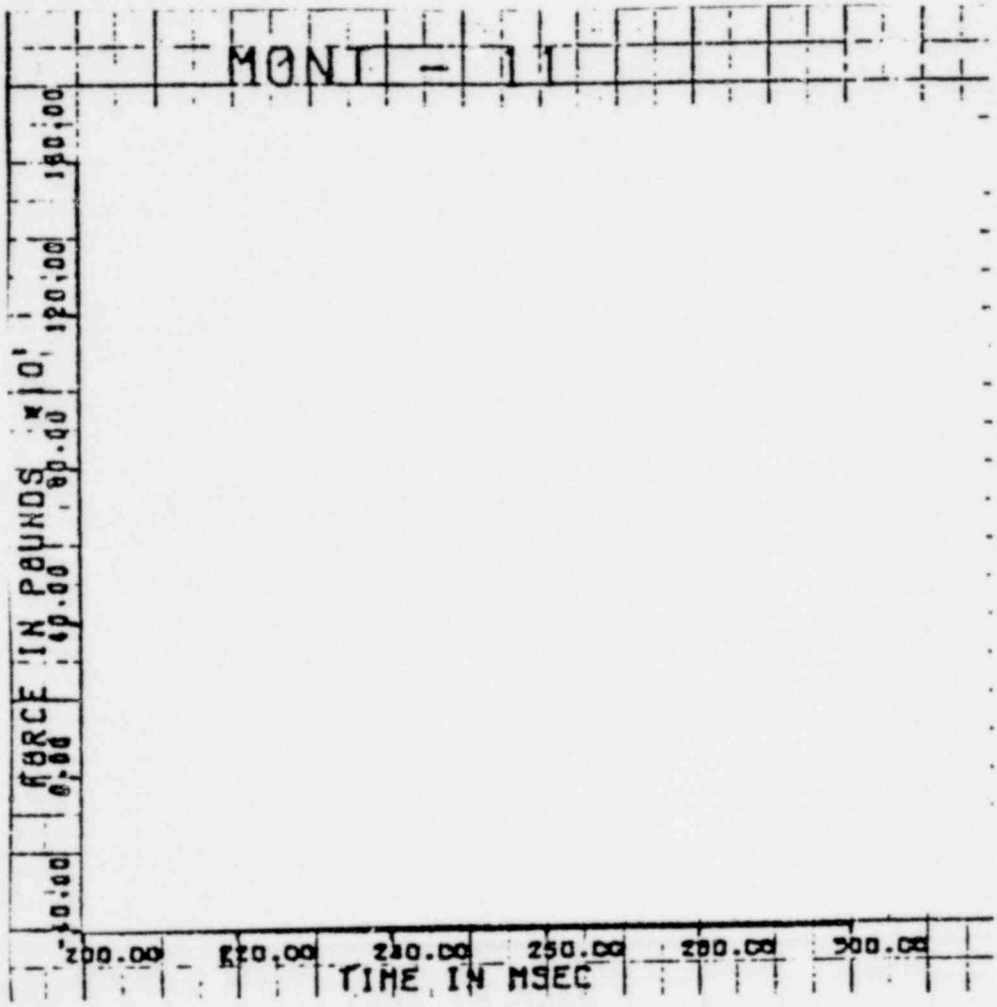

FIGURE B-24

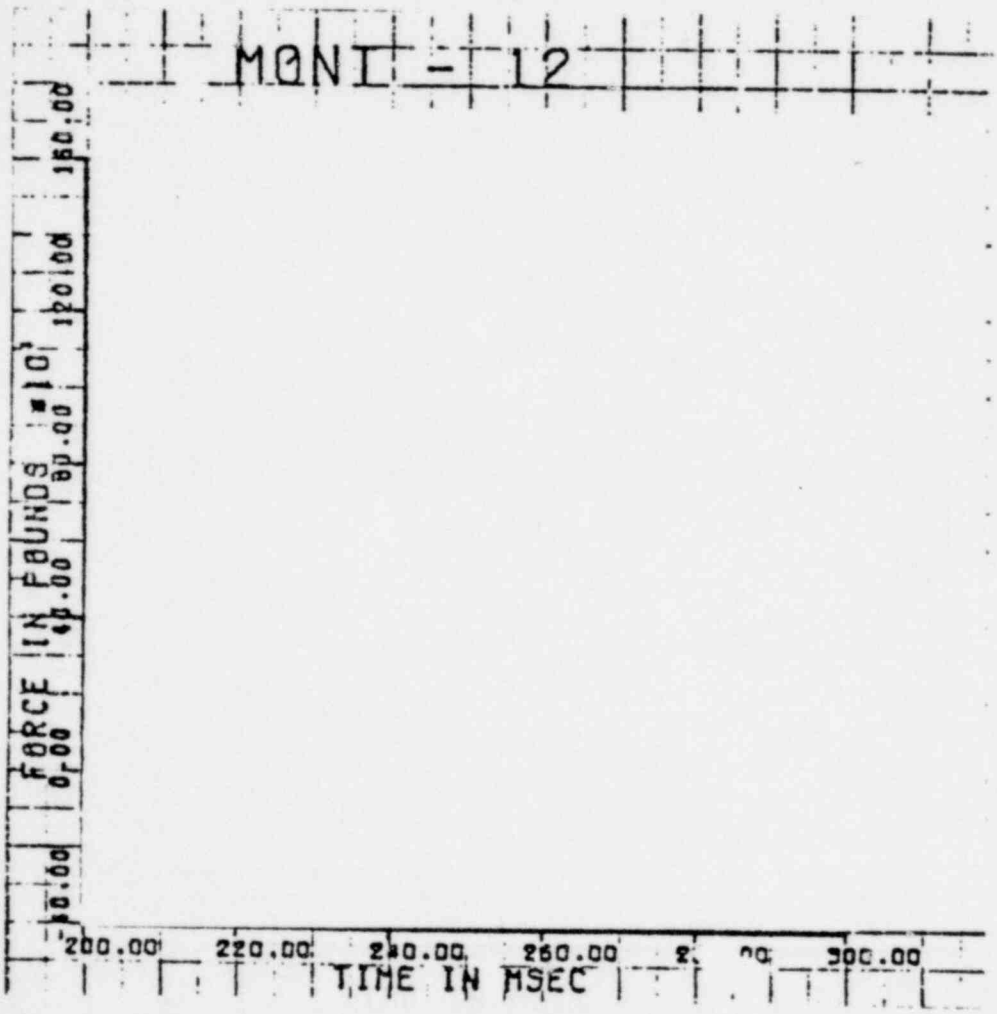

FIGURE B-25

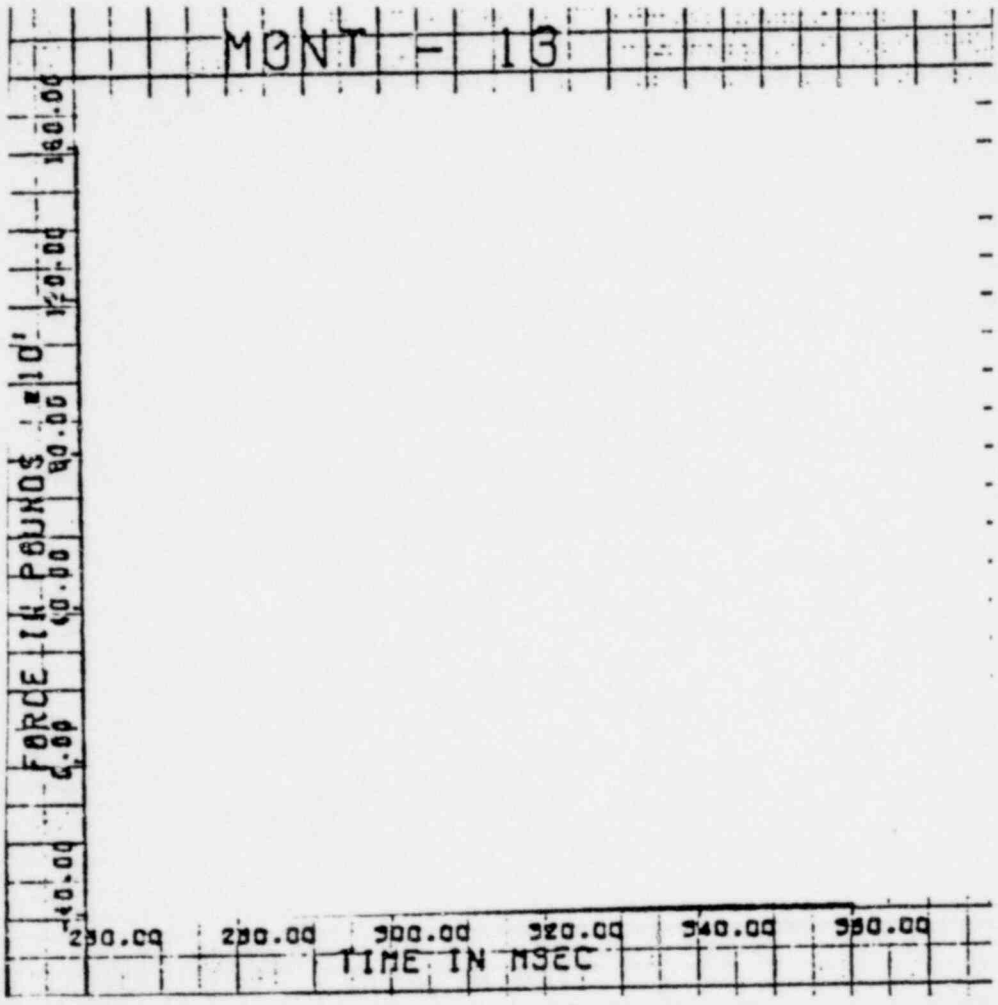

FIGURE B-26

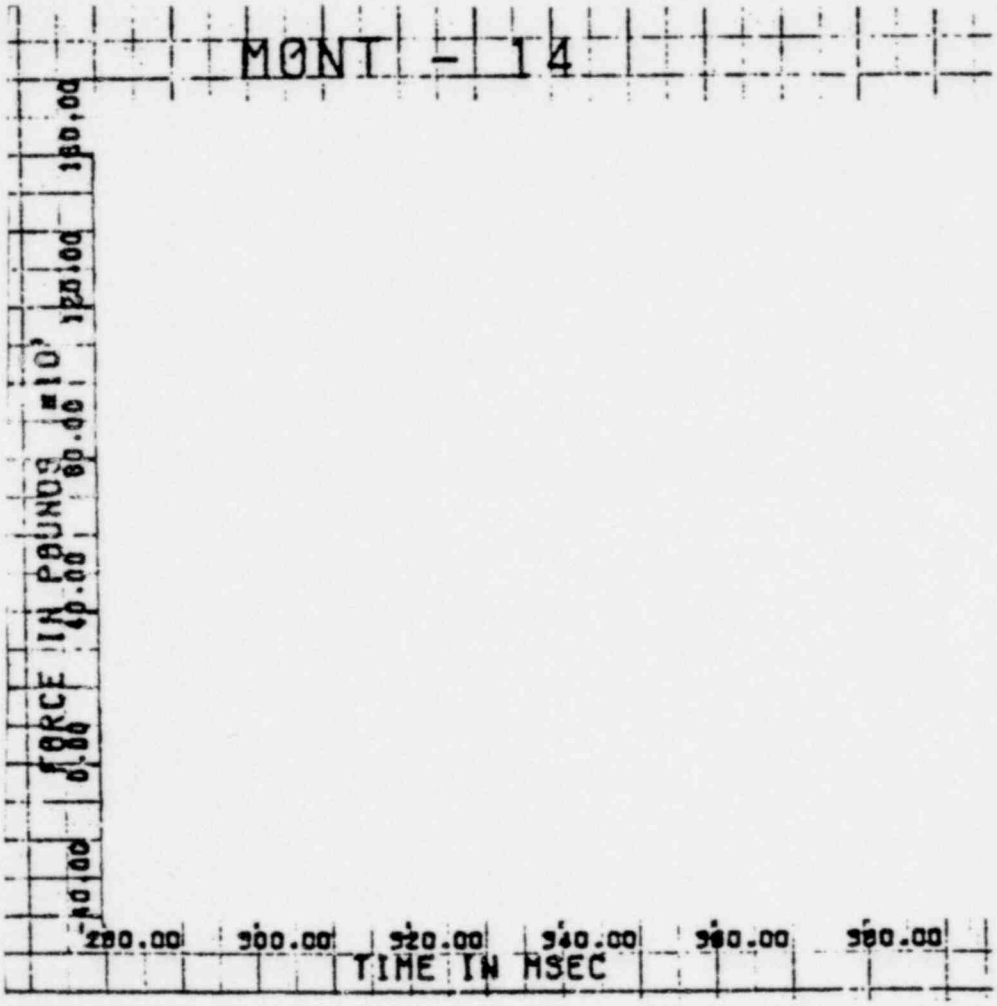

FIGURE B-27

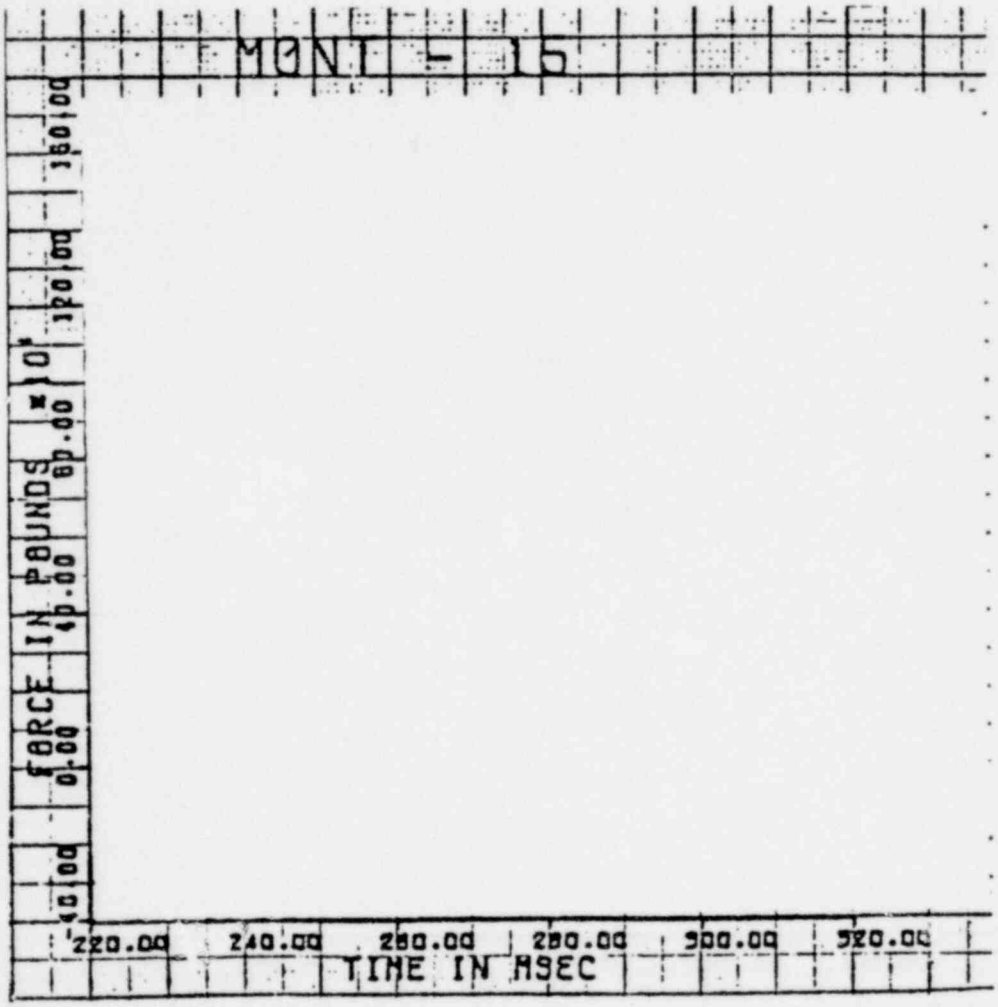

FIGURE B-28

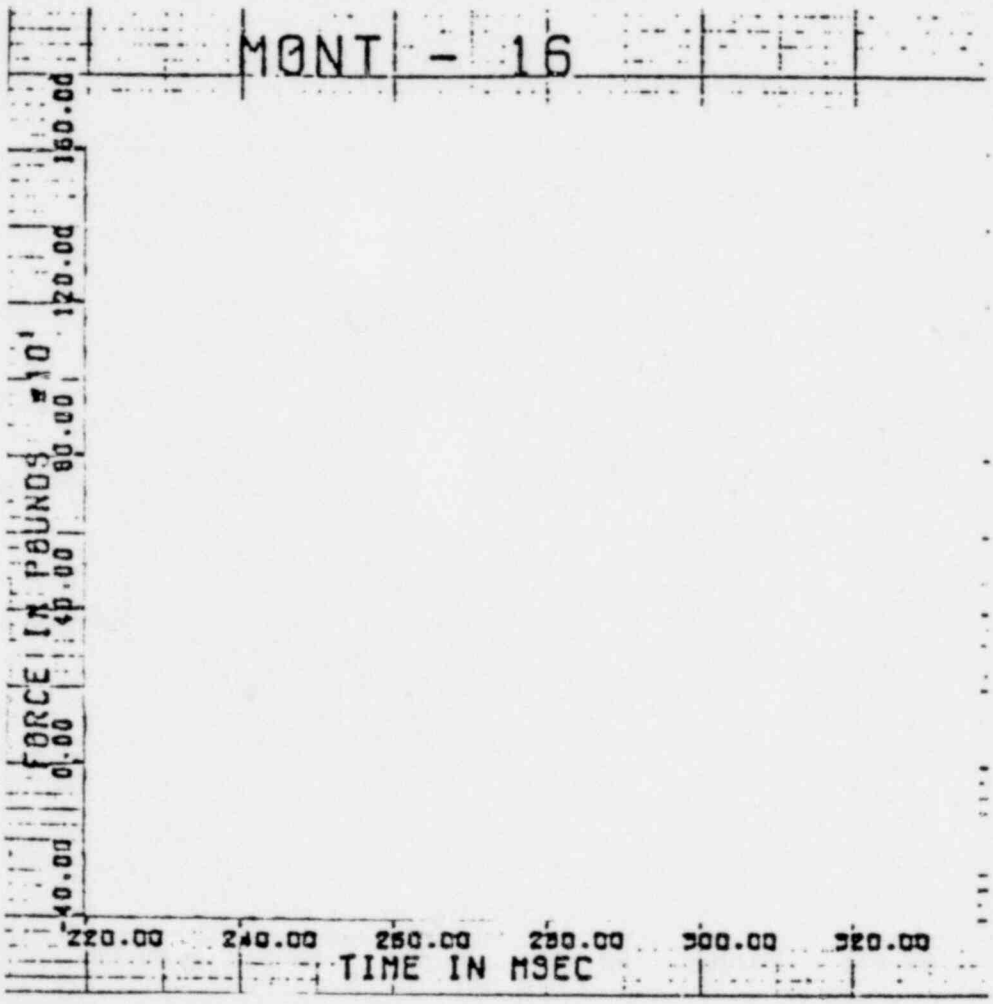

FIGURE B-29

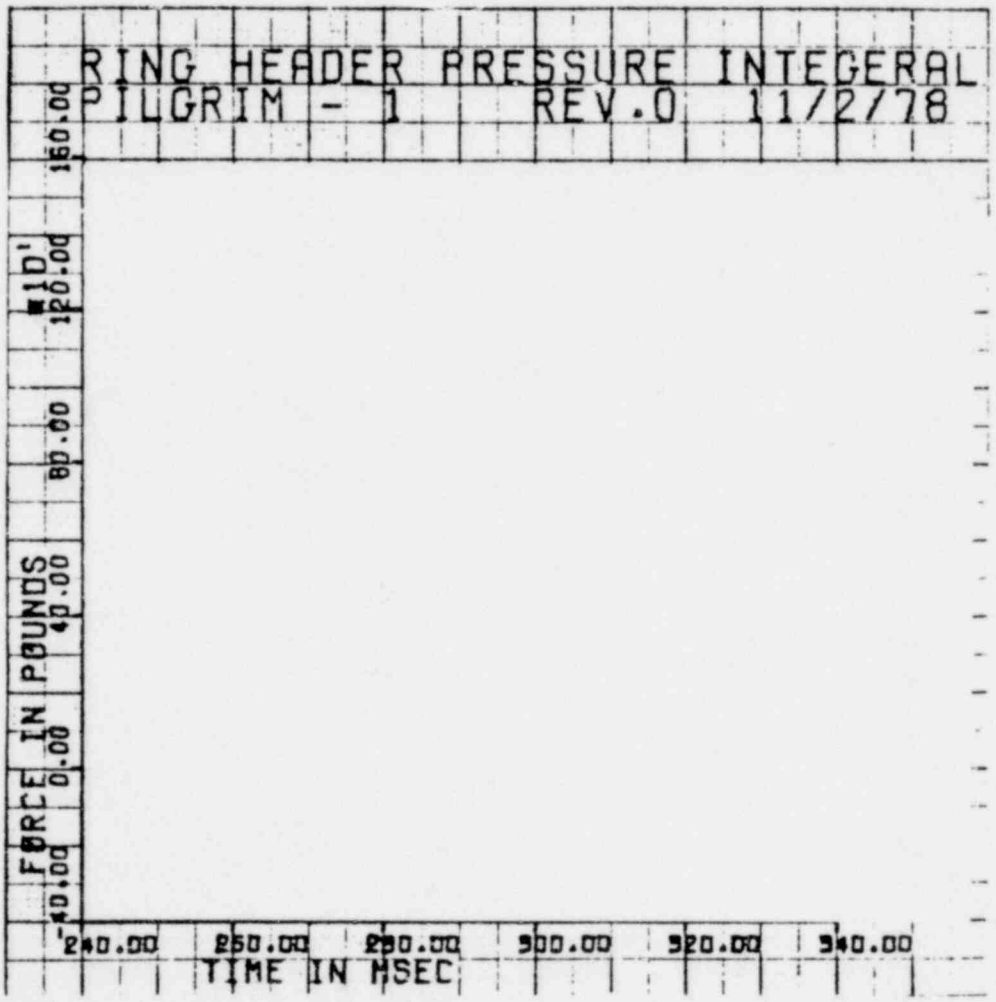

FIGURE B-30

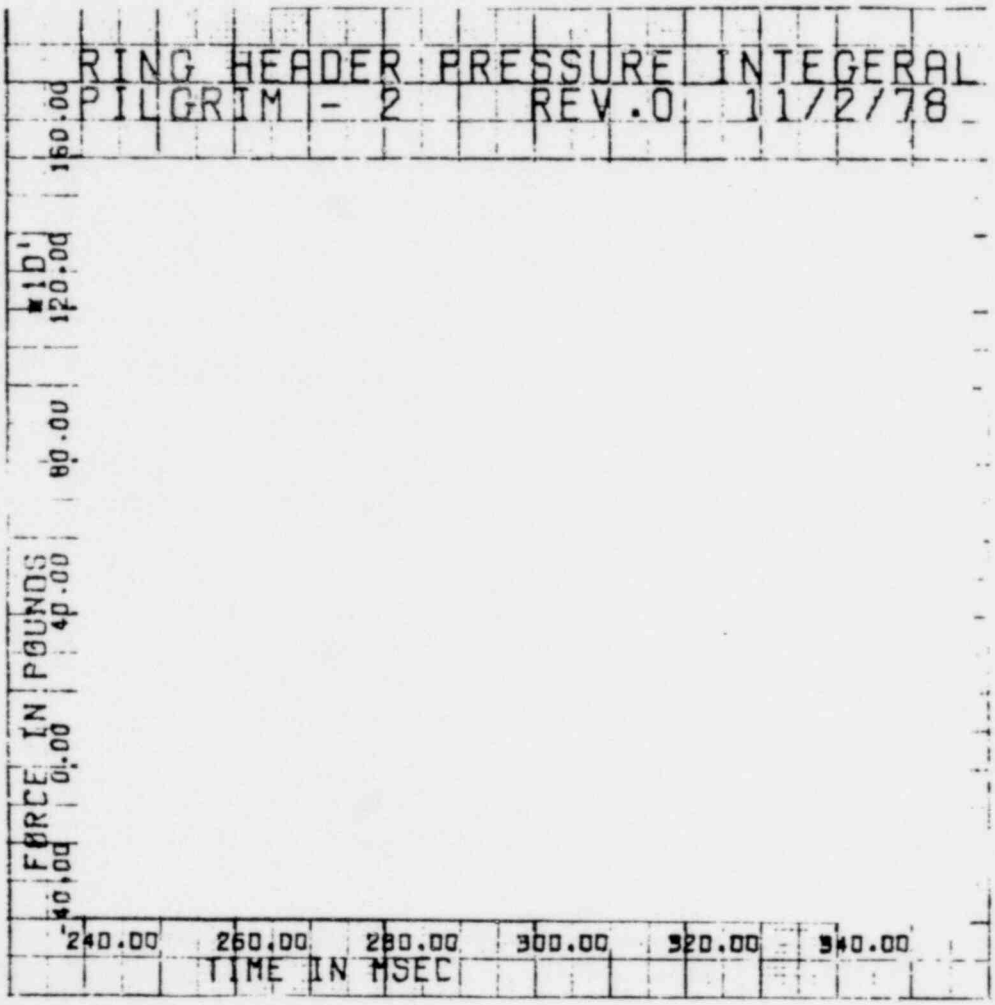

FIGURE B-31

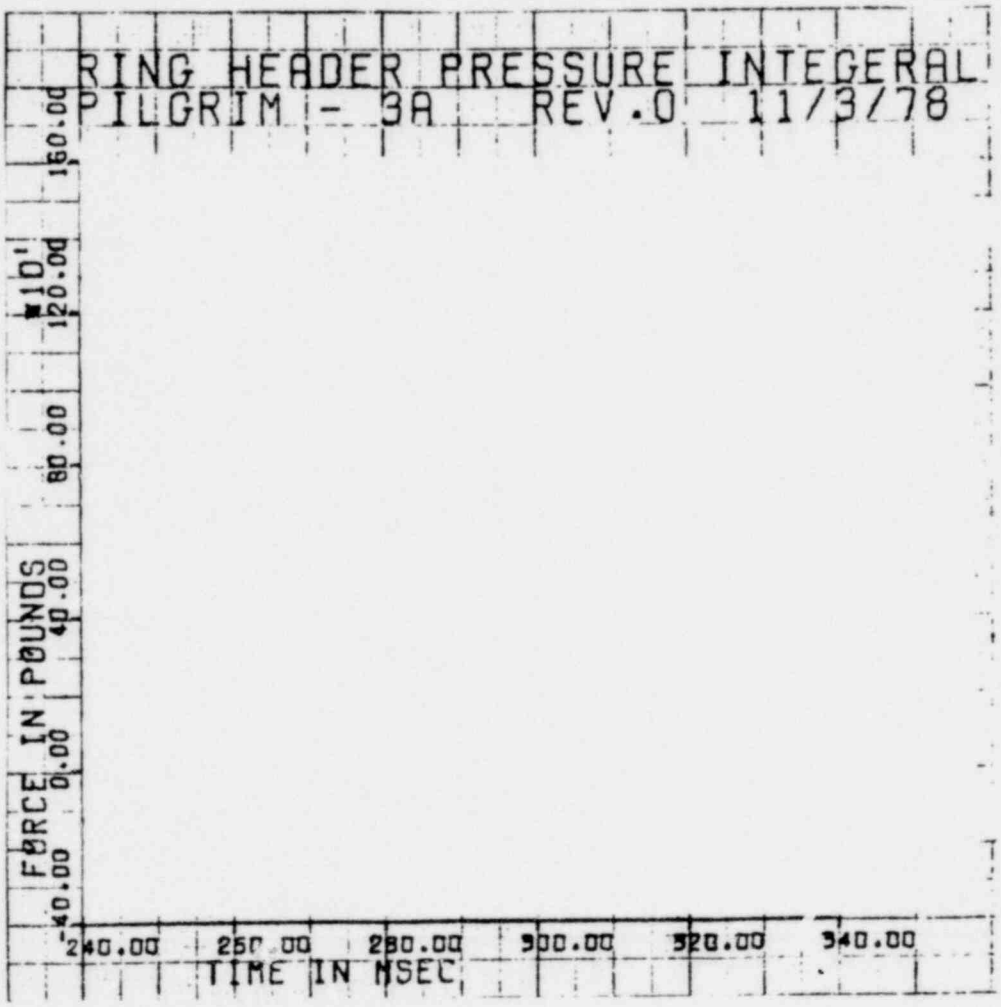

FIGURE B-3?

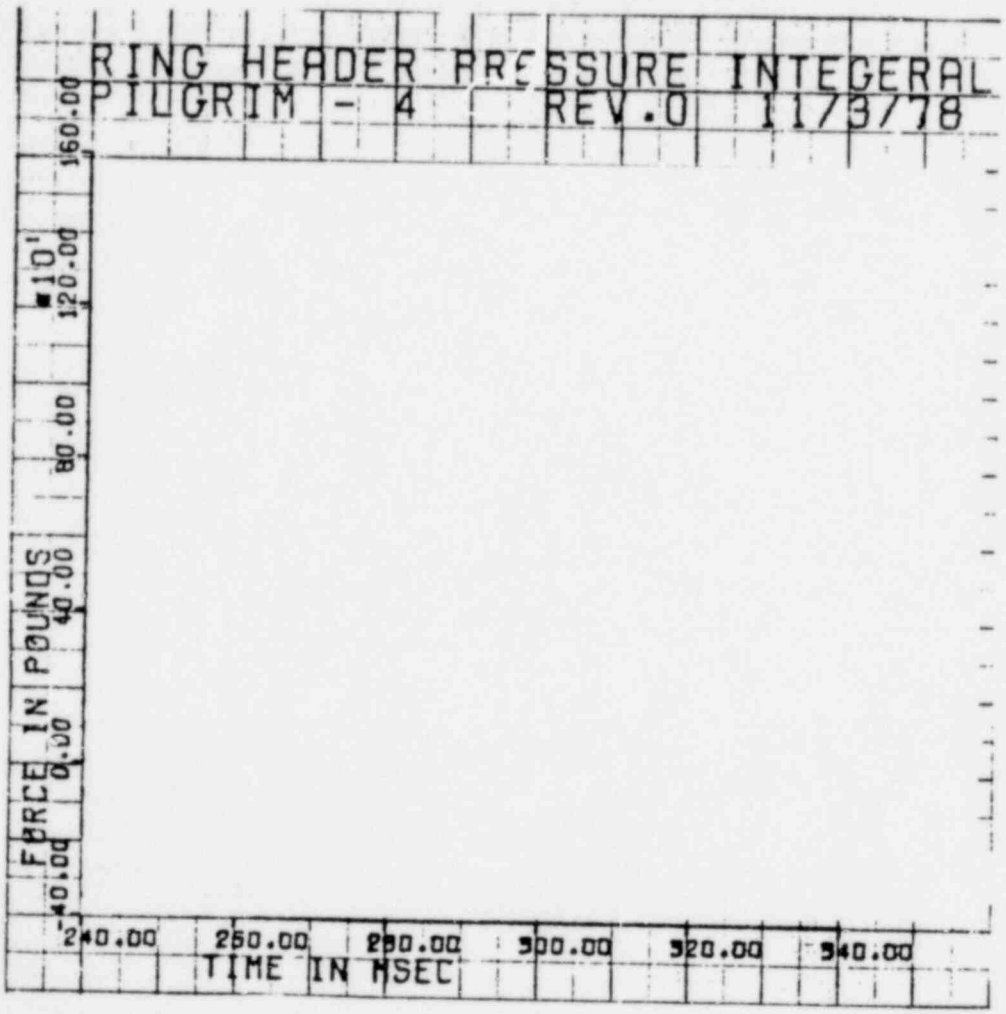

FIGURE B-33

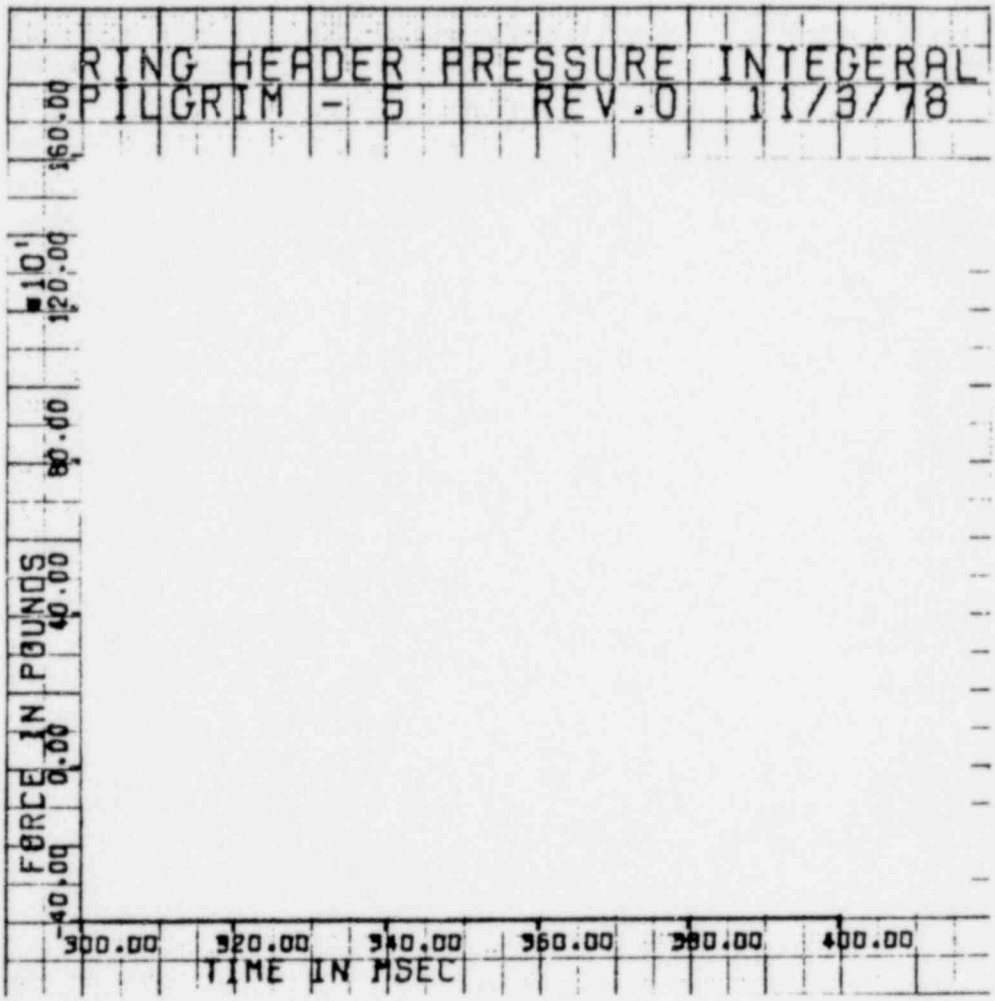

FIGURE B-34

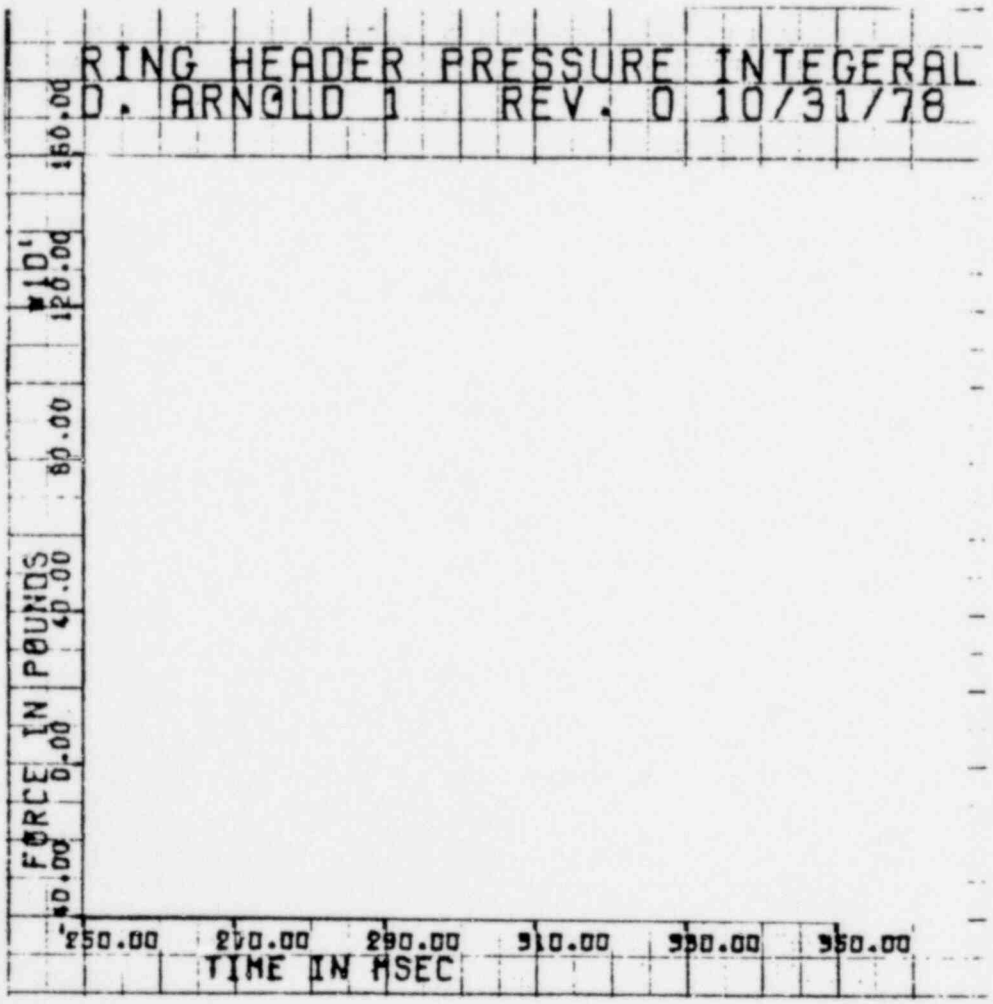

FIGURE B-35

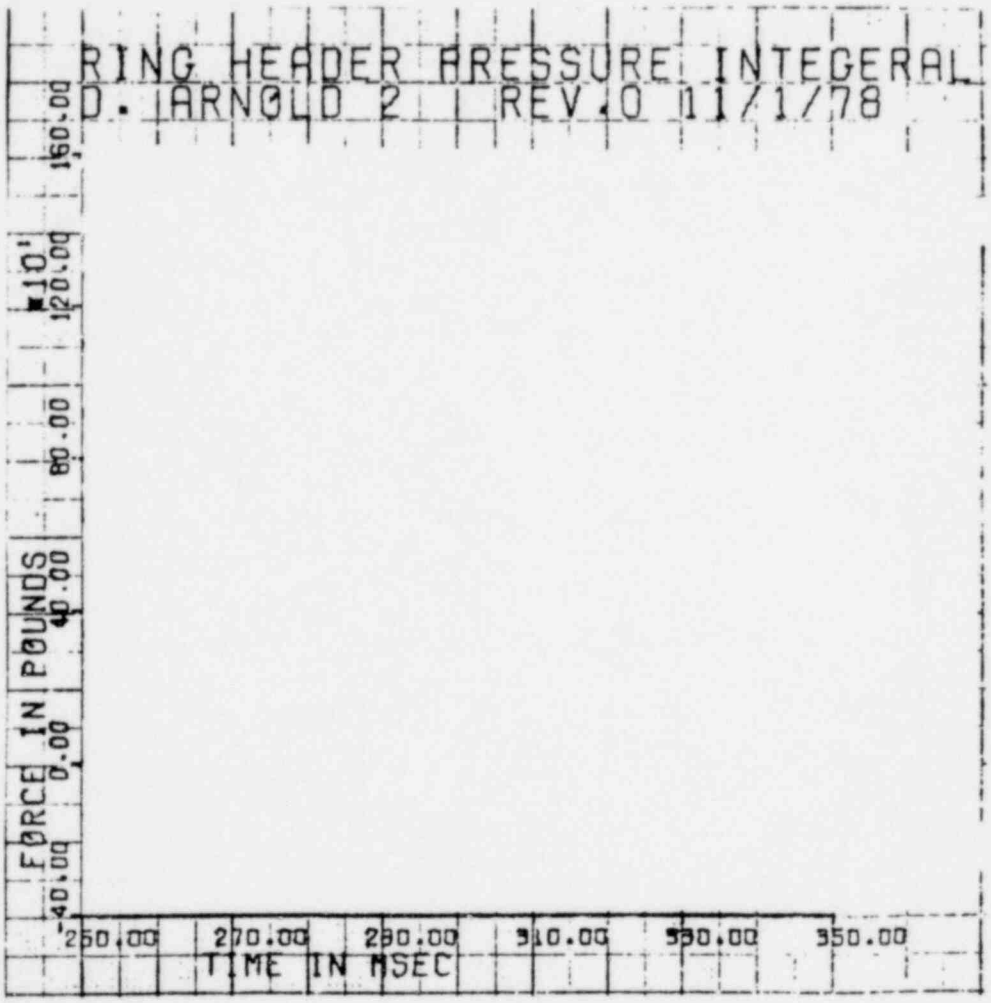

FIGURE B-36

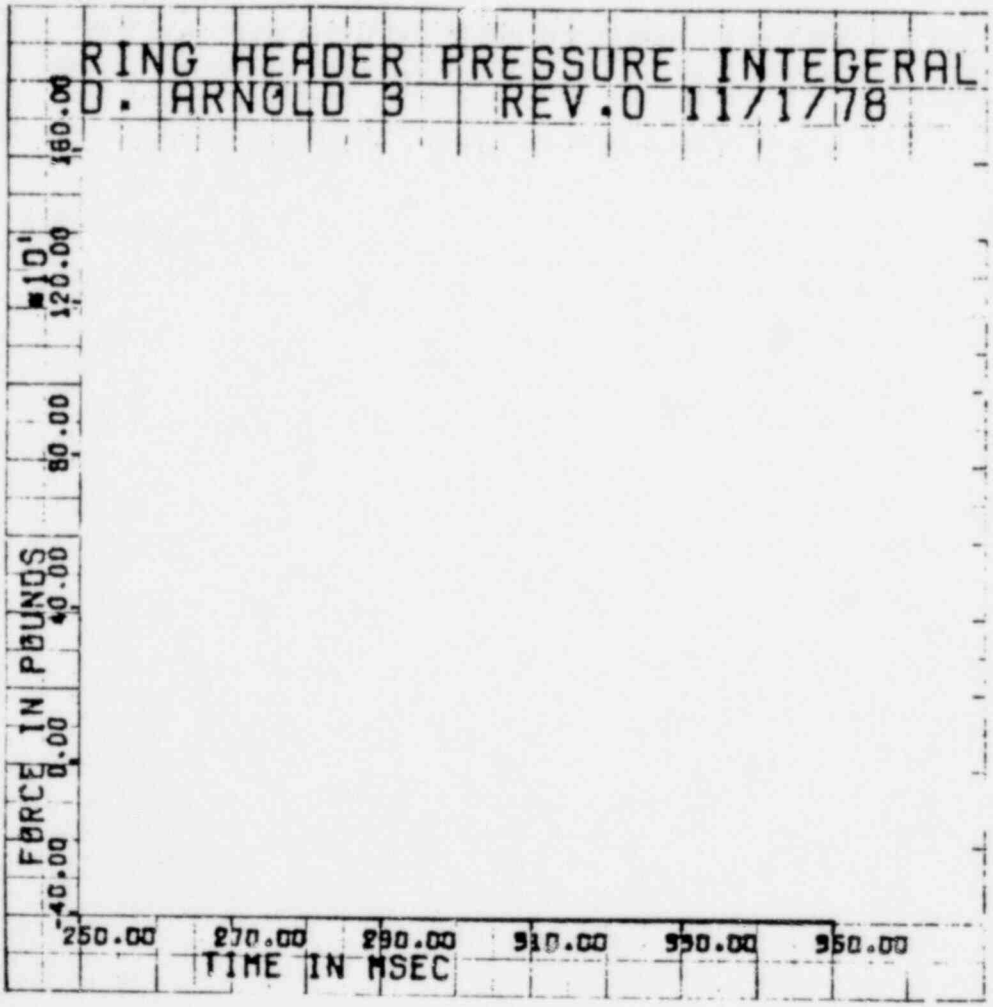

FIGURE B-37

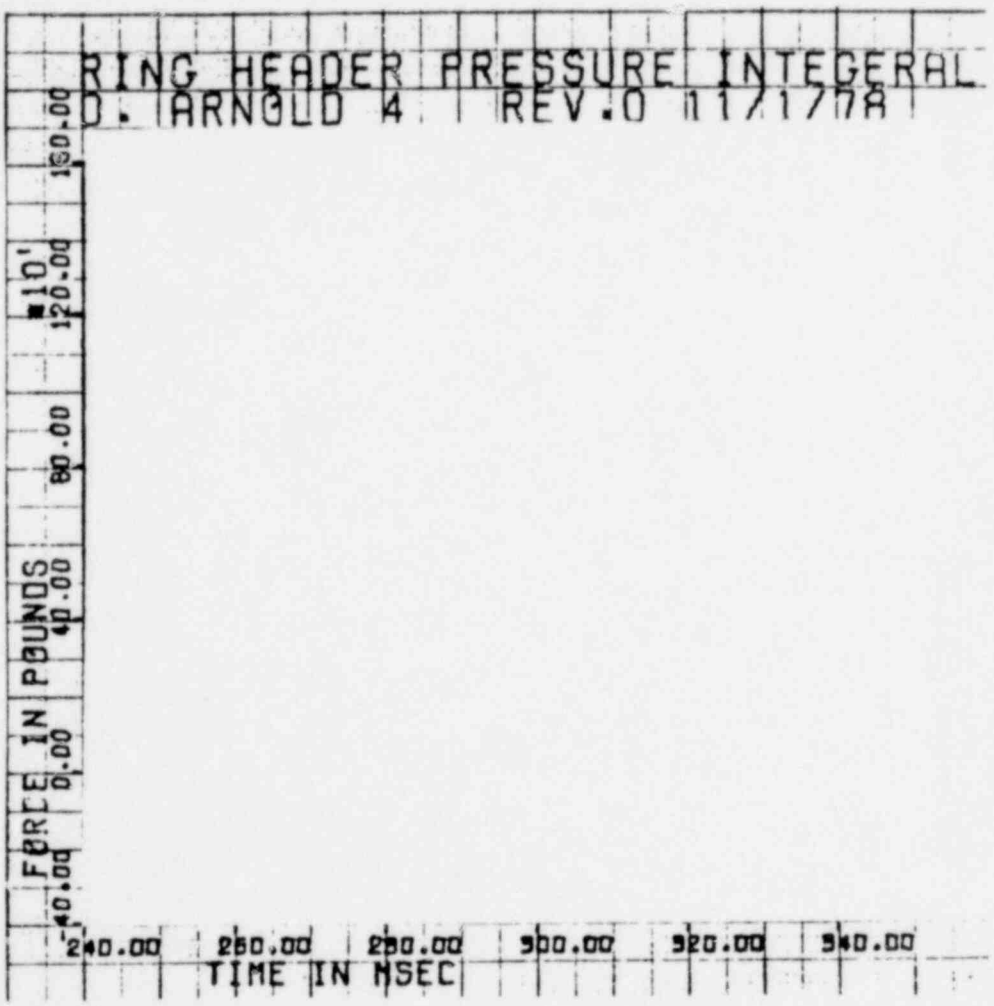

FIGURE B-38

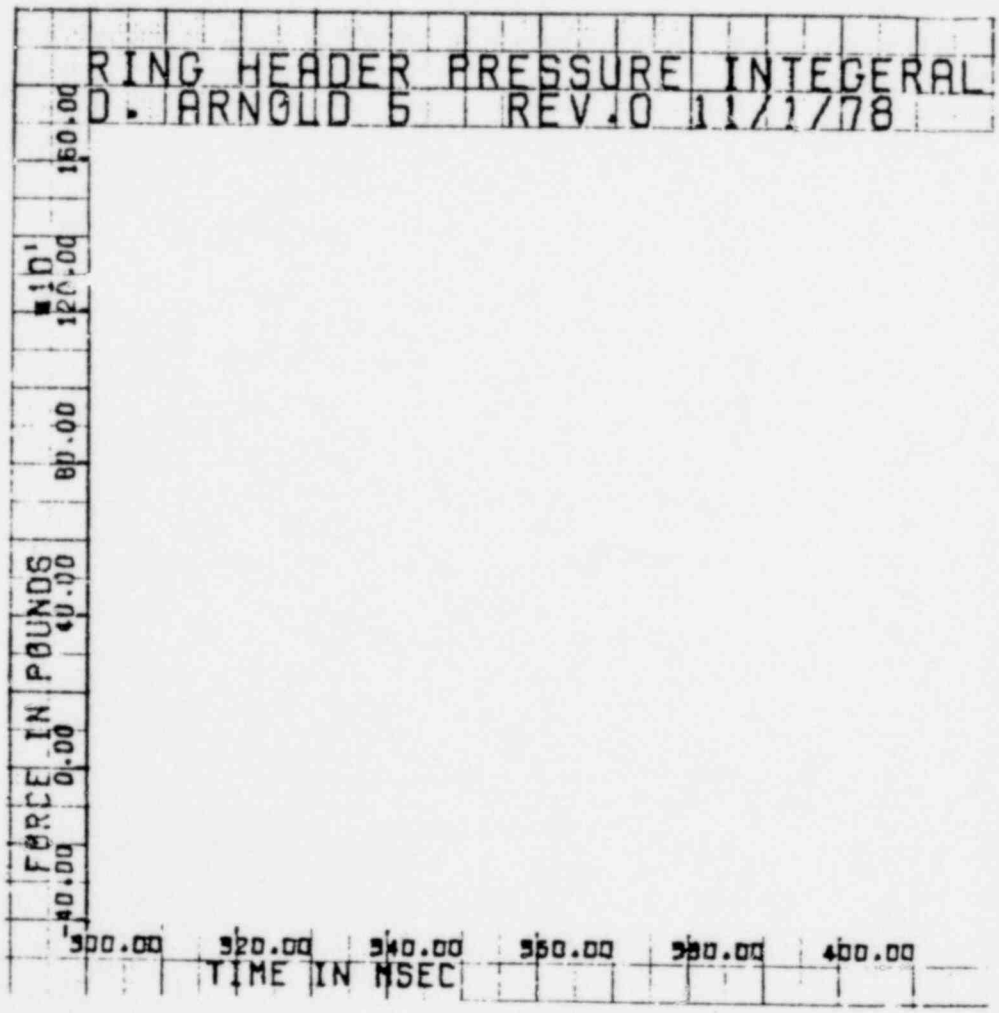

FIGURE B-39

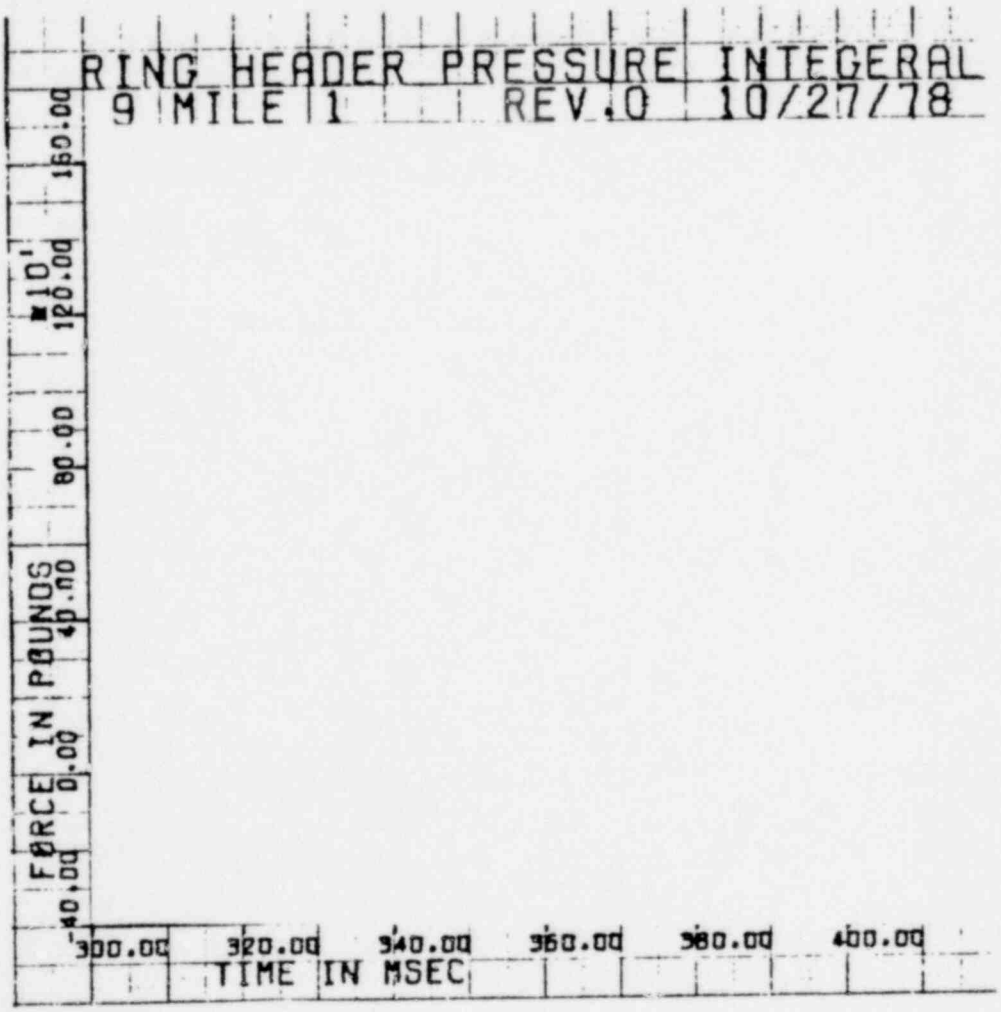

FIGURE B-40

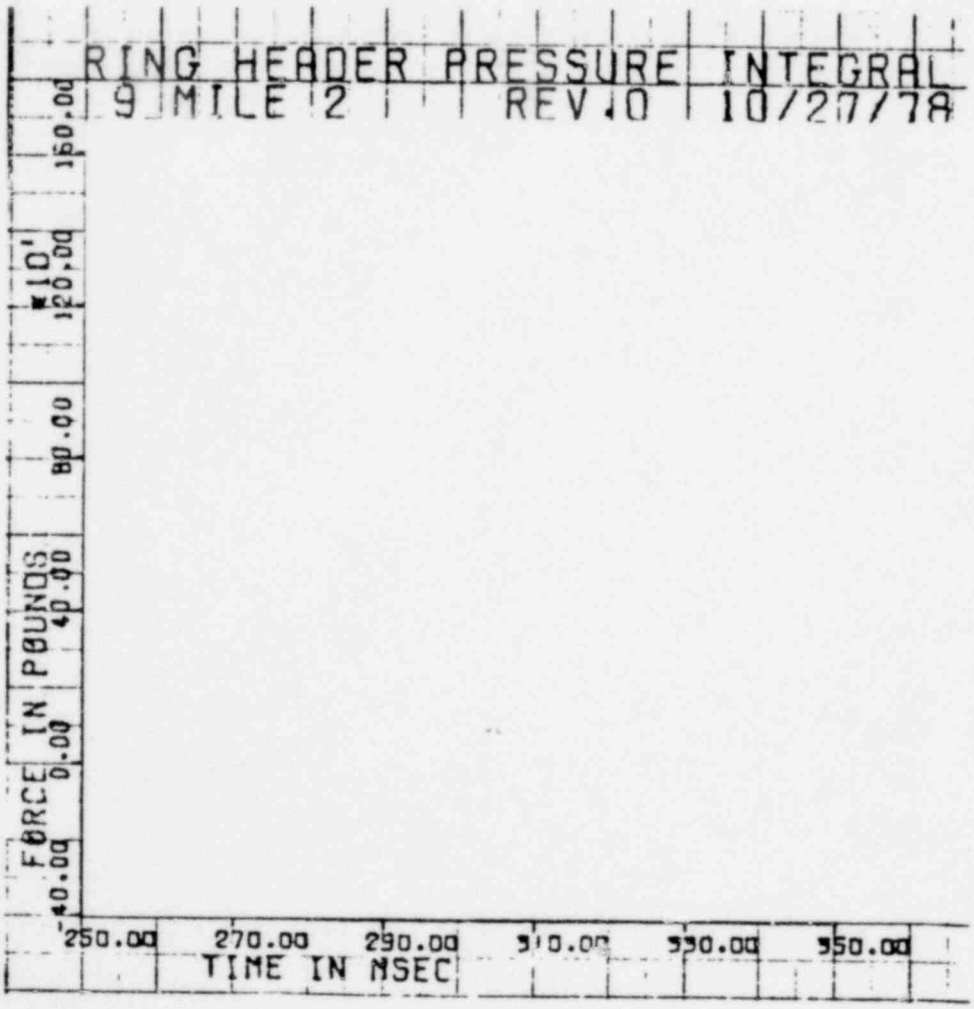

FIGURE B-41

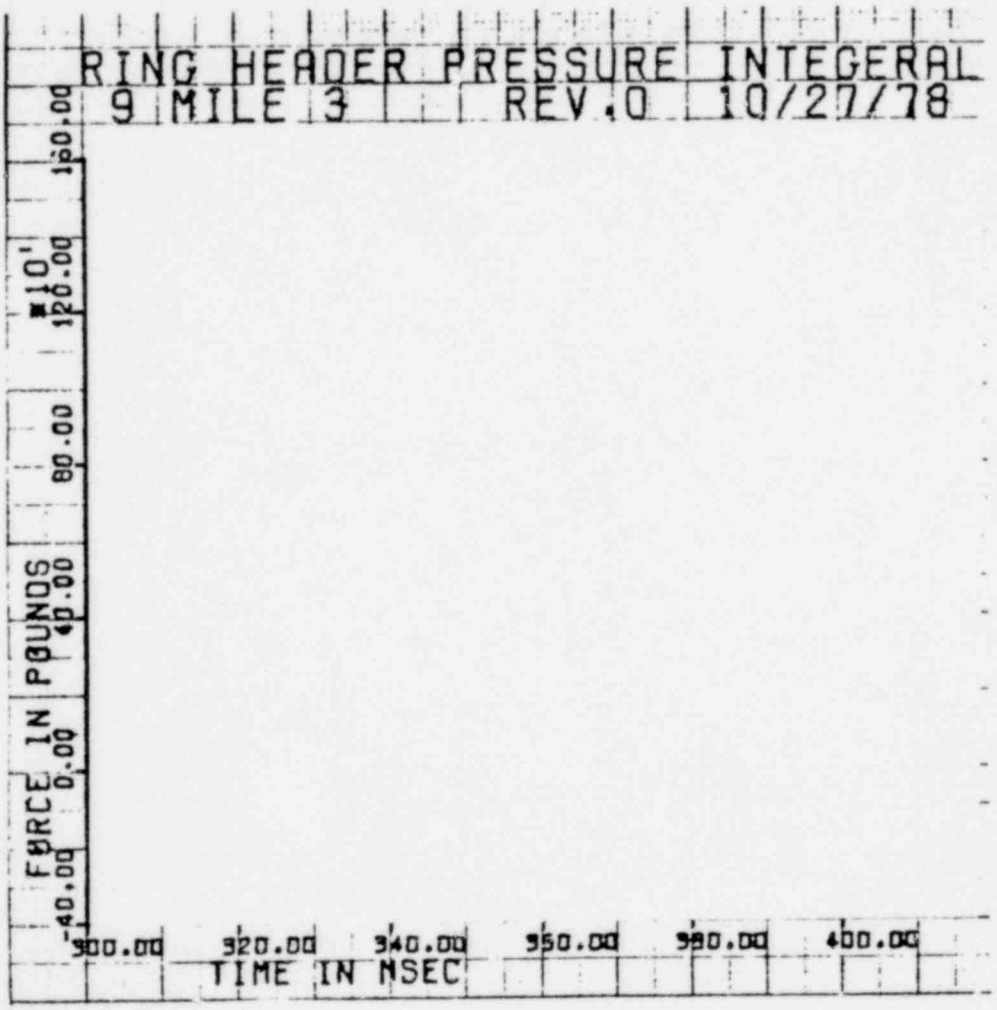

FIGURE B-42

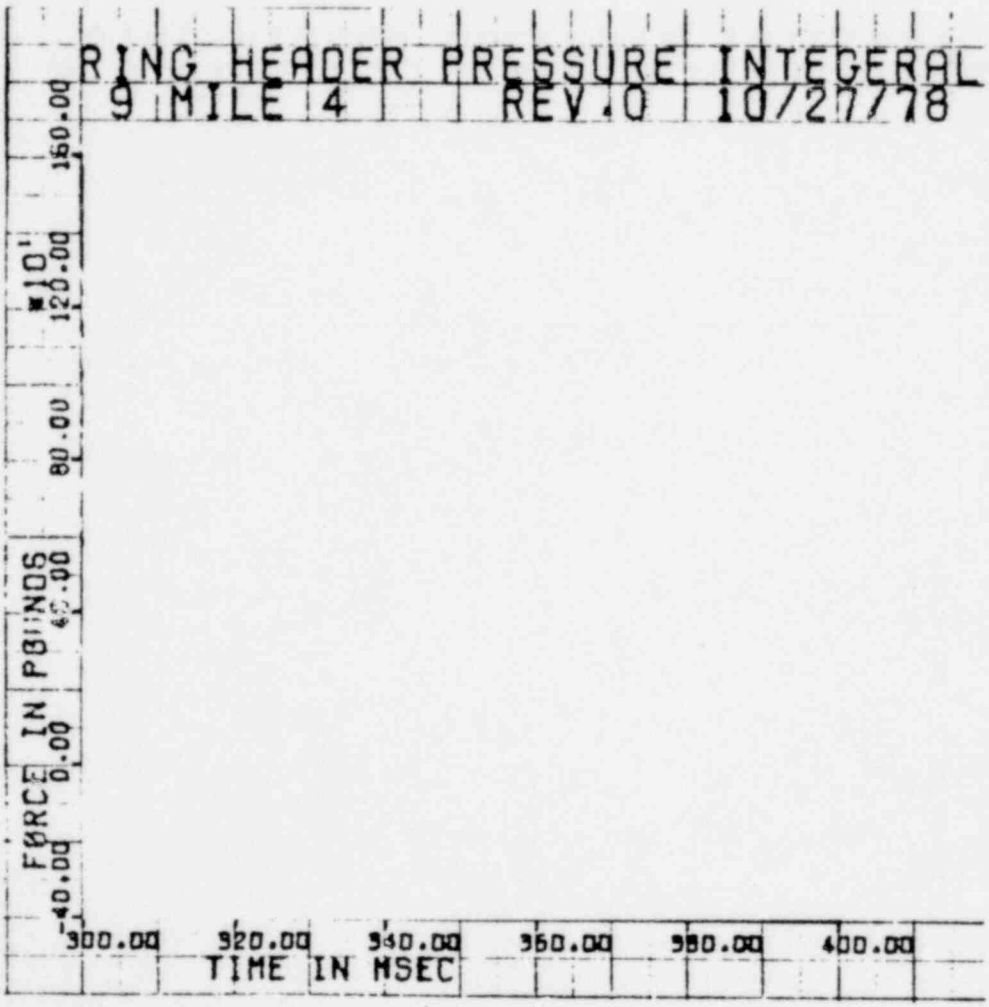

1351 039

FIGURE B-43

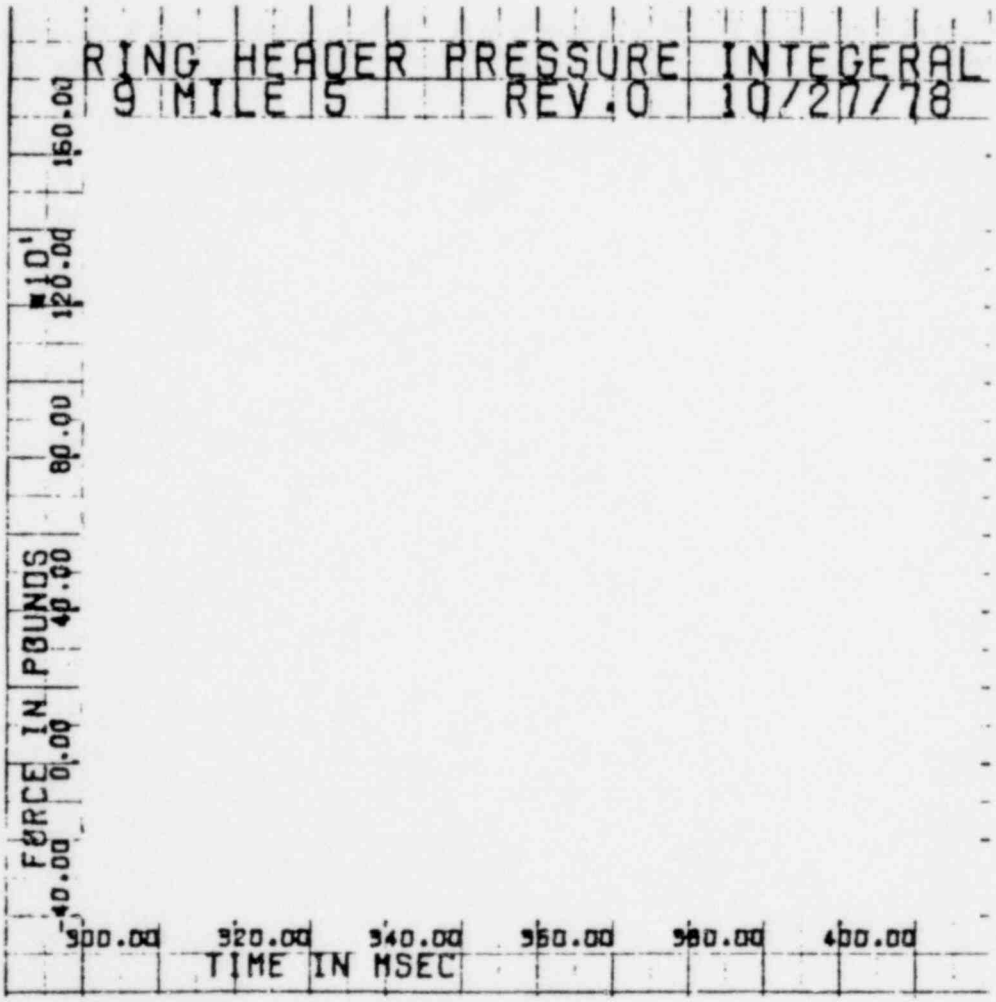

FIGURE B-44

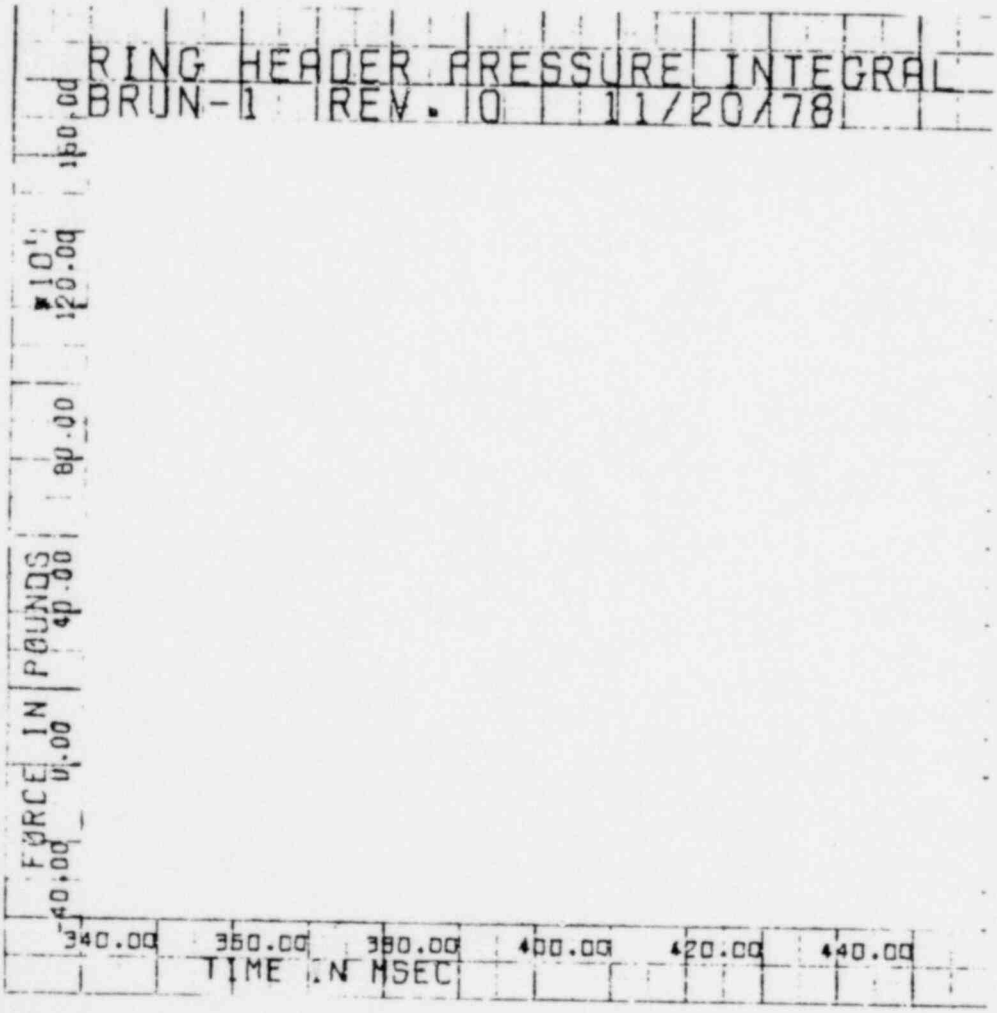

FIGURE B-45

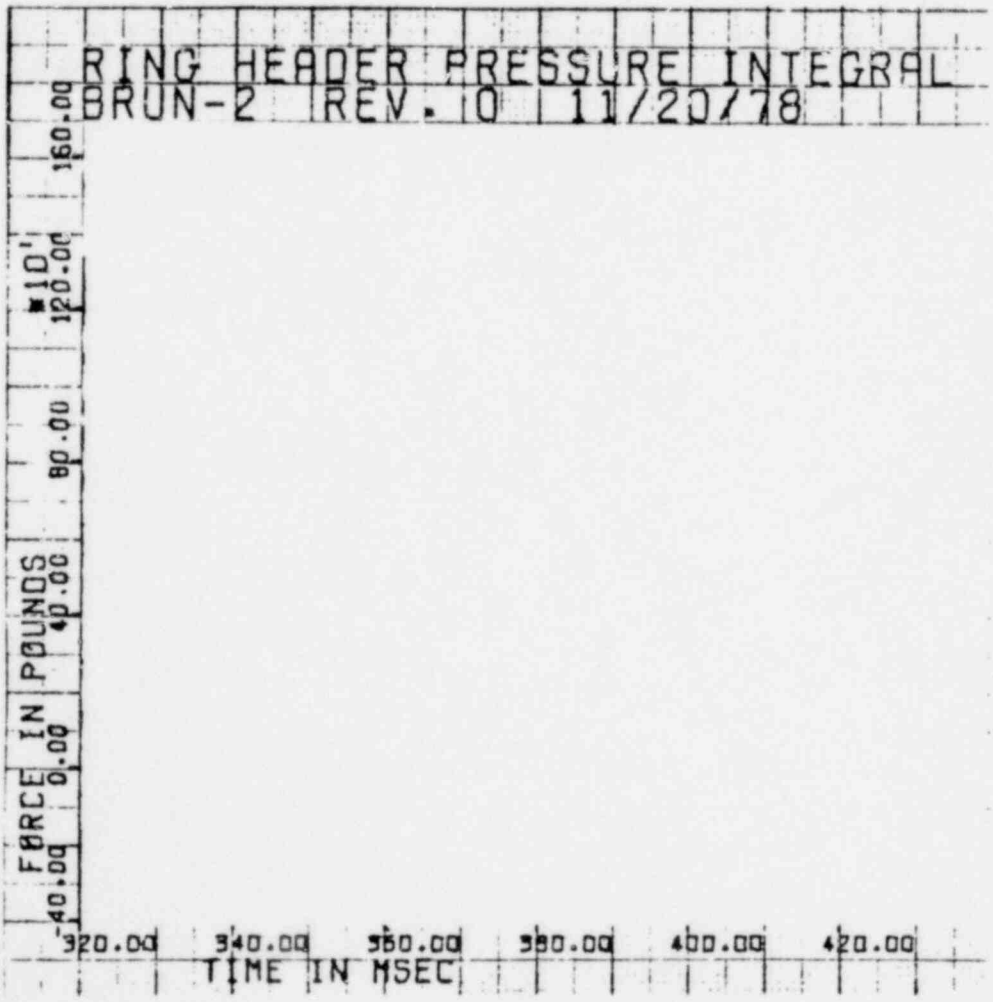

FIGURE B-46

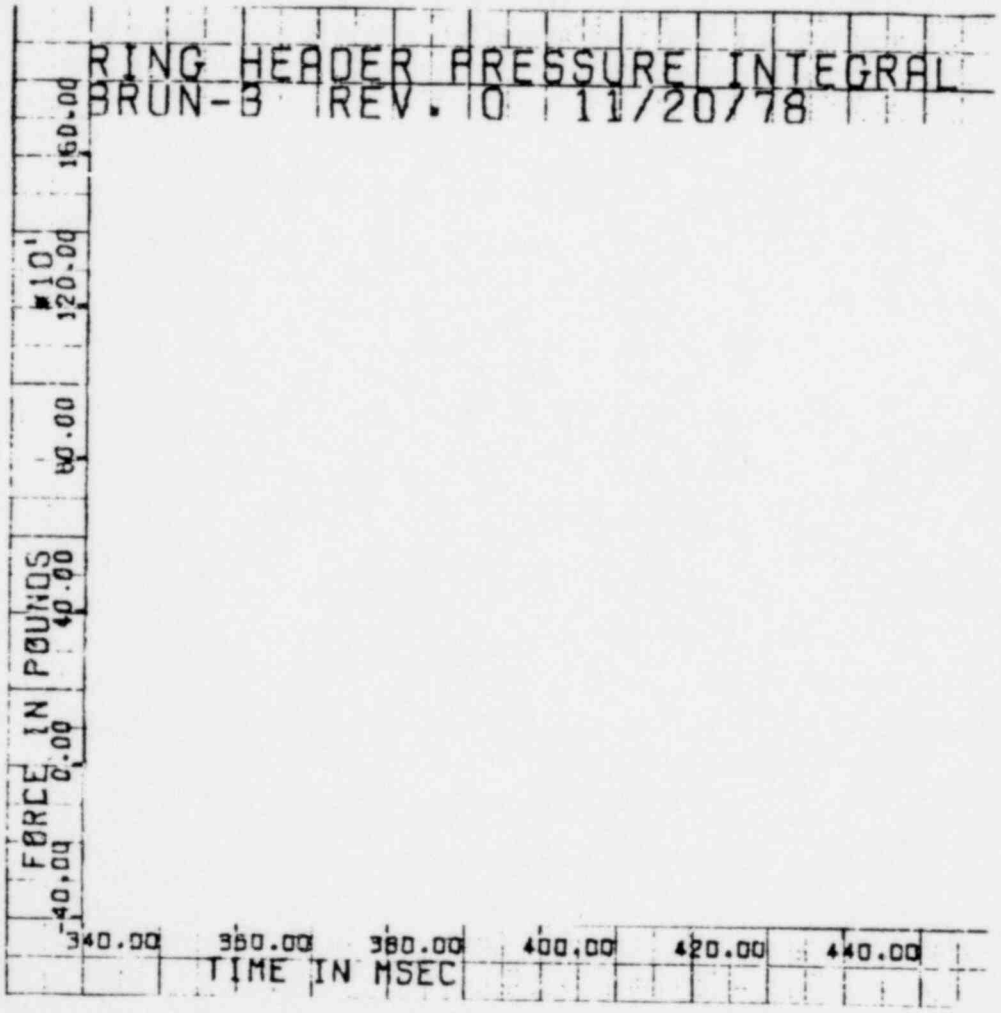

FIGURE B-47

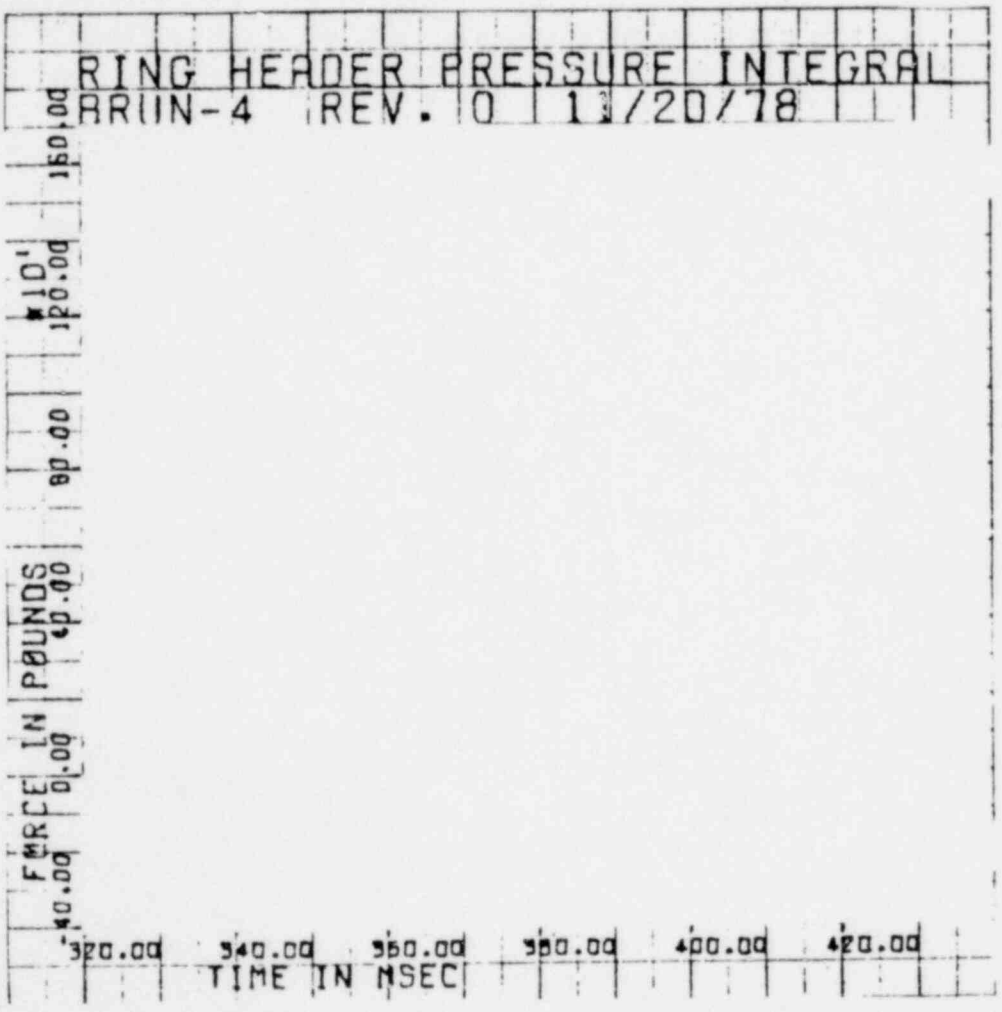

FIGURE B-48

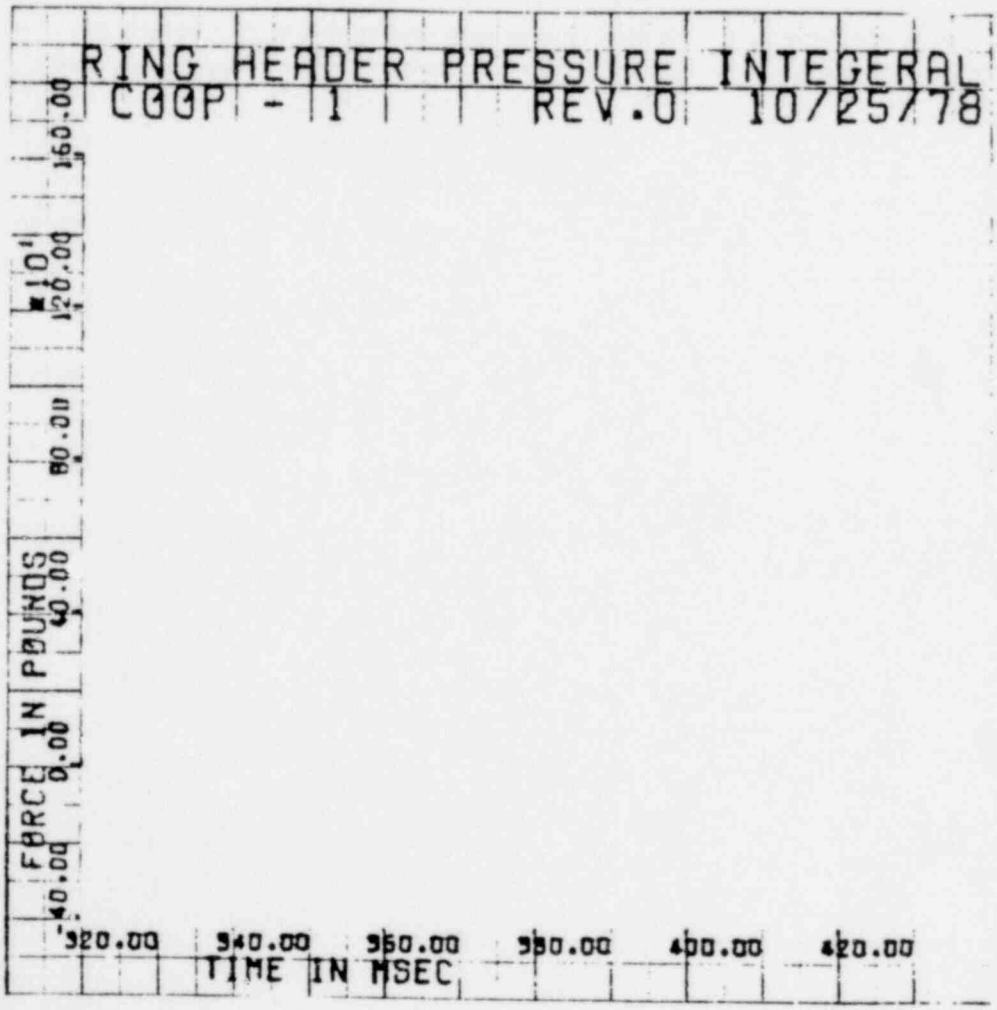

FIGURE B-49

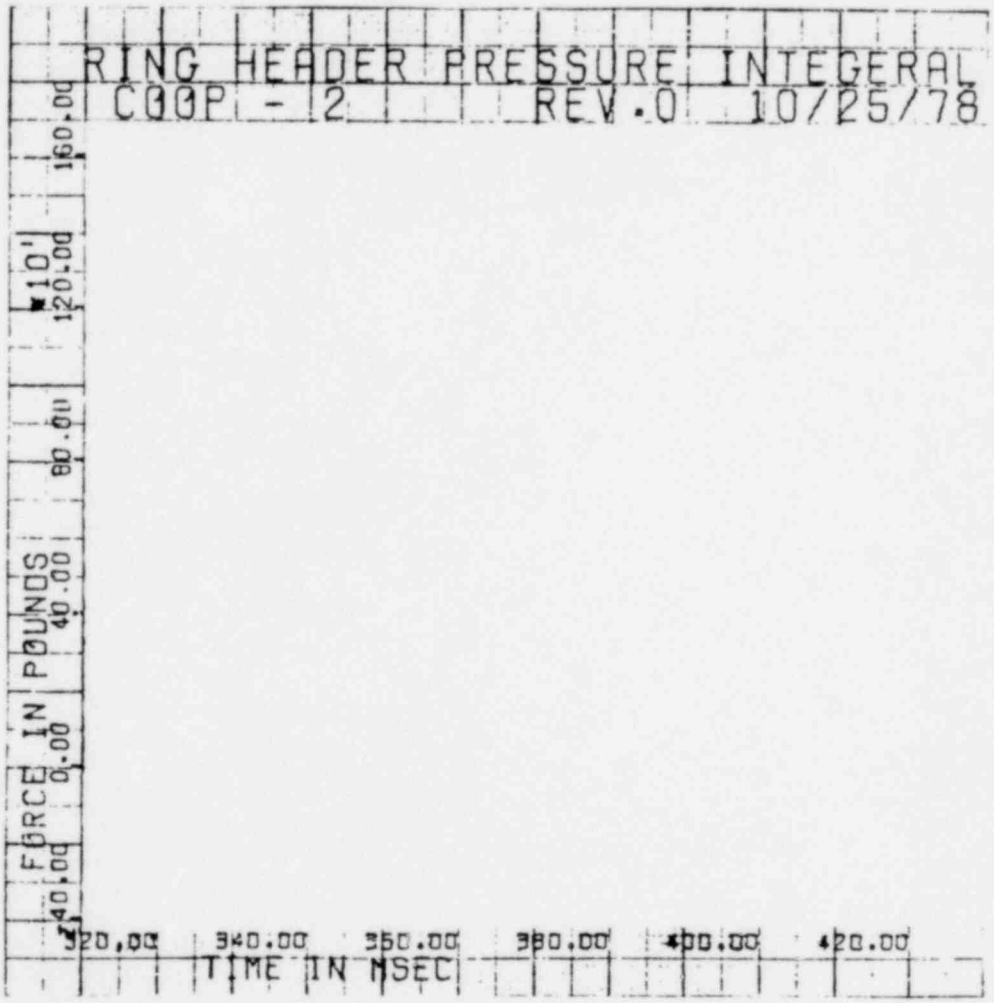

FIGURE B-50

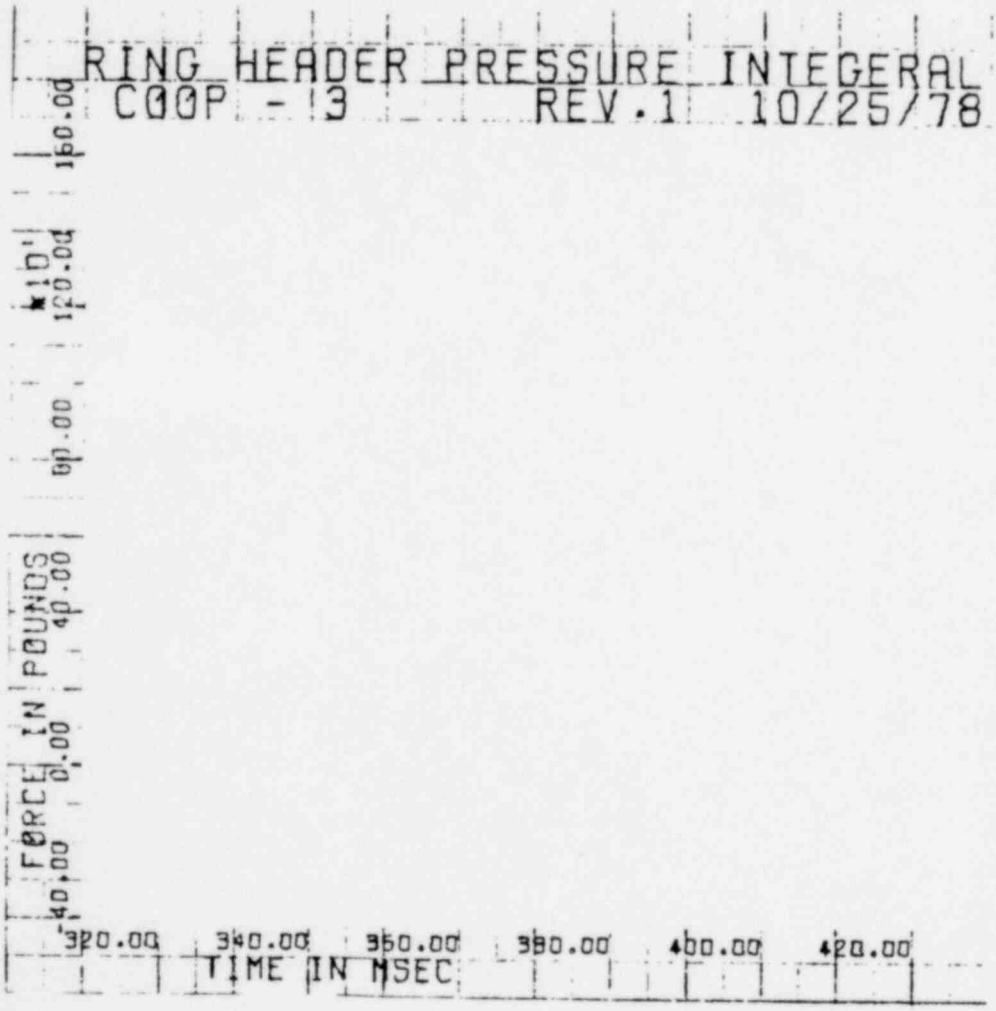

FIGURE B-51

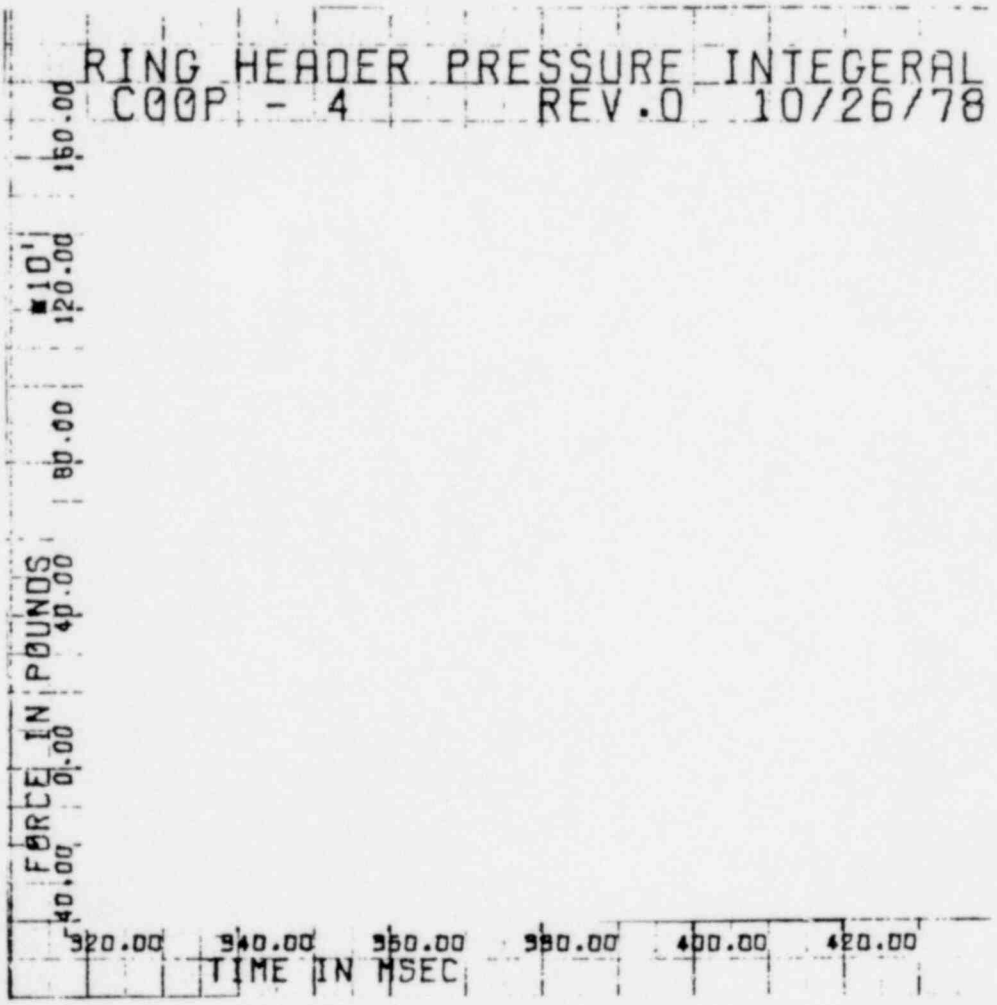

FIGURE B-52

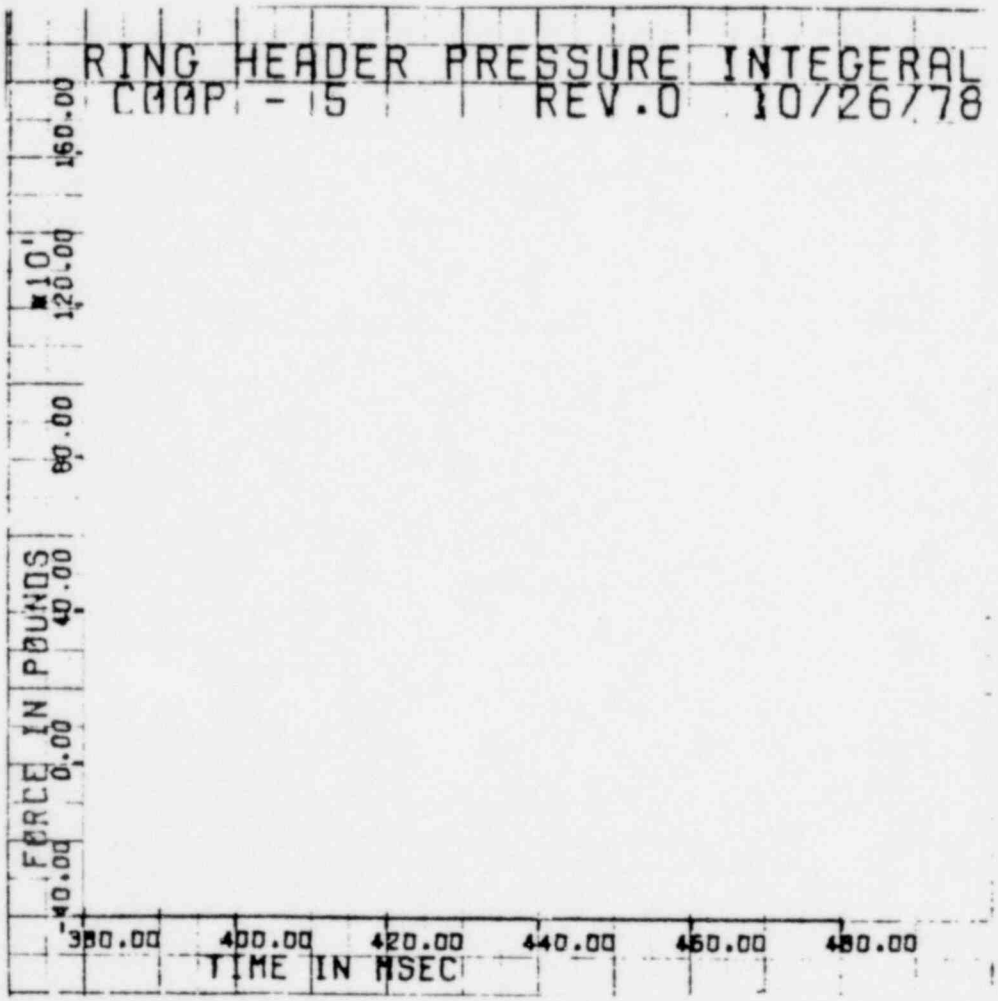

FIGURE B-53

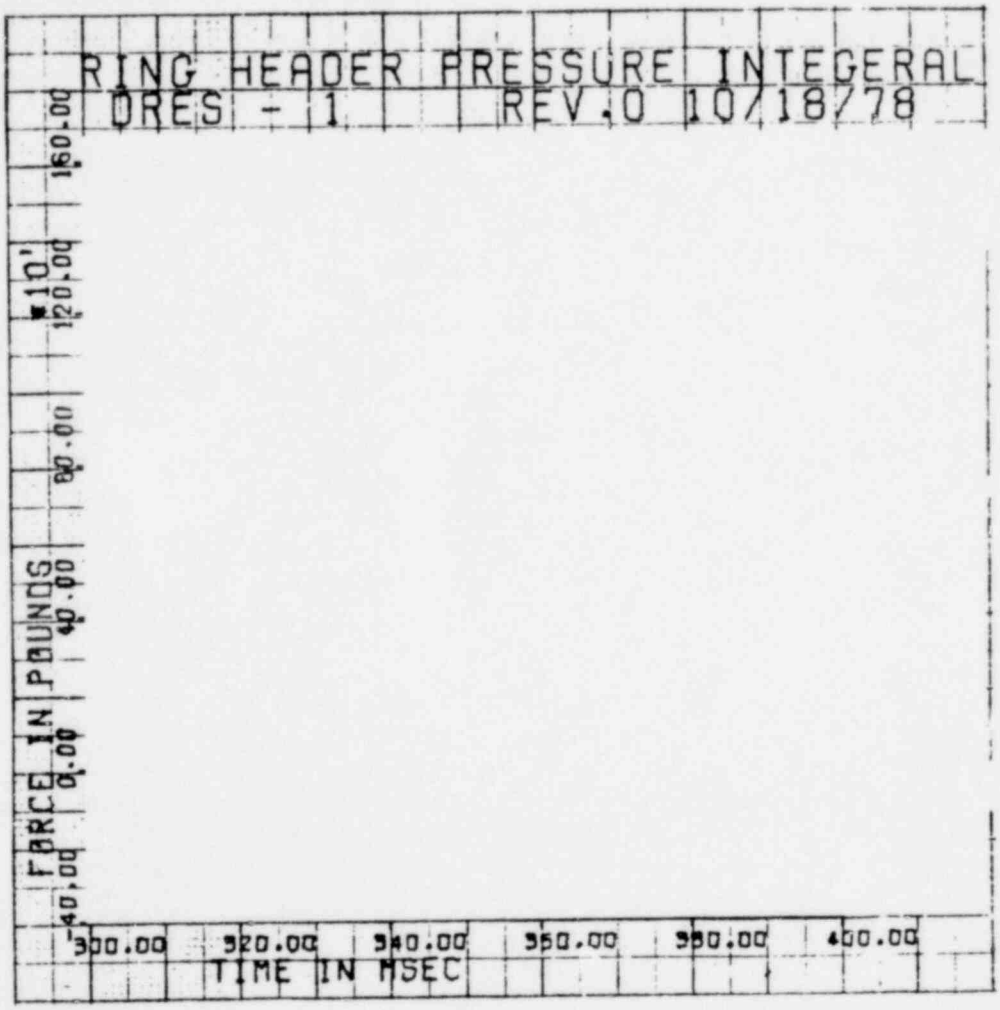

FIGURE B-54

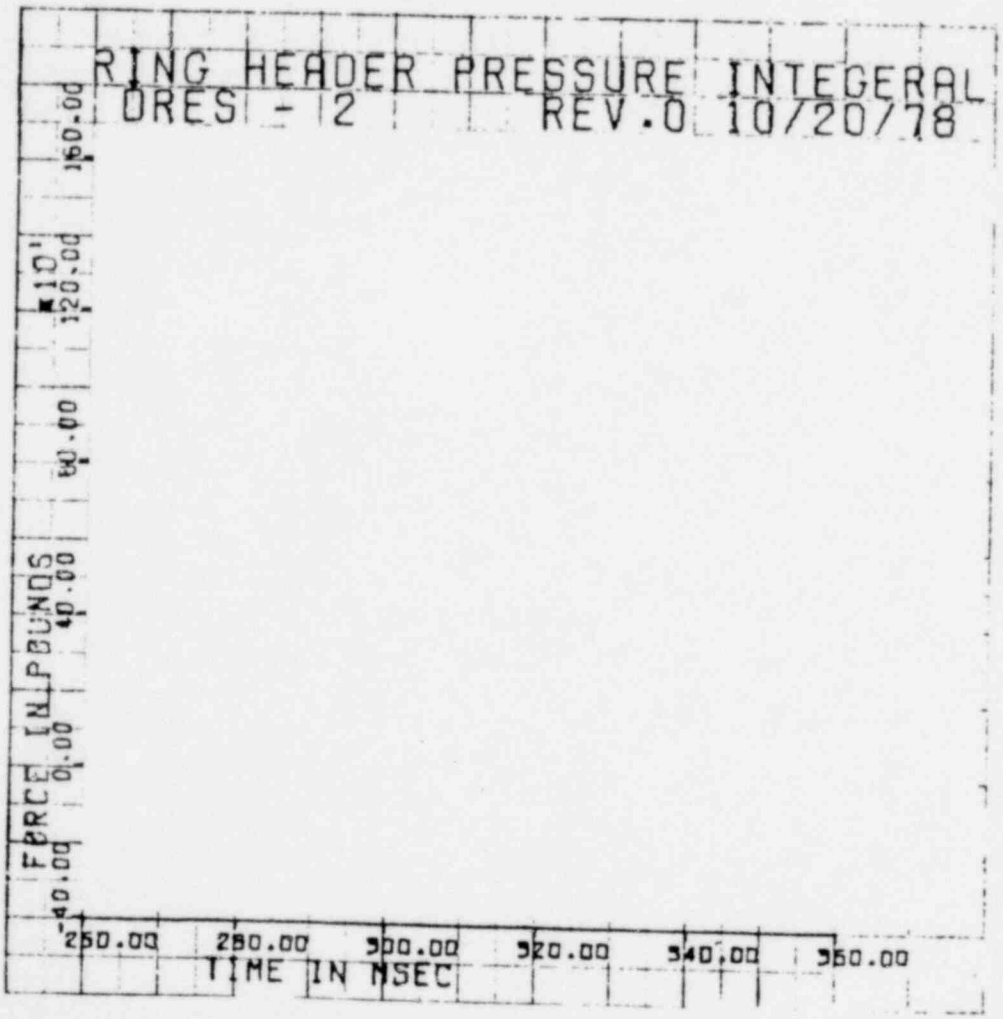

1351 051

FIGURE B-55

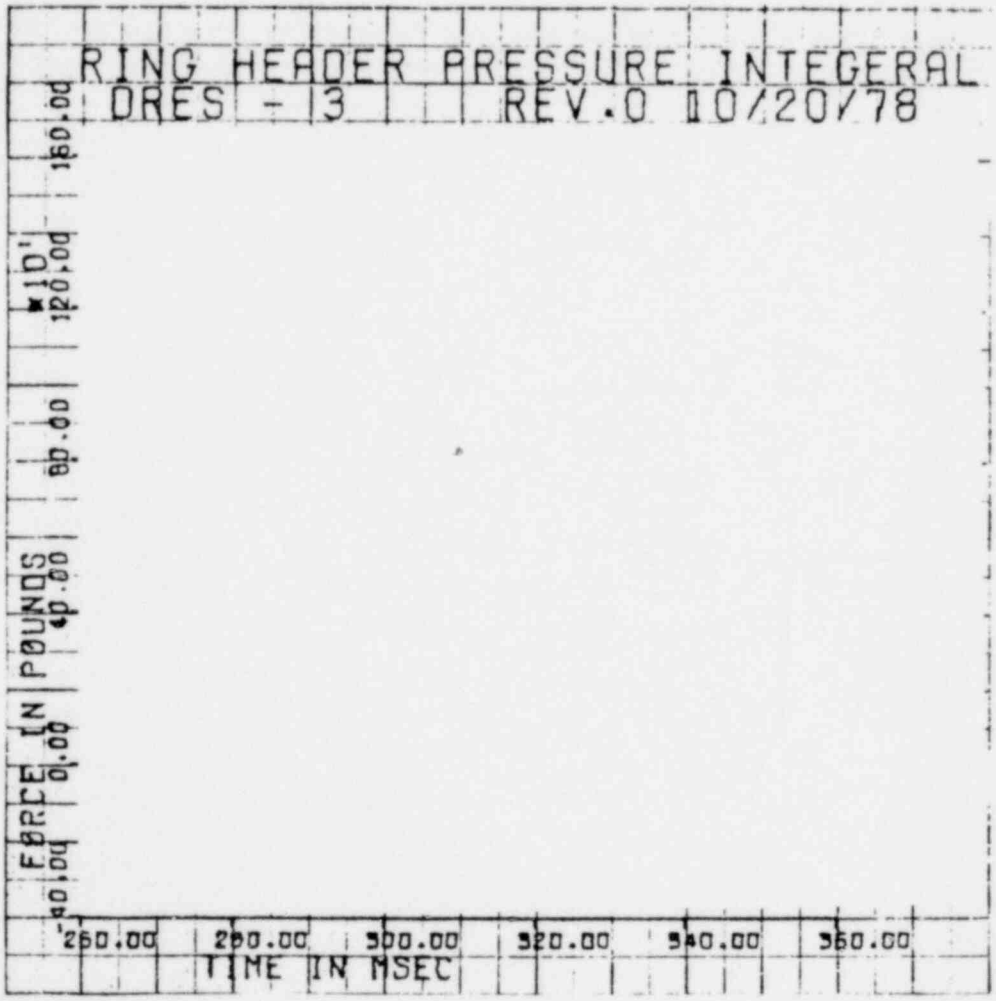

FIGURE B-56

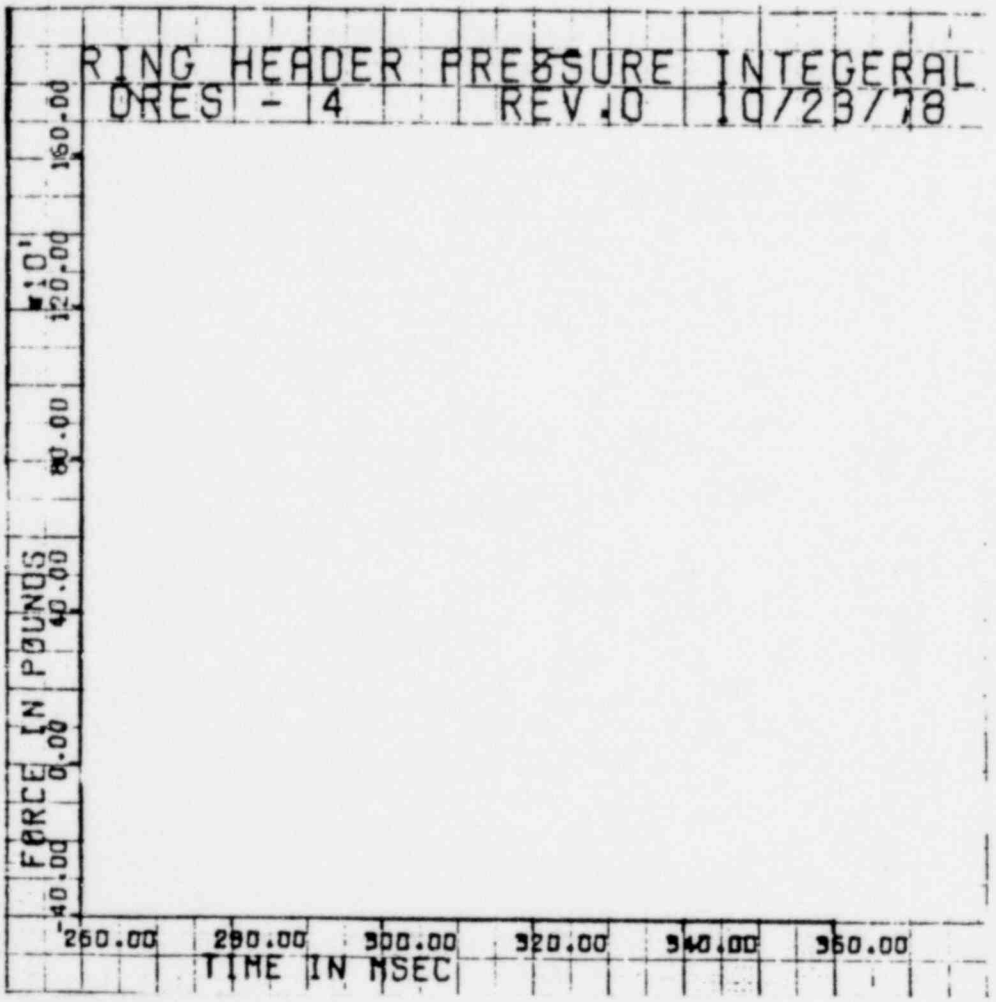

FIGURE B-57

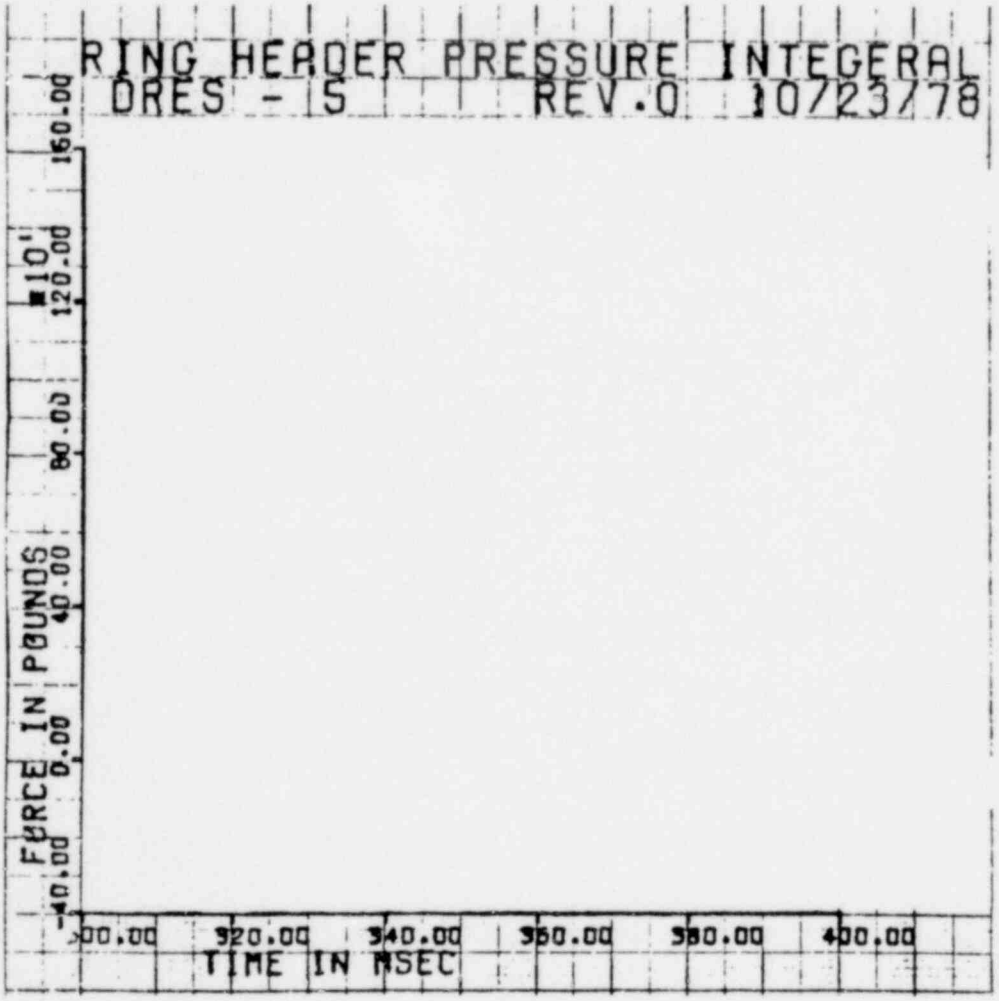

FIGURE B-58

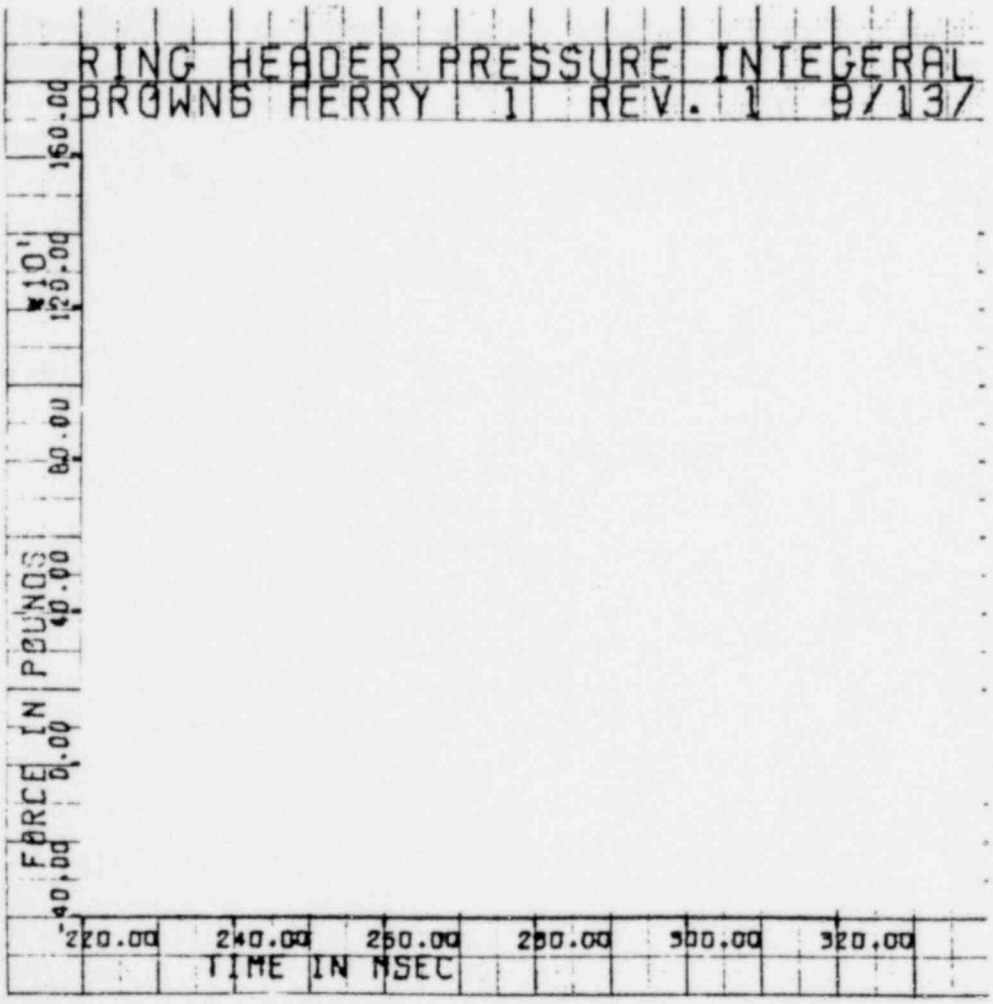

FIGURE B-59

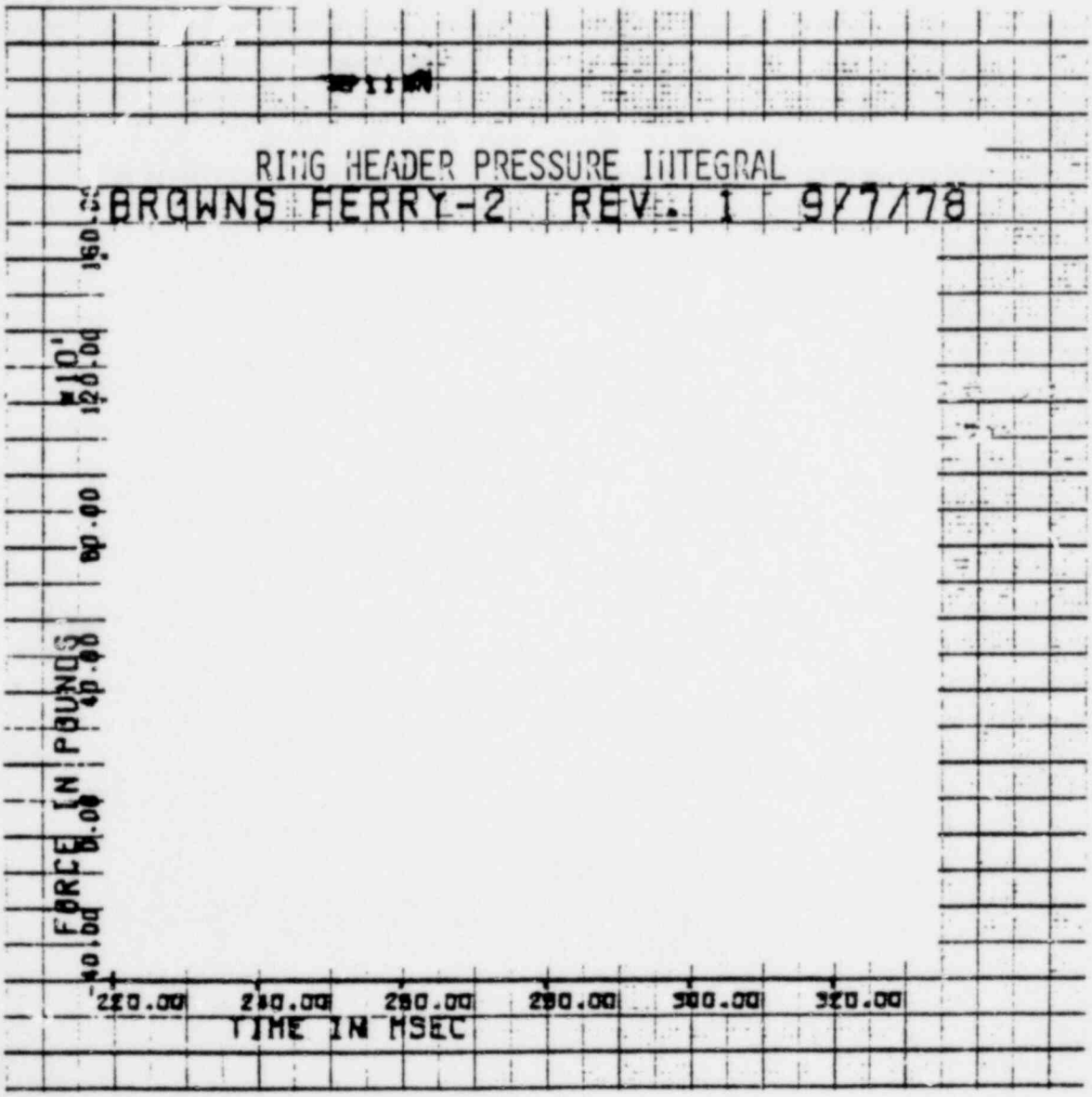

FIGURE B-60

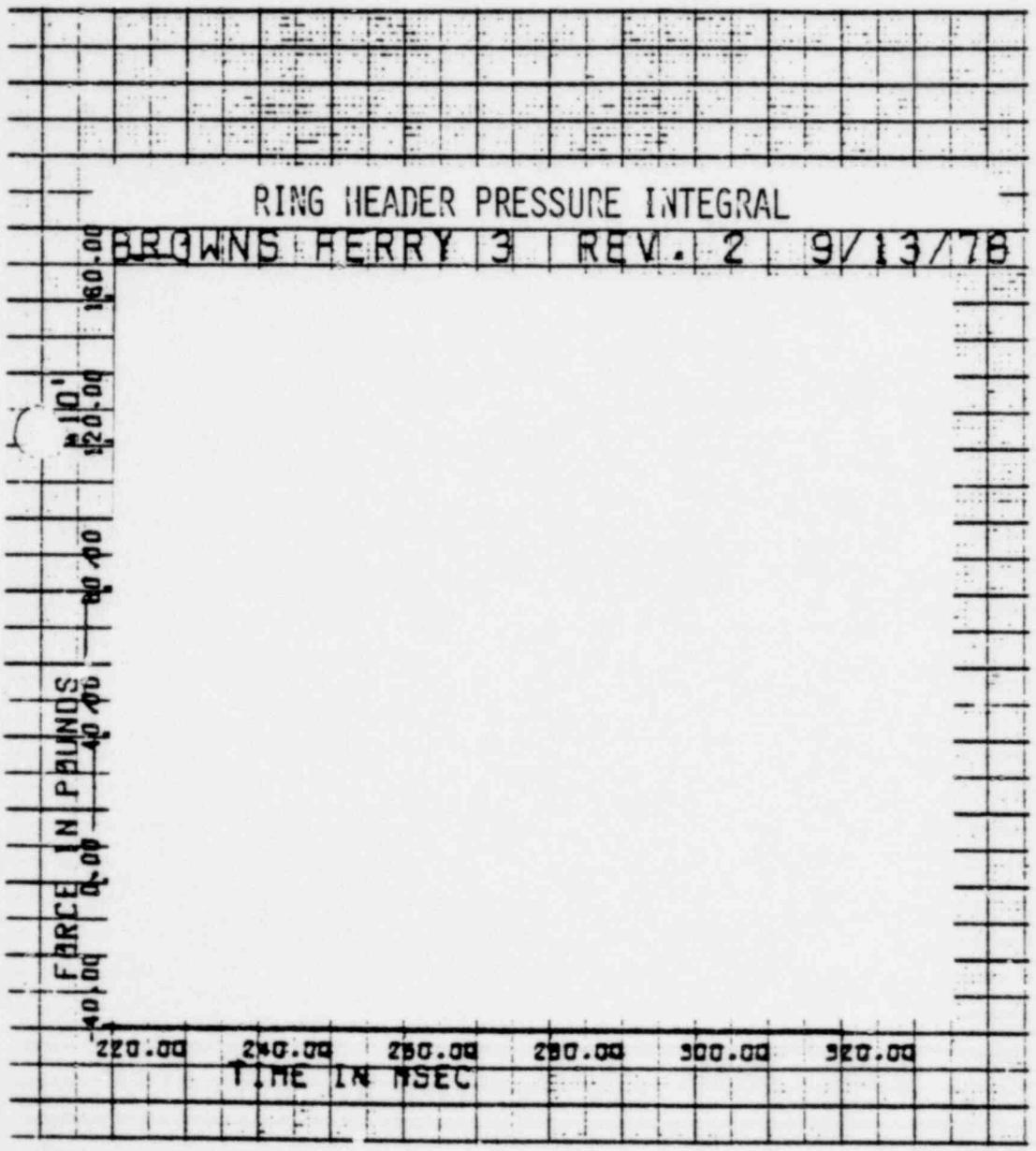

FIGURE B-61

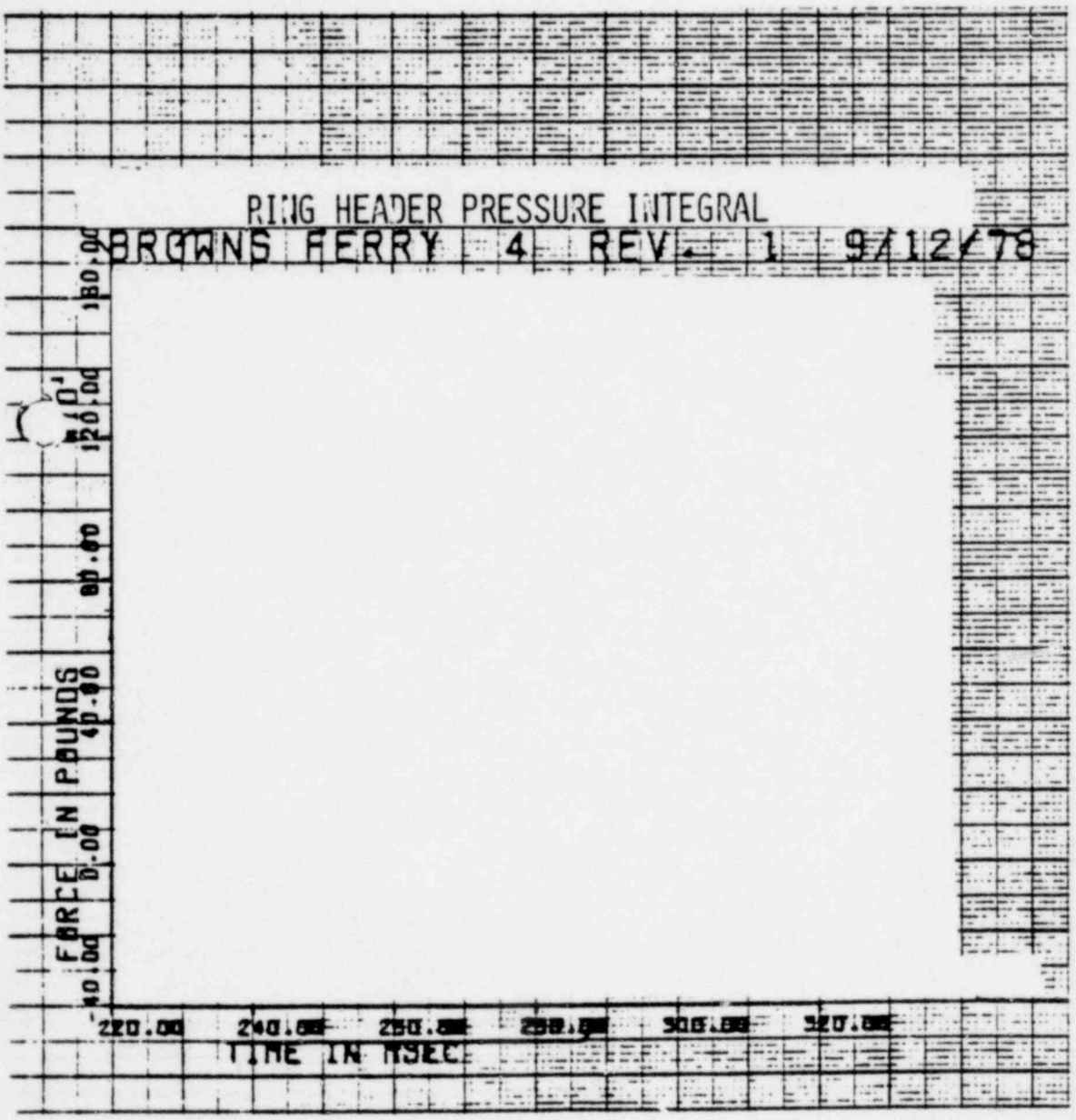

FIGURE B-62

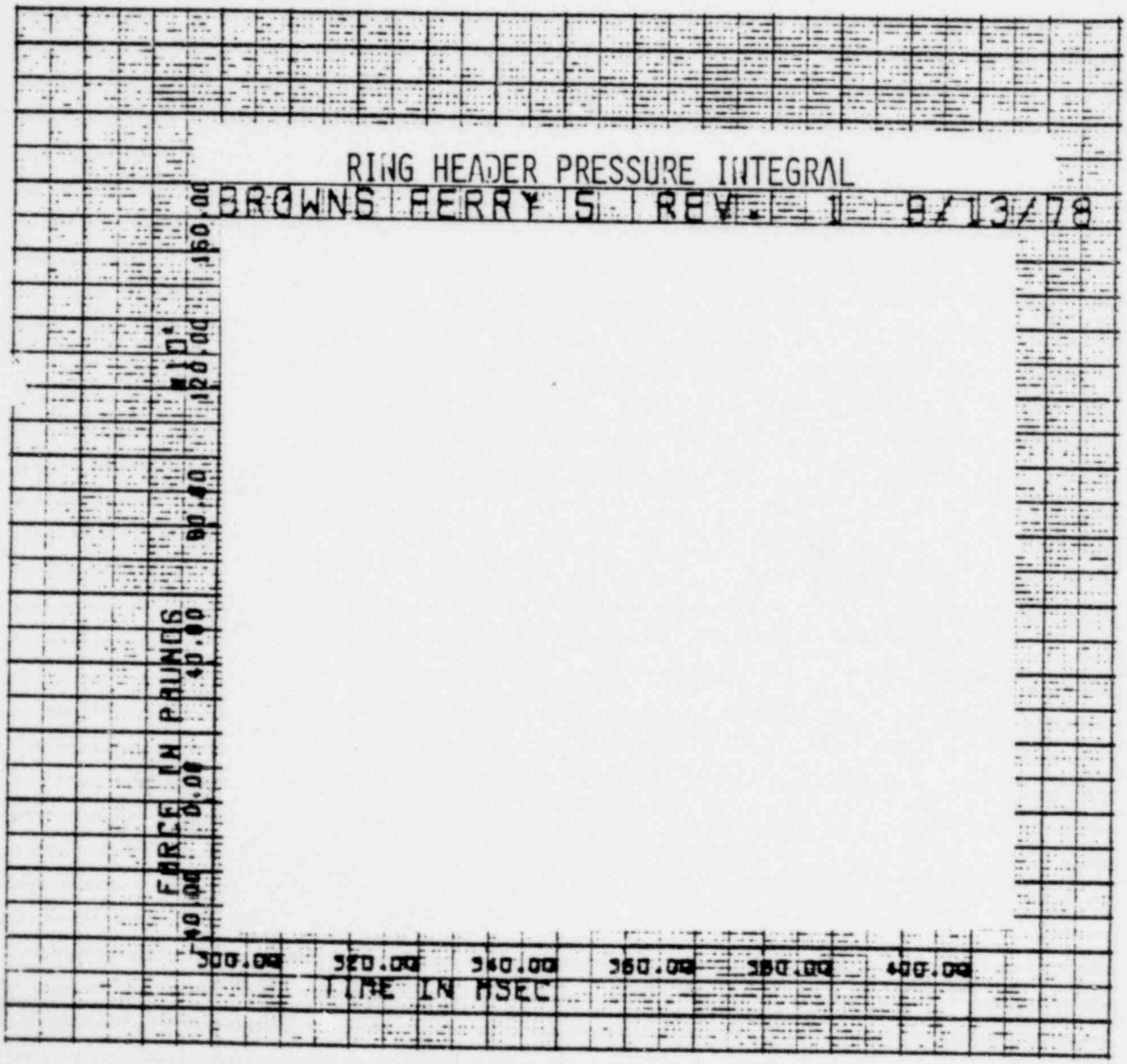

1351 059

FIGURE B-63

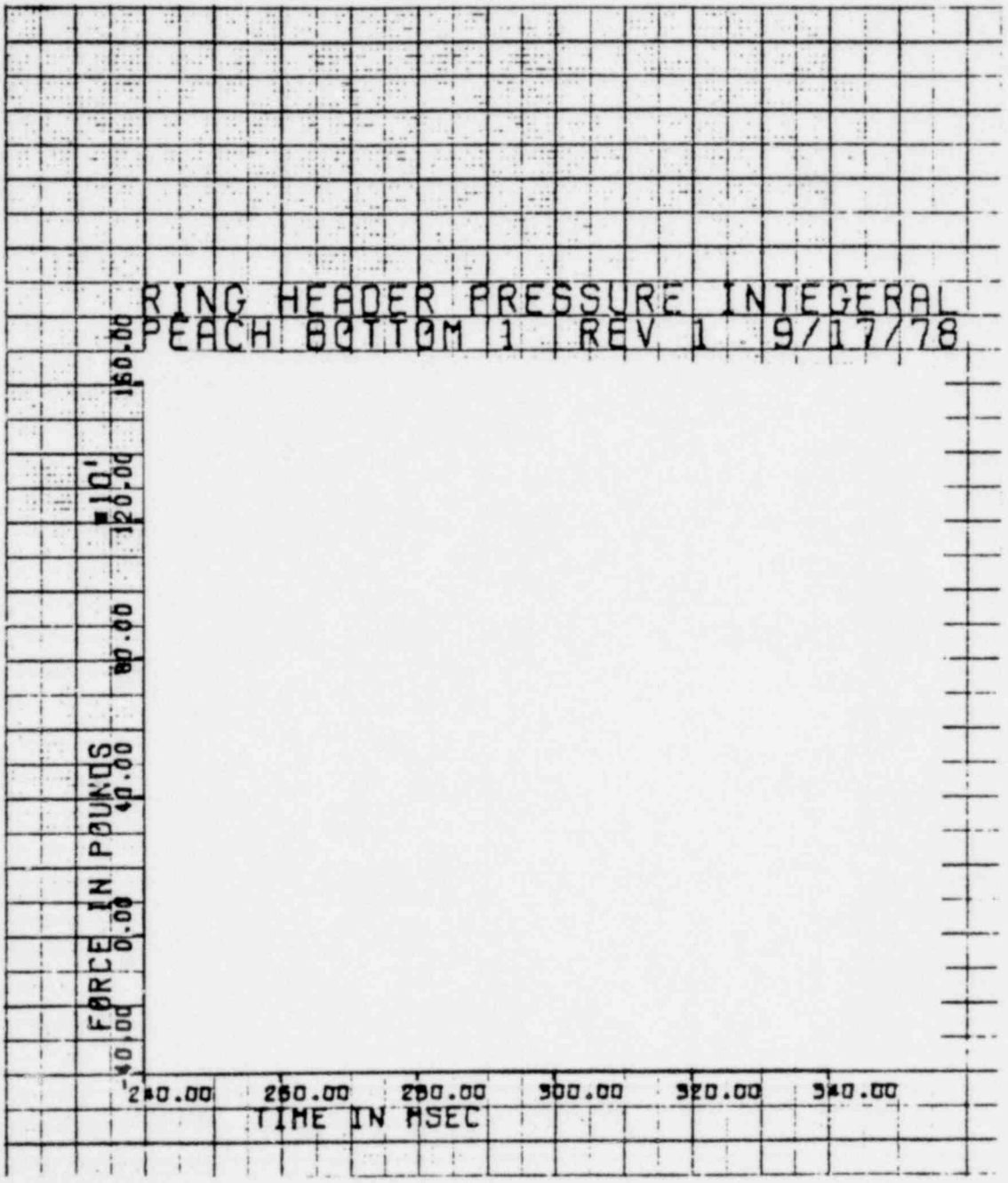

1351 060

FIGURE B-64

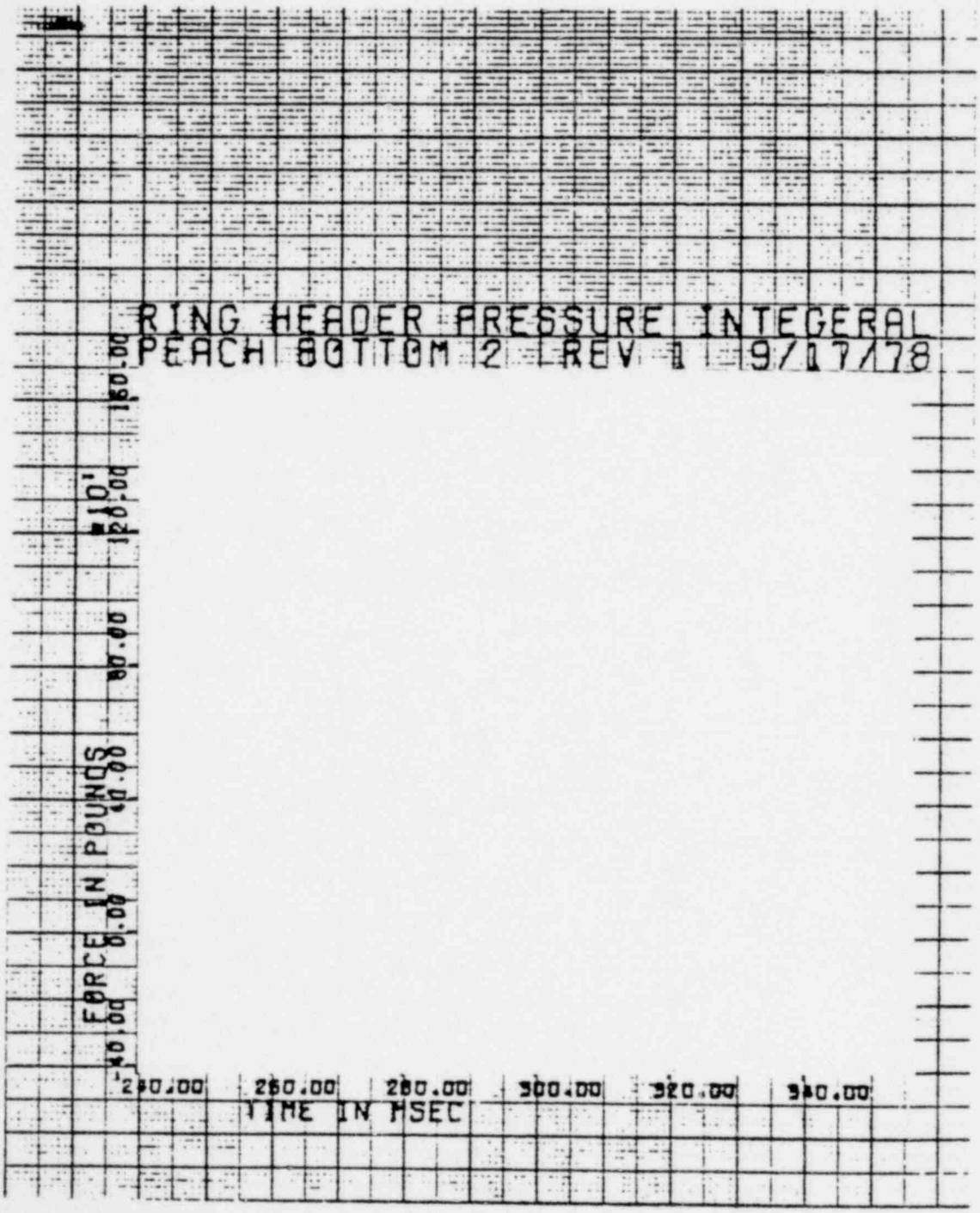

1351 061

FIGURE B-65

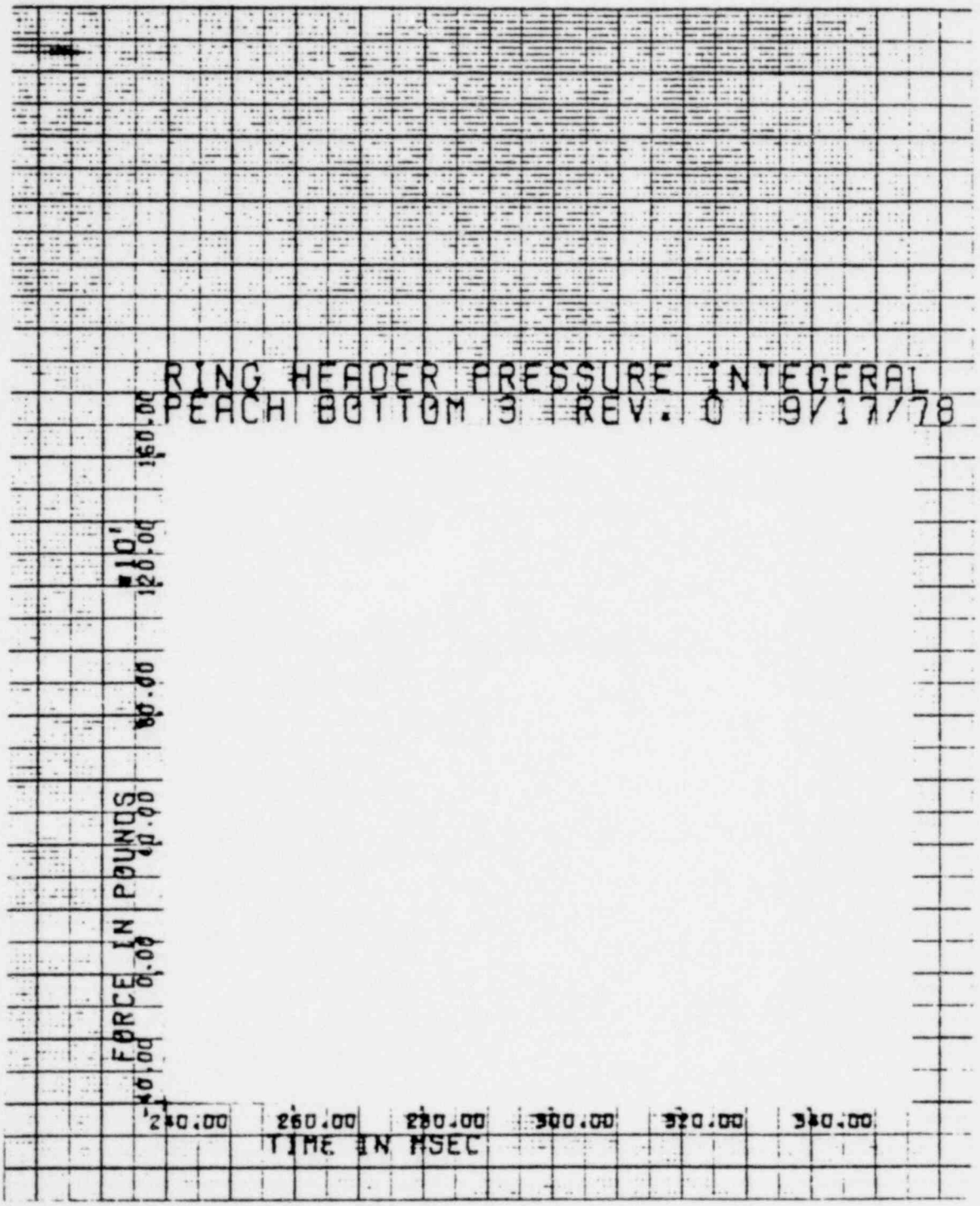

FIGURE B-66

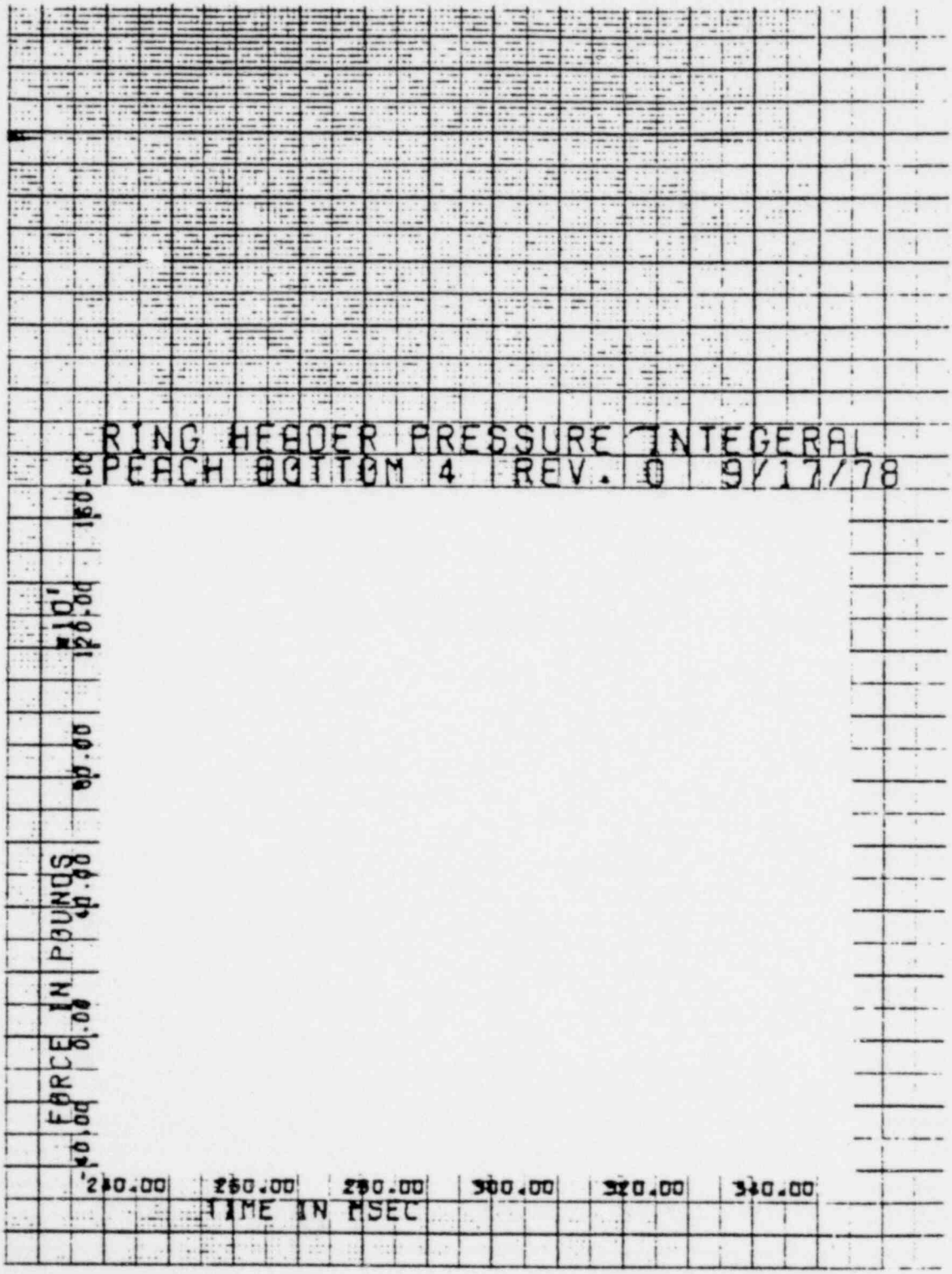
RING HEADER PRESSURE INTEGERAL
PEACH BOTTOM 4 REV. 0 9/17/78
FORCE IN POUNDS
TIME IN MSEC
1351 063

FIGURE B-67

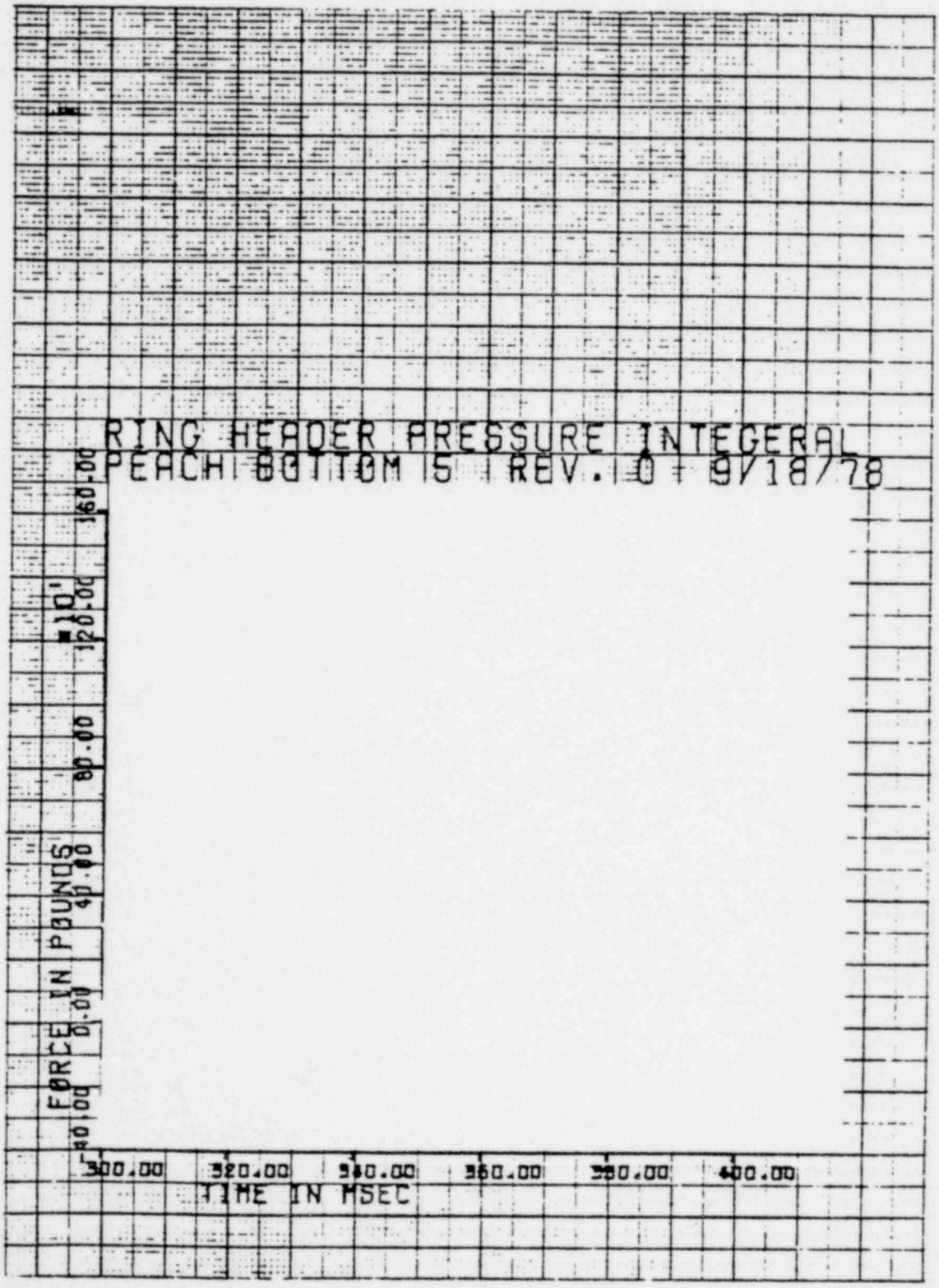

1351 064

FIGURE B-68

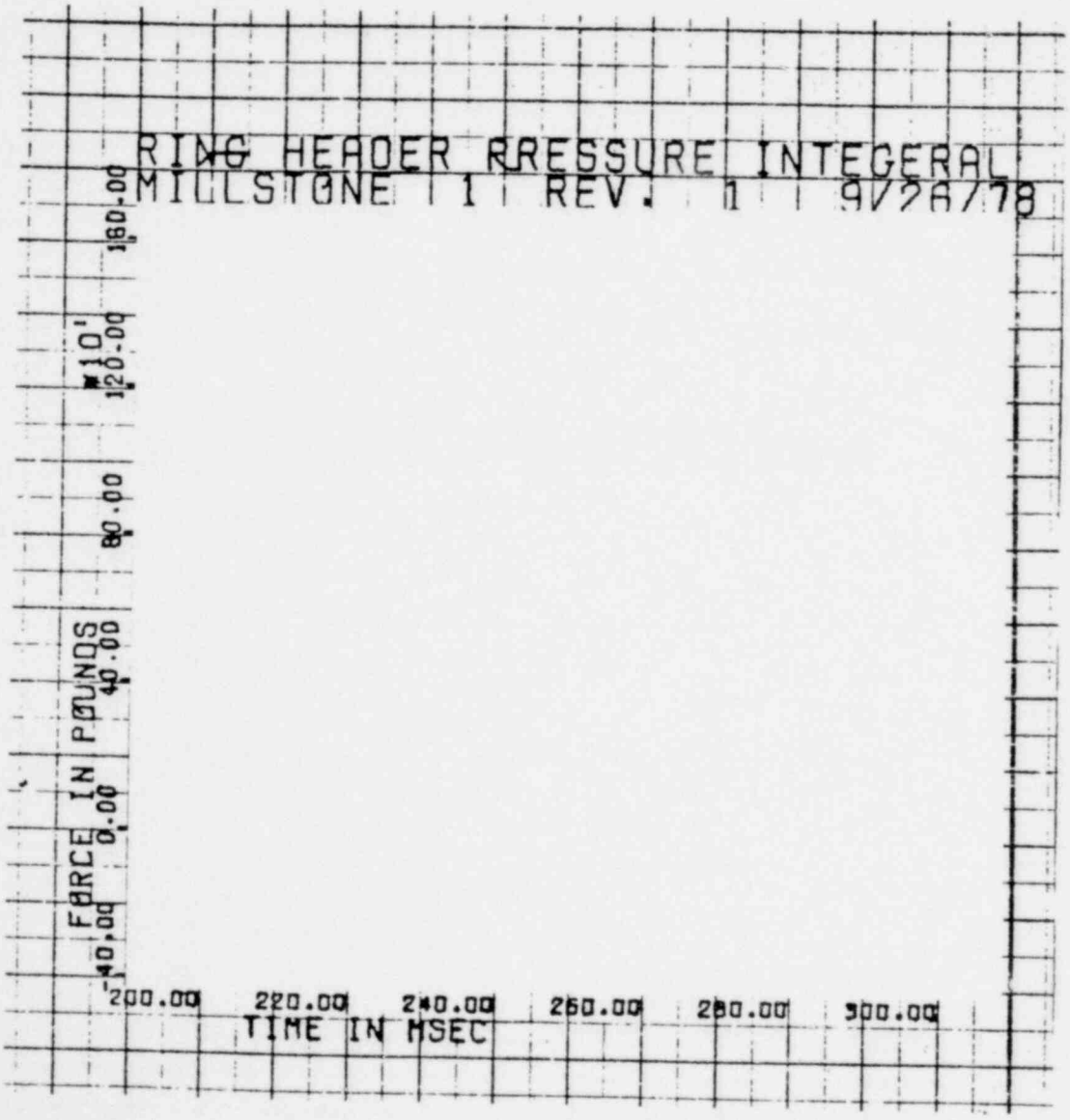

1351 065

FIGURE B-69

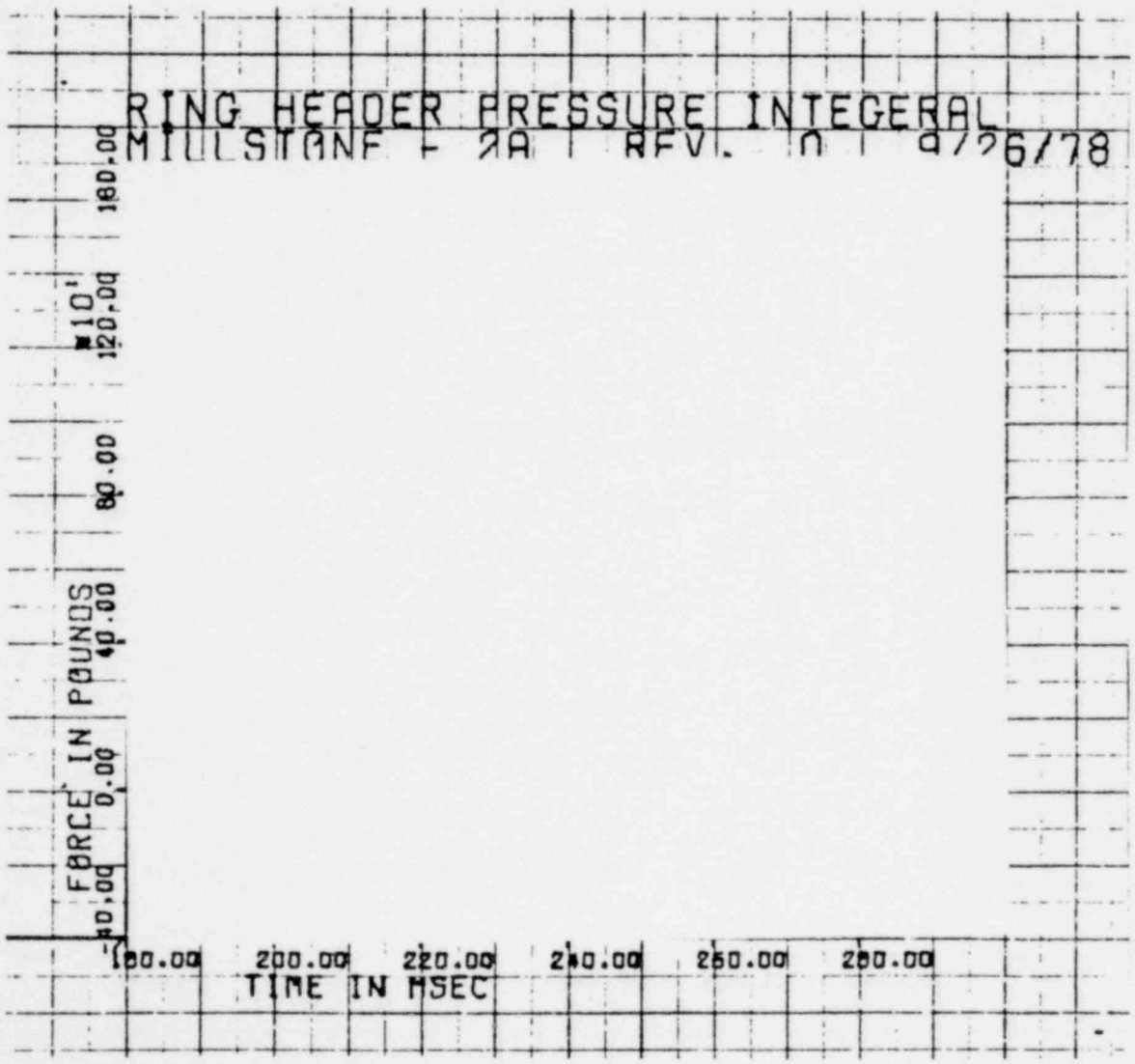

FIGURE B-70

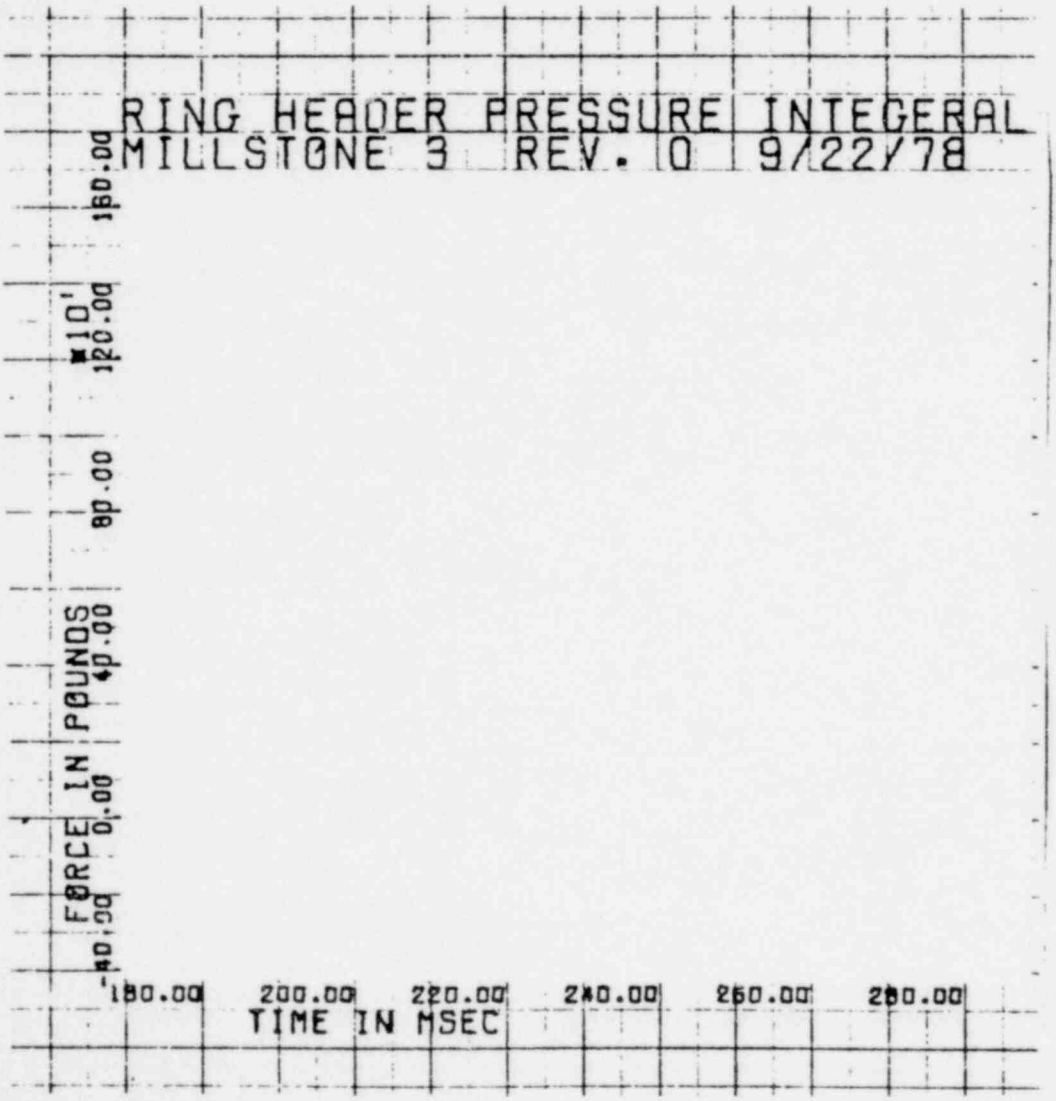

FIGURE B-71

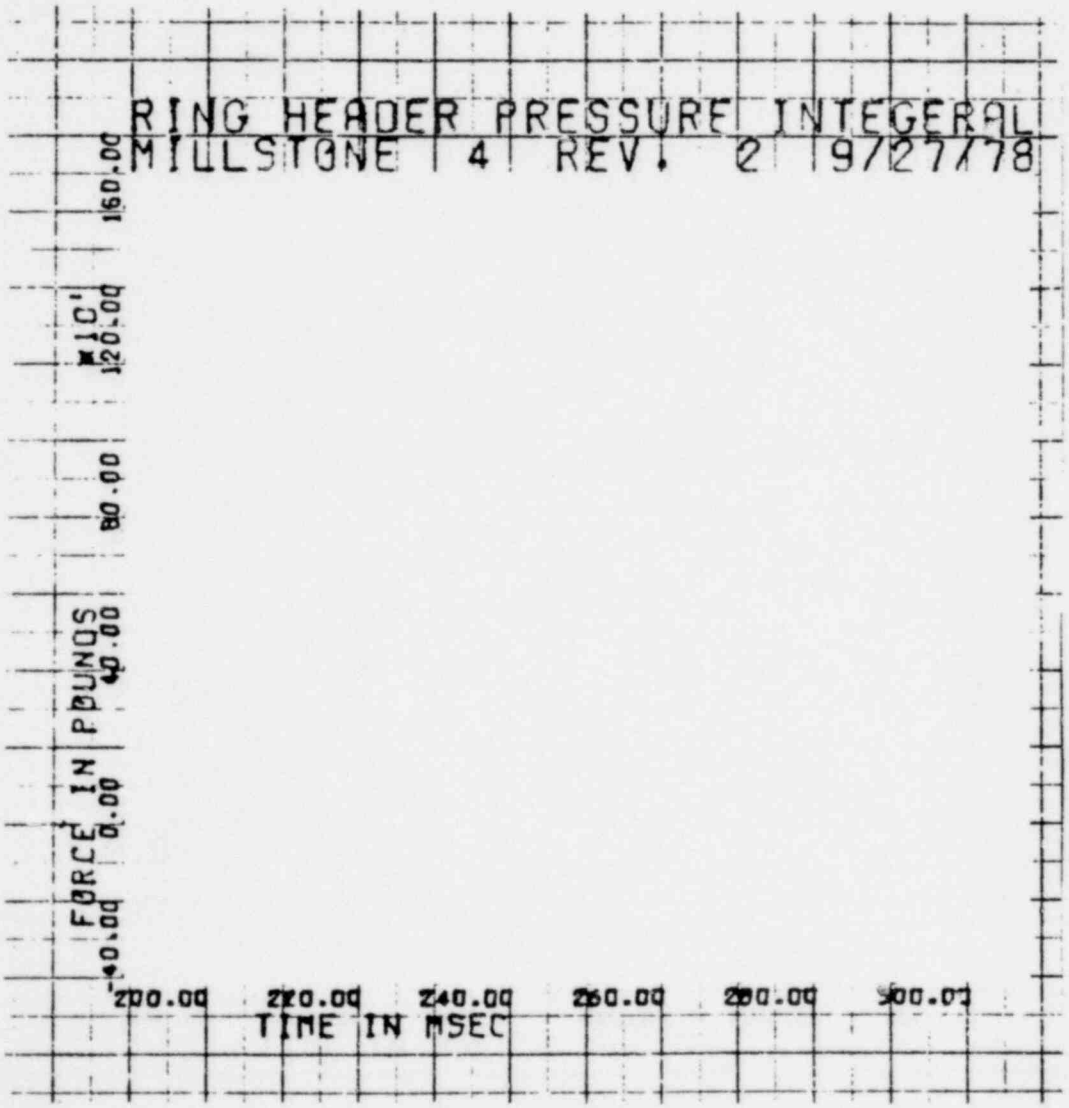

FIGURE B-72

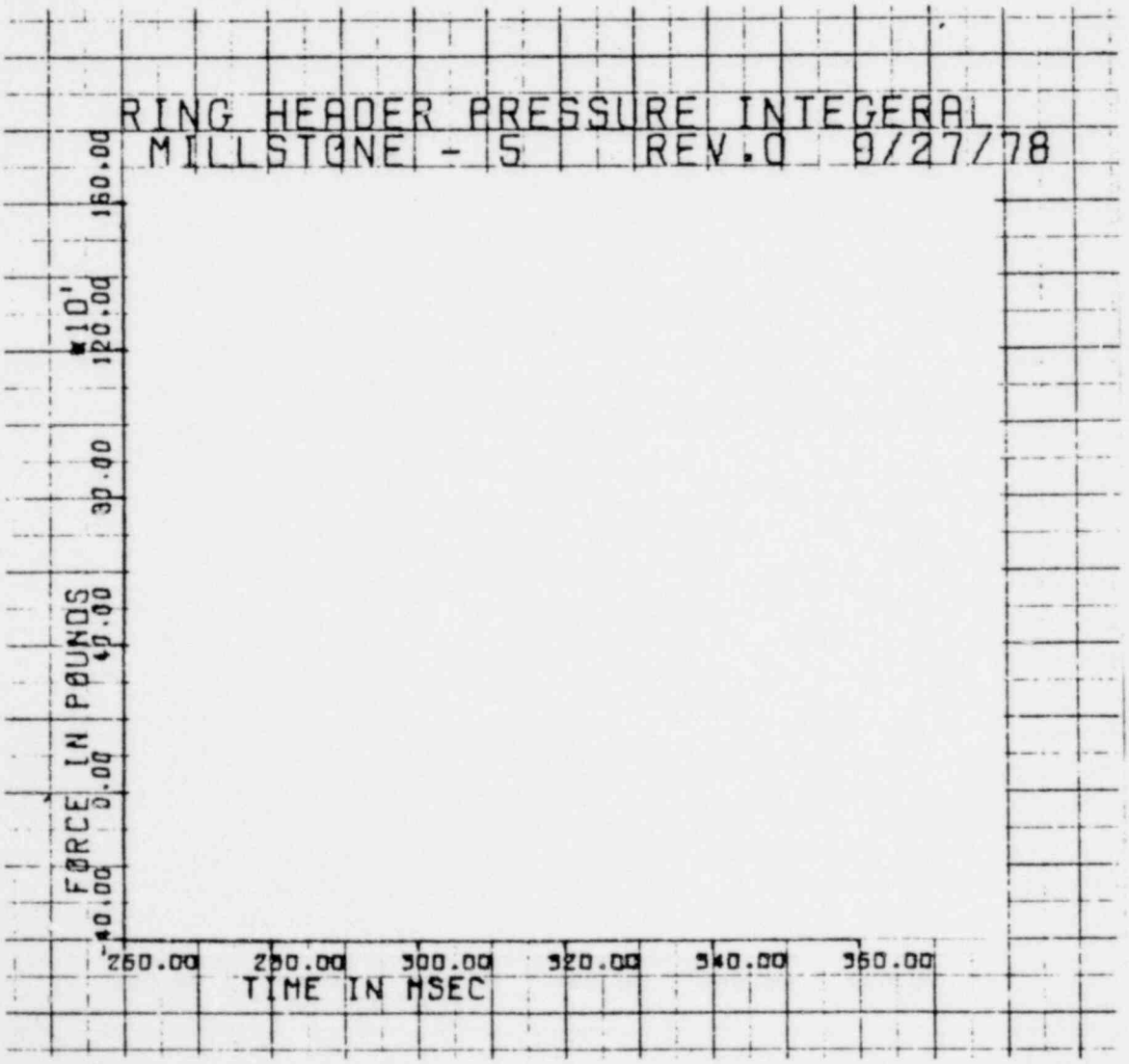

1351 069

FIGURE B-73

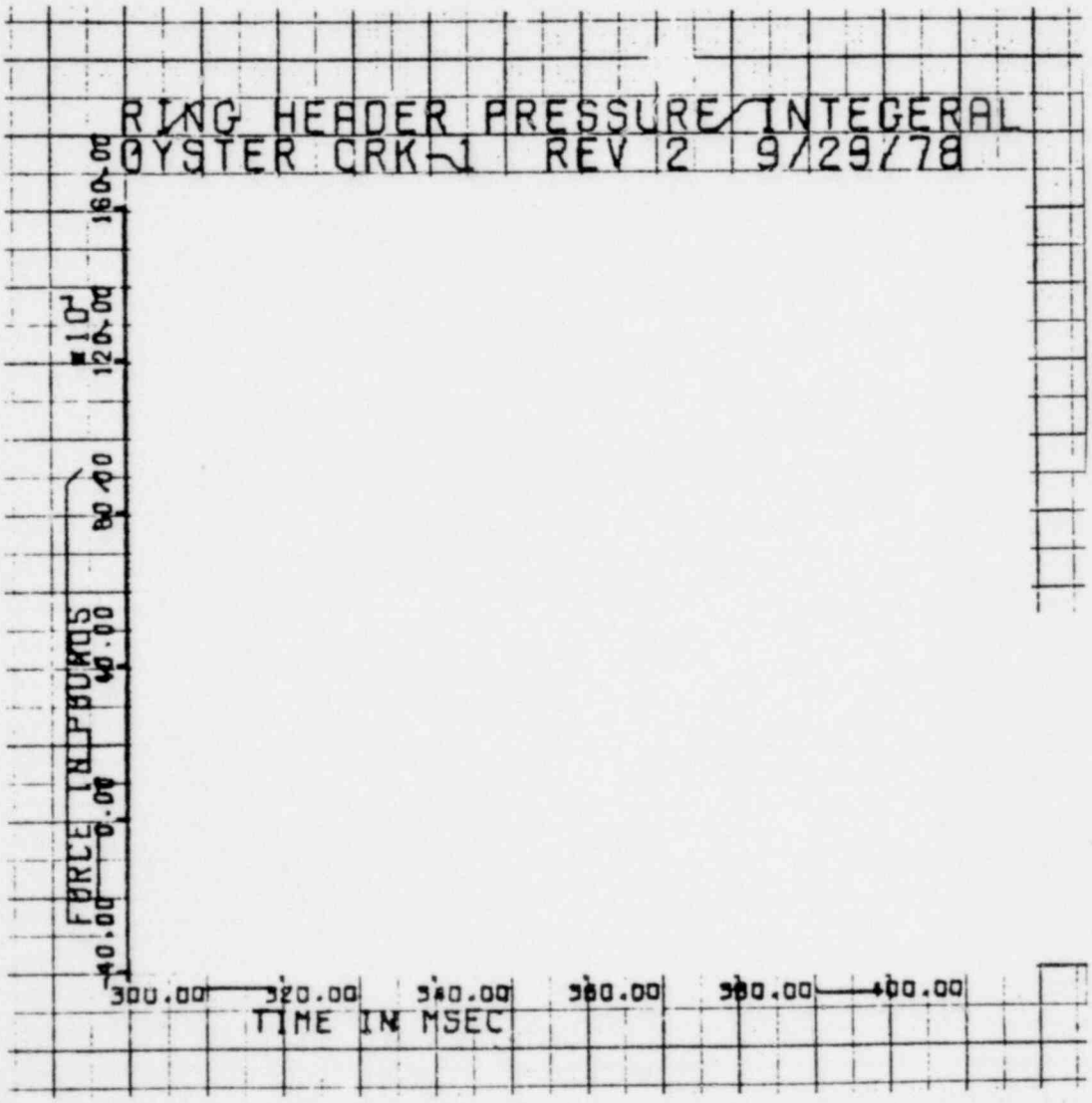

1351 070

FIGURE B-74

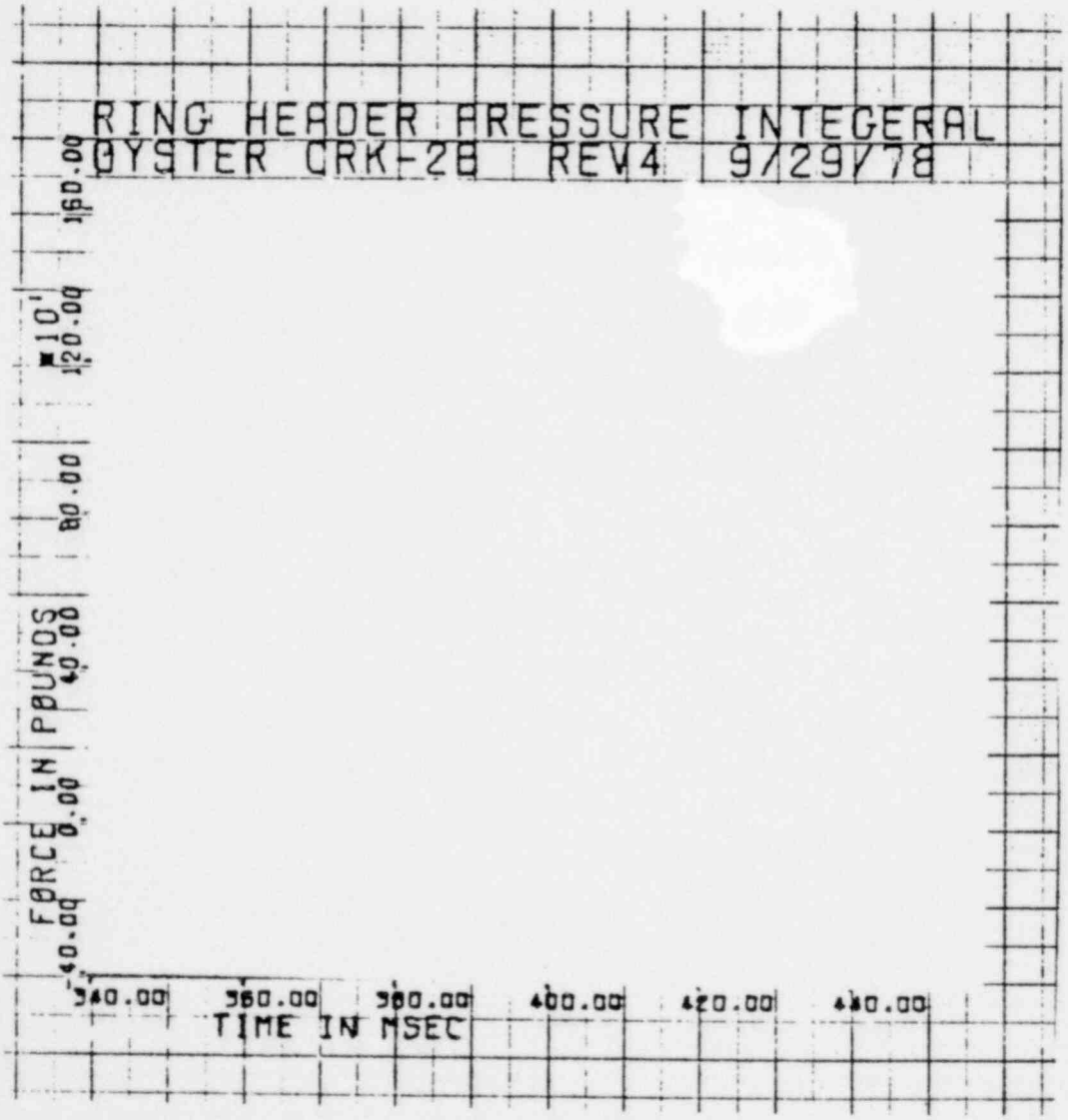

1351 071

FIGURE B-75

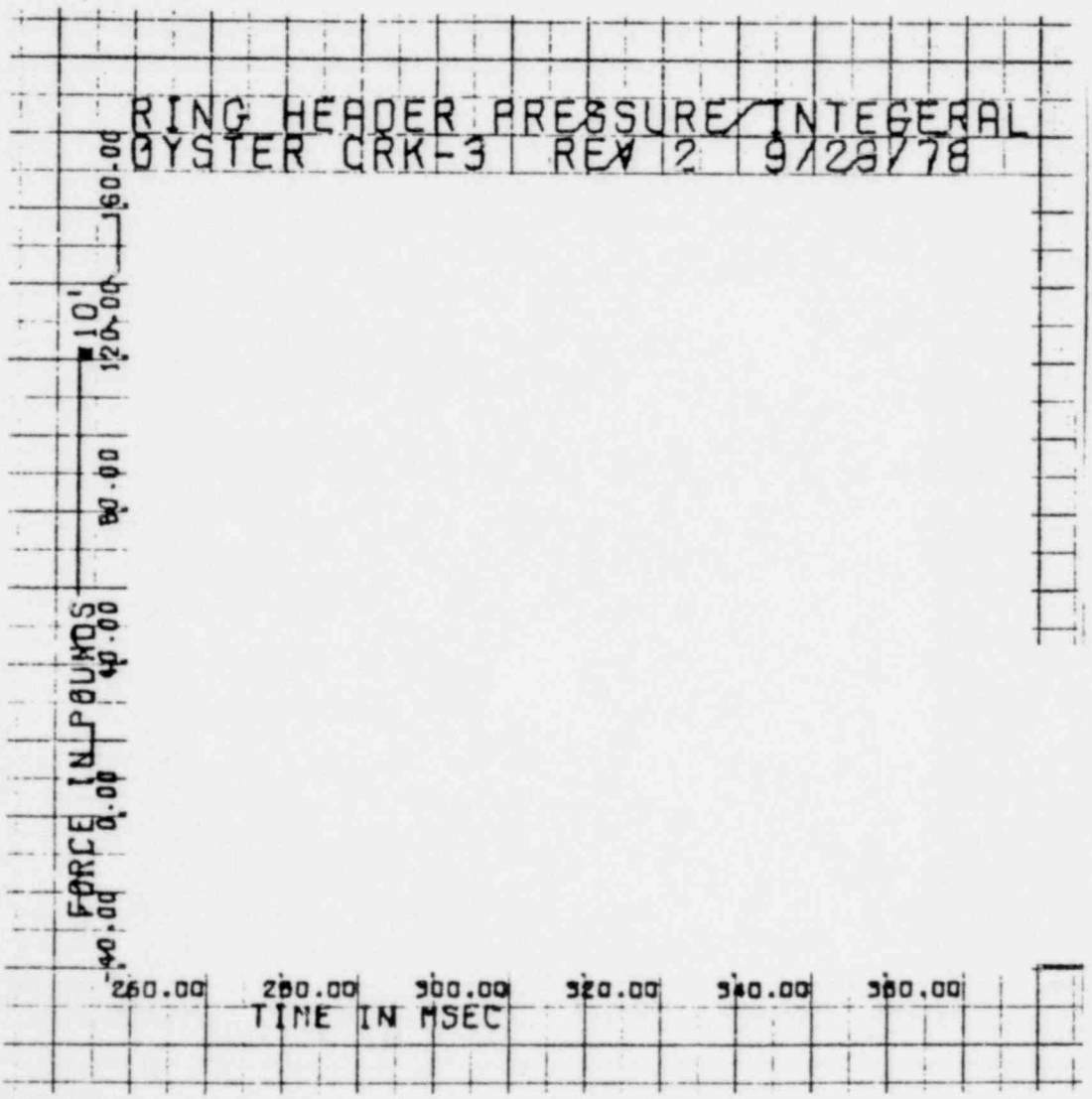

FIGURE B-76

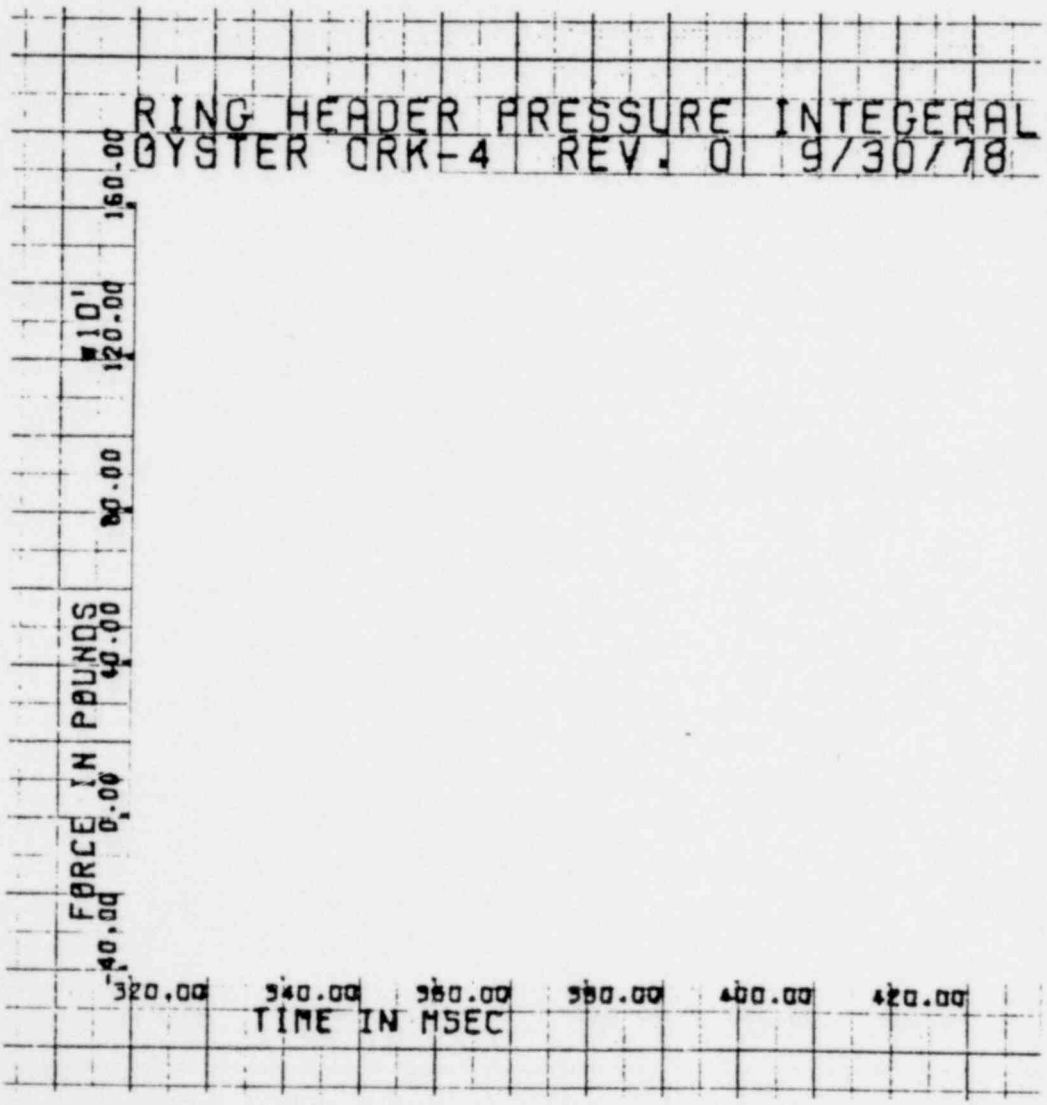

1351 073

FIGURE B-77

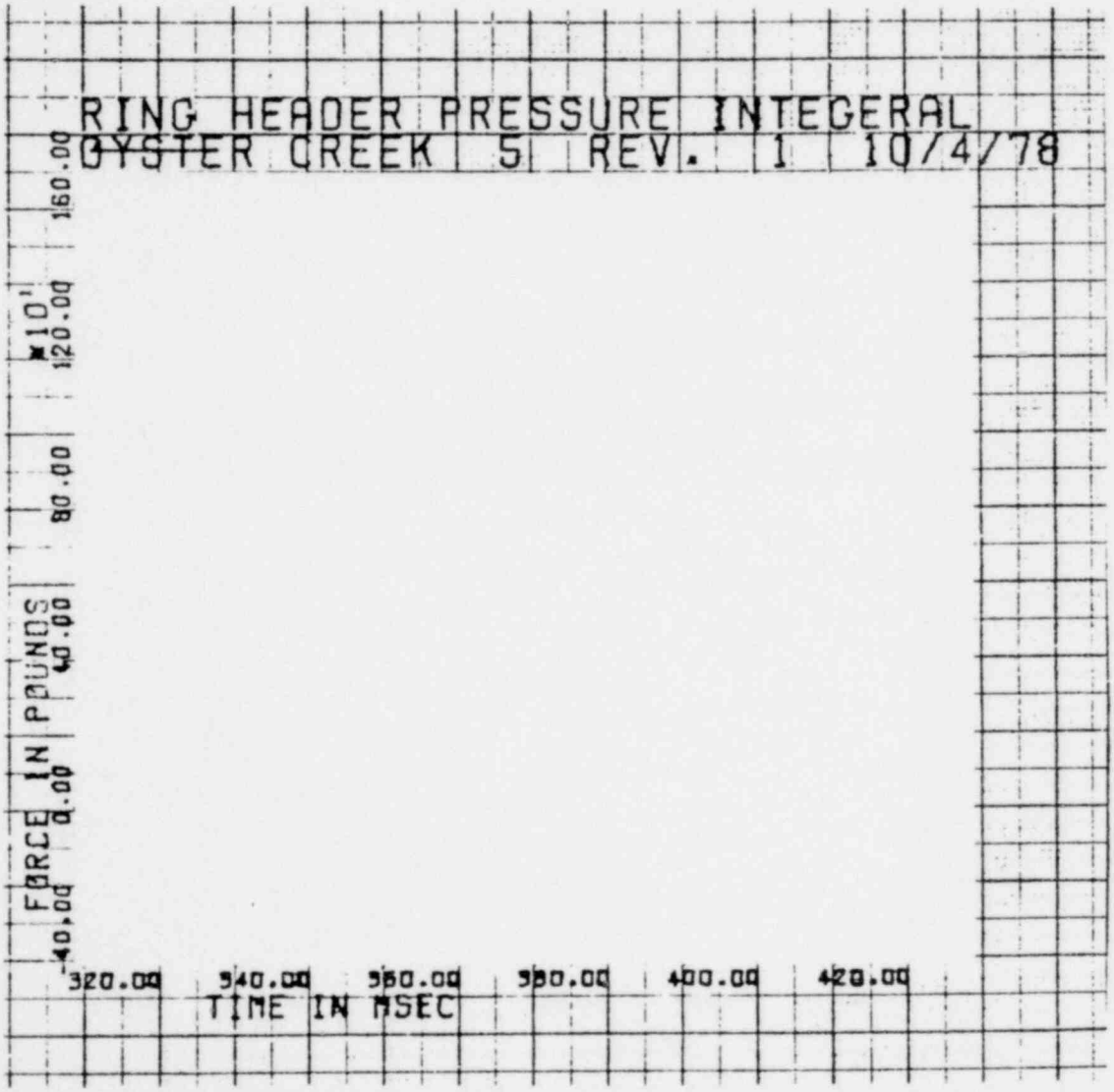

FIGURE B-78

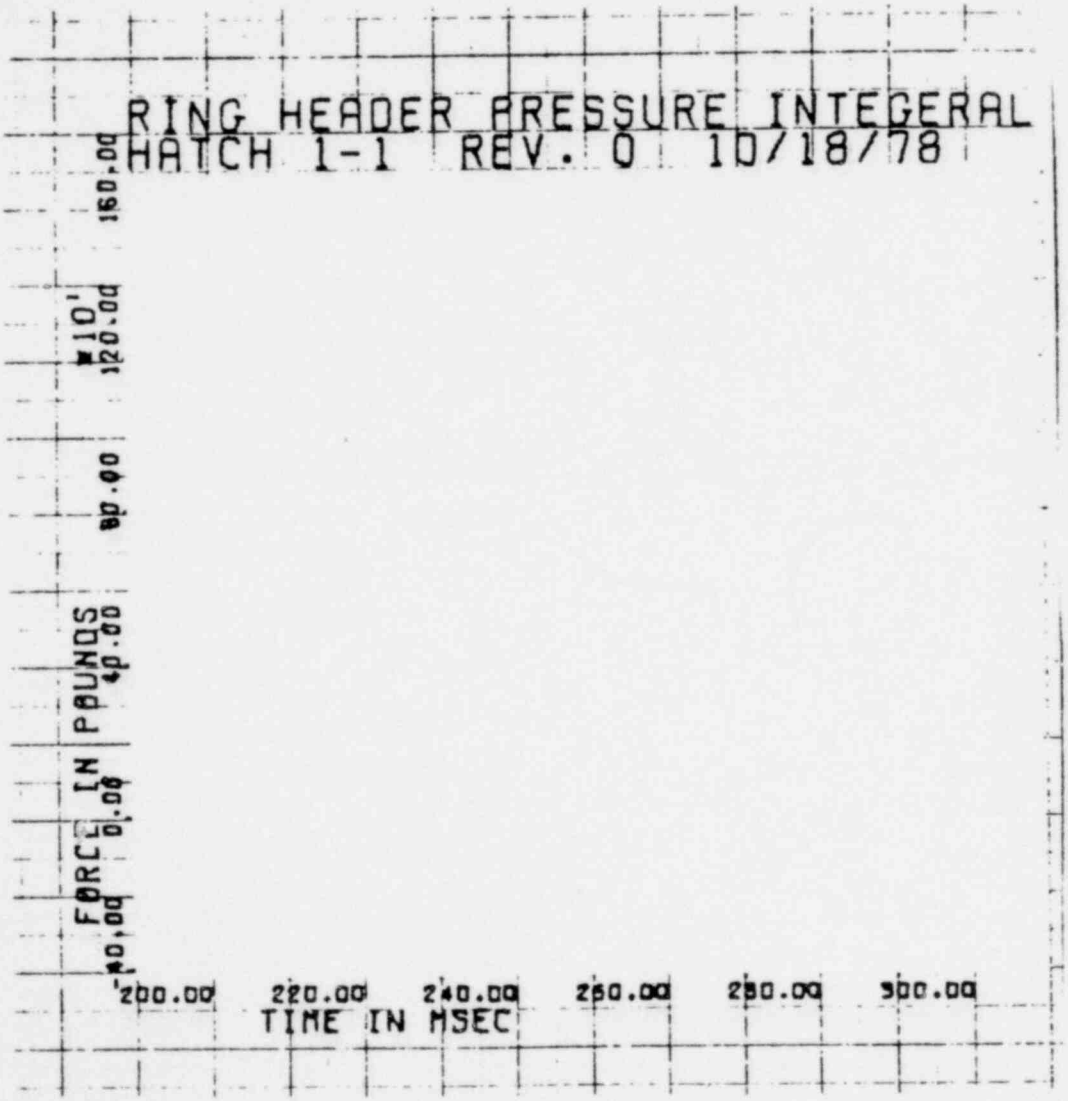

1351 075

FIGURE B-79

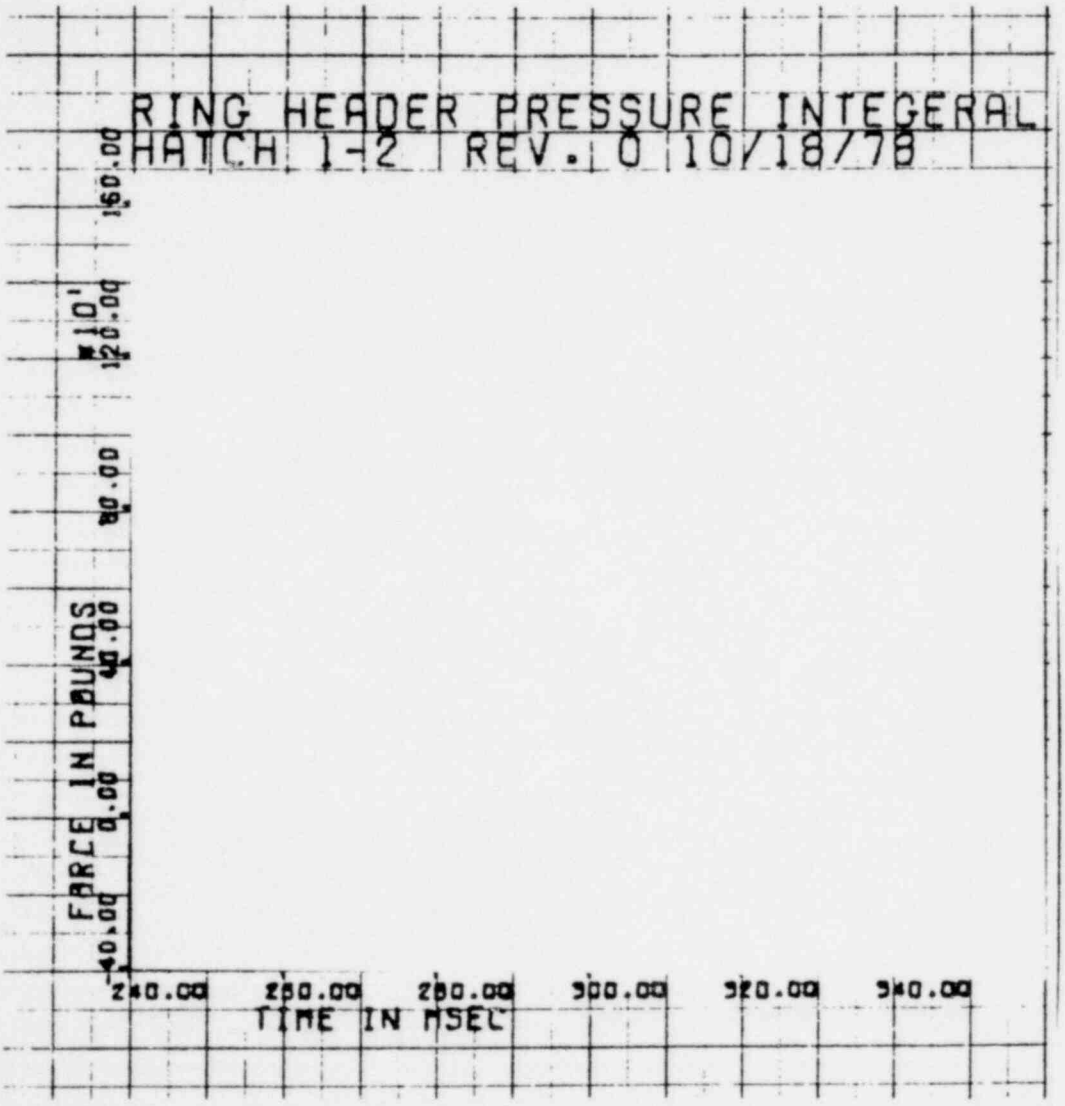

FIGURE B-80

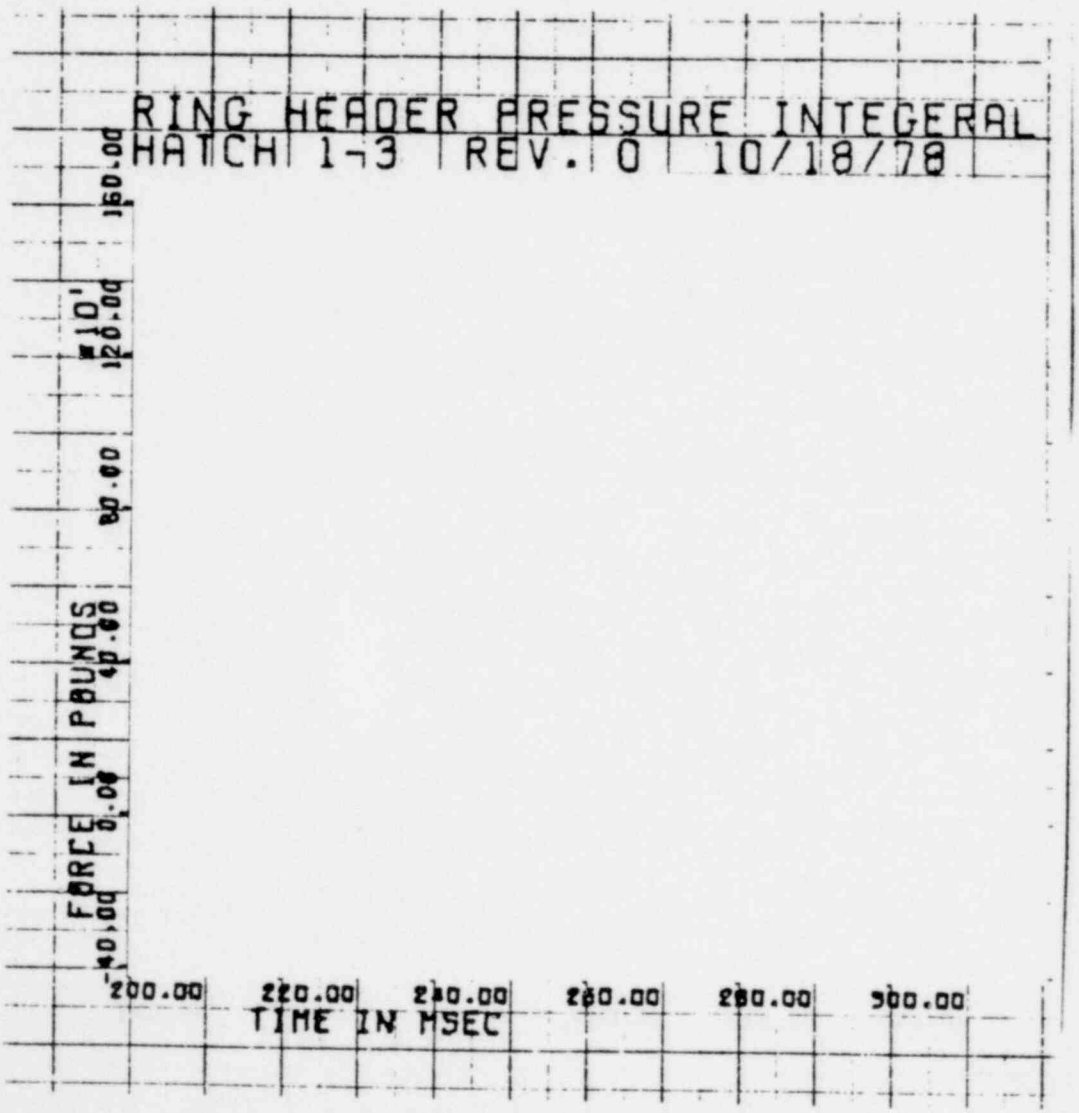

FIGURE B-81

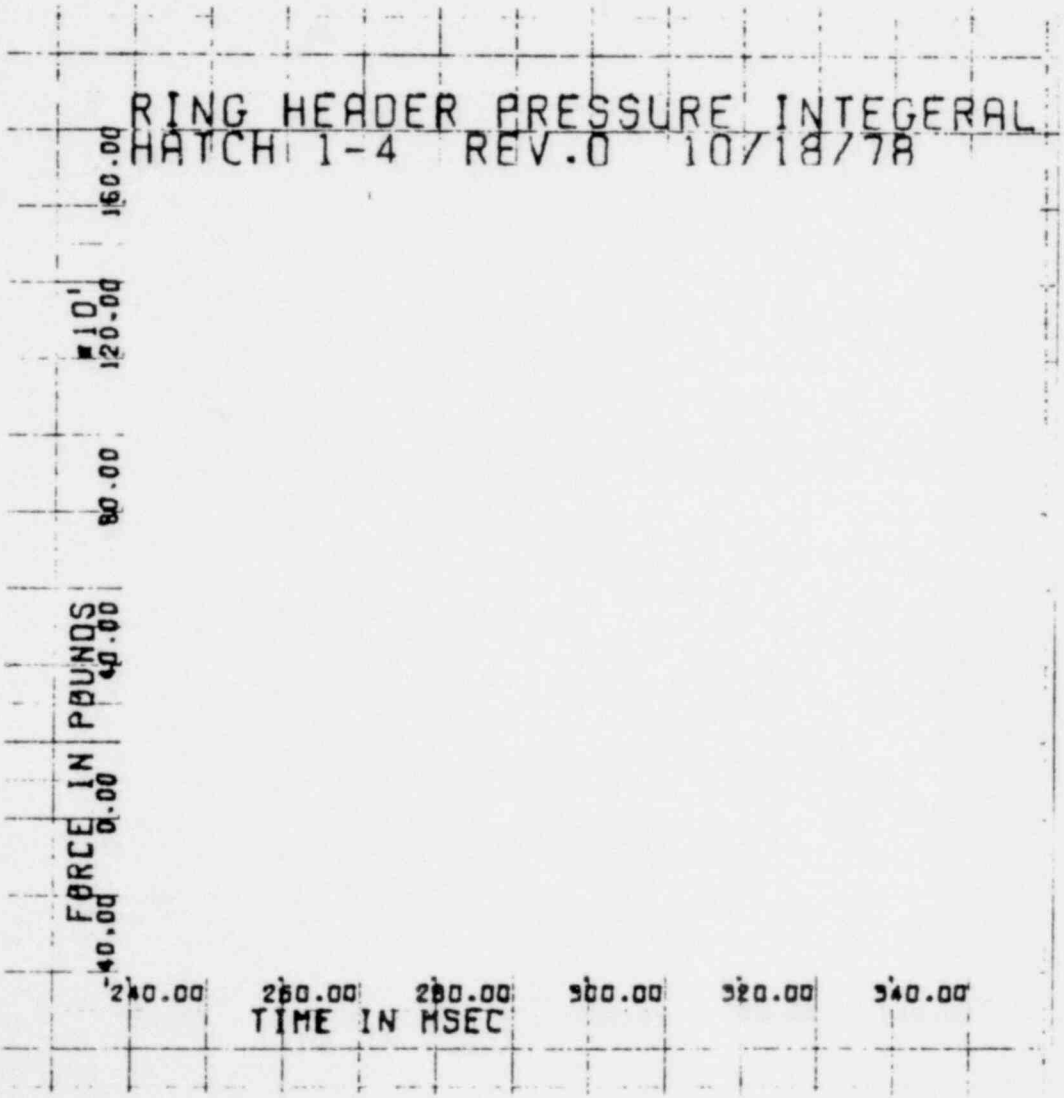

FIGURE B-82

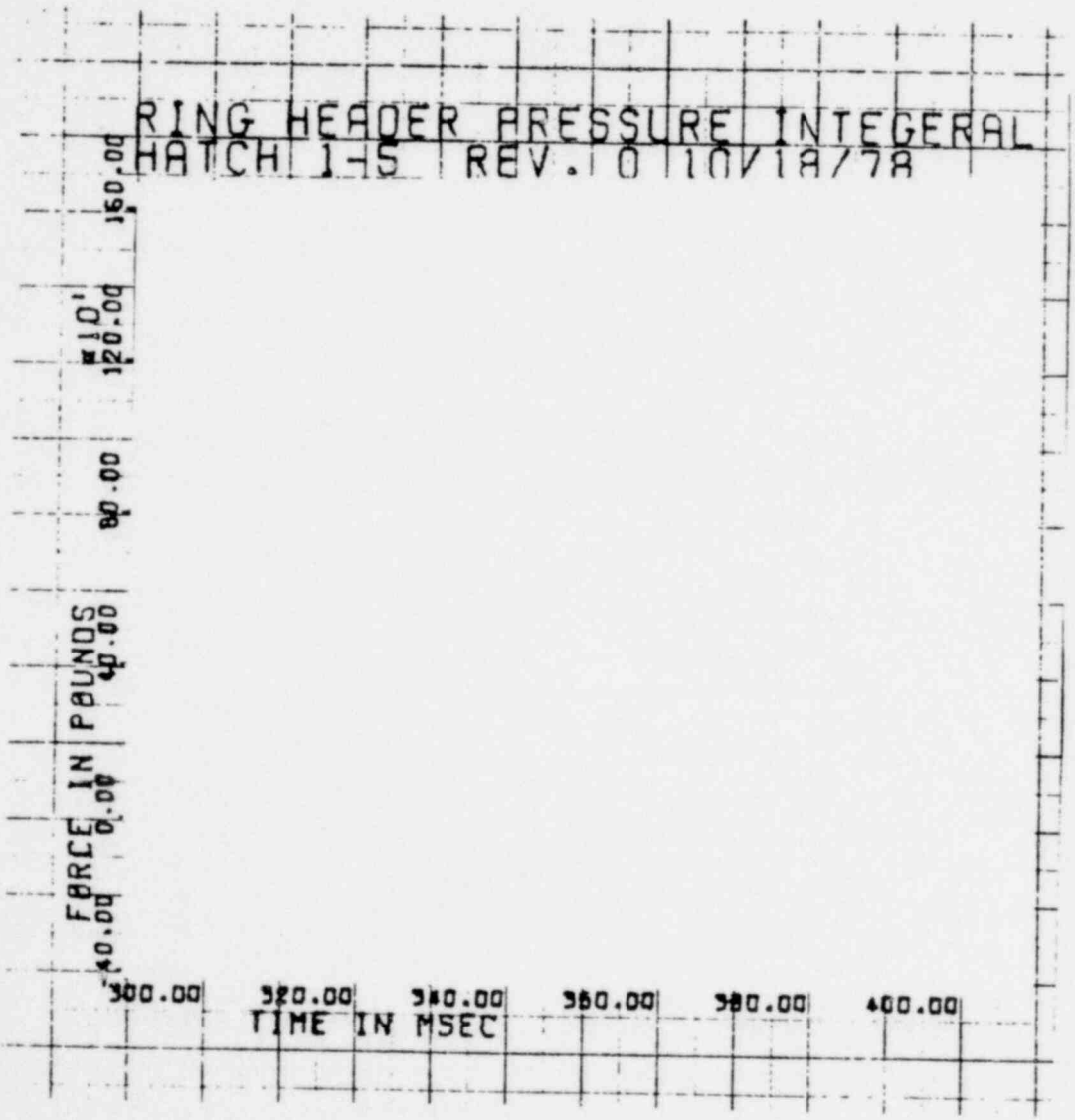

1351 079

FIGURE B-83

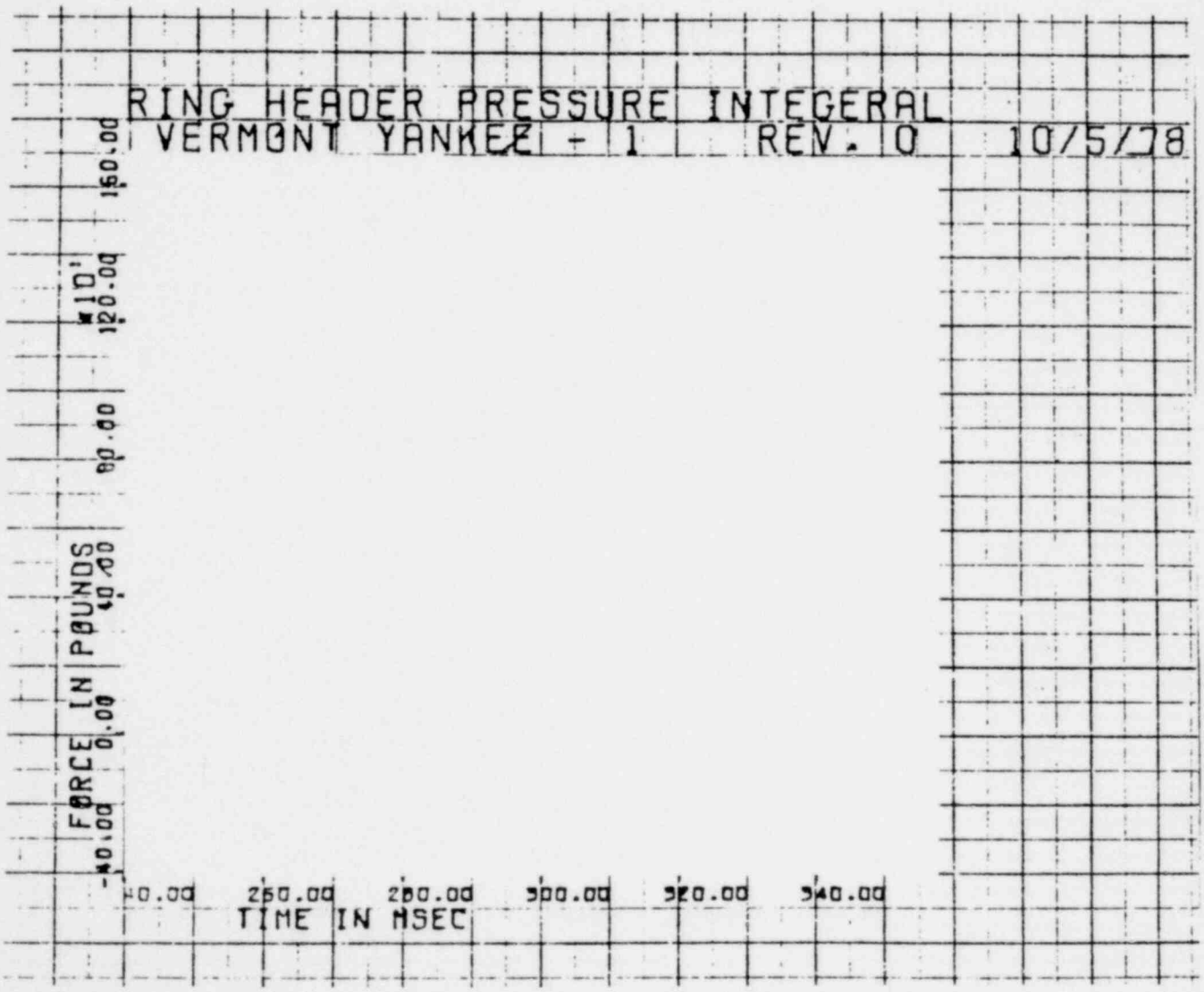

1351 080

FIGURE B-84

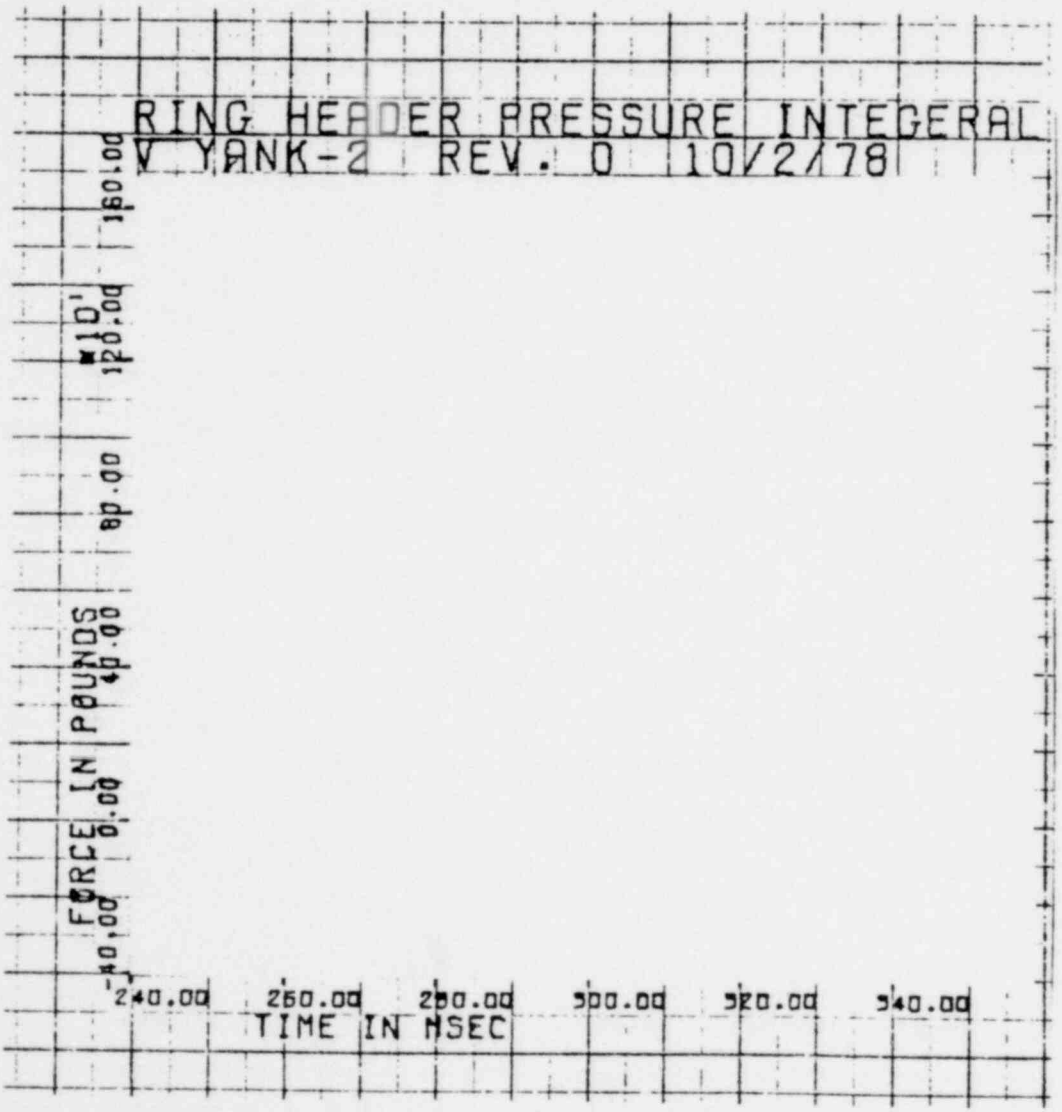

1351 081

FIGURE B-85

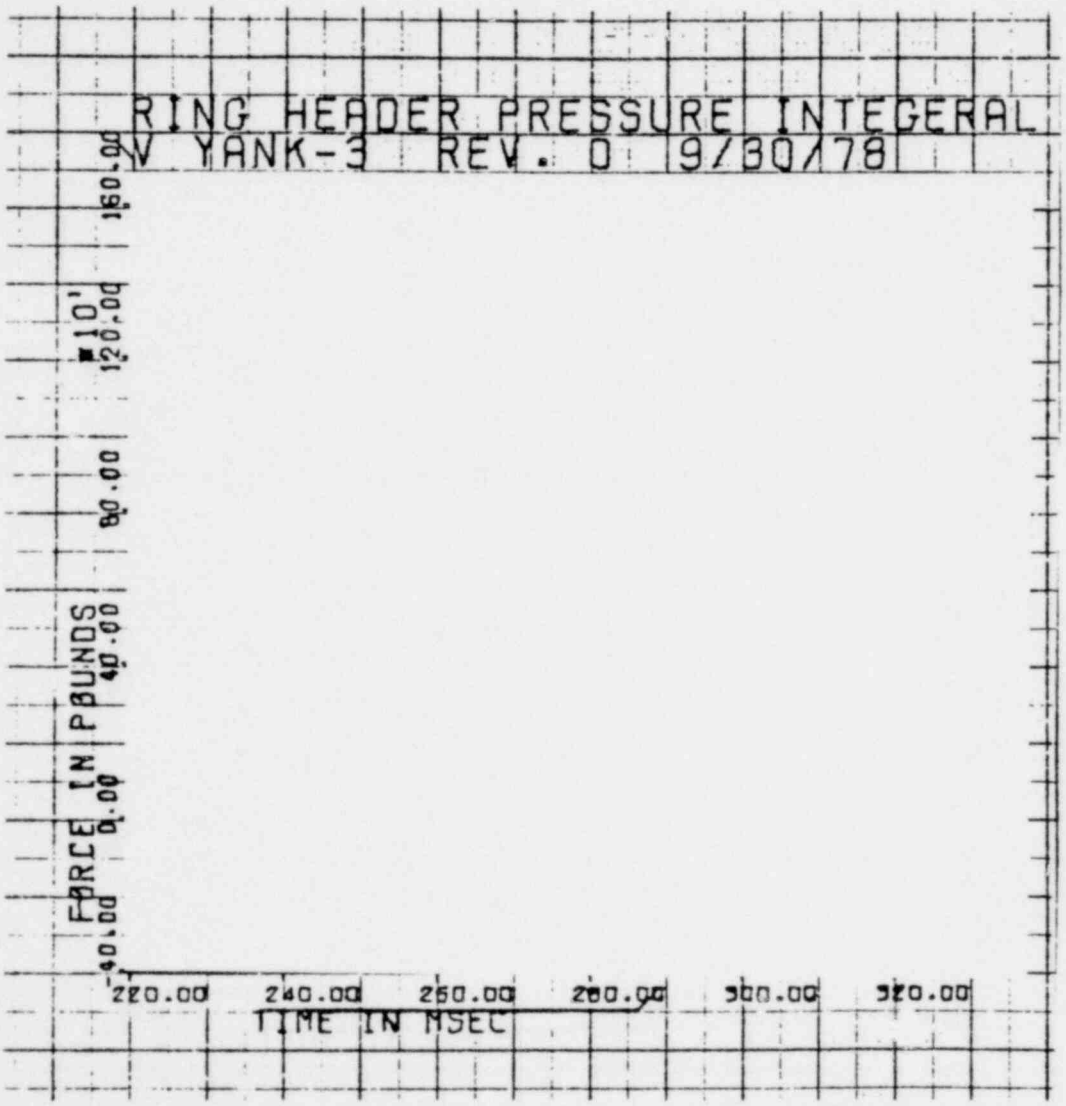

FIGURE B-86

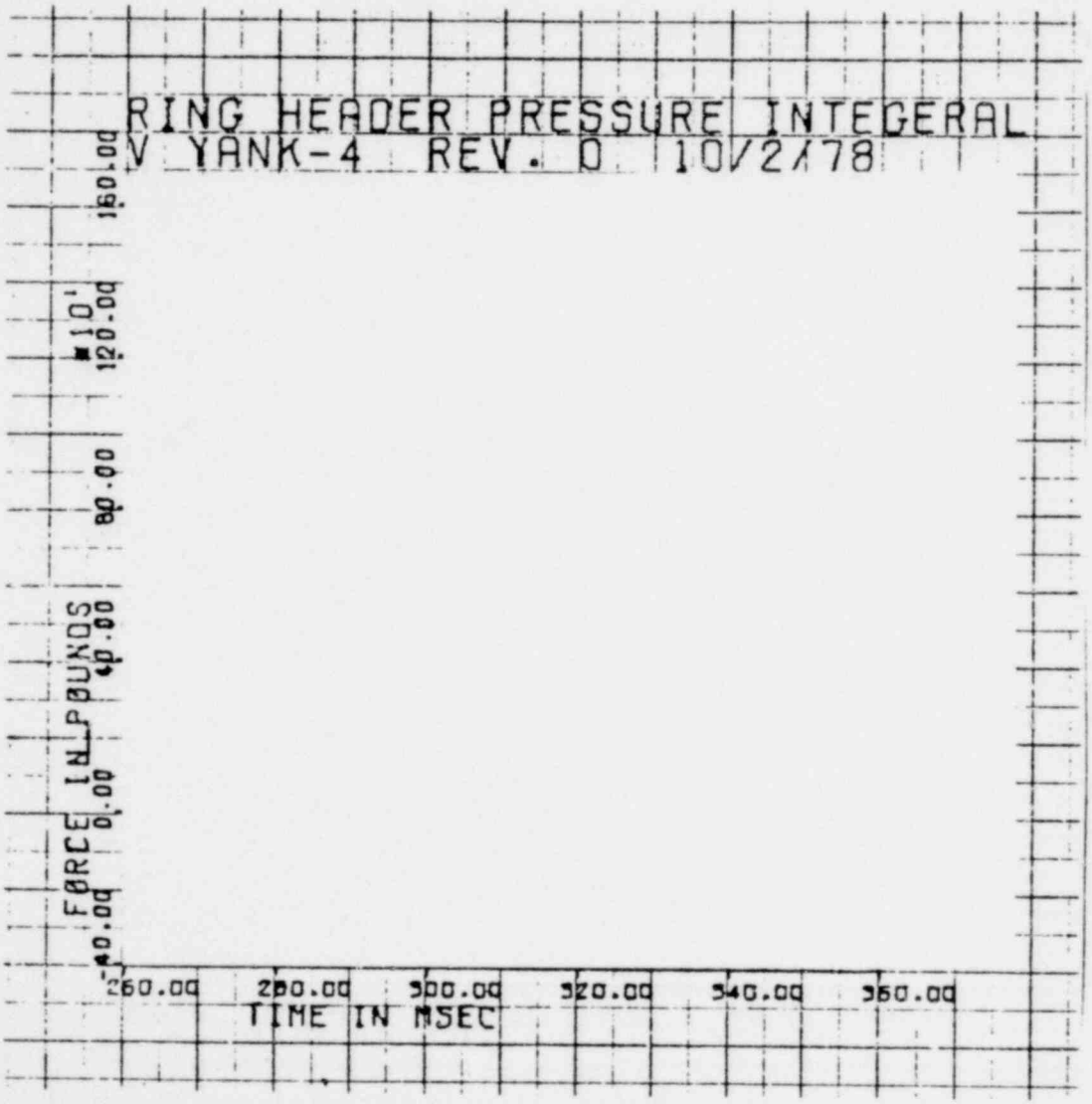

FIGURE B-87

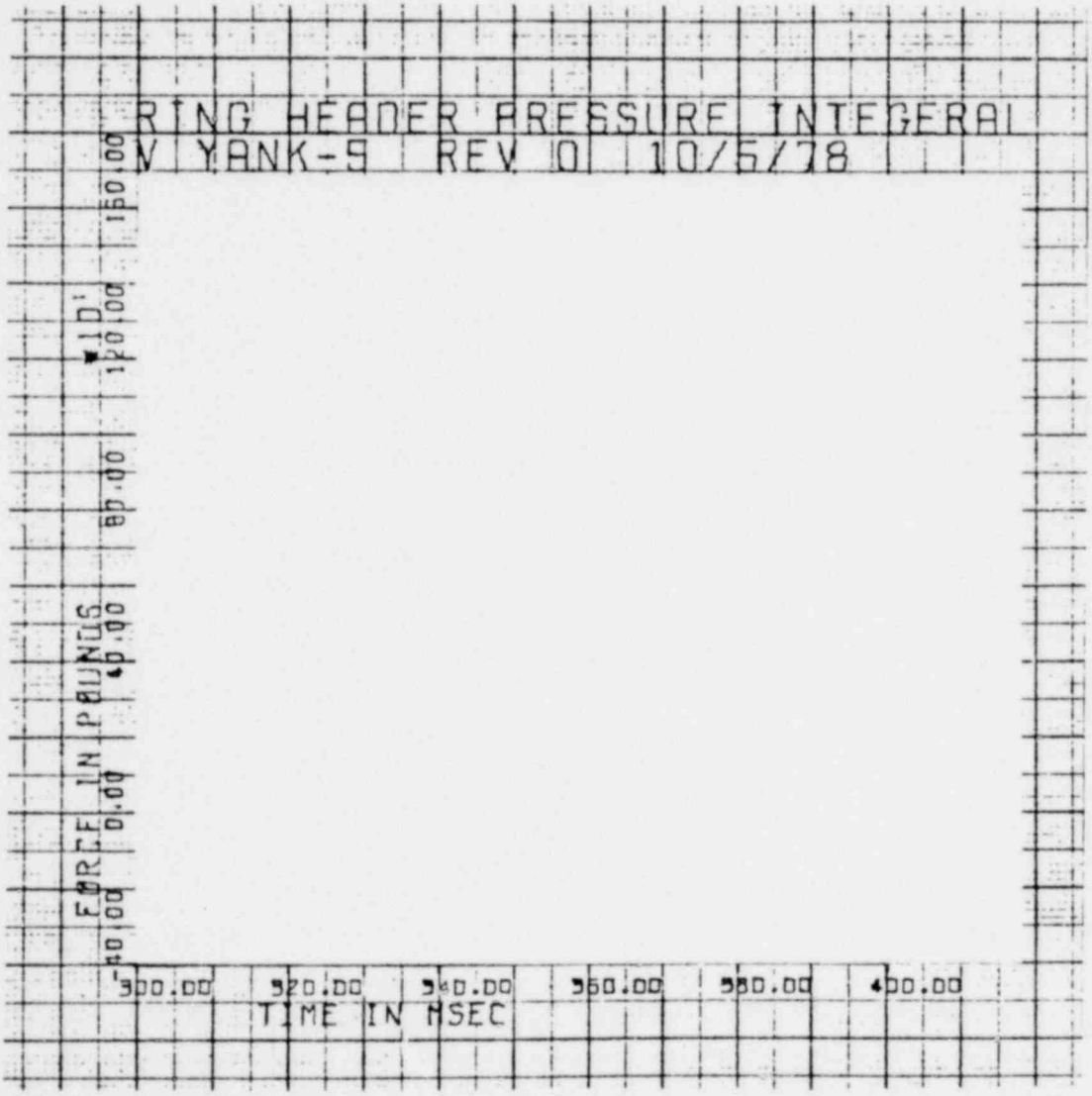

FIGURE B-88

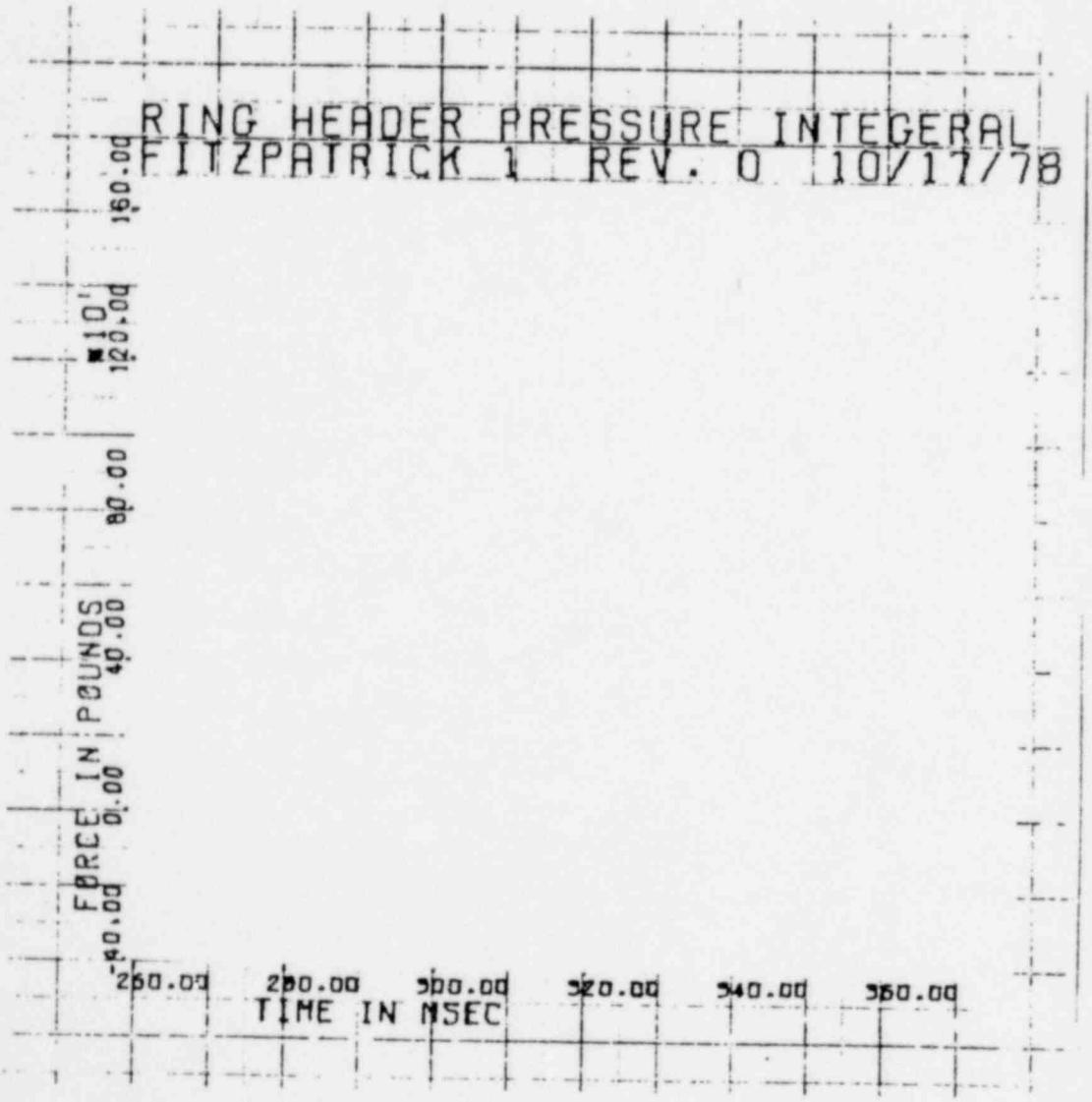

FIGURE B-89

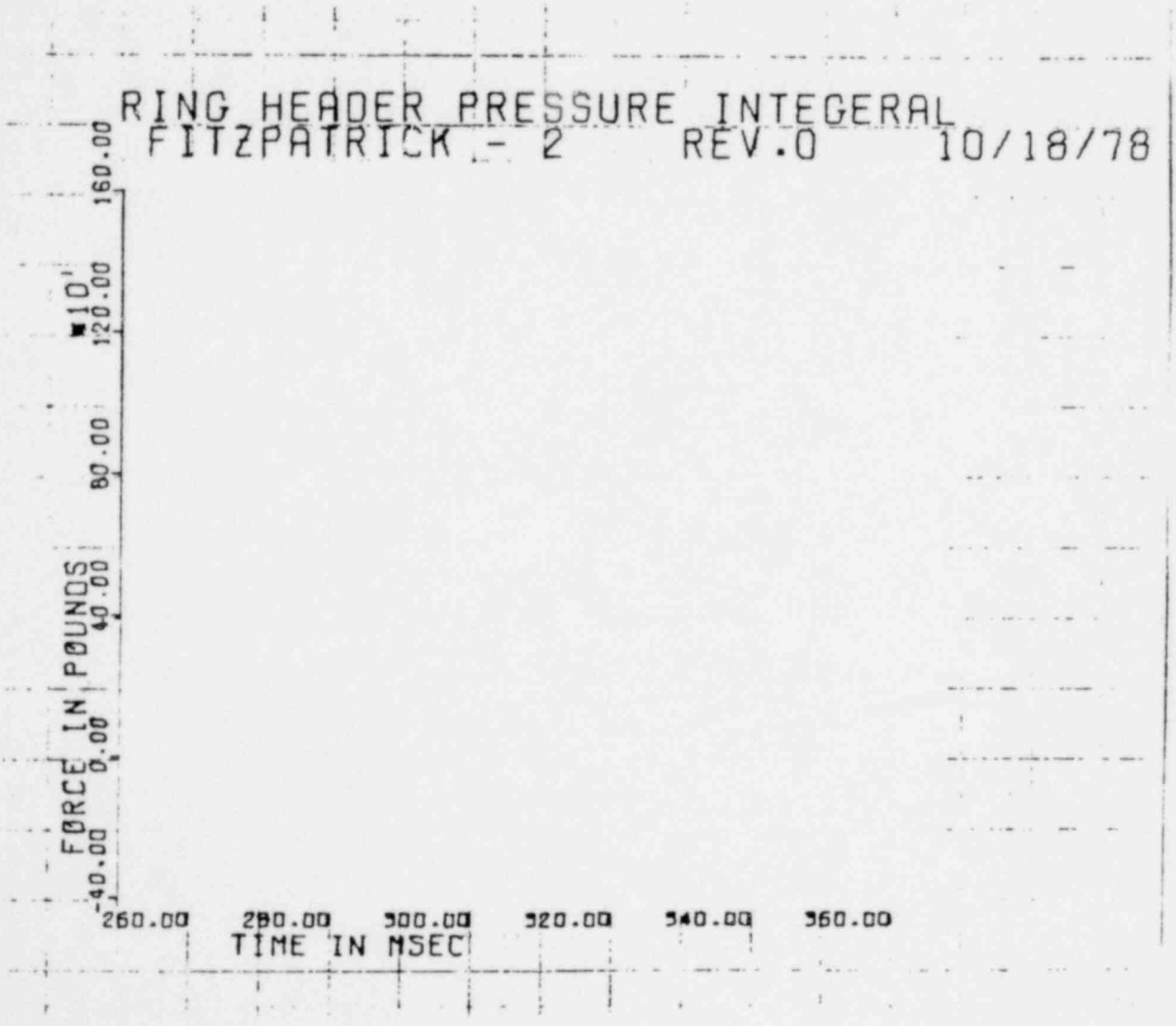

FIGURE B-90

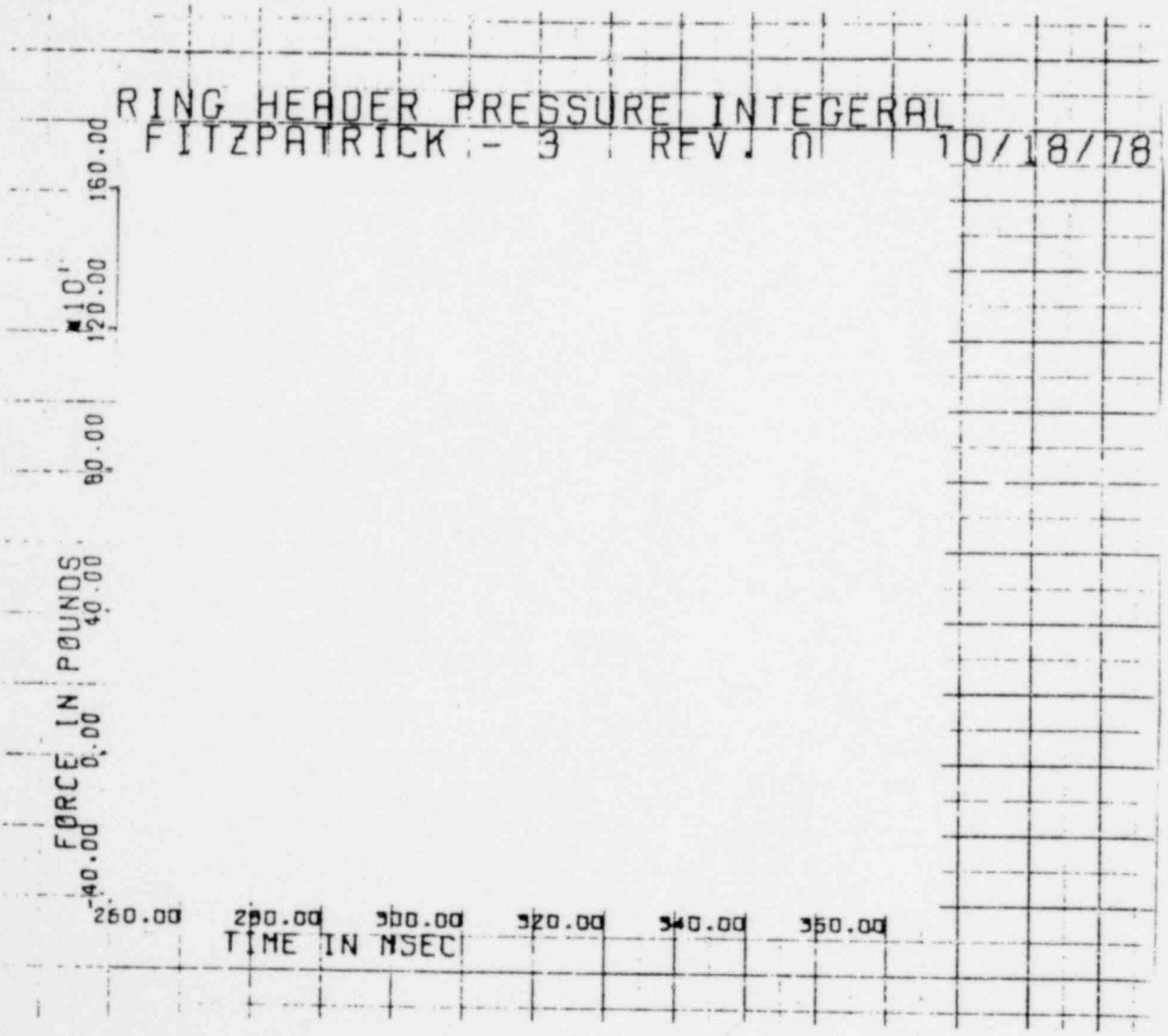

1351 087

FIGURE B-91

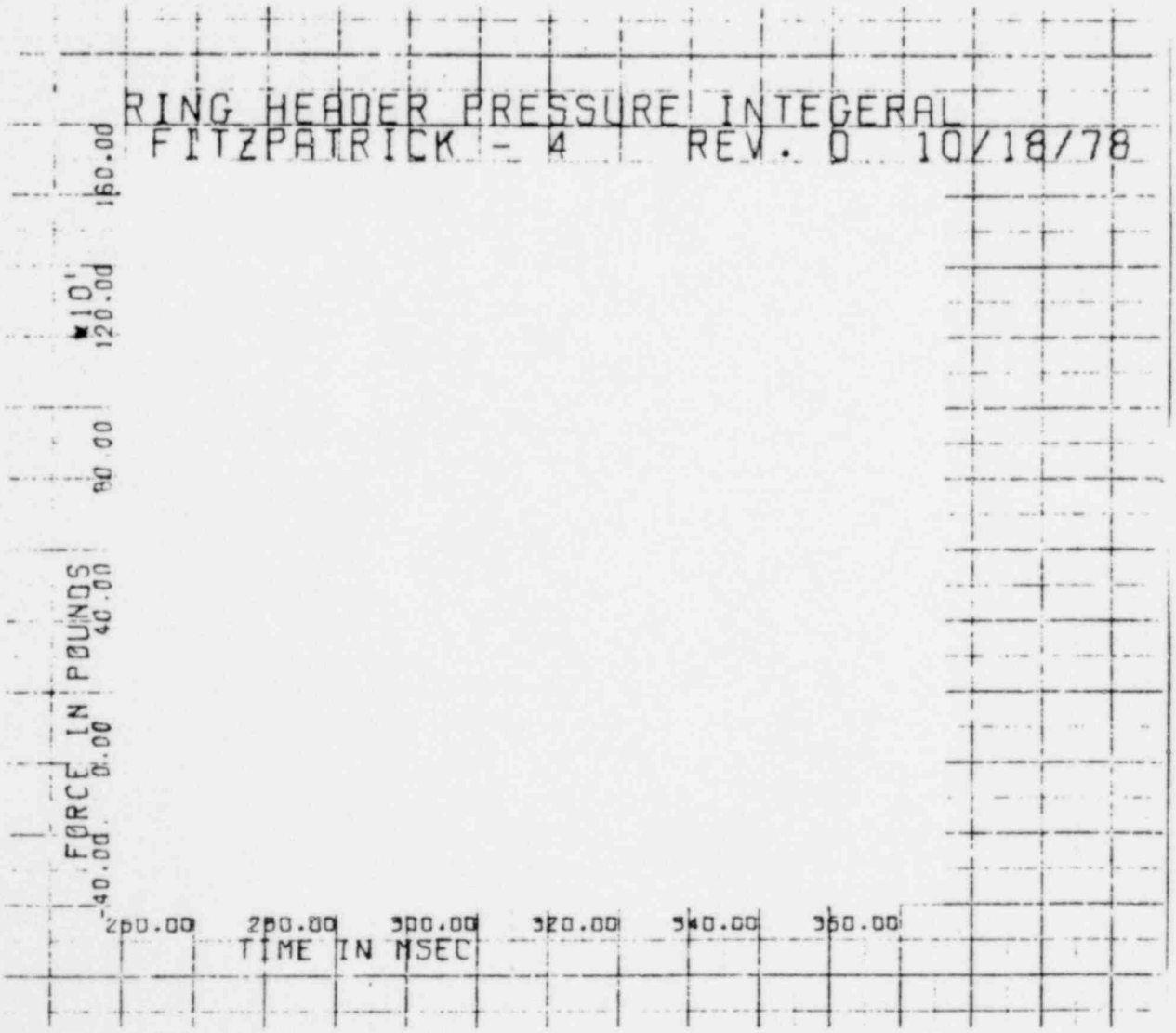

FIGURE B-92

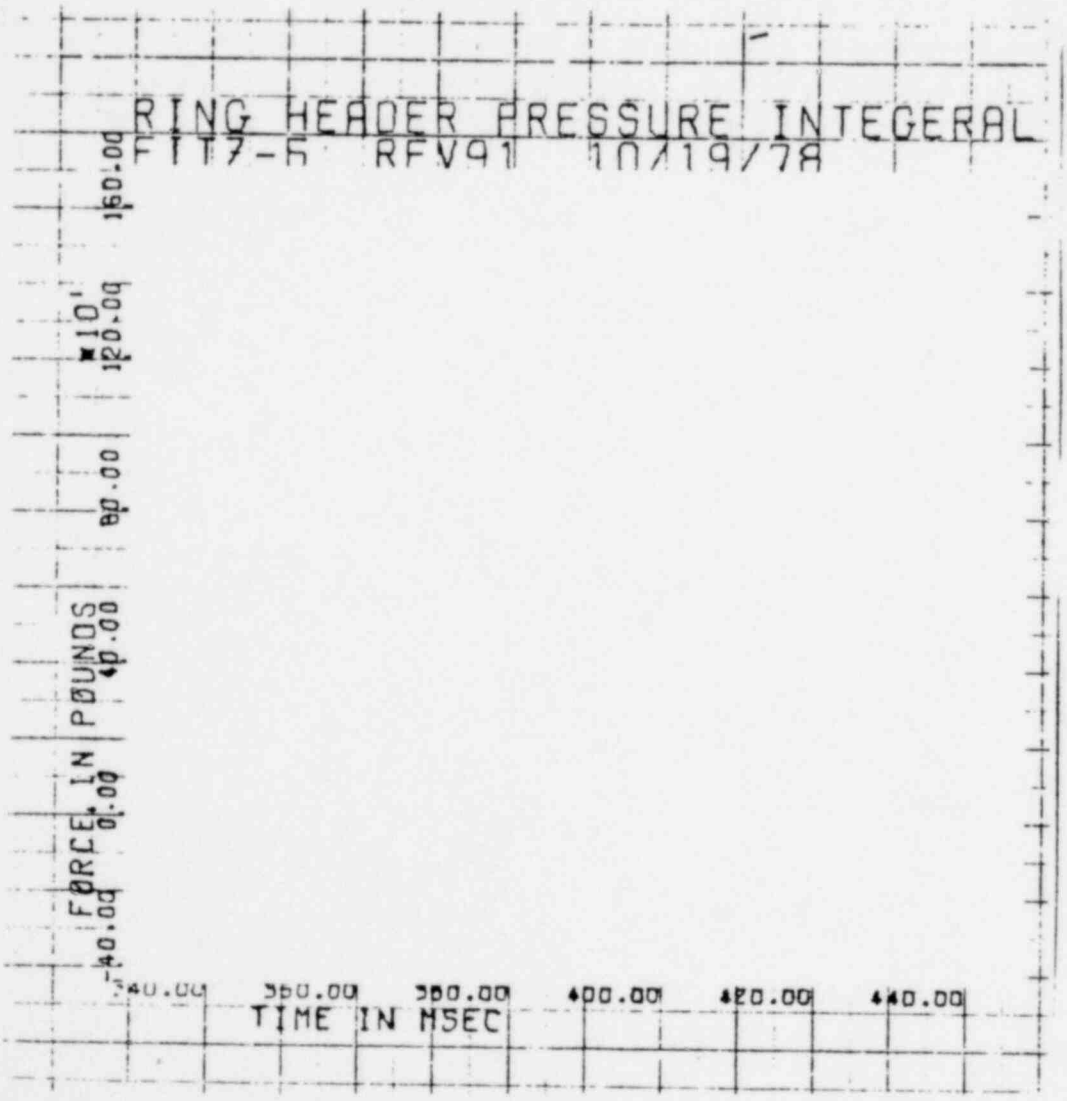

FIGURE B-93

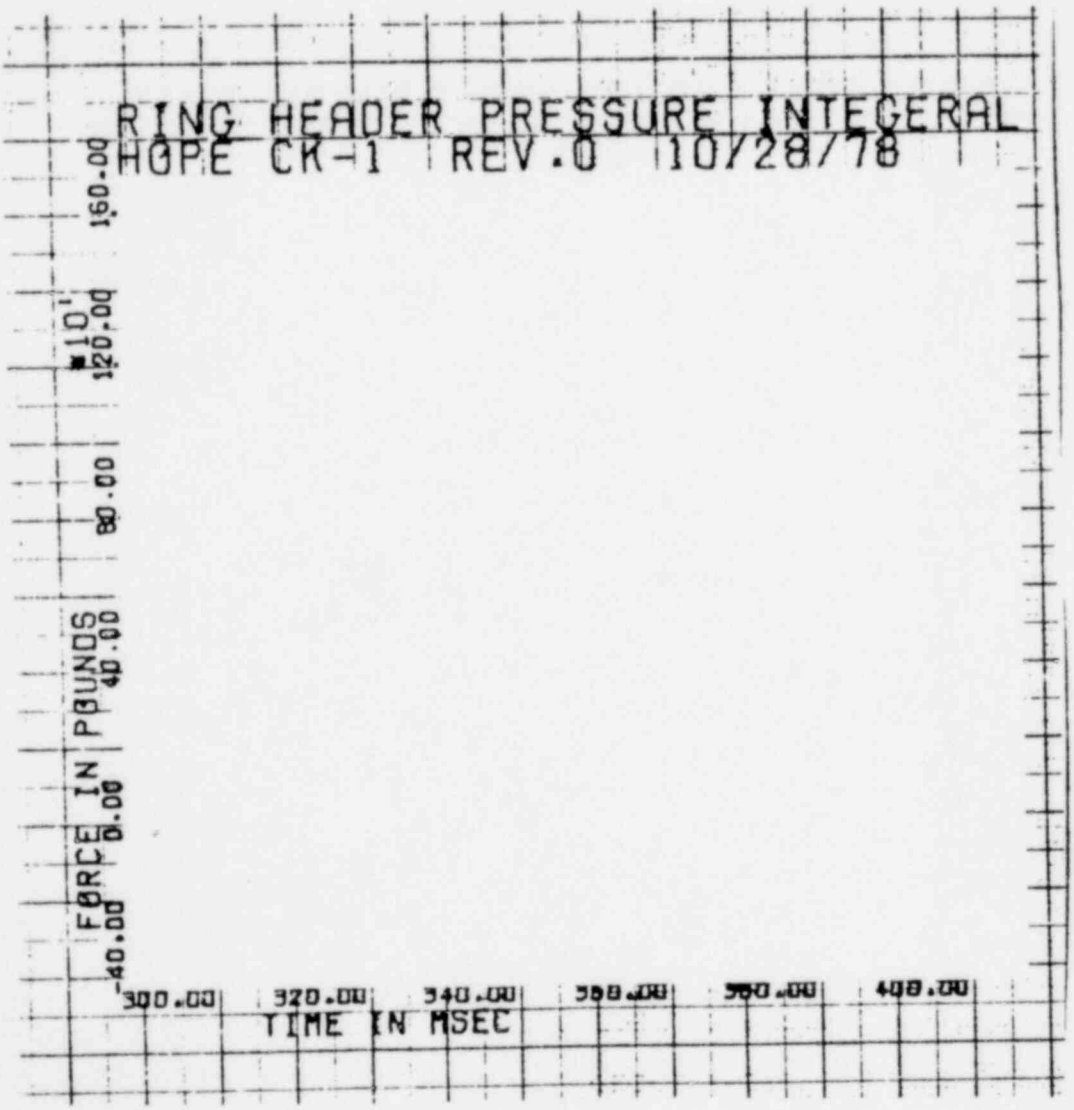

FIGURE B-94

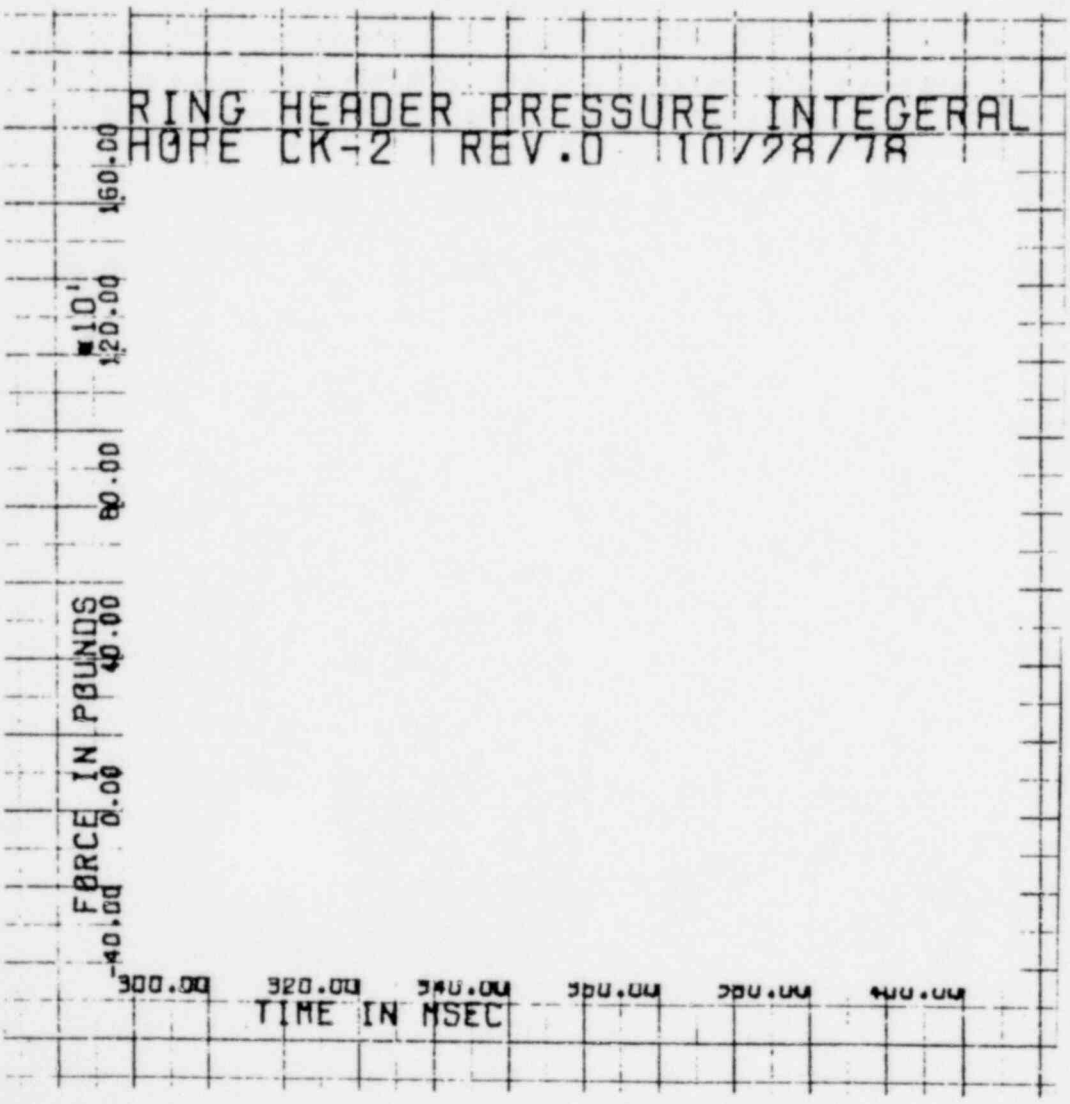

1351 091

FIGURE B-95

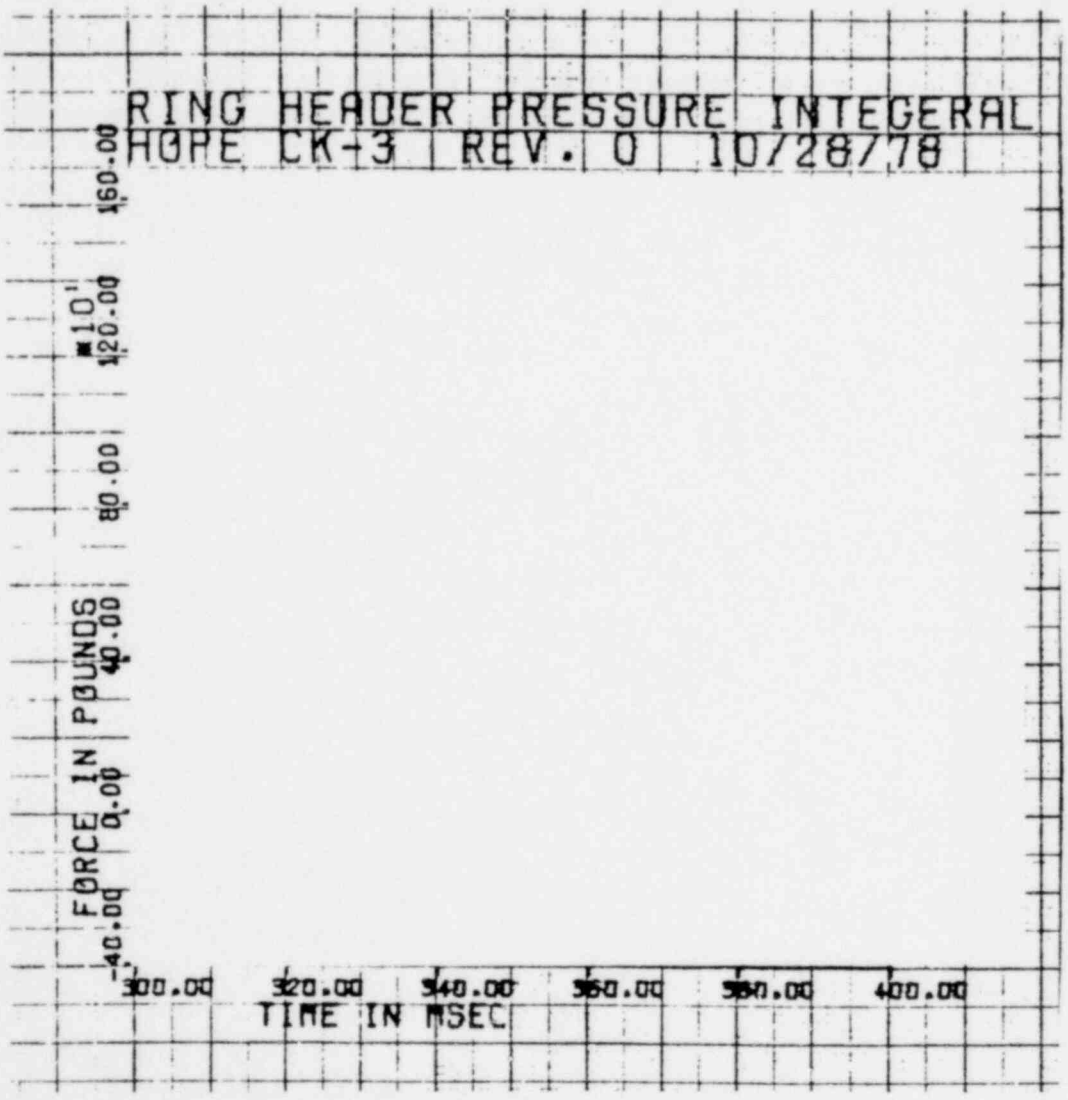

FIGURE B-96

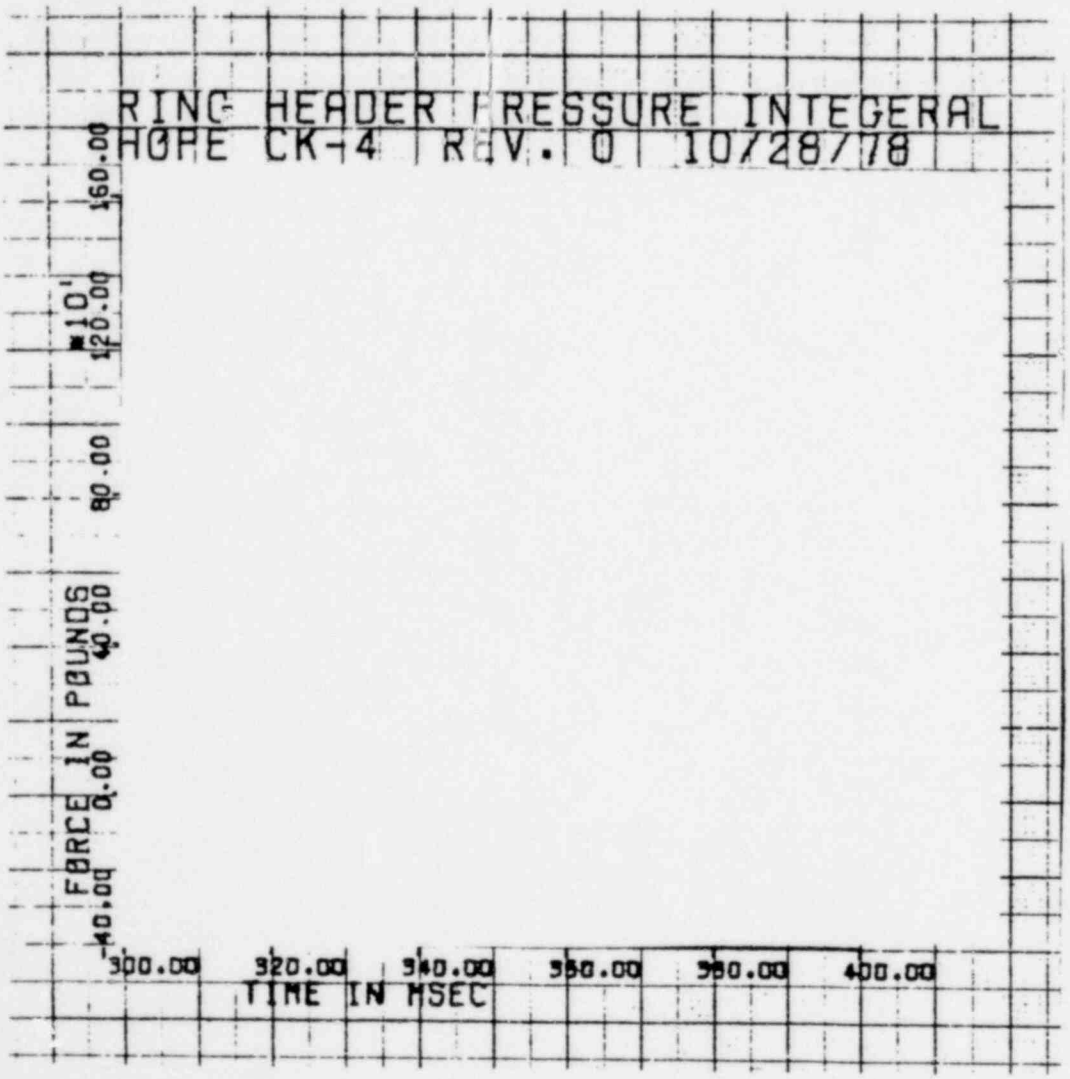

FIGURE B-97

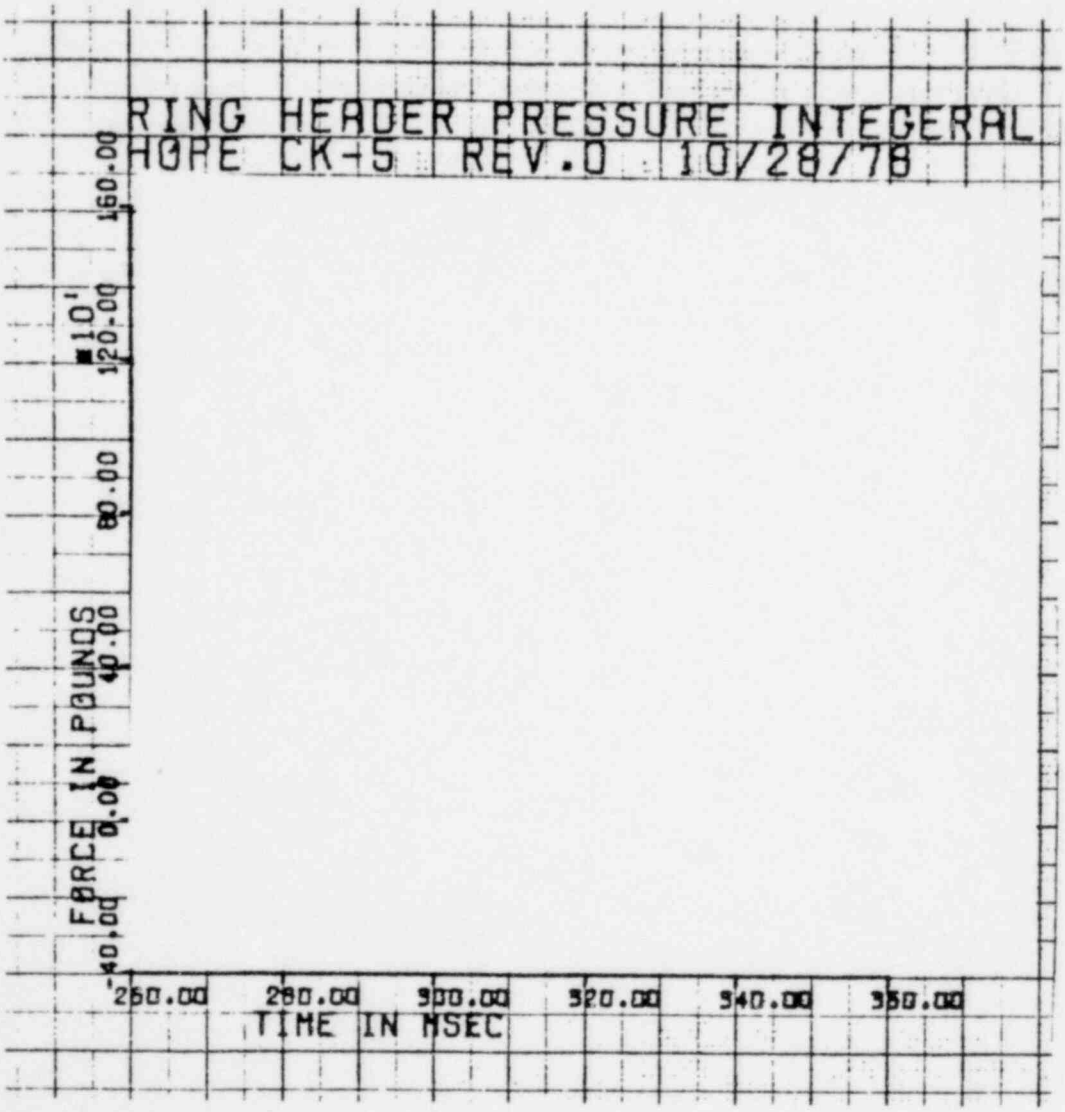

TABLE B-1

TYPICAL NODAL LAYOUT DATA

NAME	ANGULAR POSITION	DISTANCE FROM G [in]	AREA [in²]
PT3001			
PT3002			
PT3003			
PT3004			
PT3005			
PT3006			
PT3007			
PT3008			
PT3009			
PT3010			
PT3011			
PT3013			
A			
B			
C			
D			
E			
F			
G			
H			
I			
J			
K			
L			
M			
N			
O			
P			
Q			
R			
S			
T			
U			
V			
W			
X			
Y			
Z			
AA			
BB			
CC			
DD			
EE			
FF			
GG			
HH			
PT3012			
II			
JJ			
KK			
LL			
MM			

1351 095

TABLE B-2

b

TYPICAL VENT HEADER INPUT DATA

Note: This table is for illustrative purposes only - All Vent Header Digital Data is included in Table B-3 which follows.

RING HEADER PRESSURE INTEGRAL
MONT-1 REV. 0 12/05/78

DIGITAL INPUT VALUES FOR VENT HEADER IMPACT PRESSURE INTEGRATION

DATA REDUCED BY ....STEVE SHAMP.....

DATA CHECKED BY .....

MONT-1 REV. 0 12/05/78

1351 096

B-2 (Continued)

DATA REDUCED BY .....

DATA CHECKED BY .....

MONT-1 REV. 0 12/05/78

1351 097

B-2 (Continued)

ANGLE(DEG)
AXIAL POSITION (IN)
SURFACE AREA (SQ IN)
FM TIME CORRECTION (MSEC)
TONI

1351 098

TABLE B-3

SUMMARY OF VENT HEADER DIGITAL DATA

PAGES OF THIS TABLE ARE ON MICROFICHE LOCATED IN BACK OF REPORT

ALL THE MICROFICHE PAGES ARE PROPRIETARY

MATCH 2-A1 REV. 0 12/11/78

DIGITAL INPUT VALUES FOR VENT HEADER IMPACT PRESSURE INTEGRATION

DATA REDUCED BY ..... Steve Cuevas

DATA CHECKED BY .....

MATCH 2-A1 REV. 0 12/11/78

ROW NO.	TRANSDUCERS	INTERPOLATED POINTS
1	PT3001	21
	PT3002	
	PT3003	
	PT3004	
2	PT3005	21
	PT3006	
	PT3007	
	PT3008	
3	PT3009	17
	PT3010	
4	PT3011	16

1351 099

APPENDIX C

PLANT UNIQUE DATA COMPARISONS

The Plant Unique Tests provided an opportunity to evaluate a wide range of Mark I pool swell conditions. This appendix presents several comparisons of the data with special attention given to the effects of vent header deflectors and drywell/wetwell pressure differential (ΔP). The appendix concludes with a plant unique data correlation study. This study showed that the plant unique data is consistent and that most of the observed variations in the data can be explained by simple linear regressions of fundamental hydrodynamic and geometric parameters.

C.1 Comparison of Equivalent Quarter-Scale Loads

Direct comparison of plant unique test results requires adjustment of the test data to account for the different scale factors and projected areas. Table C-1 describes the basic scaling equations used to compare the results of different plant unique tests. These formulas are based on Dr. F. J. Moody's scaling laws previously described in Section 2.1. The Scale Factor (SF) referenced is the ratio of the plant full-scale torus diameter to the actual diameter of the test facility torus. The (.250/SF) multiplier is used to ratio every value back to a nominal quarter scale. Using the scaling equations shown in Table C-1, quarter-scale values of average pressure loads and pressure impulses have been calculated for the Mark I plants tested. These values, which are based on QSTF scaled mean data, do not represent a load definition. They do, however, allow a quantitative comparison of test results to be made for the plants tested.

Previously-run QSTF test data from Tasks 5.5.1 and 5.5.3-1 are given in Table C-2 for comparison with the plant unique test data. Test data normalized to quarter scale are given in Tables C-3 through C-12. In these tables, the test conditions and deflector pipe sizes are given for full scale.

C.1.1 Comparison of Torus Forces

As discussed in Section C.3, ΔP significantly mitigates torus forces. For the ΔP runs, the level of ΔP varied from 2.31 to 4.33 ft. (full scale) among the plants and the torus forces (peak average downforce pressure) varied from 0.90 to 2.48 psi. Therefore, although both ΔP and zero ΔP forces are presented in Tables C-3 through C-12, the most direct plant comparisons are at the zero ΔP condition. Even at zero ΔP, the equivalent quarter-scale torus forces showed considerable variation. Duane Arnold, Fermi 2, and Hope Creek had downforce pressures in the range of 1.46 to 2.0 psi, which were lower than other plants at zero ΔP. These

plants had relatively shallow submergence, wide torus section, and low pressurization rate. Cooper Station, Monticello, Pilgrim, and Vermont Yankee had higher torus downforces (3.09 to 3.98 psi) compared with other plants at zero ΔP. These plants had relatively deep submergence and high drywell pressurization rate. In addition, Vermont Yankee's downcomer discharge was closer to the bottom of the torus than for any other plant.

C.1.2 Comparison of Vent Header Forces

The effects of vent header deflectors tend to dominate the vent header impact forces and actually camouflage otherwise significant hydrodynamic effects, such as the level of ΔP. The Monticello and Fermi 2 "T" deflectors (pipe with structural "T"s), 29* and 25.8 inch respectively, and Peach Bottom 26 inch winged deflector (pipe with structural angles) essentially removed vent header impact. The Hatch 1 and Vermont Yankee winged deflectors 26 and 25.75 inch respectively and Dresden and Fitzpatrick pipe deflectors 20 and 30 inch respectively were relatively more effective in reducing vent header impact, compared with the Millstone 19.5 inch winged deflector, Pilgrim 16 inch pipe deflector, and Brunswick 20 inch pipe deflector. The Nine Mile Point and Oyster Creek pipe deflectors, 16 and 20 inch respectively, showed reduced peak impact pressure and peak force but rather high vent impulse. Hatch 2, Duane Arnold, Cooper Station, Browns Ferry, and Hope Creek with unprotected vent header recorded higher peak pressure and peak force than other plants with protected vent header. Duane Arnold and Hope Creek had lower impulse due to their smaller header diameter ($I \propto D^2$) or lower pool velocity.

---

* Full scale deflector width

1351 102

C.2 Effects of Vent Header Deflectors

Pipe deflectors mitigate the vent header impact by protecting the vent header bottom dead center (BDC) from direct impact. Pool impact on the pipe deflector generates a water curl at the side of the pipe that precedes the main water slug. The peak impact pressure usually occurs at the location of curl impact, which is roughly above the edge of the deflector. The peak pressure locations move away from the vent BDC as the deflector width is increased. Although the curl velocity is higher than the main pool velocity, the peak pressure is significantly reduced even with the smaller deflectors.

Eight scoping vent deflector tests were conducted to evaluate 3.36 inch (12 inches full scale) and 5.60 inch (20 inches full scale) pipe deflectors using the Monticello plant geometry. Four tests were conducted for each of the pipe deflectors to obtain statistically significant data. These tests were in addition to the plant unique deflector tests, using a "T" deflector (29 inches full scale), as part of the Monticello load definition and ΔP sensitivity tests. Figure C-1 presents the locations and magnitudes of typical vent header impact pressures for protected (Monticello) and unprotected (Hatch 2) vent headers. The peak impact pressures in the protected vent headers are reduced drastically from the unprotected vent header, even though the Monticello plant pool swell conditions were more severe than the Hatch 2 conditions. As shown in Figure C-1, the peak pressure locations move away from the vent BDC as the deflector width is increased.

Non-dimensionalized vent header impact parameters were developed to evaluate the effectiveness of deflectors on vent header impact mitigation. Non-dimensionalized values for peak local pressure (P^*_{LOCAL}), vent impact force (F^*) and hydrodynamic mass (M^*_H) are developed in Tables C-13 through 16. P^*_{LOCAL} is the ratio of the peak local impact pressure to the dynamic pressure at the estimated header impact velocity. The non-dimensional force (F^*) is the peak force divided by the

bulk pool dynamic pressure times the vent header projected area and is analogous to a drag coefficient. The non-dimensional hydrodynamic mass (M_H^*) is the ratio of the apparent hydrodynamic mass (M_H = Impulse/Bulk Velocity) and the deeply submerged hydrodynamic mass based on the cylindrical volume of the header. Values around 0.2 are typical of thick slug cylinder impact. The non-dimensionalized impact parameters are plotted against the ratio of deflector width/vent header diameter in Figures C-2 through C-4. Some scatter in the data would be expected since these first-order correlations neglect the effects of deflector geometry, deflector height above the pool, and submergence.

As discussed in the previous paragraph and shown in Figure C-2, even relatively small deflectors are very effective mitigators of peak local impact pressure. Values of P^*_{LOCAL} on the order of 1.0 indicate primarily drag load. ΔP mitigates impact pressure for unprotected headers by reducing the slug thickness at impact. Deflectors break up the slug and seem to wash out the mitigating effects of ΔP on vent header impact. Non-dimensionalized values for vent impact force (Figure C-3) and impulse (Figure C-4) show that, although these parameters are harder to mitigate than local peak pressure, they can be essentially eliminated with a large enough deflector. The non-dimensional correlations indicate that deflectors roughly half the width of the header reduce vent impact loads to negligible values. All three correlations show that the mitigating effects of ΔP for unprotected headers tend to disappear for large deflectors.

As deflector size increases, more of the pool swell impact force and momentum are removed from the vent header. However, removal of pool impact reveals a vent header downforce peak that coincides with peak torus upforce. This is illustrated in Figure C-5, which shows the acceleration corrected vent header load cell (impact force) response for Hatch 2 (unprotected vent header) and several Monticello deflector tests. Further evaluation of the vent header load transients without significant vent header impact show that a major part of the observed

downforce on the vent header can be accounted for by vent header thrust. It is felt that the remaining downforce is caused by the increase in torus air space pressure which acts on the upper half of the vent header.

The following observations were made on the effects of vent header deflectors:

a) In general pipe deflectors (especially those with angles or structural Ts) whose width is half the width of the vent header effectively mitigate the vent header impact.

b) Smaller pipes significantly reduce peak local pressures, but are not as effective at reducing peak force or impact impulse.

c) Plain pipes located too close to the water (before the pool swell can approach terminal velocity) are less effective in mitigating vent header impact than pipes located at least one foot (full scale) above the initial water surface.

d) Adding angles or structural Ts to a plain pipe seems to provide greater header impact mitigation than would be expected for a plain pipe of the same width.

e) Adding angles or structural Ts to a plain pipe seems to remove the penalty of locating the deflector too close to the water. The deflector acts more as a flow diverter and is less sensitive to the impact velocity.

f) High speed movies show that vent header deflectors divert the flow past the vent header and promote higher local penetration of the freespace.

C.3 Effects of Drywell/Wetwell Differential Pressurization (ΔP)

Plant unique operating condition tests were conducted at the minimum ΔP and maximum submergence of the operating range specified by the utilities for these tests. The data from these tests will be used as the primary basis for the final Load Definition Report loads. In addition to the operating condition tests, tests at zero ΔP were conducted to provide a data base for pool swell with loss of ΔP. Five plants (Hatch 2, Monticello, Fermi 2, Brunswick, and Hope Creek) which had four or more tests performed at zero ΔP provide a statistically significant data base for examining the effects of ΔP removal over a range of plant parameters. Measured standard deviations of the load parameters (wetwell vertical loads and vent header impact) for the five plants with four tests at zero ΔP are summarized in Table C-17 as percent of the measured mean. Standard deviations of the wetwell vertical loads are reasonably small. Monticello and Fermi 2, which were tested with a "T" deflector, had negligibly small vent header impact force.

The effects of ΔP on measured torus loads have been examined by plotting the ratio of the load at ΔP to the load without ΔP on the Y-axis against the ratio of ΔP/submergence (normalized measure of ΔP) on the X-axis. Implicit in these correlations are data points at (0, 1.0). Both the peak downforce ratio (Figure C-6) and downforce impulse ratio (Figure C-7) seem to have a well-defined linear relationship, with the exception of the Monticello and Peach Bottom ΔP data. Because the water level in the Monticello and Peach Bottom zero ΔP tests was above the downcomer bends, the stream line length is shorter on the outside of the downcomers and the downcomers clear first on that side. This phenomena called staged clearing resulted in a reduction of downforce for the zero ΔP tests.

The peak upforce ratio (Figure C-8) follows but lies below the general trend developed earlier from GE 1/12-scale tests at 4 ft. submergence (Reference 4), with the exception of the Browns Ferry test data. Some of the type II (30° bend) downcomer plants exhibited upforce oscillation,

especially at zero ΔP conditions. The fact that less upforce oscillation was observed at partial ΔP conditions may account for the increased effect of ΔP on maximum upforce observed during those tests.

Although the downforce and impulse ratios for the Browns Ferry runs (Figures C-6 and C-7) fit the data trends, the upforce ratio stayed above the trend (Figure C-8). It should be noted that Browns Ferry has 45° downcomers with the bend well above the waterline. As the pool rises past the bend, the flow is observed to separate leaving a column of air from the bend into the torus air space. During the Generic Sensitivity Tests with the standard 45° downcomers, the plot of peak upforce versus drywell pressurization rate ($\dot{p}$) indicated that as pressurization rate increases the peak upforce reaches a maximum and then declines (Reference 1). This maximum may occur because driving the pool harder (higher $\dot{p}$) causes the bubble to reach the air column above the downcomer bend earlier during the upforce transient, thus causing early breakthrough. Although the impulse increases as the pressurization rate is increased, the upforce flattens out and does not oscillate. Early bubble breakthrough in the Browns Ferry tests with the 45° downcomers may have reduced the ΔP sensitivity of peak upforce.

The vent header impact pressure ratios are presented in Figure C-9. The failure of the peak pressure ratio to show a correlation with ΔP indicates that deflector size controls the vent impact characteristics. Monticello data appear to confirm this conclusion.

C.4 Plant Unique Data Correlation Study

C.4.1 Introduction

The objective of this section is to present the results of a statistical study of the plant unique test data, performed to describe the relationships between plant parameters and pool swell loads and to demonstrate their basic consistency over the wide range of test conditions.

A series of multiple regressions were performed to fit curves generated by parameters such as the pressure differential between drywell and wetwell, submergence, and pressurization rate to a series of important pool swell parameters. The regressions were performed with a stepwise multiple regression computer program.

The data base for the statistical study was the test conditions used in and pool swell parameters generated by the Task 5.5.3-2 Plant Unique Tests, scaled to 1/4 scale values.

The statistical study indicates that the range and shape of the torus force function can be predicted on the basis of ΔP, submergence, pressurization rate, volume between orifices, and torus cell width. These five test conditions explain at least 93% of the variation which is observed in five of eight of the important torus force variables including peak downforce and downforce impulse and explain at least 80% of the other three. The study also shows that at least 78% of the total observed variation in all of the vent header force phenomena can be accounted for by variations in deflector width/vent header diameter, distance from deflector bottom to water surface, the use of an angle deflector or pipe deflector, and pressurization rate. (This lower percentage is due to the smaller size of the vent header variables in relation to the error associated with measurement.)

Even with the very simple second order models used in this study, torus and vent header data were found to correlate very well with a limited number of test conditions.

C.4.2 Multiple Regression--Some Definitions

Multiple regression produces the linear combination of independent variables, i.e., test parameters such as pressurization rate, fL/D,

etc., which best estimates a given dependent variable, such as peak torus downforce.

The linear model is as follows:

$$Y_j = a + b_1X_{1j} + b_2X_{2j} + \ldots + b_nX_{nj} + e_j$$

where Y_j is the value of the dependent variable for test j. The Y_j is considered dependent in the sense that its magnitude is influenced by the values of the independent variables, X_{ij}, (the value of plant parameter i for test j) in a linear fashion, which is described by the constant terms a_1, $b_1 \ldots$, b_n. The e_j are error terms composed of measurement errors and the influence of variables which are excluded.

If assumptions can be made about the distribution of the error terms, then estimates made with the regression can be accompanied by confidence intervals (which estimate the probability that the observed will be within a given interval).

The total sum of squared differences between the mean of the dependent variable, $\bar{Y}$, and its observed values, Yi, can be partitioned into the sum of squares which is predicted by the regression equation (SS_1), and the sum of squared error terms (SS_2):

$$\sum_i (Y_i - \bar{Y})^2 = \sum_i (Y_i' - \bar{Y})^2 + \sum_i (Y_i - Y_i')^2$$

$$SS_{TOTAL} = SS_1 + SS_2$$

where $Y_i' = a + b_1 X_{1i} + \ldots + b_nX_{ni}$ and $Y_i - Y_i' = e_i$.

The ratio of SS_1/SS_{TOT} is called R^2 and increases from zero toward one as the equation accounts for more of the observed variation in the dependent variable.

The ratio of SS_2 to the number of independent squares in SS_2 (the degrees of freedom of SS_2) is the variance of the estimate (the square of the standard error of the estimate (SEE) = variance).

Since the load definition tests are groups of tests run under identical conditions, information can be gained by further partitioning SS_2:

$$SS_2 = \sum_i \sum_j (Y_{ij} - Y'_{ij})^2 = \sum_i \sum_j (Y_{ij} - \bar{Y}_{i\cdot})^2 + SS_0$$

where Y_{ij}, and Y'_{ij} are the observed and estimated Ys for the jth test in load definition test group i, and $\bar{Y}_i$ is the mean of observed Y in group i. The ratio:

$$\frac{\sum_i \sum_j (Y_{ij} - \bar{Y}_{i\cdot})2}{\sum_i \sum_j (Y_{ij} - \bar{Y})^2} = r\%$$

is an approximate measure of the proportion of the total variation which is completely random, i.e., the proportion which comes from differences in pool swell parameters from identical tests. The r% rises as Y gets smaller in relation to its measurement error.

If two sums of squares come from identical distributions, then the ratio of the ratio of one sum of squares to its degrees of freedom to the other sum of squares to its degrees of freedom is distributed F.

An F test of the following form can be used to test if SS_1 is significantly greater than SS_2 which is the same as testing if the regression equation which produced SS_1 and SS_2 is significant:

$$\frac{SS_{1/k}}{SS_2/n-k-1} = F$$

where k = the number of variables in the equation, and n = the number of tests examined.

An F test of the following form can be used to test if an individual variable is significant:

$$\frac{SS_{i/1}}{SS_2/k-n-1} = F$$

where SS_i is the difference between SS_1 before variable i is introduced into the regression and SS_1 after i is introduced. The F-statistics are calculated, compared to an F distribution and the probability that the two sums of squares come from identical distributions is known.*

C.4.3 Test Matrix

The load definition tests make up a data base of 96 tests in 36 different combinations of 14 plant parameters. Twelve resultant pool phenomena were examined as dependent variables.

* For further reading, see Mood, Graybill, Boes. Introduction to The Theory of Statistics. McGraw Hill, 1974, Chapter X.

C.4.3.1 Plant Parameters--Their Definitions, Their 1/4 Scale Ranges, and Abbreviations

1. Total fL/D is a measure of system flow resistance, and its calculation is described in Appendix B. Range [12.9, 18.3] (fL/D).
2. $(fL/D_{VENT})/(fL/D_{DOWNCOMER})$ is a measure of the ratio of the contribution to total system flow resistance due to the vent orifice to the contribution due to the downcomer orifice. Range [0.72, 1.42]. (V/DC)
3. Pressurization rate, dP/dt, in the drywell, immediately after test initiation, in psia/millisecond. Range [25.5, 41.4]. ($\dot{P}$)
4. Initial pressure difference between the drywell and wetwell, in inches of water displaced down the downcomer. Range [0.0, 13.0]. (ΔP)
5. The volume between the vent orifice and the two downcomer orifices, in cubic feet. Range [3.16, 4.21]. (VOL)
6. Submergence is the distance from the water surface to the downcomer exit, in inches. Range [10.0, 14.4]. (SUB)
7. The distance from the bottom of the vent header to the water surface, in inches. Range [6.5, 12.2]. (HEADER-WATER GAP)
8. The torus width, in inches. Range [15.9, 27.0]. (CELL WIDTH)
9. The vent header diameter, in inches. Range [12.6, 15.0]. (HEADER DIAMETER)
10. The vertical distance from the downcomer exit to the bottom of the torus, in inches. Range [19.0, 34.5]. (DCE-TORUS GAP)
11. The distance from the deflector bottom to the water surface, in inches (Hatch 2, Cooper Station, Brown's Ferry, and Hope Creek were tested without deflectors and those tests were left out of calculations involving this variable) Range [0, 5.8]. (CLEARANCE)
12. Deflector width (wing tip to wing tip, if T-deflector; pipe diameter, if pipe) divided by vent header diameter. Range [0.000, 0.522]. (DEFLECTOR W/HEADER D)

13. Pool area at water surface less the area displaced by the downcomers divided by the effective flow area at the water surface. Range [25.7, 46.0]. (POOL/VENT)
14. A dummy variable is included to account for any differences in effect on pool swell parameters between an angle deflector (or T deflector) and a pipe deflector of equal width (Again, those tests without a deflector were left out of calculations involving this variable). (D-TYPE) equals one when the test was run with a T-deflector and zero when the test was run with a pipe.

C.4.3.2 Pool Swell Parameters

1. Peak torus downforce and peak torus down pressure. The first is the peak downforce value of the torus pressure integral, corrected for water inertia, and the second value is the first divided by torus area.
2. Peak torus upforce and peak torus up pressure. The first is the peak upforce value of the torus pressure integral, uncorrected for water inertia, and the second is the first divided by torus area.
3. Peak torus downforce impulse and peak torus downpressure impulse. The first is the integral of the torus pressure integral, uncorrected for water inertia, from To, the start of pressurization of the drywell, to the time that the torus pressure integral reaches zero again, and the second is the first divided by torus area.
4. Peak vent header upforce and peak vent header up pressure. The first is the maximum value of the vent header force from the integral of vent header pressure transducers, and the second is the first divided by vent header projected area.
5. Peak vent header force impulse and peak vent header pressure impulse. The first is the integral of the vent header force from the first vent header impact until peak impulse. The second is the first divided by vent header area.

6. Time to peak torus downforce is the difference between the time at which peak torus downforce occurred and To.
7. Time to peak torus upforce is the difference between the time at which peak torus upforce occurred and To.

All variables were scaled from the tested scale to quarter scale, according to scaling laws developed by Dr. Moody of General Electric, as discussed in section 4.1 of this report.

Regressions on the 12 pool swell parameters were done using the Statistical Package for the Social Sciences (SPSS). All 14 of the plant parameters (first order variables) and a wide variety of products and quotients of the plant parameters (second order variables) were F-tested for significance at the 99% confidence level. The eight second order variables listed in Table C-18 were found to enter into one or more of the regression equations. The simple correlation between ΔP and $\Delta P/SUB$ is greater than 0.9, so it is probably impossible to distinguish the effects of the two variables upon the dependent variable, from one another, based on this data. When the correlation between two independent variables in a regression equation is high, the variability of the estimates of their coefficients is raised as is the variability of the estimate of the dependent variable. When evaluating the second order variables, it is important to decide if the second order variable is statistically distinguishable from its component first order variables. If it is not, i.e., if the correlation between the second order variable and either of its components is greater than 0.9, then the additional complexity of a second order variable is not justified. When such a second order variable enters the regression, we cannot tell if it is describing an important second order effect or if it is acting as a proxy for one of its components. None of the second order variables except for $\Delta P/SUB$ is correlated with either of its components to a degree greater than 0.82. The reason $\Delta P/SUB$ appears

in regression equations in preference to ΔP is because ΔP/SUB had better success as an explanatory variable in those regression equations.

The correlation coefficients between variables which enter into regression equations are presented in Table C-19. The degree of multicollinearity in the equations is not greater than 0.65.

The correlation coefficients between all of the first order variables are presented in Table C-20. The simple correlation between the plant parameters did not exceed 0.9 except for the pair of pool area to vent area ratio and cell width. It is probably impossible, based on this data to distinguish between the effect of cell width and the effect of pool area/vent area. Cell width was chosen over pool area/vent area, because of its physical simplicity.

The correlation matrix among all variables that entered any equation is not reproduced, but contains no member greater than 0.82, except for the pair ΔP and ΔP/SUB, as noted above.

The ability to draw conclusions from the data is limited by the high correlation between candidate explaining variables. Cell width and pool area/vent area and the pair ΔP and ΔP/SUB are statistically indistinguishable in this data base, so the choice between them is made on an arbitrary or non-statistical basis. The range of plant configurations to which the estimates are applicable is limited to within and slightly beyond the ranges of plant configurations which make up the data base.

C.4.4 Regression Results

The regression equations listed in this section were chosen by maximizing the overall F of the equation. New variables were not introduced unless they could overcome the built-in bias of the

F-test against additional variables.[1] Variables with low individual Fs and which tended to have coefficients of opposite sign from the expected sign, or whose sign was inconsistent were eliminated from regressions on the basis that they probably represented a spurious correlation with the dependent variable.

The 90% confidence intervals (CI) are based on the assumption that the errors of the estimates are normally distributed. A chi-squared test was made of this assumption, and all of the distributions of the residuals were found to be within a normal range.[2]

The coefficient of variability (CV) is the ratio of the standard error of the estimate (SEE) to the mean of the observed variable which is being estimated. It is a more comparable measure of the variability of the estimates. R^2, r%, and SEE have been defined.

All Fs reported are significant with 99% confidence.

The following equations summarize the results of this study:

---

1 = Recall that the F-test for the equation as a whole is:

$$\frac{SS_{EXPLAINED/k}}{SS_{ERRORS/n-k-1}}$$

where k = the number of variables

and n = the number of tests

So an additional variable automatically tends to decrease the numerator and increase the denominator, thus tending to decrease F.

2= i.e., in no case could we reject the null hypothesis that the residuals were normally distributed with even 75% confidence.

1. $DN = 870.2 - 2863.6\ (\Delta P/SUB) + 8.44\ (SUB(CELL\text{-}WIDTH)) + 68.15(\dot{P})$
   a. $R^2 = 92.8\%$
   b. SEE = 310.63
      1. 90% CI = ± 511.0 — DN = peak torus downforce
      2. CV = 8.0%
   c. overall $F_{3,92} = 395.9$
   d. r% = 0.1

2. $PDN = 2.4508 - 1.5318\ (\Delta P/SUB) + 0.0038\ (\dot{P}(SUB)) - 0.0504\ (CELL\text{-}WIDTH)$
   a. $R^2 = 92.9\%$
   b. SEE = 0.17305
      1. 90% CI = ± 0.28468 — PDN = peak torus down pressure
      2. CV = 8.4%
   c. overall $F_{3,92} = 406.8$

3. $UP = -1056.1 - 1088.0\ (\Delta P/SUB) + 239.3\ (SUB) + 1.3(\dot{P}(CELL\text{-}WIDTH))$
   a. $R^2 = 79.7\%$
   b. SEE = 261.8
      1. 90% CI = ± 430.7 — UP = peak torus upforce
      2. CV = 11.8%
   c. overall $F_{3,92} = 120.4$
   d. r% = 0.1

4. $PVP = 2.1454 - 0.7361\ (TD/SUB) - 0.6180\ (\Delta P/SUB) + 0.0010\ (\dot{P})(CELL\text{-}WIDTH$
   a. $R^2 = 85.4$
   b. SEE = 0.13631
      1. 90% CI = ± 0.2242 — PUP = peak torus uppressure
      2. CV = 11.5%
   c. overall $F_{3,92} = 179$

5. $IM = -63.38 - 155.91\ (\Delta P/SUB) + 23.25\ (SUB) + 1.13(\dot{P}(VOL))$
   a. $R^2 = 94.8\%$
   b. SEE = 15.51
      1. 90% CI = ± 25.51 — IM = peak torus force impulse
      2. CV = 5.8%
   c. overall $F_{3,92} = 555.0$
   d. r% = 0.0

6. $PIM = 0.2453 - 0.0853\ (\Delta P/SUB) - 0.0692\ (CELL\text{-}WIDTH) - 0.0021(\dot{P})$
   a. $R^2 = 93.9\%$
   b. SEE = 0.01075
      1. 90% CI = ± 0.01768 — PIM = peak torus pressure impulse
      2. CV = 7.6%
   c. overall $F_{3,92} = 469.2$

7. VP = 1004.9 - 1424.7 (DEFLECTOR W/HEADER D) - 106.9 (CLEARANCE) - 149.6 (D-TYPE)
   a. $R^2 = 80.0\%$
   b. SEE = 77.8
      1. 90% CI = ± 128.0 — VP = peak vent header upforce
      2. CV = 40.6%
   c. overall $F_{3,69} = 92.0$
   d. r% = 10.2

8. PVP = 3.7917 - 5.2880 (DEFLECTOR W/HEADER D) - 0.4129 (CLEARANCE) - 0.6362 (D-TYPE)
   a. $R^2 = 77.9\%$
   b. SEE = 0.3217
      1. 90% CI = ± 0.5292 — PVP = peak vent header uppressure
      2. CV = 45.4%
   c. overall $F_{3,69} = 81.2$

1351 118

9. VM = 1.025 - 29.035 (DEFLECTOR W/HEADER D) + 0.665 ($\dot{P}$)
   - 4.661 (D-TYPE)
   a. R^2 = 84.0%
   b. SEE = 2.359
      1. 90% CI = ± 3.881
      2. CV = 30.2%
   c. overall $F_{3,69}$ = 120.2
   d. r% = 4.2

   VM = peak vent header force impulse

10. PVM = 0.0068 - 0.1054 (DEFLECTOR W/HEADER D) + 0.0024 ($\dot{P}$)
    - 0.0187 (D-TYPE)
    a. R^2 = 80.6%
    b. SEE = 0.0099
       1. 90% CI = ± 0.01629
       2. CV = 34.5%
    c. overall $F_{3,69}$ = 95.5

    PVM = peak vent header pressure impu

11. B1 = 149.4 - 62.76 (ΔP/SUB) + 0.72 (VOL-SUB) - 0.09 (fL/D·$\dot{P}$)
    a. R^2 87.7%
    b. SEE = 9.45
       1. 90% CI = ± 15.55
       2. CV = 8.7%
    c. overall $F_{3,93}$ = 217.7
    d. r% = 3.9

    B1 = time to peak torus downforce

12. B3 = 139.27 - 8.33 (ΔP) + 16.68 (SUB) - 1.57($\dot{P}$)
    a. R^2 = 97.0%
    b. SEE = 7.432
       1. 90% CI = ± 12.23
       2. CV = 3.0%
    c. overall $F_{3,93}$ = 976.4
    d. r% = 0.1

    B3 = time to peak torus upforce

C.4.5 Conclusions

The criteria by which to judge a regression are the proportion of observed variation in the dependent variable that it accounts for (R^2), the variability of its estimates (CV), and its overall significance (F).

		R^2	CV	$F_{3,93}$	$F_{3,69}$	r%
1.	Time to peak torus upforce	97.0%	3.0%	976.4		0.1
2.	Peak torus force impulse	94.8%	5.8%	555.0		0.0
3.	Peak torus pressure impulse	93.9%	7.6%	469.2		*
4.	Peak torus down pressure	92.9%	8.4%	406.8		*
5.	Peak torus downforce	92.8%	8.0%	395.9		0.1
6.	Time to peak torus downforce	87.7%	8.7%	217.7		3.9
7.	Peak torus uppressure	85.4%	11.5%	179.3		*
8.	Peak torus upforce	79.9%	11.8%			*
9.	Peak vent header force impulse	84.0%	30.2%	120.4	120.2	4.2
10.	Peak vent header pressure impulse	80.6%	34.5%		95.2	*
11.	Peak vent header force	80.0%	40.6%		92.0	10.2
12.	Peak vent header pressure	77.9%	45.5%		81.2	*

The regressions in the first group of five are the most successful. They all explain a large percentage of the observed variation and have a small enough SEE to be useful in estimating the dependent variable.

* = not calculated

They are also distinguished from the second group by the size of their overall F statistic. The Fs for the first group are roughly two times as large or more than the Fs in the second group.* This means we should weight the regressions in group one more highly in our determination of the relationships which are important to the pool phenomena, than the regressions in group two.

The first group has a lower level of r% than the second one. The r% is a measure of the proportion of total variation in the dependent variable which is attributable to variation between tests run at identical test conditions. This part of total variation is not available to be explained by a better model and is characterized as random. When two dependent variables are measured using similar devices, the variable which is smaller in magnitude will have the higher r%, because a greater proportion of observed variation in the smaller variable will be due to random measurement error. The r% for peak torus upforce and downforce is less than 0.1%, and the r% for the smaller peak vent header force is 10.2%. The r% for vent header force impulse is greater than the r% for torus force impulse because of the smaller size of the former, with a constant level of measurement accuracy (similarly for times to peak torus downforce and upforce).

The higher the r%, the lower the possible R^2, because of the greater size of the unexplainable component in unexplained variation. The smaller variables, time to torus downforce, and the vent header forces, are more difficult to explain than the larger variables, time to torus upforce and the torus forces, because a greater proportion of the measured value of the smaller variables is due to

---

* = F statistics of different degrees of freedom are not strictly comparable, but at these high levels of F the difference is negligible.

1351 121

measurement error. This high degree of measurement error is born out by the higher percentage of repeat test variation in these small variables.

The following table summarizes the independent variables and their effect on the dependent variables from regressions in the first group of five.

1. $\Delta P/SUB, \Delta P$ has a ± effect on dep variable
   - peak torus downforce
   - peak torus downforce pressure
   - peak torus force impulse
   - peak torus pressure impulse
   - time to peak torus upforce

2. $\dot{P}$ has a ± effect on dep. variable
   - time to peak torus upforce
   + peak torus pressure impulse
   + peak torus downforce

3. SUB has a ± effect on dep. variable
   + time to peak torus upforce
   + peak torus force impulse

4. CELL WIDTH has a - effect on peak torus down pressure

5. SUB(CELL WIDTH) has a + effect on peak torus downforce

6. $\dot{P}$ (SUB) has a + effect on peak torus down pressure

7. $\dot{P}$ (VOL) has a + effect on peak torus force impulse

8. CELL WIDTH/SUB has a - effect on peak torus pressure impulse

The effect of increased ΔP (increased ΔP/SUB) has been observed to decrease peak torus forces as well as to move the torus force function towards To, i.e., speed up the event and reduce times to peak upforce and downforce. The regression equations bear out the fact that increased ΔP is a very significant mitigator of torus loads, and tends to speed up the event.

The effect of increased $\dot{P}$ has been observed to increase the peak torus forces, and speed up the event. In equations for time to peak torus upforce, peak torus pressure impulse, and peak torus downforce, where $\dot{P}$ appears as a first order variable, these tendencies are found to be significant determinants of the three events in the expected way.

$\dot{P}$ also appears in two second degree variables. The interpretation of the sign of the coefficient of a second degree variable is more complicated. The selection of $\dot{P}$(SUB) in the equation for peak torus down pressure and $\dot{P}$(VOL) in the equation for peak torus force impulse, in favor of their components, means that there is a significant interaction between the two variables in the determination of downforce, i.e., there appears to be a non-linear aspect in the way $\dot{P}$ and SUB, in the equation for peak torus down pressure and $\dot{P}$ and (VOL) in the equation for peak torus force impulse affect their dependent variables. We observe that both second order variables have a positive sign, so if we hold either constant and increase the other, there is a positive effect on the dependent variable. This is consistent with our knowledge about $\dot{P}$ and SUB. (It may also indicate that the effect of increased (VOL) on the torus impulse is positive).

The effect of increased SUB is to increase torus forces and slow down the event (because increased SUB increases vent clearing time). SUB appears in the equations for time to peak torus upforce and peak torus force impulse to bear out these tendencies.

The regression equation indicates that increases in (CELL WIDTH) appear to have a significant negative effect on peak torus down pressure. Two kinds of interaction effects between (CELL WIDTH) and (SUB) were found to be significant. SUB(CELL WIDTH) has a positive effect on peak torus downforce. (CELL WIDTH)/SUB, the other kind of interaction, appears in peak torus pressure impulse with a negative sign. In other words, if we hold SUB constant and increase (CELL WIDTH), peak torus pressure impulse will decrease. This is consistent with the negative sign on (CELL WIDTH) in peak torus down pressure. If we hold (CELL WIDTH) constant and increase SUB, peak torus down pressure will increase.

Eight variables seem to be the most significant in the determination of the size and shape of the torus force curve. They are also sufficient to explain at least 93% of the variation observed in five of the important variables which describe that curve. The worst estimate which these eight produce is within 14% of the observed value 90% of the time.

The regressions for peak vent header force and impulse have lower Fs and R^2 than the regressions for the first group, so they are generally less significant and certainly explain less of the observed variation. Their CVs are also much higher. The reason for the greater difficulty of these dependent variables is the smaller size of the dependent variables in relation to measurement error.

The following table summarizes the independent variables which appear in the vent header force regressions and the sign of their coefficient.

1. Deflector width/vent header diam.
   has a ± effect on dep. variable
   - peak vent header force
   - peak vent header pressure

- peak vent header force impulse
- peak vent header pressure impulse

2. Deflector to water surface, distance
   - peak vent header force
   - peak vent header pressure

3. Differential effect of T-deflector vs. pipe
   - peak vent header force
   - peak vent header pressure
   - peak vent header force impulse
   - peak vent header pressure impulse

4. $\dot{P}$
   + peak vent header force impulse
   + peak vent header pressure impulse

Dependent variables (DEFLECTOR W/HEADER D) and (D-TYPE) appear in all four equations. As expected, increases in deflector to vent header ratio tend to decrease peak vent header force. An angle deflector also appears to be more effective at reducing vent header forces than a pipe of similar cross-section.

An increase in the distance from deflector bottom to water surface is a significant reducer of peak vent header forces.

An increase in $\dot{P}$ seems to be a significant positive factor in the determination of vent header impulse, as expected.

C.4.6 Summary

Multiple regression using a simple second degree model has allowed the correlation of all of the torus and vent header quantities with

a small set of test conditions. The coefficients in the regression equation make consistent physical sense. The high degree of explanatory power of these simple models verifies the consistency of the data with the relationships presented here.

As expected, some of the regressions were less successful than others. Peak torus downforce, downforce impulse, and time to peak upforce correlated well, while the vent header parameters, peak torus upforce, and time to torus downforce correlated less well. The dominant effect of the vent deflector on vent header loads together with the relatively small vent header loads occurring with deflectors probably account for the relative difficulty of the vent header loads. The effect of the vent deflector on torus uploads was not explored, and may contribute to the determination of torus upforce.

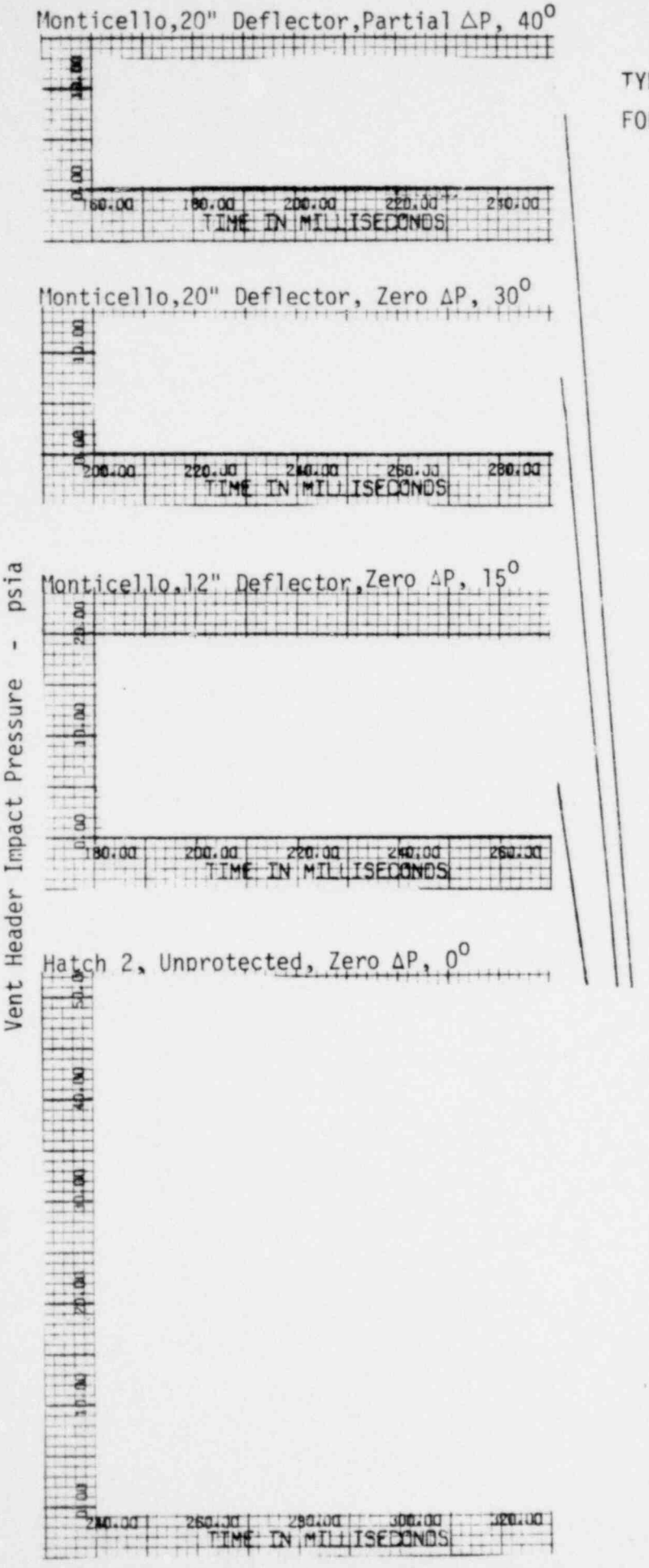

Figure C-1

TYPICAL VENT HEADER IMPACT PRESSURES
FOR PROTECTED AND UNPROTECTED HEADER

1351 127

FIGURE C-2

NORMALIZED MAXIMUM LOCAL IMPACT PRESSURE VERSUS NORMALIZED DEFLECTOR WIDTH

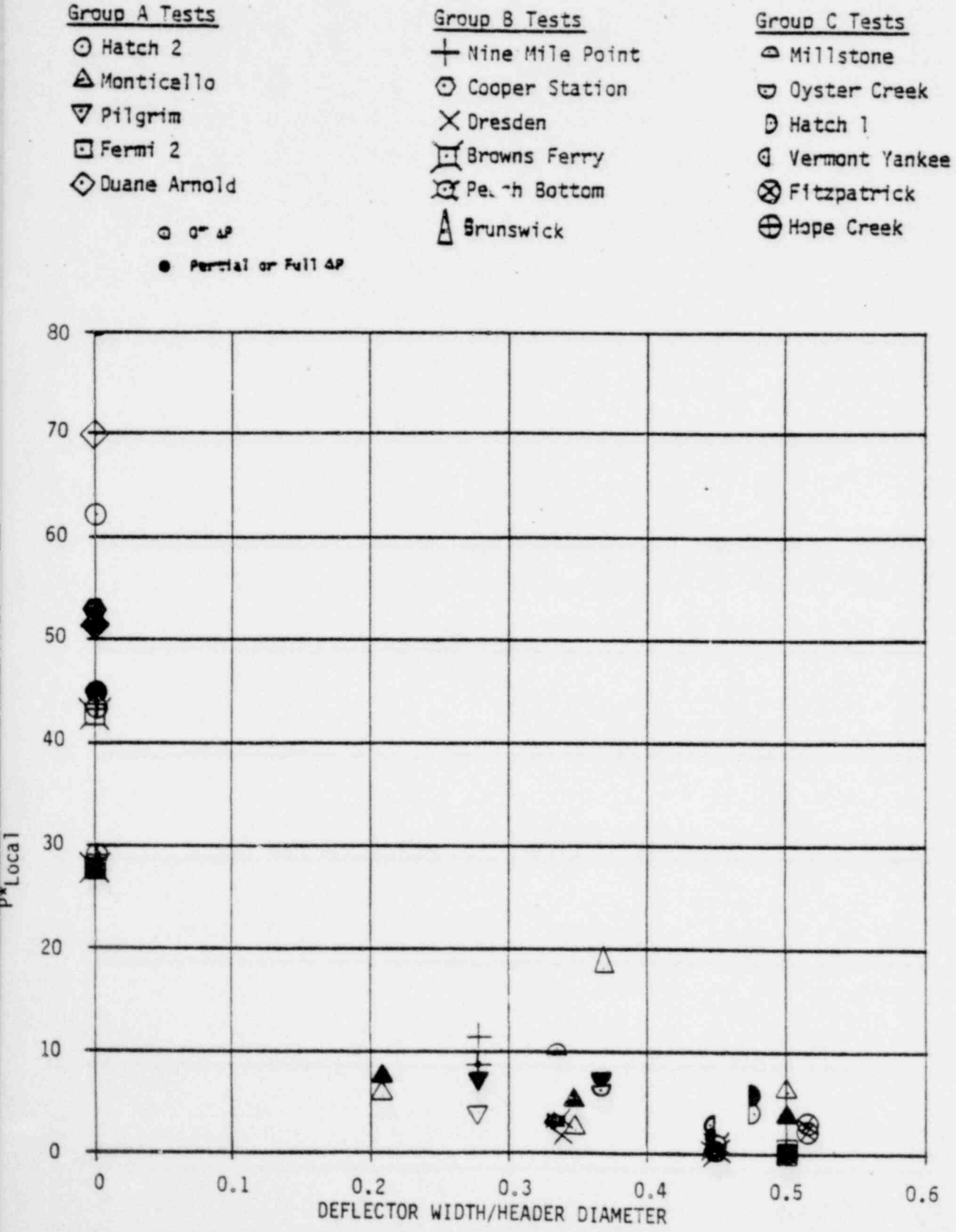

FIGURE C-3

NORMALIZED MAXIMUM VENT HEADER FORCE VERSUS NORMALIZED DEFLECTOR WIDTH

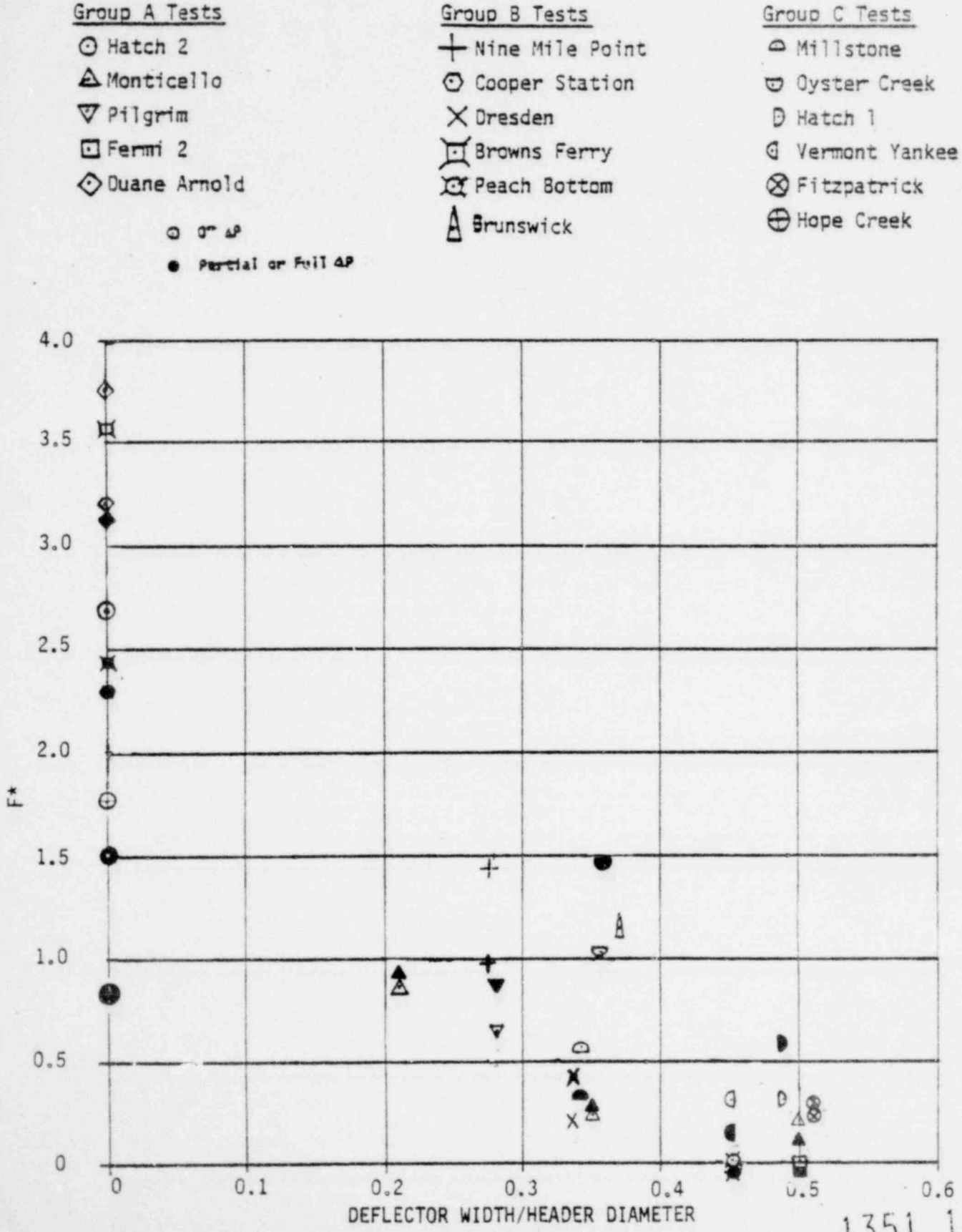

1351 129

FIGURE C-4

NORMALIZED IMPACT FORCE IMPULSE VERSUS NORMALIZED DEFLECTOR WIDTH

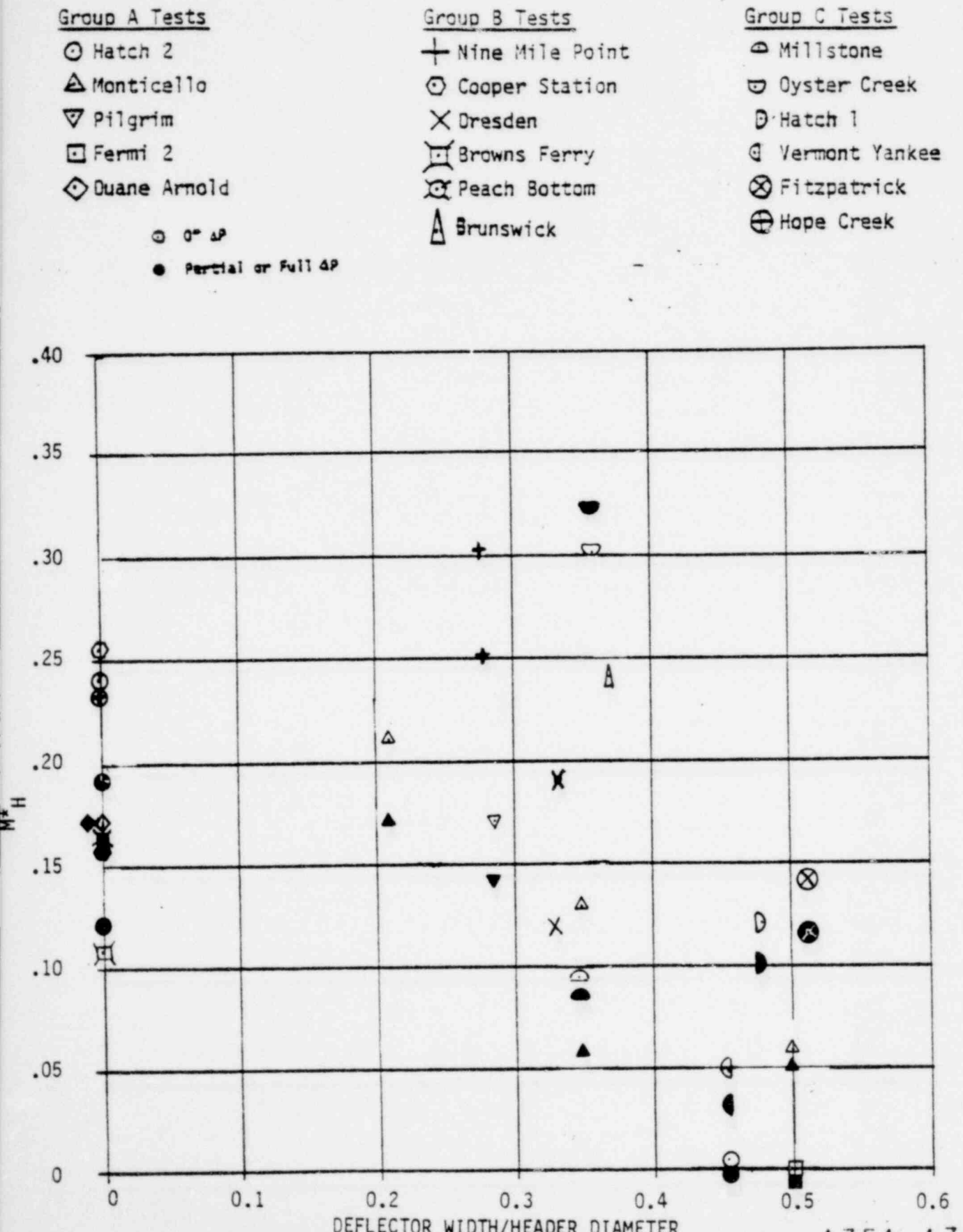

1351 130

FIGURE C-5

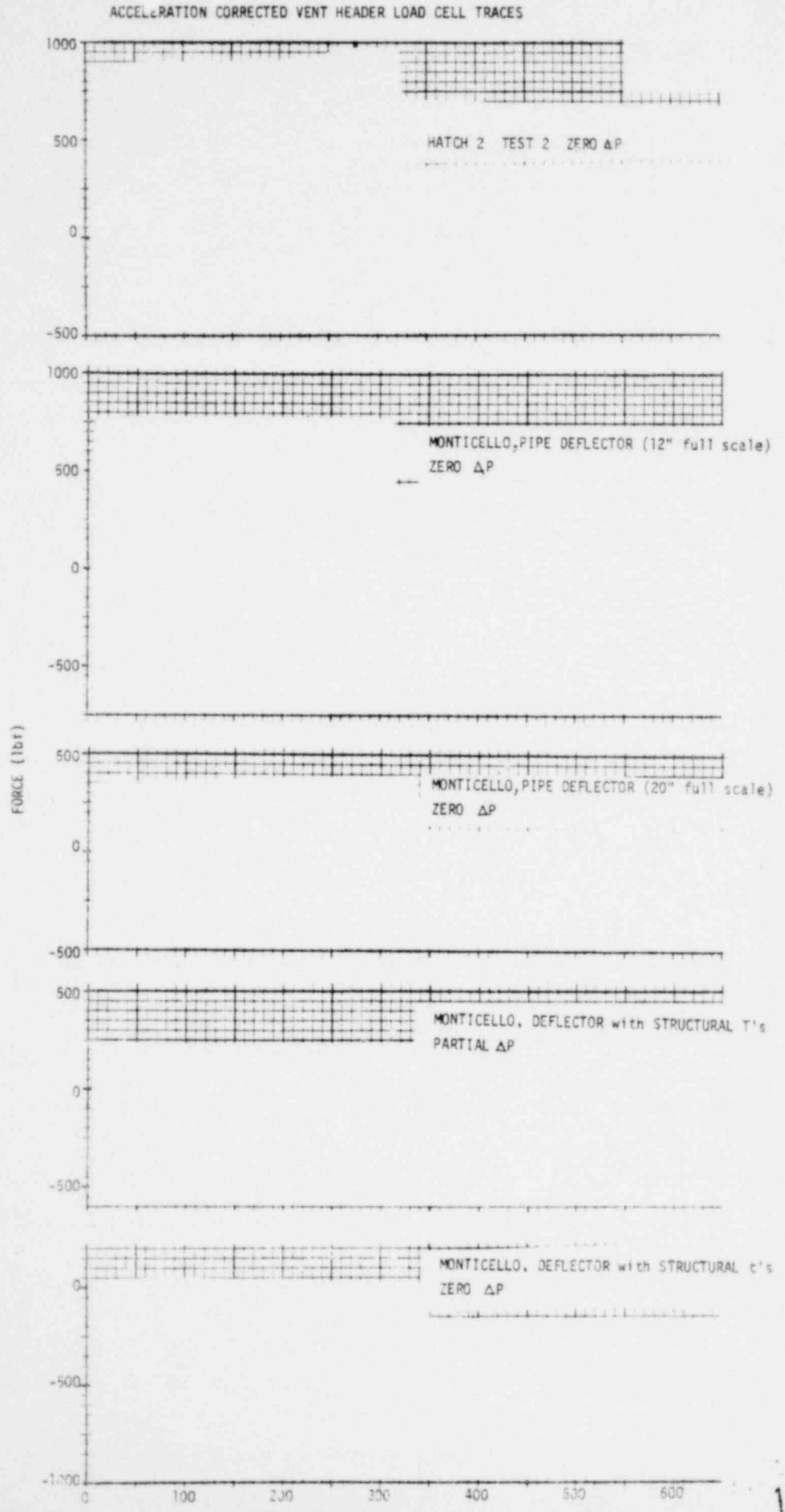

FIGURE C-6

PEAK DOWNFORCE

Group A Tests	Group B Tests	Group C Tests
○ Hatch 2	+ Nine Mile Point	⌓ Millstone
△ Monticello	⊙ Cooper Station	⌓ Oyster Creek
▽ Pilgrim	× Dresden	D Hatch 1
⊡ Fermi 2	⊡ Browns Ferry	C Vermont Yankee
◇ Duane Arnold	⊙ Peach Bottom	⊗ Fitzpatrick
		⊕ Hope Creek

Note: (1) Brunswick only tested at zero ΔP.

(2) Solid symbol is used for mean of 4 tests with standard deviation.

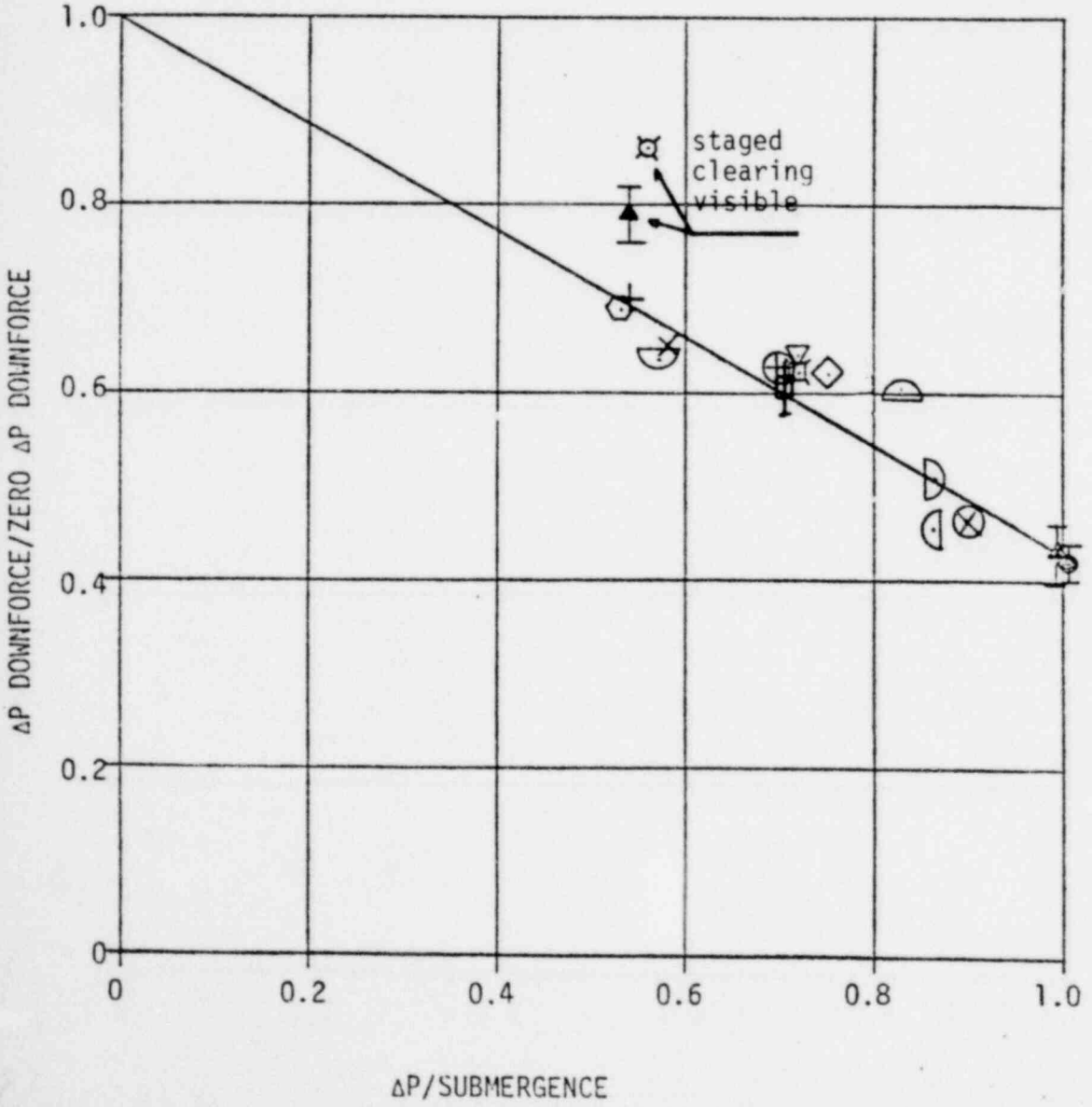

FIGURE C-7

DOWNFORCE IMPULSE

Group A Tests	Group B Tests	Group C Tests
⊙ Hatch 2	+ Nine Mile Point	⌓ Millstone
△ Monticello	⊙ Cooper Station	⌓ Oyster Creek
▽ Pilgrim	× Dresden	D Hatch 1
□ Fermi 2	⊡ Browns Ferry	◐ Vermont Yankee
◇ Duane Arnold	⊡ Peach Bottom	⊗ Fitzpatrick
		⊕ Hope Creek

Note: (1) Brunswick only tested at zero ΔP.

(2) Solid symbol is used for mean of 4 tests with standard deviation.

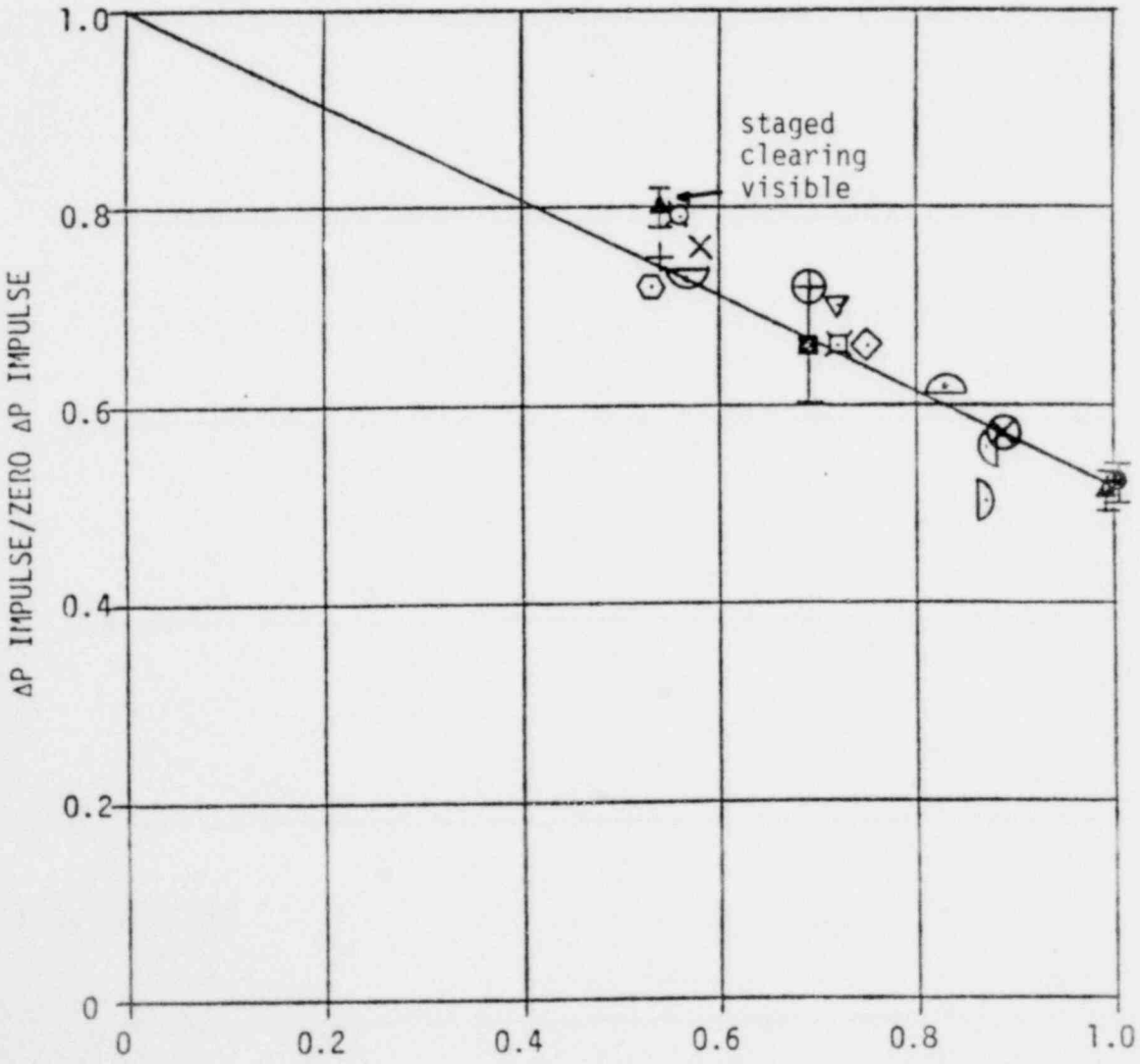

1351 133

FIGURE C-8

PEAK UPFORCE

Group A Tests	Group B Tests	Group C Tests
⊙ Hatch 2	+ Nine Mile Point	◠ Millstone
△ Monticello	⊙ Cooper Station	◡ Oyster Creek
▽ Pilgrim	× Dresden	D Hatch 1
⊡ Fermi 2	⊡ Browns Ferry	◖ Vermont Yankee
◇ Duane Arnold	⊡ Peach Bottom	⊗ Fitzpatrick
		⊕ Hope Creek

Note: (1) Brunswick only tested at zero ΔP.

(2) Solid symbol is used for mean of 4 tests with standard deviation.

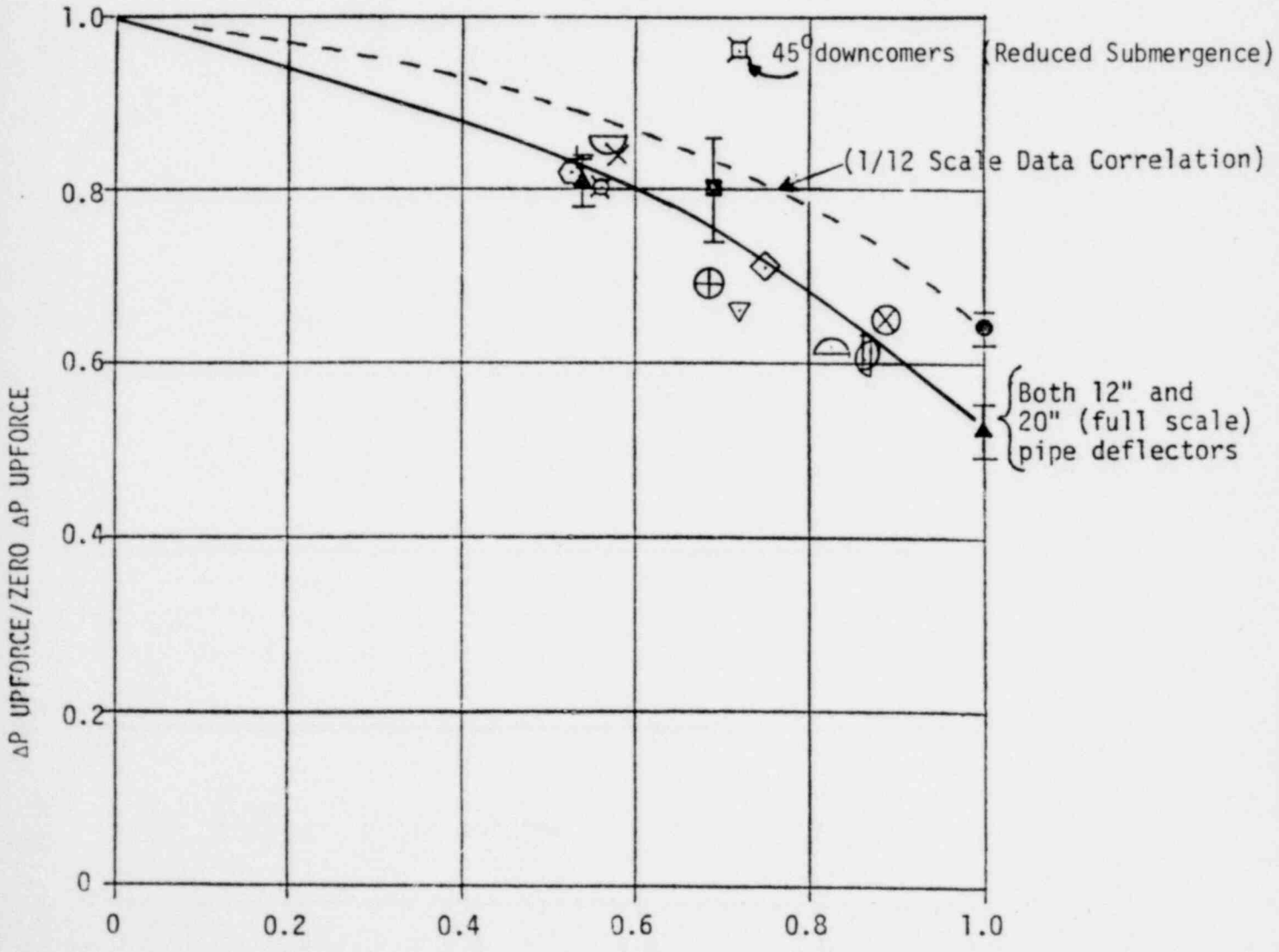

1351 134

FIGURE C-9

PEAK LOCAL VENT HEADER IMPACT PRESSURE RISE*

Group A Tests

- Hatch 2
- Monticello-"T" deflector
- Monticello-20" pipe deflector
- Monticello-12" pipe deflector
- Pilgrim-16" pipe deflector
- Duane Arnold

Group B Tests

- Nine Mile Point-16" pipe deflector
- Cooper Station
- Dresden-20" pipe deflector
- Browns Ferry

Group C Tests

- Millstone
- Oyster Creek
- Hatch 1
- Vermont Yankee
- Fitzpatrick
- Hope Creek

*Not Shown
Fermi and Peach Bottom - Negligible impact pressur
Brunswick - Only tested at zero ΔP.

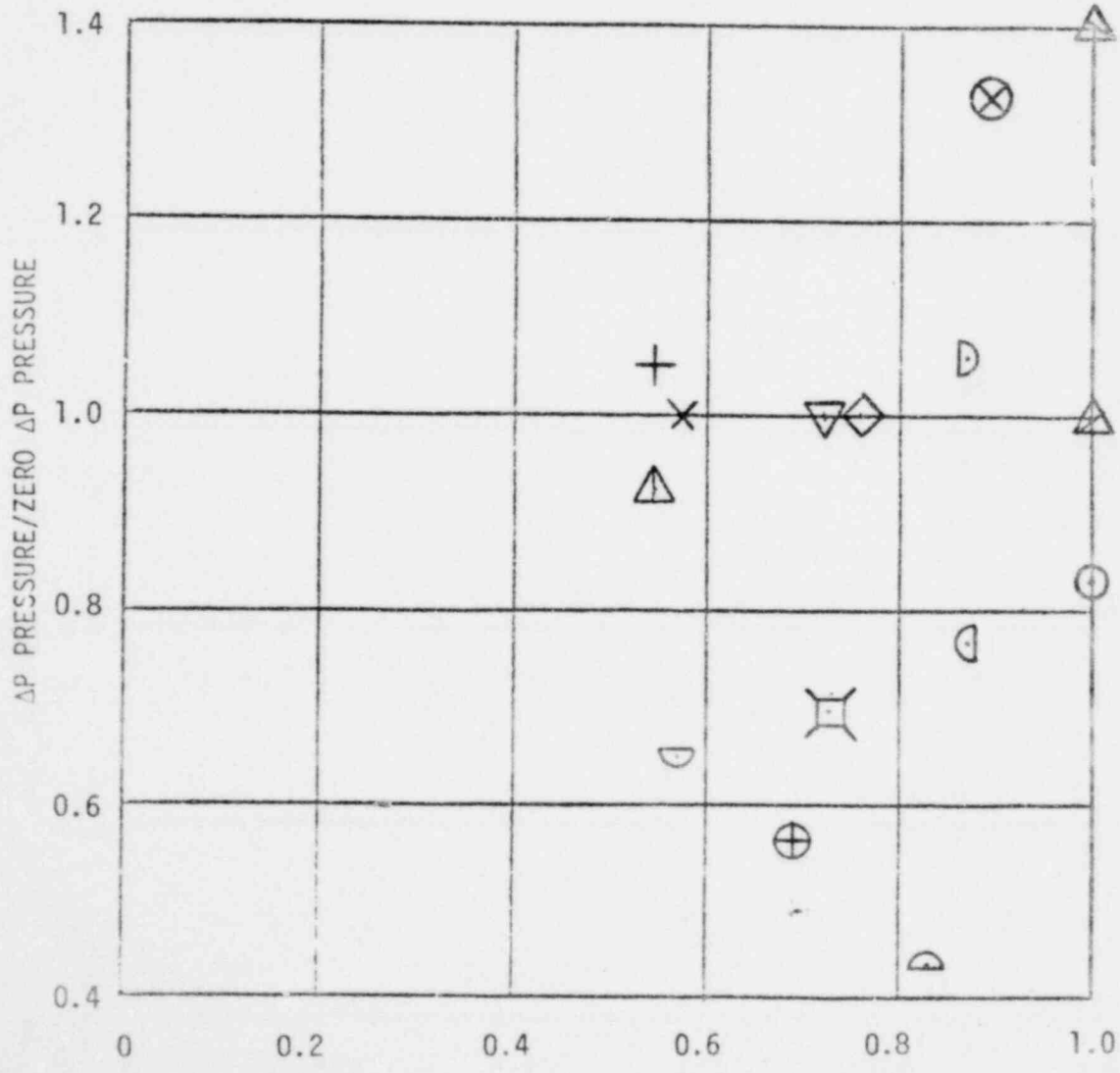

TABLE C-1

EQUATIONS FOR CONVERTING MEASURED VALUES TO EQUIVALENT 1/4-SCALE VALUES

(1) Peak Average Downforce Pressure = Mean Peak Downforce/$Area_T$[8] X 0.2500/SF[9]

(2) Average Downforce Impulse per Unit Area (psi-sec) = Mean Downforce Impulse/$Area_T$ X $(0.2500/SF)^{7/2}$

(3) Peak Average Upforce Pressure = Mean Peak Upforce/$Area_T$ X 0.2500/SF

(4) Vent Impact Velocity = Mean Vent Impact Velocity x $\sqrt{0.2500/SF}$

(5) Average Vent Impact Impulse per Unit Area (psi-sec) = Mean Vent Impact Impulse*/$Area_H$ X $(0.2500/SF)^{7/2}$

(6) Peak Average Vent Impact Pressure = Mean Peak Vent Impact Force**/$Area_H$[10] X 0.2500/SF

(7) Peak Local Impact Pressure Rise = Peak Local Impact Pressure Rise X 0.2500/SF

(8) $Area_T$ = QSTF Torus Projected Area = 93" X Torus Width

(9) SF = Scale Factor = 93"/Plant Torus Minor Diameter, in

(10) $Area_H$ = QSTF Header Projected Area = Head OD X Length

*from load cell

**from pressure integral

TABLE C-2

SOME BENCHMARK VALUES FOR
QUARTER-SCALE COMPARISON OF PLANT UNIQUE TEST DATA

Test Conditions (Full Scale)	Reference Plant STP	QSTF TASK 5.5.1 Large Orifice	QSTF TASK 5.5.1 Medium Orifice	TASK 5.5.3-1 Reference Condition
Submergence, ft.	4	4	4	3'4"
ΔP, ft.	0	0	4	3'4"
Drywell $\dot{P}$, psi/sec	56	69.2	47.0	56
Deflector	None	None	None	None
Test Data				
(1) Peak Average Downforce Pressure, psi				
(2) Average Downforce Impulse per Unit Area, psi-sec				
(3) Peak Average Upforce Pressure, psi				
(4) Vent Impact Velocity, ft/sec				
(5) Average Vent Impact Impulse per Unit Area, psi-sec				
(6) Peak Average Vent Impact Pressure, psi				
(7) Peak Local Impact Pressure Rise, psi				
(8) Torus Area, in^2		2027	2027	2027
(9) Scale Factor		0.2500	0.2500	0.2500
(10) Header Area, in^2		318	318	318

1351 137

TABLE C-3

QUARTER-SCALE COMPARISON OF PLANT UNIQUE TEST DATA

Test Conditions (Full Scale)	Hatch 2		Pilgrim	
	Tests 1 - 4	Tests 5 - 8	Test 1 - 4	Test 5
Submergence, ft.	4'4"	4'4"	4.8'	4.8'
ΔP, ft.	0	4'4"	3.46'	0
Drywell $\dot{P}$, psi/sec	58	58	67.4	67.4
Deflector	None	None	16" Pipe	16" Pipe

Test Data

(1)	Peak Average Downforce Pressure, psi			
(2)	Average Downforce Impulse per Unit Area, psi-sec			
(3)	Peak Average Upforce Pressure, psi			
(4)	Vent Impact Velocity, ft/sec			
(5)	Average Vent Impact Impulse per Unit Area, psi-sec			
(6)	Peak Average Vent Impact Pressure, psi			
(7)	Peak Local Impact Pressure Rise, psi			
(8)	Torus Area, in^2	2609	1983	
(9)	Scale Factor	0.276	0.2627	
(10)	Header Area, in^2	417.19	310	
(11)	Pool Area/Vent Area	39.5	31.8	

1351 138

TABLE C-4

QUARTER-SCALE COMPARISON OF PLANT UNIQUE TEST DATA

Test Conditions (Full Scale)	Monticello Tests 1-4	Monticello Tests 5-8
Submergence, ft.	4'3"	→
ΔP, ft.	2'3.7"	0
Drywell $\dot{P}$, psi/sec	72.5	→
Deflector	14" Pipe with 29" Wide "T" Sections	

Test Data

(1)	Peak Average Downforce Pressure, psi	
(2)	Average Downforce Impulse per Unit Area, psi-sec	
(3)	Peak Average Upforce Pressure, psi	
(4)	Vent Impact Velocity, ft/sec	
(5)	Average Vent Impact Impulse per Unit Area, psi-sec	
(6)	Peak Average Vent Impact Pressure, psi	
(7)	Peak Local Impact Pressure Rise, psi	
(8)	Torus Area, in^2	2027
(9)	Scale Factor	0.2801
(10)	Header Area, in^2	343
(11)	Pool Area/Vent Area	29.8

1351 139

TABLE C-5

QUARTER-SCALE COMPARISON OF PLANT UNIQUE TEST DATA

Test Conditions (Full Scale)	Monticello Tests 9,10	Tests 11,12	Tests 13,14	Tests 15,16
Submergence, ft.	3'4" →			
ΔP, ft.	0	Full	0	Full
Drywell $\dot{P}$, psi/sec	72.5 →			
Deflector	20" Pipe →		12" Pipe →	

Test Data

)	Peak Average Downforce Pressure, psi	
)	Average Downforce Impulse per Unit Area, psi-sec	
3)	Peak Average Upforce Pressure, psi	
4)	Vent Impact Velocity, ft/sec	
5)	Average Vent Impact Impulse per Unit Area, psi-sec	
6)	Peak Average Vent Impact Pressure, psi	
7)	Peak Local Impact Pressure Rise, psi	
8)	Torus Area, in^2	2027
9)	Scale Factor	0.2801
0)	Header Area, in^2	343
)	Pool Area/Vent Area	29.8

1351 140

TABLE C-6

QUARTER-SCALE COMPARISON OF PLANT UNIQUE TEST DATA

Test Conditions (Full Scale)	Fermi 2		Duane Arnold	
	Tests 1-4	Tests 5-8	Tests 1-4	Test 5
Submergence, ft.	3.33	3.33	3.38	3.33
ΔP, ft.	2.31	0.0	2.53	0.0
Drywell $\dot{P}$, psi/sec	54.4	54.4	44.2	44.2
Deflector	12 inch pipe with 25.8 inch wide "T" Deflector		None	None
Test Data				
(1) Peak Average Downforce Pressure, psi				
(2) Average Downforce Impulse per Unit Area, psi-sec				
(3) Peak Average Upforce Pressure, psi				
(4) Vent Impact Velocity, ft/sec				
(5) Average Vent Impact Impulse per Unit Area, psi-sec				
(6) Peak Average Vent Impact Pressure, psi				
(7) Peak Local Impact Pressure Rise, psi				
(8) Torus Area, in^2	2536		2194	
(9) Scale Factor	0.2541		0.3019	
(10) Header Area, in^2	352		297 (253)*	
(11) Pool Area/Vent Area	45.3		55.5	

1351 141

TABLE C-7

QUARTER-SCALE COMPARISON OF PLANT UNIQUE TEST DATA

Test Conditions (Full Scale)	Nine Mile Point Tests 1 - 4	Nine Mile Point Test 5	Brunswick Tests 1 - 4
Submergence, ft.	4.25	4.25	4.33
ΔP, ft.	2.31	0	0
rywell $\dot{P}$, psi/sec	58.6	58.6	56.7
eflector	16" Pipe	16" Pipe	20" Pipe
est Data			
1) Peak Average Downforce Pressure, psi			
2) Average Downforce Impulse per Unit Area, psi-sec			
3) Peak Average Upforce Pressure, psi			
4) Vent Impact Velocity, ft/sec			
5) Average Vent Impact Impulse per Unit Area, psi-sec			
6) Peak Average Vent Impact Pressure, psi			
7) Peak Local Impact Pressure Rise, psi			
8) Torus Area, in^2	2086		2157
9) Scale Factor	0.2870		0.2672
0) Header Area, in^2	358		325
1) Pool Area/Vent Area	26.7		32.5

142

TABLE C-8

QUARTER-SCALE COMPARISON OF PLANT UNIQUE TEST DATA

Test Conditions (Full Scale)	Cooper Station		Dresden	
	Tests 1 - 4	Test 5	Tests 1 - 4	Test 5
Submergence, ft.	4.375	4.375	4.00	4.00
ΔP, ft.	2.31	0	2.31	0
Drywell $\dot{P}$, psi/sec	74.0	74.0	61.1	61.1
Deflector	None	None	20" Pipe	20" Pipe
Test Data				
(1) Peak Average Downforce Pressure, psi				
(2) Average Downforce Impulse per Unit Area, psi-sec				
(3) Peak Average Upforce Pressure, psi				
(4) Vent Impact Velocity, ft/sec				
(5) Average Vent Impact Impulse per Unit Area, psi-sec				
(6) Peak Average Vent Impact Pressure, psi				
(7) Peak Local Impact Pressure Rise, psi				
(8) Torus Area, in^2	2436		2083	
(9) Scale Factor	0.2696		0.2583	
(10) Header Area, in^2	347		327	
(11) Pool Area/Vent Area	40.1		34.0	

1351 143

TABLE C-9

QUARTER-SCALE COMPARISON OF PLANT UNIQUE TEST DATA

est Conditions (Full Scale)	Browns Ferry Tests 1 - 4	Browns Ferry Test 5	Peach Bottom Tests 1 - 4	Peach Bottom Test 5
ubmergence, ft.	3.5	3.5	4.4	4.4
ΔP, ft.	2.5	0	2.5	0
ywell $\dot{P}$, psi/sec	62.4	62.4	55.5	55.5
flector	None	None	26"(Winged)	26"(Winged)

st Data

) Peak Average Downforce Pressure, psi

) Average Downforce Impulse per Unit Area, psi-sec

) Peak Average Upforce Pressure, psi

) Vent Impact Velocity, ft/sec

) Average Vent Impact Impulse per Unit Area, psi-sec

) Peak Average Vent Impact Pressure, psi

) Peak Local Impact Pressure Rise, psi

) Torus Area, in^2	2061	2063
) Scale Factor	0.25	0.25
) Header Area, in^2	319	313
) Pool Area/Vent Area	41.1	36.2

1351 144

TABLE C-10

QUARTER-SCALE COMPARISON OF PLANT UNIQUE TEST DATA

Test Conditions (Full Scale)	Millstone		Oyster Creek	
	Tests 1 - 4	Test 5	Tests 1 - 4	Test 5
Submergence, ft.	3.33	3.33	4.06	4.06
ΔP, ft.	2.77	0	2.31	0
Drywell $\dot{P}$, psi/sec	66.9	66.9	54.5	54.5
Deflector	19.5"*	19.5"*	20"	20"
Test Data				
(1) Peak Average Downforce Pressure, psi				
(2) Average Downforce Impulse per Unit Area, psi-sec				
(3) Peak Average Upforce Pressure, psi				
(4) Vent Impact Velocity, ft/sec				
(5) Average Vent Impact Impulse per Unit Area, psi-sec				
(6) Peak Average Vent Impact Pressure, psi				
(7) Peak Local Impact Pressure Rise, psi				
(8) Torus Area, in^2	1982.8		1532.6	
(9) Scale Factor	.2627		.2583	
(10) Header Area, in^2	310.3		225.6	
(11) Pool Area/Vent Area	32.06		27.17	

* For deflectors with side extensions, reported dimension is tip-to-tip.

TABLE C-11

QUARTER-SCALE COMPARISON OF PLANT UNIQUE TEST DATA

Test Conditions (Full Scale)	Hatch #1		Vermont Yankee	
	Tests 1 - 4	Test 5	Tests 1 - 4	Test 5
Submergence, ft.	4.0	4.0	4.54	4.54
ΔP, ft.	3.46	0.0	3.93	0.0
Drywell $\dot{P}$, psi/sec	65.68	65.68	74.7	74.7
Deflector	26"*	26"*	25.75"	25.75"

Test Data

(1)	Peak Average Downforce Pressure, psi		
(2)	Average Downforce Impulse per Unit Area, psi-sec		
(3)	Peak Average Upforce Pressure, psi		
(4)	Vent Impact Velocity, ft/sec		
(5)	Average Vent Impact Impulse per Unit Area, psi-sec		
(6)	Peak Average Vent Impact Pressure, psi		
(7)	Peak Local Impact Pressure Rise, psi		
(8)	Torus Area, in^2	2608.9	2027.4
(9)	Scale Factor	.2760	.2801
(10)	Header Area, in^2	417.0	342.8
(11)	Pool Area/Vent Area	39.6	58.8

* For deflectors with side extensions, reported dimension is tip-to-tip

1351 146

TABLE C-12

QUARTER-SCALE COMPARISON OF PLANT UNIQUE TEST DATA

Test Conditions (Full Scale)	Fitzpatrick		Hope Creek	
	Tests 1 - 4	Test 5	Tests 1 - 4	Test 5
Submergence, ft.	4.417	4.417	3.33	3.33
ΔP, ft.	3.92	0.0	0.0	2.31
Drywell $\dot{P}$, psi/sec	59.7	59.7	52.8	52.8
Deflector	30" Pipe	30" Pipe	None	None
Test Data				
(1) Peak Average Downforce Pressure, psi				
(2) Average Downforce Impulse per Unit Area, psi-sec				
(3) Peak Average Upforce Pressure, psi				
(4) Vent Impact Velocity, ft/sec				
(5) Average Vent Impact Impulse per Unit Area, psi-sec				
(6) Peak Average Vent Impact Pressure, psi				
(7) Peak Local Impact Pressure Rise, psi				
(8) Torus Area, in^2	2067.4		2529.6	
(9) Scale Factor	.2627		.2527	
(10) Header Area, in^2	320.2		352.6	
(11) Pool Area/Vent Area	33.69		45.18	

* Possible spurious signal - no other value above 4 psia

1351 147

Table C-13

NON-DIMENSIONALIZED VENT HEADER IMPACT DATA

Plant	Hatch 2		Monticello					
Deflector	None		3.36" Pipe (12" Full Scale)		5.60" Pipe (20" Full Scale)		8.15" Wide "T" Deflector (29" Full Scale)*(1)	
Header Diameter (ft)	1.25		1.34		1.34		1.34	
Header Length (ft)	2.31		1.77		1.77		1.77	
Submergence (in)	14.35		11.19		11.19		14.29	
	Tests 1-4	Tests 5-8	Tests 13-14	Tests 15-16	Tests 9-10	Tests 11-12	Tests 5-8	Tests 1-4
ΔP (in. of water)								
Impact Velocity (ft/sec) at 6" Off from Pool Centerline								
Maximum Local Impact Pressure (psi)								
Maximum Vent Header Force (lbf)								
Impact Force Impulse (lb-sec)								
P^*_{LOCAL} (dimensionless unit)	61.8	45.0	5.2	7.0	2.2	5.2	6.2	3.6
F^* (dimensionless unit)	2.7	1.5	0.86	0.92	0.26	0.28	0.24	0.12
M^*_H (dimensionless unit)	0.24	0.12	0.21	0.17	0.13	0.06	0.06	0.05

P^*_{LOCAL} = (Maximum Local Impact Pressure x $2g_c$ x 144)/([Impact Velocity]^2 x Water Density)

F^* = (Maximum Vent Header Force x $2g_c$)/(Projected Area x [Impact Velocity]^2 x Water Density)

M^*_H = (Impact Force Impulse x g_c)/([π x Diameter^2/4] x Length x Impact Velocity x Water Density)

*(1) = "T" deflector is a standard pipe with structural "T"s

1351 148

Table C-14

NON-DIMENSIONALIZED VENT HEADER IMPACT DATA

Plant	Pilgrim		Duane Arnold		Fermi 2		Peach Bottom	
Deflector	4.20" Pipe Deflector (16.0" Full Scale)		None		6.566" Wide "T" Deflector (25.8" Full Scale)*(1)		6.5" Winged Deflector (26" Full Scale)*(2)	
Header Diameter (ft)	1.26		1.07		1.09		1.21	
Header Length (ft)	1.68		1.92		2.23		1.79	
Submergence (in)	15.13		12.08	12.24	10.16		13.2	
	Test 5	Tests 1-4	Test 5	Tests 1-4	Tests 5-8	Tests 1-4	Tests 5	Tests 1-4
ΔP (in. of water)								
Impact Velocity (ft/sec) at 6" Off from Pool Centerline								
Maximum Local Impact Pressure (psi)								
Maximum Vent Header Force (lbf)								
Impact Force Impulse (lb-sec)								
P^*_{LOCAL} (dimensionless unit)	4.1	7.2	69.8	51.2	0.0	0.0	0.0	0.0
F^* (dimensionless unit)	0.69	0.88	3.75	3.13	0.0	0.0	0.0	0.0
M^*_H (dimensionless unit)	0.17	0.14	0.17	0.17	0.0	0.0	0.0	0.0

P^*_{LOCAL} = (Maximum Local Impact Pressure x $2g_c$ x 144)/([Impact Velocity]^2 x Water Density)

F^* = (Maximum Vent Header Force x $2g_c$)/(Projected Area x [Impact Velocity]^2 x Water Density)

M^*_H = (Impact Force Impulse x g_c)/([π x Diameter^2/4] x Length x Impact Velocity x Water Density)

*(1) = "T" deflector is a standard pipe with structural "T"s

*(2) = Winged deflector is a standard pipe with structural angles

Table C-15

NON-DIMENSIONALIZED VENT HEADER IMPACT DATA

Plant	Nine Mile Point		Brunswick	Cooper Station		Dresden		Browns Ferry	
Deflector	4.59" Pipe Deflector (16.0" Full Scale)		5.34" Pipe Deflector (20.0"Full)	None		5.17" Pipe Deflector (20.0" Full Scale)		None	
Header Diameter (ft)	1.39		1.21	1.14		1.26		1.25	
Header Length (ft)	1.79		1.86	2.12		1.80		1.77	
Submergence (in)	14.64		11.89	14.15		12.4		10.5	
	Test 5	Tests 1-4	Tests 1-4	Test 5	Tests 1-4	Test 5	Tests 1-4	Test 5	Tests 1-4
ΔP (in. of water)									
Impact Velocity (ft/sec) at 6" Off from Pool Centerline									
Maximum Local Impact Pressure (psi)									
Maximum Vent Header Force (lbf)									
Impact Force Impulse (lb-sec)									
P^*_{LOCAL} (dimensionless unit)	11.4	9.5	18.1	–	52.4	1.5	3.0	42.7	27.7
F^* (dimensionless unit)	1.46	1.03	1.16	3.26	2.34	0.21	0.43	3.60	2.40
M^*_H (dimenionless unit)	0.31	0.25	0.24	0.25	0.16	0.12	0.19	0.17	0.11

P^*_{LOCAL} = (Maximum Local Impact Pressure x $2g_c$ x 144)/([Impact Velocity]^2 x Water Density)

F^* = (Maximum Vent Header Force x $2g_c$)/(Projected Area x [Impact Velocity]^2 x Water Density)

M^*_H = (Impact Force Impulse x g_c)/([π x Diameter^2/4] x Length x Impact Velocity x Water Density)

*(1) No data at T1 location

TABLE C-16

NON-DIMENSIONALIZED VENT HEADER IMPACT DATA

Plant	Millstone		Oyster Creek		Hatch #1		Vermont Yankee		Fitzpatrick		Hope Creek	
Deflector	5.2" Winged Deflector 19.5" Full Scale 16" Pipe		5.17" Pipe Deflector 20" Full Scale		7.17" Winged Deflector 26" Full Scale 18" Pipe		7.21" Winged Deflector 25.75" Full Scale 16" Pipe		7.88" Pipe Deflector 30" Full Scale		No Deflector	
Header Diameter (ft)	1.26		1.20		1.25		1.34		1.26		1.09	
Header Length (ft)	1.71		1.31		2.31		1.77		1.77		2.25	
Submergence (in)	10.50		12.58		13.25		15.26		13.92		10.10	
	Tests 1-4	Test 5	Tests 1-4	Test 5	Tests 1-4	Test 5	Tests 1-4	Test 5	Tests 1-4	Test 5	Tests 1-4	Test 5
ΔP (in. of water)												
Impact Velocity (ft/sec) at 6" Off from Pool Centerline												
Maximum Local Impact Pressure (psi)												
Maximum Vent Header Force, (lbf)												
Impact Force Impulse lb-sec												
P^*_{LOCAL} (dimensionless unit)	3.05	9.65	7.61	7.05	5.49	3.56	1.93	2.23	2.52	2.21	42.81	27.79
F* (dimensionless unit)	0.33	0.60	1.46	1.06	.59	.28	0.20	0.32	0.23	.22	1.72	0.89
M^*_H (dimensionless unit)	0.09	.10	0.32	.30	0.10	0.12	0.03	0.05	0.12	0.14	0.23	0.19

P^*_{LOCAL} = (Maximum Local Impact Pressure x $2g_c$ x 144)/([Impact Velocity]^2 x Water Density)

F* = (Maximum Vent Header Force x $2g_c$)/(Projected Area x [Impact Velocity]^2 x Water Density)

M^*_H = (Impact Force Impulse x g_c)/([π x Diameter^2/4] x Length x Impact Velocity x Water Density)

Note: Deflector dimension is overall diameter (tip-to-tip) except where specifically noted.

The term "Winged Deflector" refers to a deflector with side extensions.

1351 151

TABLE C-17

MEASURED STANDARD DEVIATION AS PERCENT
OF MEASURED MEAN AT ZERO ΔP CONDITIONS

Plant	Hatch 2	Monticello	Fermi 2	Brunswick	Hope Creek
Test Conditions (Full Scale)					
Submergence (ft)	4.33	4.25	3.33	4.33	3.33
Drywell Pressurization Rate (psi/sec)	58.0	72.5	54.4	56.7	52.8
Pool Area/Vent Area	39.5	29.8	45.3	32.5	45.18
Deflector Type	None	29 in."T"	25.8 in."T"	20 in. Pipe	None
Load Parameters*					
Wetwell Vertical Loads:					
Peak Downforce (%)	5.2	2.5	4.9	3.3	1.6
Downforce Impulse (%)	2.0	2.0	5.5	1.1	4.2
Peak Upforce (%)	3.3	1.8	2.7	1.9	3.3
Vent Header Impact:					
Peak Impact Force (%)	6.7	negligible	negligible	26.6	21.8
Impact Force Impulse (%)	20.4	negligible	negligible	4.3	12.2
Peak Local Pressure (%)	8.5	negligible	negligible	24.7	16.8

*Load parameters are standard deviations expressed as percent of the measured mean at zero ΔP (mean of four tests).

TABLE C-18 MATRIX OF SIMPLE CORRELATIONS FOR EACH SECOND DEGREE VARIABLE USED IN REGRESSIONS

1. $\frac{\Delta P/SUB}{\Delta P}$

SUB	$\Delta P/SUB$

2. $\frac{SUB\ (CELL\ WIDTH)}{SUB}$

CELL WIDTH	SUB (CELL WIDTH)

3. $\frac{\dot{P}\ (SUB)}{\dot{P}}$

SUB	$\dot{P}$ (SUB)

4. $\frac{\dot{P}\ (CELL\ WIDTH)}{\dot{P}}$

CELL WIDTH	$\dot{P}$ (CELL WIDTH)

5. $\frac{CELL\ WIDTH/SUB}{CELL\ WIDTH}$

SUB	CELL WIDTH/SUB

6. $\frac{\dot{P}\ (VOL)}{\dot{P}}$

VOL	$\dot{P}$ (VOL)

7. $\frac{VOL\ (SUB)}{VOL}$

SUB	VOL (SUB)

8. $\frac{fL/D\ (\dot{P})}{fL/D}$

$\dot{P}$	fL/D ($\dot{P}$)

TABLE C-19 MATRICES OF SIMPLE CORRELATIONS BETWEEN VARIABLES USED IN REGRESSIONS

1. PEAK TORUS DOWNFORCE

ΔP/SUB		
SUB (CELL WIDTH)		
	$\dot{P}$	ΔP/SUB

2. PEAK TORUS DOWNPRESSURE

ΔP/SUB		
$\dot{P}$ (SUB)		
	CELL WIDTH	ΔP/SUB

3. PEAK TORUS UPFORCE

ΔP/SUB		
SUB		
	$\dot{P}$ (CELL WIDTH)	ΔP/SUB

4. PEAK TORUS UPPRESSURE

CELL WIDTH/SUB		
ΔP/SUB		
	$\dot{P}$ (CELL WIDTH)	CELL WIDTH/SUB

5. PEAK TORUS DOWNFORCE IMPULSE

ΔP/SUB		
SUB		
	$\dot{P}$ (VOL)	ΔP/SUB

6. PIM

ΔP/SUB		
CELL WIDTH/SUB		
	$\dot{P}$	ΔP/SUB

1351 454

TABLE C-19(Continued)

7. PEAK VENT HEADER FORCE AND PEAK VENT HEADER PRESSURE

(DEFLECTOR W/HEADER D)
(CLEARANCE)

(D-TYPE) (DEFLECTOR W/HEADER D)

8. PEAK VENT HEADER FORCE IMPULSE AND PEAK VENT HEADER PRESSURE IMPULSE

(DEFLECTOR W/HEADER D)
$\dot{P}$

(D-TYPE) (DEFLECTOR W/HEADER D)

9. TIME TO PEAK TORUS DOWN FORCE

$\Delta P/SUB$
(VOL) (SUB)

$fL/D\ (\dot{P})$ $\Delta P/SUB$

10. TIME TO PEAK TORUS UPFORCE

ΔP
SUB

$\dot{P}$ ΔP

TABLE C-20 MATRIX OF SIMPLE CORRELATIONS BETWEEN ALL FIRST ORDER VARIABLES

	fL/D	$\dot{P}$	ΔP	VOL	SUB	HEADER-WATER GAP	CELL WIDTH	HEADER DIAMETER	DCE - TORUS GAP	DEFLECTOR W / HEADER D	POOL AREA / VENT AREA	D-TYPE	V/DC
$\dot{P}$													
ΔP													
VOL													
SUB													
HEADER - WATER GAP													
CELL WIDTH													
HEADER DIAMETER													
DCE - TORUS GAP													
DEFLECTOR W / HEADER D													
POOL AREA / VENT AREA													
D-TYPE													
V/DC													
CLEARANCE													

* = simple correlation greater than 0.9

APPENDIX D

EFFECTIVE POOL MASS DURING PEAK UPFORCE

D.1 Purpose

In the event that the net vertical upforce applied to the torus were to exceed the weight of the torus and its contents some upward displacement of the torus could result. To evaluate this potential event it is necessary to account for the reduction in the inertial mass which would resist torus movement due to the mass of water suspended at the time of maximum upforce on the torus. It is the purpose of this Appendix to provide estimated values of the fractional reduction in effective pool mass at the time of peak upforce for each of the plant unique test configurations. This reduced pool mass does not affect the torus forces presented in Section 3 and Appendix A, since these were referenced to the full water weight. The effective mass simply provides an estimate of the vertical inertia resisting upward displacements of the torus.

D.2 Discussion of Phenomena

A typical trace of net vertical forces exerted on the torus by a simulated LOCA is shown in the schematic of Figure D-1. At t = 0 the gravitational force of the pool is subtracted from the torus pressure integral so that the initial value of torus force is zero. As the event progresses the rapid bubble formation causes an upward acceleration of the upper part of the pool mass and a reaction downforce applied to the torus. At the time of peak downforce the bubbles are relatively small within a continuous body of water (see typical photographs in Appendix E). However, at the time of peak upforce (maximum pressure difference between the free space and bubbles) the bubbles are large. The upper part of the pool at this time consists of some relatively thin ligaments of water surrounding the bubbles and some froth. The inertial resistance of much of the upper part of the pool to an assumed upward motion of the torus would be low.

An indication of the quantity of suspended water near the time of peak upforce is clearly evident from the measured forces. This is shown in Figure D-1. The upforce decreases rapidly after its peak value and then typically reaches a plateau with varying degrees of oscillation. This plateau occurs because the pool weight acting on the torus is less than it was at t = 0. The magnitude of force at such a plateau can be used to estimate the fraction of pool mass that is suspended and would not be effective in impeding upward displacement of the torus.

Rough estimates of the quantity of suspended water at the time of peak upforce can also be made by evaluation of the high speed movies. While the accuracy of the visual method is not precise due to three dimensional effects, values obtained by this technique scatter both higher and lower than the values obtained from the pressure integral data reported below, implying further support for interpreting the "plateau" as the weight of suspended water.

D.3 Results of Analysis

Results of analysis of the pressure integral data for each plant are presented in Table D-1.

FIGURE D-1

TYPICAL TORUS PRESSURE INTEGRAL

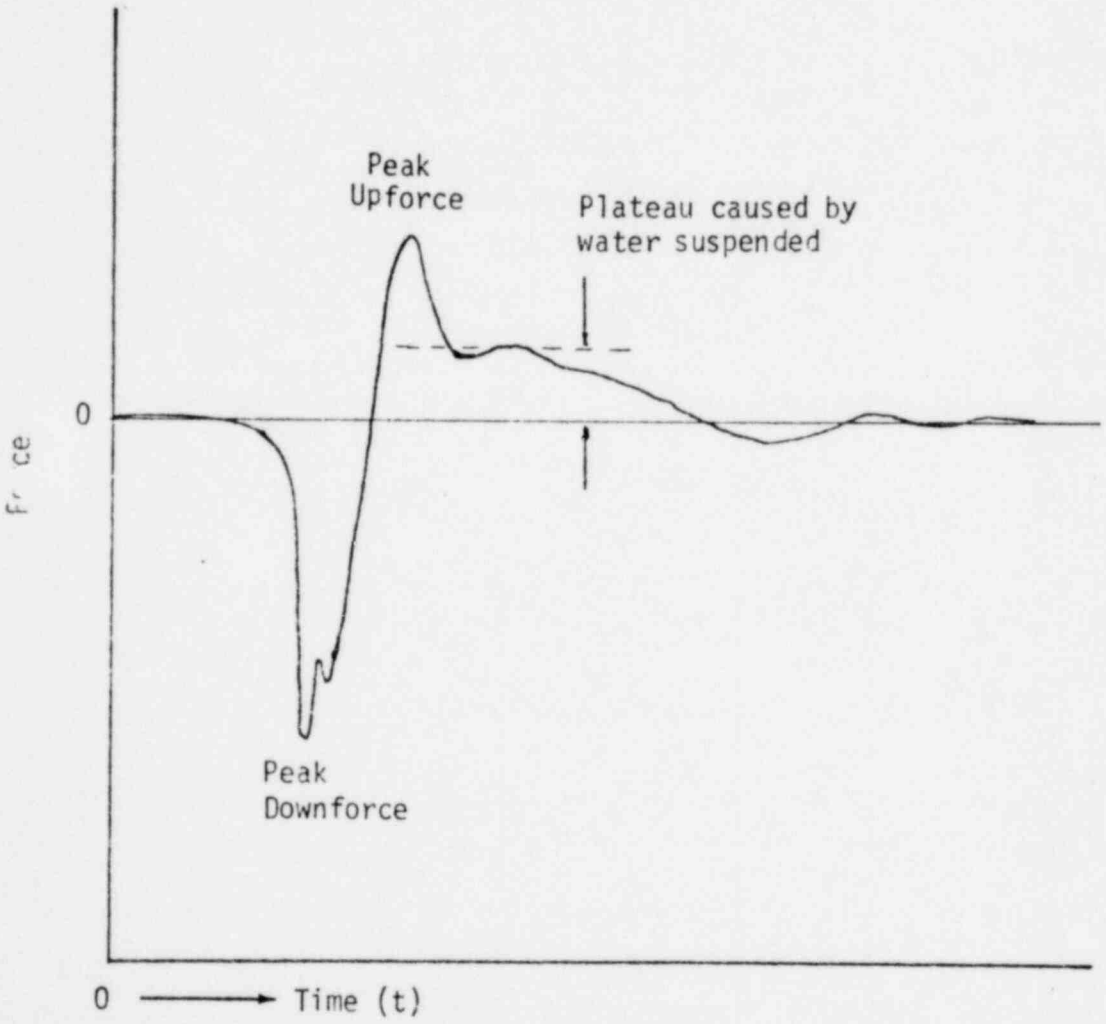

TABLE D-1

WEIGHT FRACTION OF POOL WATER SUSPENDED

Plant	Tests	$\left(\frac{\Delta P}{\text{Submergence}}\right)$ **	Plateau * Value(lbs)	Pool Weight (lbs)	Weight Fraction Water Suspended
Hatch 2	1-4	0			
	5	1.0			
Monticello	1-4	0.53			
	5	0			
Fermi	1-4	0.69			
	5	0			
Pilgrim	1-4	0.72			
	5	0			
Duane Arnold	1-4	0.75			
	5	0			
Nine Mile Point	1-4	0.54			
	5	0			
Brunswick	1-4	0			
Cooper Station	1-4	0.53			
	5	0			
Dresden	1-4	0.59			
	5	0			
Browns Ferry	1-4	0.71			
	5	0			
Peach Bottom	1-4	0.58			
	5	0			
Millstone	1-4	0.83			
	5	0			
Oyster Creek	1-4	0.56			
	5	0			
Hatch 1	1-4	0.86			
	5	0			
Vermont Yankee	1-4	0.86			
	5	0			
Fitzpatrick	1-4	0.89			
	5	0			
Hope Creek	1-4	0			
	5	0.69			

* See Figure D-1

** ΔP/Submergence = the fraction of the downcomer water leg removed by ΔP.

APPENDIX E

PHOTOGRAPHIC RESULTS

Figures E-1 through E-17 present the sequence of major events, which occurred during a typical load definition test from each of the plant unique tests. The photographs are from the high speed movies taken during the tests.

Figure E-1
HATCH 2, TEST 2

Figure E-2
MONTICELLO, TEST 2

Figure E-3
PILGRIM, TEST 3

Figure E-4
FERMI, TEST 3

Figure E-5
DUANE ARNOLD, TEST 3

Figure E-6
NINE MILE POINT, TEST 3

Figure E-7
BRUNSWICK, TEST 3

Figure E-8
COOPER STATION, TEST 3

Figure E-9
DRESDEN, TEST 3

Figure E-10
BROWNS FERRY, TEST 3

Figure E-11
PEACH BOTTOM, TEST 3

Figure E-12
MILLSTONE, TEST 3

Figure E-13
OYSTER CREEK, TEST 3

Figure E-14
HATCH 1, TEST 3

Figure E-15
VERMONT YANKEE, TEST 3

Figure E-16
FITZPATRICK, TEST 3

Figure E-17
HOPE CREEK, TEST 3

APPENDIX F

MEASUREMENT UNCERTAINTY ANALYSIS

An uncertainty analysis was performed to insure that the error bands associated with calculated test output fell within acceptable limits. Many of the important test values (such as enthalpy flow) were calculated based on several measured test parameters. While each of the individual parameters has its own error band, the combination of several different parameters has an entirely different error band. In addition, the errors associated with a single sensor may not reflect the total error band of the data from the system using that sensor.

To arrive at these error bands, the following aproach was used. Each sensor system was analyzed as a number of different sources of error. For example, a pressure transducer would be assumed to have a specified error inherent in its construction, an analog to digital conversion error, a signal conditioning error and a frequency response error. The total uncertainty for this single sensor was assumed to be the square root of the sum of the squares of errors contributed by each component part.

To combine the errors of several different sensors to achieve a calculated value, it was assumed that each of the independent errors was normally distributed over its range, and the calculated value was a linear function of its independent variables.

Table F-1 lists the major variables of interest, their nominal values, range of values during load definition tests, and uncertainty intervals based on a 95% confidence level.

TABLE F-1

SUMMARY OF UNCERTAINTY ANALYSIS

Variable	Nominal Value	Range of Variable	% Uncertainty (95% Confidence Level)
Measured Values:			
Drywell Orifice Upstream Pressure, psia	60	45→90	±0.12
Wetwell Pressure, psia	7.5	4.2→16.0	±0.4
Drywell Pressure, psia	7.5	3.7→16.0	±0.4
Torus Load Cell, lbf Maximum Downforce	17,000*	13,000→ 20,500**	±0.15
Maximum Upforce	8,000*	10,000→ 6,000**	±0.31
Vent Header Load Cell, lbf	600*	0→1,600**	±1.4
Downcomer Orifice ΔP, psid	3.5	2.5→5.0	±1.4
Torus Accelerometer, g	0.15	-0.3→+0.3	±6.7
Downcomer Air Temperature °F	115	100→135	±1.4
Vent Header Impact Pressure, psia	25	0→80	±2.0
Vent Header Accelerometer, g	2.0	-5.0→+5.0	±3.5
Initial Submergence, Inches	12.5	10.1→15.26	±0.6
Drywell/Wetwell ΔP, in. of water	8.5	0→13.2	±0.8
Vent Resistance Calibration:			
Total fL/D	16.0	12.6→18.8	6.0

*Typica' values of load definition tests
**Represents range of load definition tests

TABLE F-1 (continued)

SUMMARY OF UNCERTAINTY ANALYSIS

Variable	Nominal Value	Range of Variable	% Uncertainty (95% Confidence Level)
Calculated Values:			
Critical Nozzle Flow Rate, lbm/sec	7.7	5.7→10.1	±1.8
Enthalpy Flow into Pool, Btu/sec (based on downcomer orifice differential pressure and upstream temperature)	450	300→600	±4.8
Spatial Integral of Torus Pressures (force), lbf			
Maximum Downforce	4,700*	2,400→ 8,600**	±1.6
Maximum Upforce	2,700*	1,300→ 4,400**	±1.7
Inertia Corrected Torus Load Cell, lbf			
Maximum Downforce	5,000*	2,500→ 8,900**	±1.9
Maximum Upforce	2,800	1,500→ 4,400**	±2.3
Impulse of Torus Spatial Pressure Integral, lbf-sec	330*	190→540**	±2.0
Spatial Integral of Vent Header Impact Pressures (force), lbf	470*	0→1,700**	±5.0
Inertia Corrected Vent Header Load Cell, lbf	430*	0→1,800**	±8.3
Impulse of Vent Header - Load Cell Corrected, lbf-sec	7.0*	0→13.0**	±8.4

*Typical values of load definition tests
**Represents range of load definition tests

APPENDIX G

VENT RESISTANCE EVALUATION

Prior to each set of load definition tests it was necessary to experimentally determine the vent resistance in the Quarter Scale Test Facility and, if necessary, adjust flow orifices to bring the vent system fL/D and the fL/D split within the required range. This Appendix describes the test requirements, the experimental method, and a discussion of the analytical technique used for data reduction. A computer model is also described which calculated vent system fL/D values during an actual test which agreed with the values obtained by pretest calibration.

G.1 Test Requirements

Based on the scaling laws, the enthalpy flow ($\dot{H} \propto \rho AVC_p T$) is scaled by $SF^{7/2}$ where SF is the scaling factor. Since ρ is equal to P/RT from the ideal gas law, the enthalpy flow can be expressed as follows:

$$\dot{H} \propto PAV$$

where P = pressure
A = flow area
V = velocity

Since the pressures are proportional to scale factor and areas are proportional to the scale factor squared,

$$\dot{H} \propto (SF)(SF^2)V$$

Consequently for subscale tests, the vent system velocities must be proportional to the square root of the scale factor. This scaling requirement has been met in all QSTF tests by placing flow orifices in the vent system.

For the quarter scale tests performed to evaluate scaling (Reference 2, Figures 3-5), the quarter scale exit velocity-pressure ratio characteristic

was calibrated to match scaled-up, 1/12 scale values. However, for the plant unique tests, vent resistance requirements were based on calculated full scale plant unique vent system fL/D values, adjusted to subscale by the relationship

$$(fL/D)_{SS} = (fL/D)_{FS} \times (1/SF) \times (T/T_D)$$

where

$(fL/D)_{SS}$ = vent system total fL/D for subscale test

$(fL/D)_{FS}$ = vent system total fL/D for full scale plant

SF = scaling factor

T = initial test temperature

T_D = initial nominal bulk drywell temperature

The initial test temperature was 70°F (530°R) and the initial nominal bulk drywell temperature was a utility input.

For compressible flow the use of the Fanno equations (see Section G.3) with the above scaling relationship is slightly conservative, becauce it results in a slightly higher subscale flow velocity than required. For a full scale fL/D of 5 at a pressure ratio of 0.8, the Fanno equations would predict an exit velocity of 321 ft/sec which scaled to quarter scale, requires a velocity of 160.5 ft/sec (neglecting temperature differences). This is equivalent to a quarter scale fL/D of 20.5 which is slightly higher than 20.0 obtained by using the fL/D scaling relationship. For additional conservatism the plant unique vent resistance tested was always equal to or less than the scaled, full scale vent fL/D. An fL/D tolerance of +0, -2 was allowed from the scaled, full scale vent fL/D.

Tests conducted during Task 5.5.3-1 (Reference 1) with flow orifices located only in the main vent showed that increasing the vent system volume downstream of the vent system flow orifice increased the torus and vent header loads. Prior to vent clearing and during the early stages of bubble growth the volume downstream of the orifice acts as an accumulator which helps to maintain bubble pressure when the bubble begins to overexpand.

A quantitative measure of vent system capacitance is the change in vent system stored mass from a constant pressure condition (prior to vent clearing) to a steady state flow condition. This reduction in stored mass is available to help pressurize the bubbles following vent clearing. A plot of the static pressure vs. vent system volume can be used to calculate vent system capacitance. The difference in area between the PV characteristic before vent clearing and the PV characteristic with steady state flow is proportional to the change in stored mass in the vent system.

Normalized vent system capacitance diagrams have been prepared comparing several Mark I plants to QSTF conditions as shown in Figure G-1. The vent system capacitance is proportional to the area above the fraction of incompressible static pressure drop versus fraction of vent system volume characteristics. For simplicity the non-orifice QSTF vent system flow losses (~15% of the total) have been shown as a distributed loss. The Mark I characteristics are for an average downcomer pair having an average cell vent header volume and the fractional pressure drops associated with the second pair of downcomers.

The Mark I vent system characteristics for the five plants evaluated are all similar both in shape and in capacitance. This is due to the strong plant to plant geometric similarities in the Mark I vent system. The vent system can be almost exactly modeled by four pressure drops and four volume increments. Combining the downcomer inlet and bend losses and lumping the downcomer volume would reduce the number of pressure drops and volume increments to three with little loss in accuracy.

The Mark I vent system capacitance can be closely modeled for subscale tests with two properly placed orifices based on the vent capacitance characteristics shown in Figure G-1. For an orifice at the entrance to the vent system and a pair of orifices in the downcomer, a 50%, 50% split in vent system resistance provides essentially the same area as and closely approximates the shape of the Mark I characteristics.

Data from the Task 5.5.3-1 tests (Reference 1) indicated that moving the flow orifices from the downcomer to the entrance of the main vent increased downloads by roughly 6% and uploads and pool velocity (at vent header impact) by roughly 15%. The vent capacitance characteristics for these two orifice locations lie respectively above (less capacitance) and below the Mark I vent system characteristics. For the plant unique tests a tolerance of ±10% was allowed for the vent/downcomer orifice fL/D split. Assuming that the capacitance sensitivity observed in Task 5.5.3-1 is roughly proportional to the area above the capacitance characteristics shown in Figure G-1 then varying the orifice split by ±10% would be expected to vary downloads by about ±1% and uploads and pool velocity by about ±2%. As shown in Table G-1 most plants tested had higher capacitance than the nominal 50/50 characteristics.

The plant unique tests were conducted with less than the scaled vent system fL/D which tended to increase the loads. The test specification placed a +0, -2 tolerance on fL/D and as a result most plants were tested at least one fL/D less than their scaled values. Based on the capacitance and fL/D sensitivities reported in Reference 1, the increase in download and pool velocity that occurred by moving the orifice was roughly equivalent to the increase for an fL/D reduction of 4. Therefore, an fL/D reduction of 1 seems to have an effect on the loads roughly equivalent to increasing the capacitance by 25%.

The geometry of the QSTF is such that although the downcomer and vent header volumes are scaled, the main vent volume is less than the scaled Mark I volume. Therefore, although the total drywell plus vent system volume is scaled, the capacitance of the QSTF vent system is reduced by roughly 15 to 20%. Based on the fL/D margin discussed in the previous paragraph, the 50/50 orifice split used in the QSTF vent system still provides a prototypical model of the Mark I vent system flow rates.

G.2 Experimental Method

The basic experimental method consisted of discharging the facility air reservoir (about 500 cubic feet initially charged with air) through the vent system. During this test, the front door was removed from the wetwell so that the downcomer exit was at ambient pressure. A typical reservoir blowdown would last approximately 15 seconds and during this time sufficient data was taken to allow determination of the instantaneous mass flux into the drywell as well as the pressure drop across the vent system. A quasi-steady flow was established within one to two seconds. Neglecting mass storage terms in the drywell and vent system during the quasi-steady portion of the test, allows the system fL/D to be calculated as described in the following section.

The following measurements were digitally sampled at 500 samples per second during the test (see Figure G-2 for measurement locations):

P_c = Pressure at the charging orifice
T_c = Temperature at the charging orifice
P_o = Drywell Pressure
T_o = Vent total temperature (assume equal to downcomer temperature)
P_2 = Vent header static pressure

In addition to these the ambient pressure (P_3) was recorded from a barometer located at the facility. Due to the temperature sensitivity of the pressure transducers used for these measurements (Sensometrics SP-65) it was necessary to thermally isolate them from direct contact with the flow. This was accomplished by attaching the transducers to a length of copper tubing, the other end of which communicated with the location at which the pressure measurement was to be made.

The digitally sampled data was stored on magnetic tape and later plotted as a function of time. Data was read off the graphs and entered into a computer code which made the vent resistance calculations.

1351 186

G.3 Analytical Methods

Plant unique vent flow losses are simulated by the use of two flow orifices (Figure G-2). One of the flow orifices is placed at the main vent entrance and a pair of identical orifices are installed in the downcomer. The total flow loss is then obtained by summing the losses through the two flow orifices.

The vent system fL/D was calculated from measured data using the Fanno equations which describe compressible flow with friction. This method requires that the mass flow through the system ($\dot{m}$) be known. The mass flow was calculated from measured fluid properties upstream of the drywell flow control (inlet) orifice using the orifice flow equations in the following form:

$$\dot{m} = \frac{0.4739\, A_c\, P_c}{\sqrt{1-\beta^4}} \sqrt{\frac{2g}{R\,T_c}} \quad ; \quad \frac{P_o}{P_c} \leq 0.528$$

$$\dot{m} = \frac{0.98\, A_c\, Y\, 2g}{\sqrt{1-\beta^4}} \sqrt{\frac{(P_c - P_o)\, P_c}{R\,T_c}} \quad ; \quad \frac{P_o}{P_c} > 0.528$$

where A_c = Flow orifice area (in^2)

R = Gas constant (53.3 ft. lbf/lbm °R)

g = 32.17 lbm ft./lbf sec^2

β = D_c/D_o (where D_o is the diameter of the pipe containing the flow orifice)

and $Y \equiv \left\{3.5\, P_R^{1.429} \left[\frac{1-(P_R)^{0.286}}{1-P_R}\right] \left[\frac{1-\beta^4}{1-\beta^4(P_R)^{1.429}}\right]\right\}^{1/2}$

$P_R = P_o/P_c$

P_c, T_c, and P_o are defined earlier (see Figure G-2). Having determined the mass flow into drywell ($\dot{m}$), the vent fL/D was calculated with the Fanno equations as follows:

$$W_1 = \frac{\dot{m}}{P_0 Ag}\sqrt{\frac{R\,T_o}{\gamma}}; \quad W_1 = M_1\left(1 + \frac{\gamma-1}{2} M_1^2\right)^{\frac{-(\gamma+1)}{2(\gamma-1)}}$$

$$W_2 = \frac{\dot{m}}{P_2 Ag}\sqrt{\frac{R\,T_o}{\gamma}}; \quad W_2 = M_2\left(1 + \frac{\gamma-1}{2} M_2^2\right)^{\frac{-(\gamma+1)}{2(\gamma-1)}}$$

$$W_3 = \frac{\dot{m}}{P_3 Ag}\sqrt{\frac{R\,T_o}{\gamma}}; \quad W_3 = M_3\sqrt{1 + \frac{\gamma-1}{2} M_3^2}$$

$$(fL/D)_1 = \frac{1}{\gamma}\frac{M_2^2 - M_1^2}{M_2^2\, M_1^2} + \frac{\gamma+1}{2\gamma}\ln\left(\frac{\left(1+\frac{\gamma-1}{2} M_2^2\right) M_1^2}{\left(1+\frac{\gamma-1}{2} M_1^2\right) M_2^2}\right)$$

$$(fL/D)_2 = \frac{1}{\gamma}\frac{M_3^2 - M_2^2}{M_3^2\, M_2^2} + \frac{\gamma+1}{2\gamma}\ln\left(\frac{\left(1+\frac{\gamma-1}{2} M_3^2\right) M_2^2}{\left(1+\frac{\gamma-1}{2} M_2^2\right) M_3^2}\right) + 1$$

$$(fL/D) = (fL/D)_1 + (fL/D)_2$$

Here P_0 = Drywell Pressure, P_2 = Vent header pressure, P_3 = Ambient Pressure, T_0 = Drywell Temperature, A = Reference downcomer area from hydrodynamic conditions, and $\gamma = 1.4$.

For each selected data point during the test, W_1, W_2, and W_3 are calculated from measured or derived quantities. The corresponding values of M_1, M_2, and M_3 are calculated by an iterative procedure, and the flow losses through the vent orifice $(fL/D)_1$ and downcomer orifice $(fL/D)_2$ are calculated from the above algebraic expressions. Finally, the total vent resistance (fL/D) is obtained from the sum of $(fL/D)_1$ and $(fL/D)_2$.

G.4 Typical Test Data

The calculated total vent resistance (fL/D) and its distribution as a function of the ratio between the ambient and the drywell pressure for 17 power plants tested are presented in Figures G-3 through G-36 and summarized in Table G-1.

Although the calculated values of vent system fL/D presented in Figures G-3 through G-36 exhibit some scatter this scatter is felt to be primarily caused by uncertainties in the calculated fL/D and not by real variations in fL/D with vent system pressure ratio. Therefore, the fL/D values presented in Table G-1 are the average of the calculated values of fL/D over the pressure ratio range from 0.8 to 0.9. Since the Fanno equations are based on pressure differences, the calculated fL/D values become more sensitive to the uncertainty in the measured pressures at high vent system pressure ratios. The pressure ratio range of 0.8 to 0.9 was selected for fL/D calibration to provide a nearly incompressible fL/D at a low enough pressure ratio to minimize measurement error. The pressure signals especially in the drywell contain high frequency acoustic noise with an amplitude of a few tenths of a psi. The pressure uncertainty caused by this noise is felt to be largely responsible for the scatter in calculated fL/D. The measurement uncertainty analysis indicated an fL/D uncertainty of 6% at 95% confidence.

G.5 Vent System fL/D Model

A computer model was developed to calculate vent system fL/D during an actual wet test using QSTF pressure and temperature measurements. The model calculations of overall vent system fL/D and fL/D split agreed well with the pretest values obtained by dry blowdown calibrations. This result provides additional confidence that the QSTF met the specified test requirements for vent system fL/D.

During a pool swell test, the following parameters were measured as a function of time.

- P_o, drywell pressure
- P_c, charging orifice upstream pressure
- P_1, vent pressure
- T_1, vent temperature (actually in the flow stream just upstream of the downcomer orifice)

1351 189

ΔP, downcomer orifice differential pressure

P_B, "Bubble" pressure (actually wall pressure near the downcomer exit)

Two methods were selected for calculating flow losses: 1) constructing a mass balance for the drywell by using orifice equations, 2) constructing a mass balance for either the drywell or vent header from pressure and temperature measurements.

Method 1: Orifice Flow Model

$$\dot{m}_i - \dot{m}_o = \frac{dM}{d\theta} \qquad (1)$$

where

$\dot{m}_i$ = input from charging orifice
$\dot{m}_o$ = outflow to vent system
θ = time
M = instantaneous drywell gas mass

In this analysis, the upper vent orifice and the lower vent orifice are used as metering orifices. Since the charging orifice operates under critical flow conditions ("choked flow") during a test,

$$\dot{m}_i = \frac{0.4379 A_c P_c}{\sqrt{1 - \beta^4}} \sqrt{\frac{2g_c}{RT_c}} \qquad (2)$$

where

A_c = orifice flow area
g_c = Newton's Law Conversion Factor, 32.174 ft-lb/lb_f-sec^2
R = gas constant, 1546 ft-lb_f/lb-mole-°F
T_c = absolute temperature upstream of orifice
β = ratio of orifice diameter to pipe diameter
P_c = charging orifice upstream pressure

The inlet temperature to the charging orifice can either be assumed constant at initial conditions (nominally 70°F) or allowed to vary with tank pressure (assuming adiabatic blowdown). The adiabatic blowdown relation used is:

$$T^* = (M^*)^{\gamma-1}$$

where

$T^* = T/T_{initial}$
$M^* = M/M_{initial}$
γ = specific heat ratio

Since the vent header orifice is operating at a subcritical pressure ratio,

$$\dot{m}_c = \frac{C_D A Y_1}{\sqrt{1 - \beta^4}} \sqrt{\frac{2 g_c P_2 \Delta P}{R T_2}} \qquad (3)$$

where

C_D = discharge coefficient, measured during quasi-steady blowdown
ΔP = pressure difference between drywell and vent header
P_2 = drywell pressure
T_2 = drywell temperature
A = orifice flow area
β = ratio of orifice diameter to pipe diameter
Y_1 = expansion factor (function of downstream/upstream pressure ratio, specific heat ratio, and β)
R = gas constant
g_c = Newton's Law Conversion factor

In finite difference form, Equation (1) becomes:

$$\frac{M' - M}{\Delta\theta} = \dot{m}_i - \dot{m}_{o,a} \qquad (4)$$

where

M' = instantaneous drywell gas mass at end of time step = $P_2' V_d/RT_2'$

P_2' = drywell pressure at end of time step

V_d = drywell volume

T_2' = drywell temperature at end of time step

$\dot{m}_{o,a}$ = average value of $\dot{m}$ over the time step = $(\dot{m}_o + \dot{m}_o')/2$

T_2' appears in both M' and $\dot{m}_o'$, so an iterative loop can be set up to determine the temperature that satisfies Equation (4) at each time step.

After closure, values of $\dot{m}_o'$, P_2', and P_1' are used to calculate $(fL/D)_1$ by the Fanno equations presented in Section G.3.

Method 2: State Equation Model

$$\left(\frac{dM}{d\theta}\right)_i = \frac{M_{i+1} - M_i}{2\,\Delta\theta} \qquad (5)$$

The mass in either the vent system or drywell is known as a function of time, since both pressure and temperature are measured. The drywell volume used is the specified drywell volume for each plant. The vent header volume used is that volume between the upper vent orifice and the downcomer orifice. That is, the volume of the downcomer legs is subtracted from total vent volume. This has the effect of slightly (~1%) overestimating the exit dump losses attributed to the lower portion of the system.

The measured vent orifice temperature is assumed to represent the absolute temperature in both the vent and the drywell.

For this method, $\dot{m}_o$ can be directly calculated without use of orifice equations.

$$\dot{m}_o = \dot{m}_i - \frac{dM}{d\theta}$$

fL/D is then calculated by the Fanno equations.

Brunswick-3 was used as a sample case for program checkout and for exploring computational sensitivities. Three data sets were constructed which represented reasonable approaches to data analysis. They were:

1. Average Rate.

A relatively sparse data set (8 points) was selected which only approximated the initial pressures, but which accurately matched the average slope of the pressure curves after vent clearing.

2. Digital Fill-in

The initial pressure histories were filled in with added entries from the digital output; test termination values were selected from the digital list with no effort to eliminate random data noise.

3. Smoothed Digital

A time frame was selected by noting natural break points (slope changes) from the quick-look plots. Data entries were selected from the digital output by local smoothing; that is, a mean value was constructed by averaging local values to remove signal noise.

The first data set probably best represents average values. The second data set is an objective selection and the third data set "best" models detailed behavior during the test.

Figure G-37 summarizes the calculated Brunswick-3 overall fL/D for Method 2 (three input data sets) and for Method 1 (average rate data). Also plotted are the quasi-steady values and the test specification limits for Brunswick. The calculated values all agree reasonably well and illustrate the uncertainties inherent in the various data fitting approaches. It is difficult to support Method 1 as necessarily "better" than Method 2. It is fair to say that the differences between them represent uncertainty in the achieved value of overall fL/D. Overall fL/D during the test was about 16 (the mean specified value), with an uncertainty of plus or minus 1.

The Method 2 drywell mass balance terms are displayed on Figure G-38. The mass rate into the drywell is about 7 lbm/sec. The storage term (during steady flow) is about 3 lbm/sec; the outflow about 4 lbm/sec. Hence, the storage term is significant for a proper drywell mass balance; meaningful results depend on an accurate approximation of that term.

The Method 2 vent system mass balance (Figure G-39) shows that the storage term is only about 10% of the throughput, so that the vent header computation is much less sensitive to pressure and temperature derivatives than is the drywell computation.

Figure G-40 is a comparison of drywell $\dot{m}_o$ computed by Methods 1 and 2. The Method 1 calculation yields slightly (5 to 10%) higher mass outflow from the drywell than Method 2. It is not clear how much of the difference was attributable to uncertainties in vent orifice discharge coefficient. Subsequent analysis showed that much of the difference was due to drift of the vent pressure transducer. When that drift is "corrected", the two values agree very closely. In any event, both methods yield nearly

the same values for drywell mass flux and storage terms. The differences are well within the uncertainty for upper orifice discharge coefficient.

The vent orifice thermocouple (used as a primary input for Method 2 calculations) frequently yielded erratic values. After the orifice temperature rise, rapid drops and oscillations were seen, apparently due to moisture or water deposition or impact. Solutions to the drywell continuity equation are not particularly sensitive to the value of temperature (since only the absolute temperature appears in the mass storage term). The solutions are, however, quite sensitive to the temperature slope. This can be seen by expanding the mass storage term as follows:

$$\frac{dM}{d\theta} = \frac{d}{d\theta}\left(\frac{PV}{RT}\right) = \frac{V}{RT}\frac{dP}{d\theta} - \frac{PV}{RT^2}\frac{dT}{d\theta} \qquad (6)$$

$$= \frac{V}{RT}\frac{dP}{d\theta} - M\left(\frac{1}{T}\frac{dT}{d\theta}\right)$$

For our sample case, the first term on the right side of Equation (6) at 600 msec into the test is 3 to 4 lbm/sec, while M is 2 to 3 lbm. Accordingly, a temperature rate slope of 30 to 50 percent per second (a commonly observed value during oscillations) has a significant contribution to the continuity mass balance.

Starting with the Millstone test series, the vent orifice thermocouple was moved up into the vent to reduce the possibility of moisture influence. Figure G-41 illustrates a typical response during that series, characterized by a rise to 120-130°F and a gradual decline during the remainder of the test.

The fL/D split between the upper and lower orifices is sensitive to the measured vent pressure during a test. The vent pressure measurement typically displayed a downward shift relative to the drywell transducers

after valve closing (when pressures are equalized between the drywell and vent). This shift may be thermally induced, since the vent transducer housing was subjected to some heating during the run. The magnitude of the shift was typically 0.1 to 0.3 psi.

Since typical pressure differences between vent and bubble were 0.6 and 0.8 psi, the pressure drift significantly influenced the fL/D split. This shift also influences the Method 1 mass balance solution, but has a negligible effect on calculated Method 2 mass rates and overall fL/D.

Fortunately, a "calibration" point was provided during every test after valve closure (when the drywell and vent pressures equalize). These end-point values provided a reasonable quantitative assessment of the vent transducer drift.

Figure G-42 shows the percent of total fL/D attributable to the downcomer, $(fL/D)_2$, for several cases. The quasi-steady results attributed approximately 53% of the overall fL/D to the downcomers. The fL/D split calculated by Method 2 is shown for Brunswick tests 1 and 3 for the "raw" data (which used average slope fit to the vent pressure) and for an "adjusted" pressure history (which used actual measured values at 400 msec into the test and adjusted the value of vent pressure at test termination). The vent pressure drift is apparent. The later values for $(fL/D)_2$ drift down noticably and fall below 40% at the end of the test. The adjusted values, however, remain well within the specified band and agree well with the quasi-steady values.

The following assumptions and data adjustments should be made for any computation of fL/D during pool swell testing:

1. Computed results are inaccurate until after vent clearing, when a reasonably steady ramp pressure transient is achieved.

2. A relatively simple tabulation of temperatures and pressures should be used for the calculation. Care should be taken to utilize the average slope of data obtained during steady ramp conditions.

3. When valid vent temperature measurements are available, Method 2 computations probably best represent system response.

4. When moisture impact causes fluctuations in temperature measurements, an estimated temperature response of a quick ramp to 120-130°F and a slight decline over the remainder of the test will yield reasonable results.

5. The end point measured vent pressure should be adjusted to that drywell pressure which is achieved after valve closing and system stabilization.

6. When accurate vent temperatures are not available, Method 1 calculated with a modified pressure trace will provide a valuable redundant check on system fL/D.

7. The vent temperature is an accurate approximation to the drywell temperature.

In conclusion, a technique (based on drywell and vent header mass balances) for calculating the fL/D distribution during the course of a pool swell test shows good agreement with the quasi-steady blowdown calibration of resistance coefficient. The model vent system for the Brunswick plant showed a pool-swell test $(fL/D)_T$ of about 16 $\pm$ 1 with a nearly 50-50 fL/D split, as compared with a quasi-steady $(fL/D)_T$ of approximately 16.3 and a fL/D split of about 53-47. The good agreement between this analytical technique and the experimental fL/D equations provides confidence that the facility does meet the tests requirements for fL/D.

FIGURE G-1 VENT CAPACITANCE DIAGRAMS FOR THE QSTF AND REPRESENTATIVE MARK I PLANTS

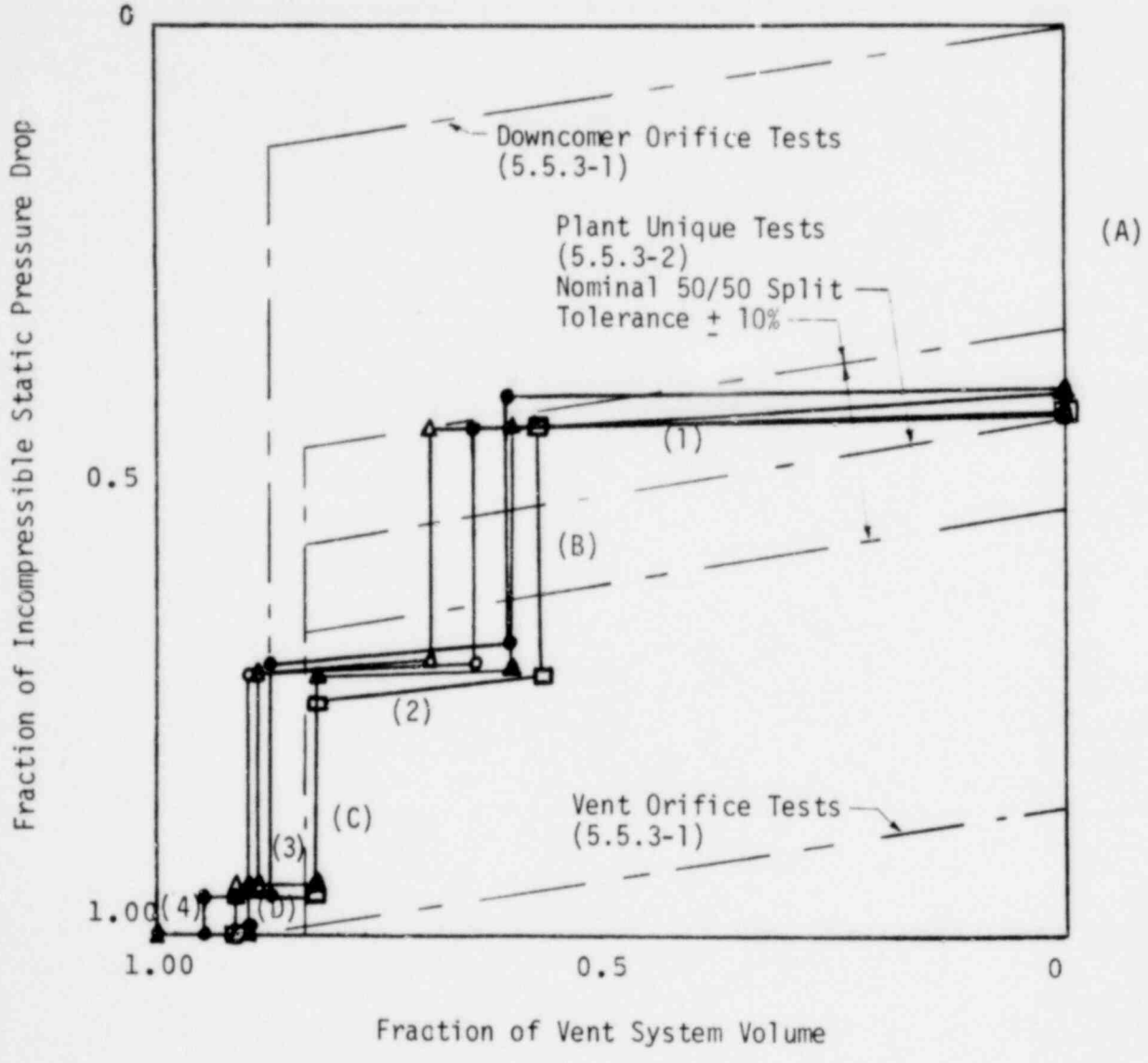

Legend for Mark I Characteristics

Pressure Drops	Volume Increments	Plant
Blast Shield	(1) Main Vent	Cooper Station
Vent Pipe to Vent Header	(2) Vent Header	Oyster Creek
Vent Header to Downcomer	(3) Downcomers to Bend	Nine Mile Pt.
Downcomer Bend	(4) Downcomers Bend to Exit	Peach Bottom
		Duane Arnold

FIGURE G-2 - FACILITY GEOMETRY

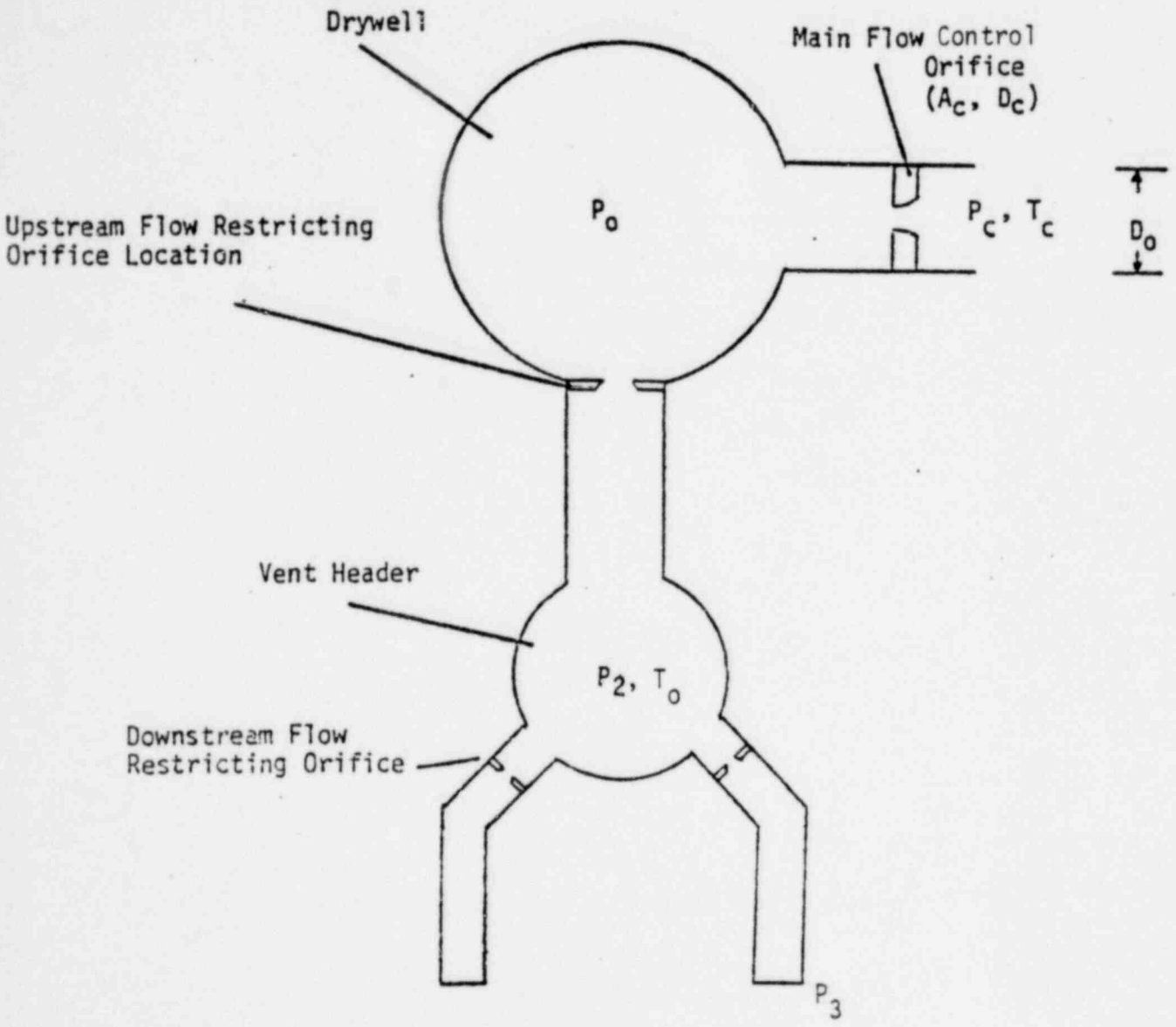

1351 199

FIGURE G-3

CALCULATED VENT HEADER RESISTANCE fL/D

Hatch 2 Tests

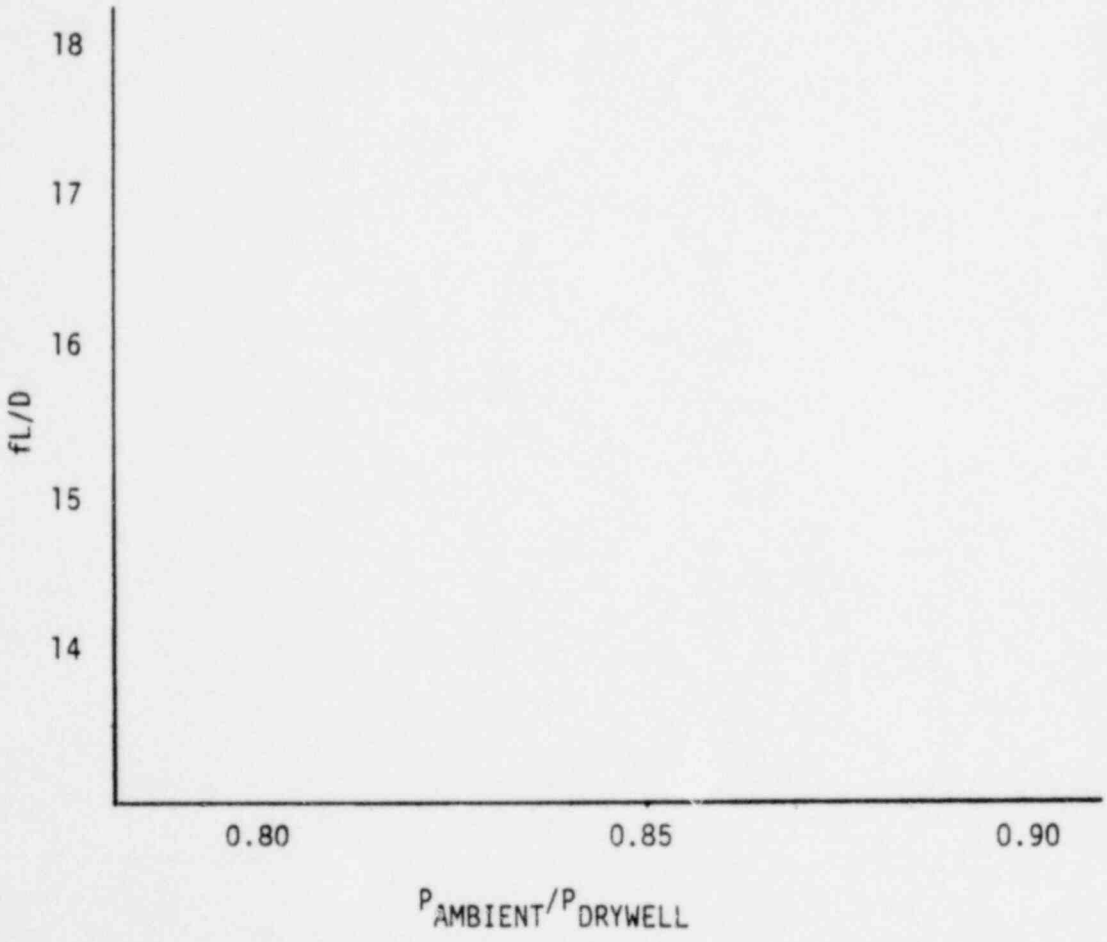

FIGURE G-4

VENT RESISTANCE (fL/D) DISTRIBUTION

Hatch 2 Tests

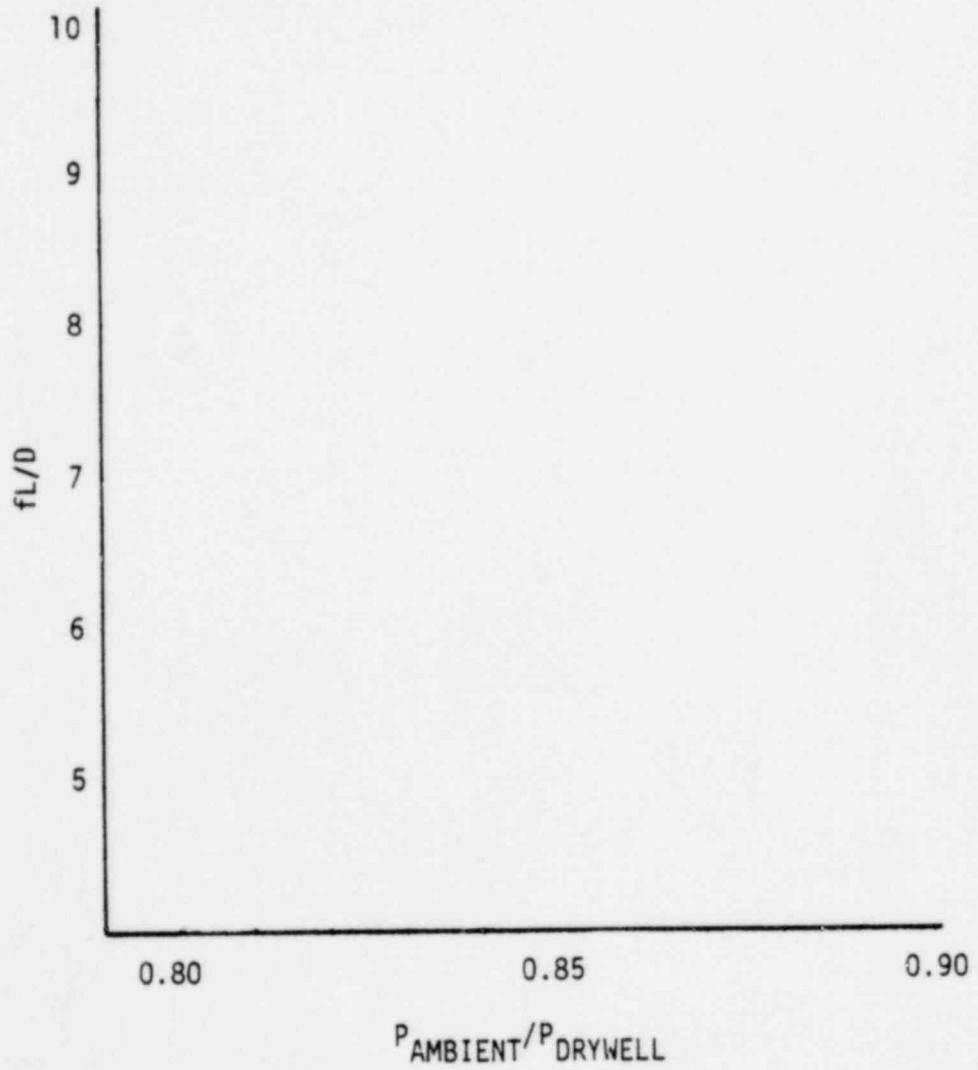

1351 201

FIGURE G-5

CALCULATED VENT HEADER RESISTANCE fL/D

Monticello Tests

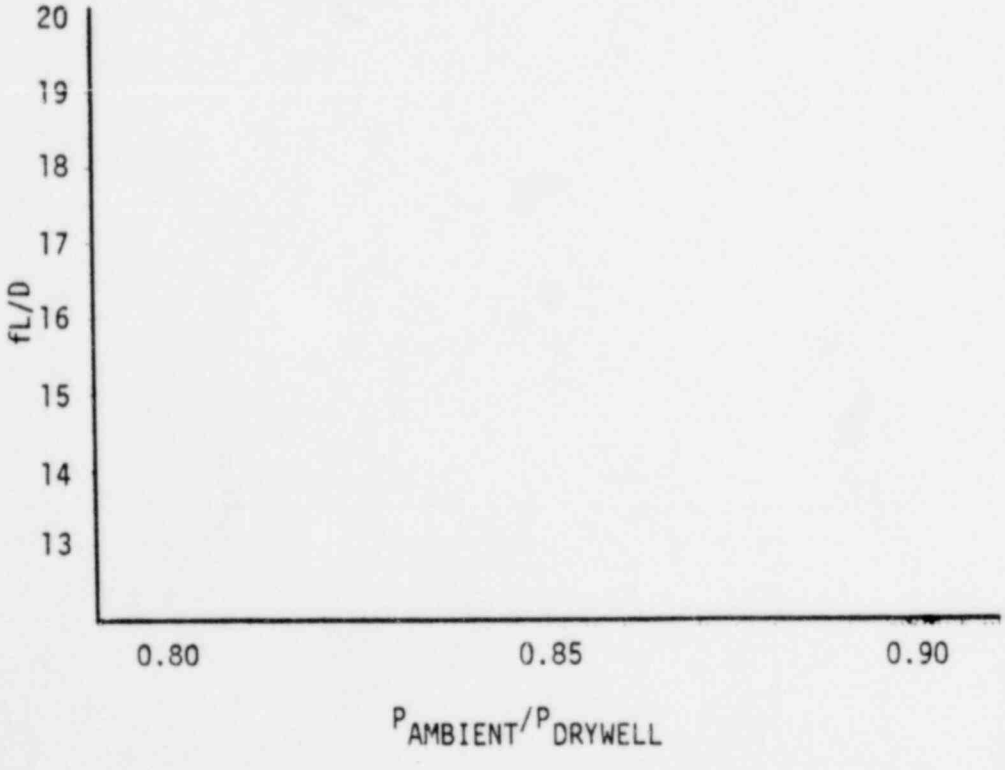

1351 202

FIGURE G-6

VENT RESISTANCE (fL/D) DISTRIBUTION

Monticello Tests

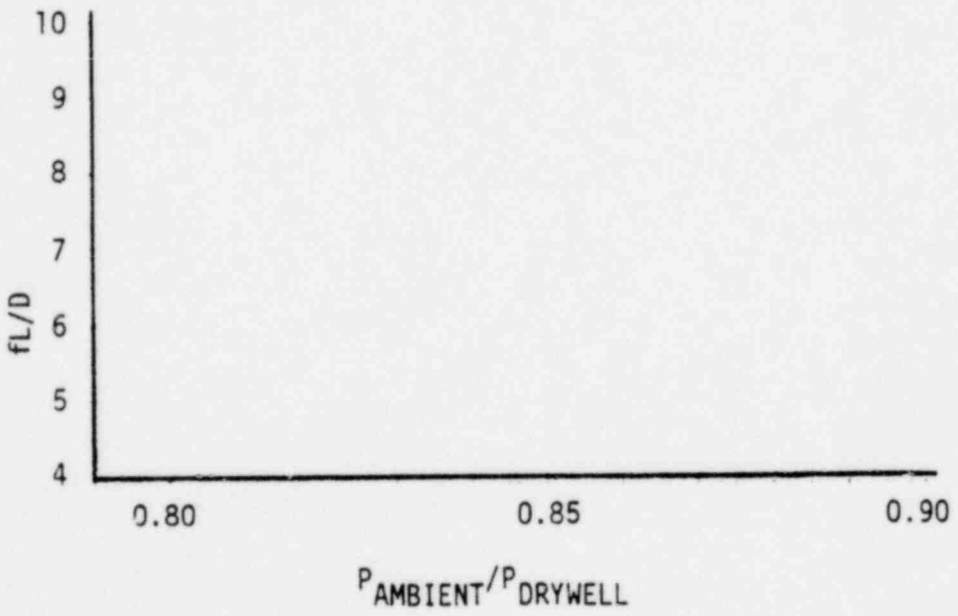

* 40% to 60% of actual total fL/D

1351 203

FIGURE G-7

CALCULATED VENT HEADER RESISTANCE fL/D

Pilgrim Tests

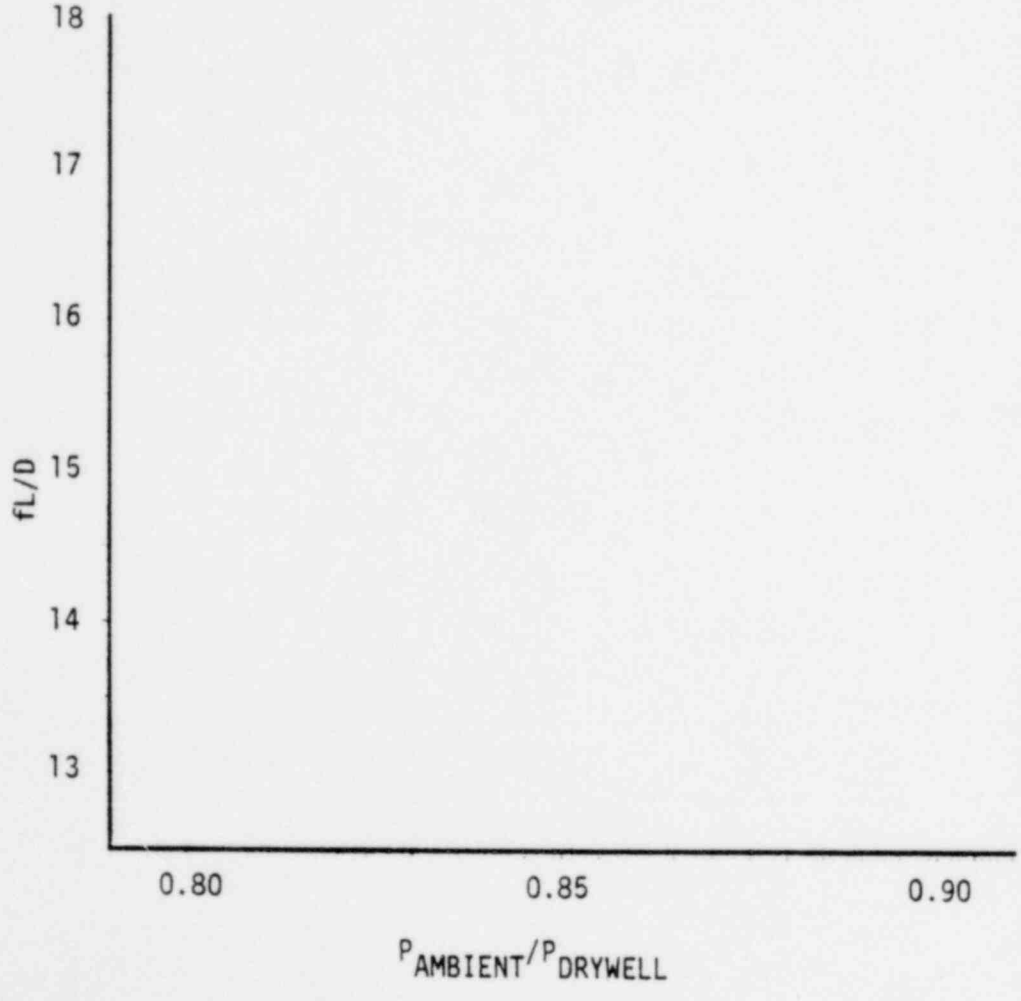

1351 204

FIGURE G-8

VENT RESISTANCE (fL/D) DISTRIBUTION

Pilgrim Tests

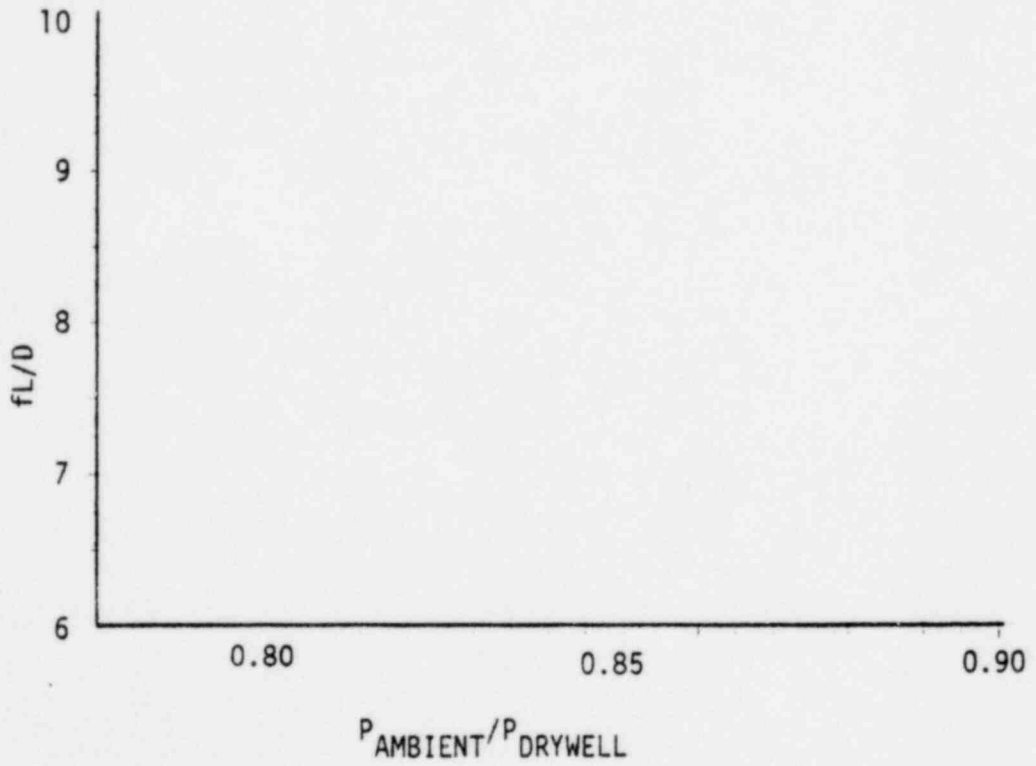

1351 205

FIGURE G-9

CALCULATED VENT HEADER RESISTANCE fL/D

Fermi 2 Tests

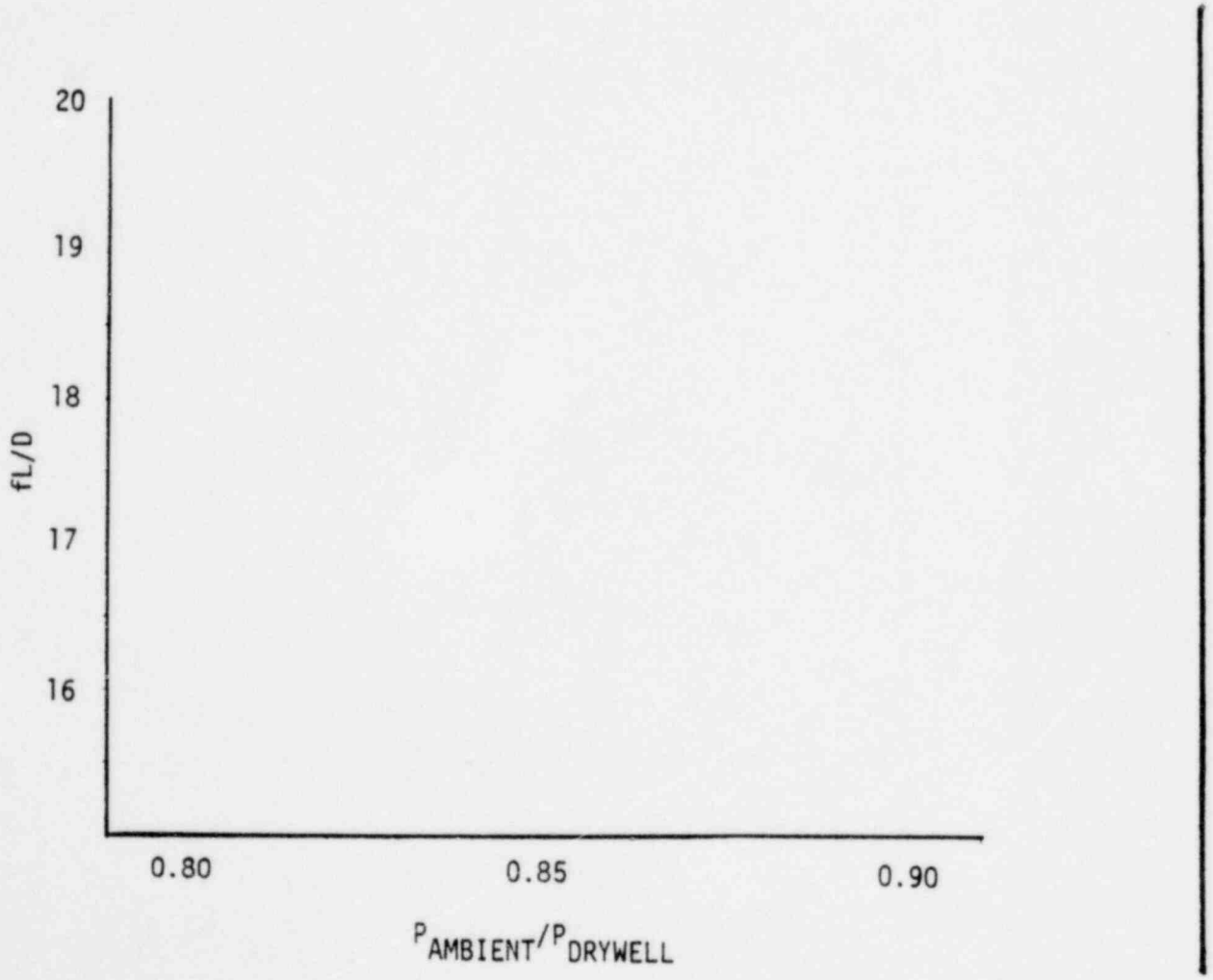

1351 206

FIGURE G-10

VENT RESISTANCE (fL/D) DISTRIBUTION

Fermi Tests

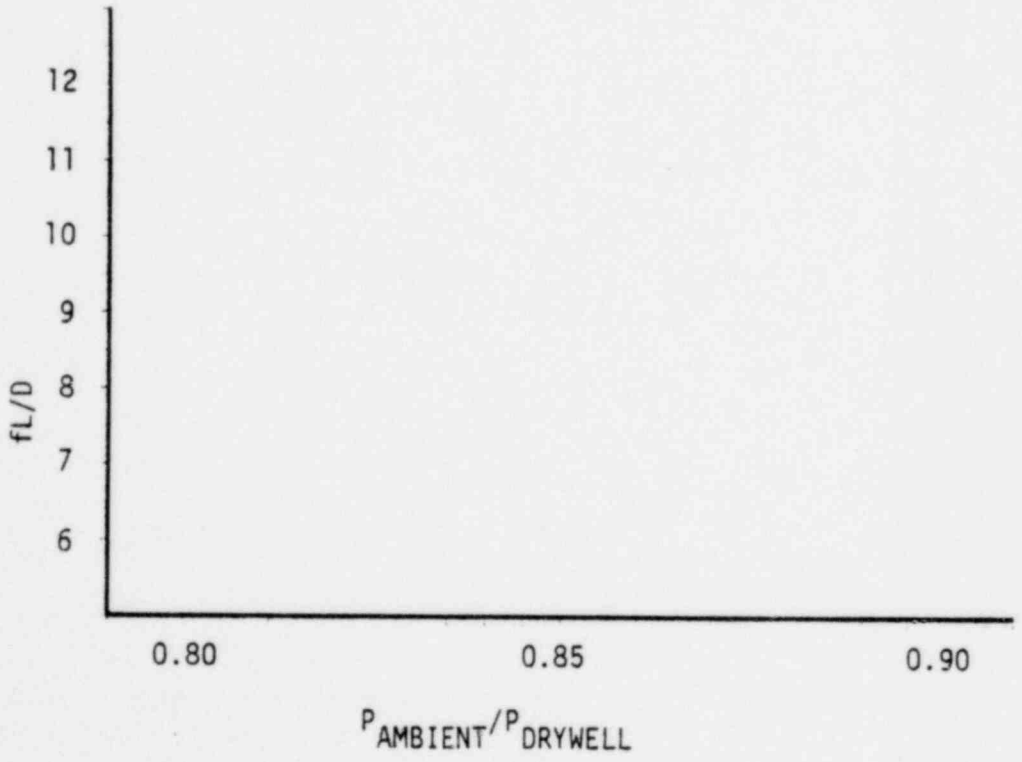

FIGURE G-11

CALCULATED VENT HEADER RESISTANCE fL/D

Duane Arnold Tests

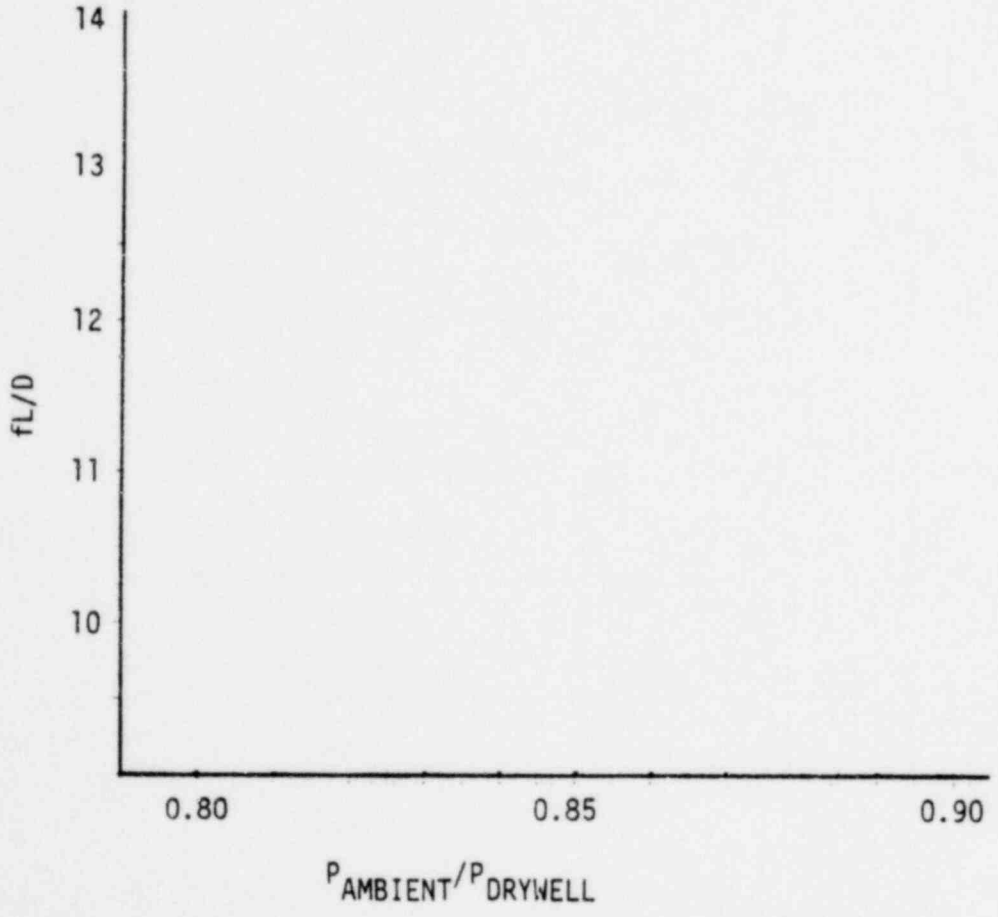

FIGURE G-12

VENT RESISTANCE (fL/D) DISTRIBUTION

Duane Arnold Tests

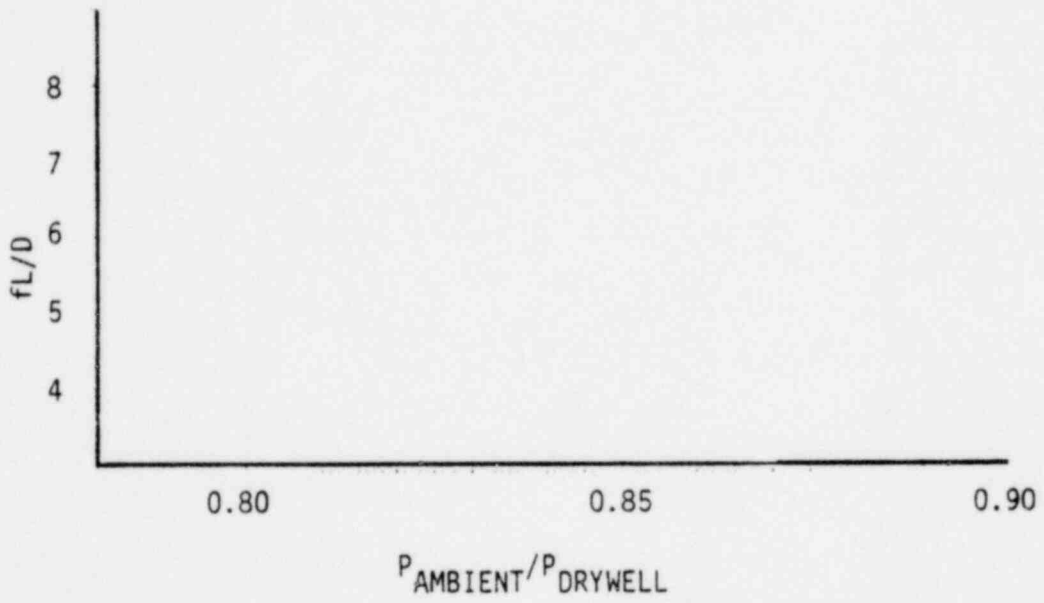

1351 209

FIGURE G-13

CALCULATED VENT HEADER RESISTANCE fL/D

Nine Mile Point Tests

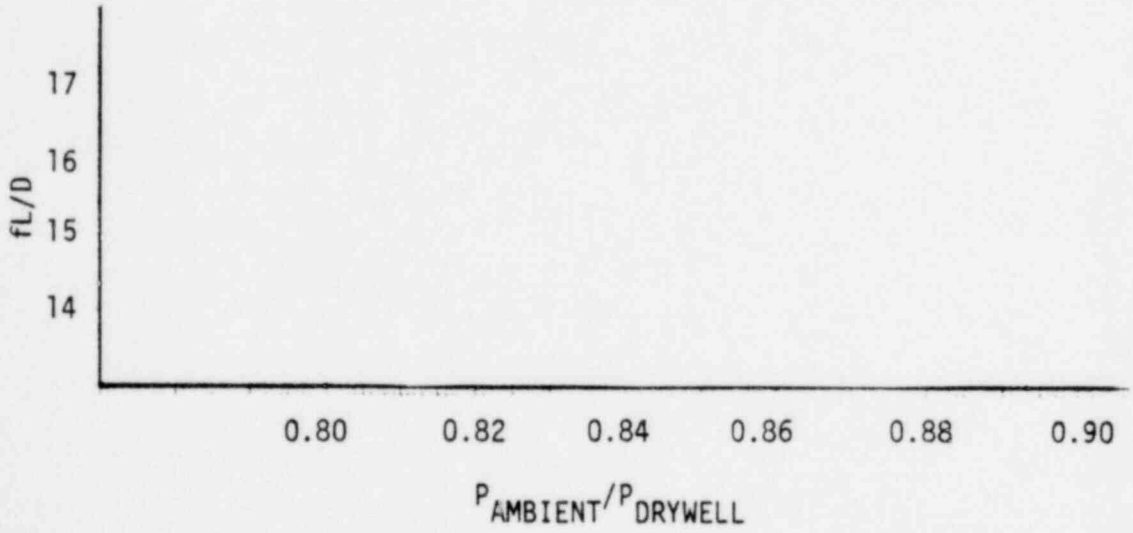

FIGURE G-14

VENT RESISTANCE (fL/D) DISTRIBUTION

Nine Mile Point Tests

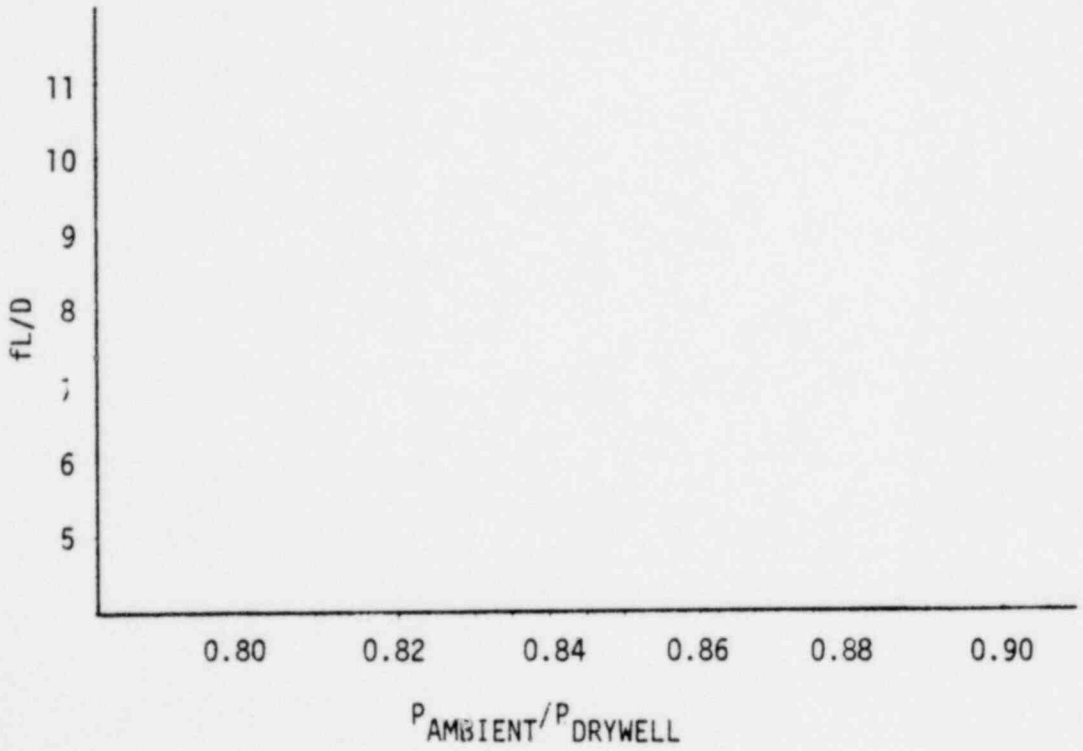

1351 211

FIGURE G-15 CALCULATED VENT RESISTANCE fL/D

BRUNSWICK TESTS

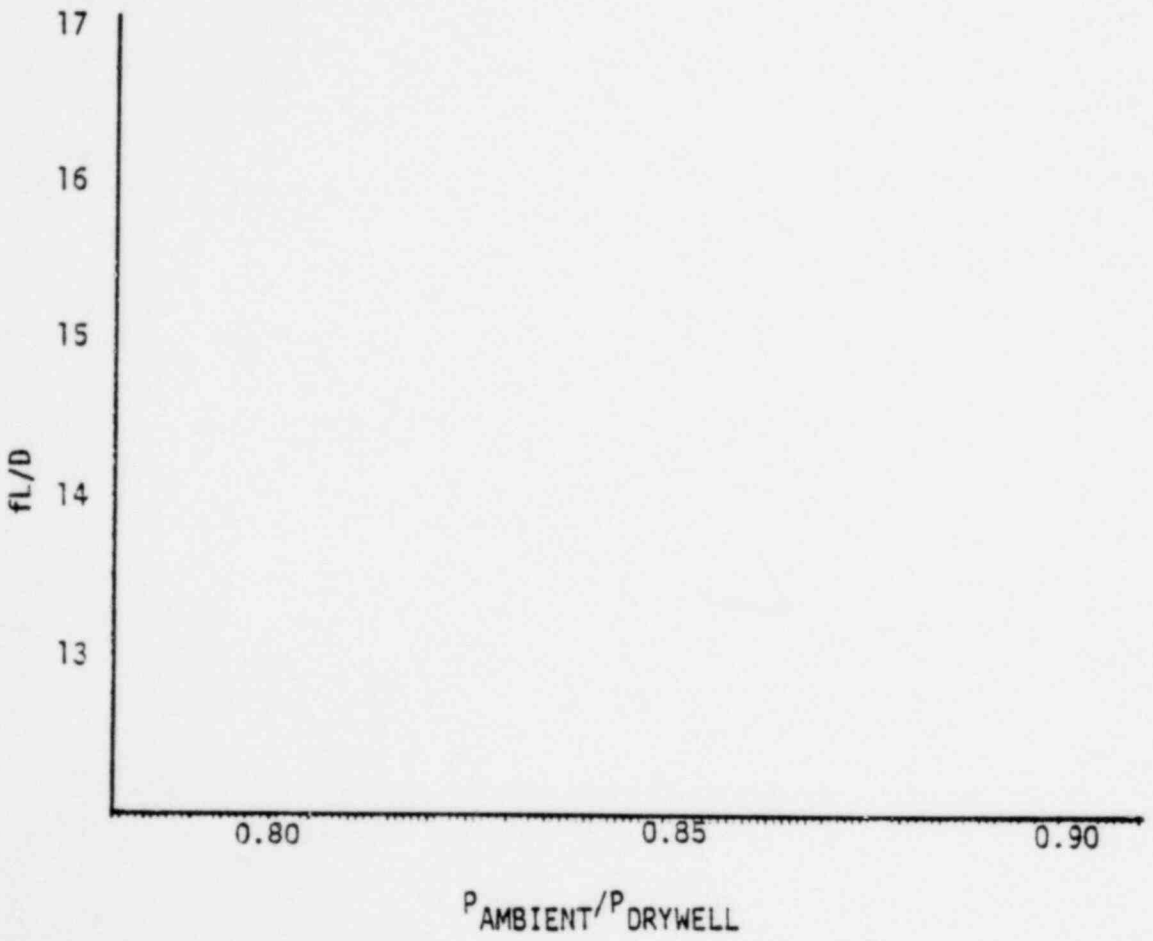

FIGURE G-16 VENT RESISTANCE (fL/D) DISTRIBUTION

BRUNSWICK TESTS

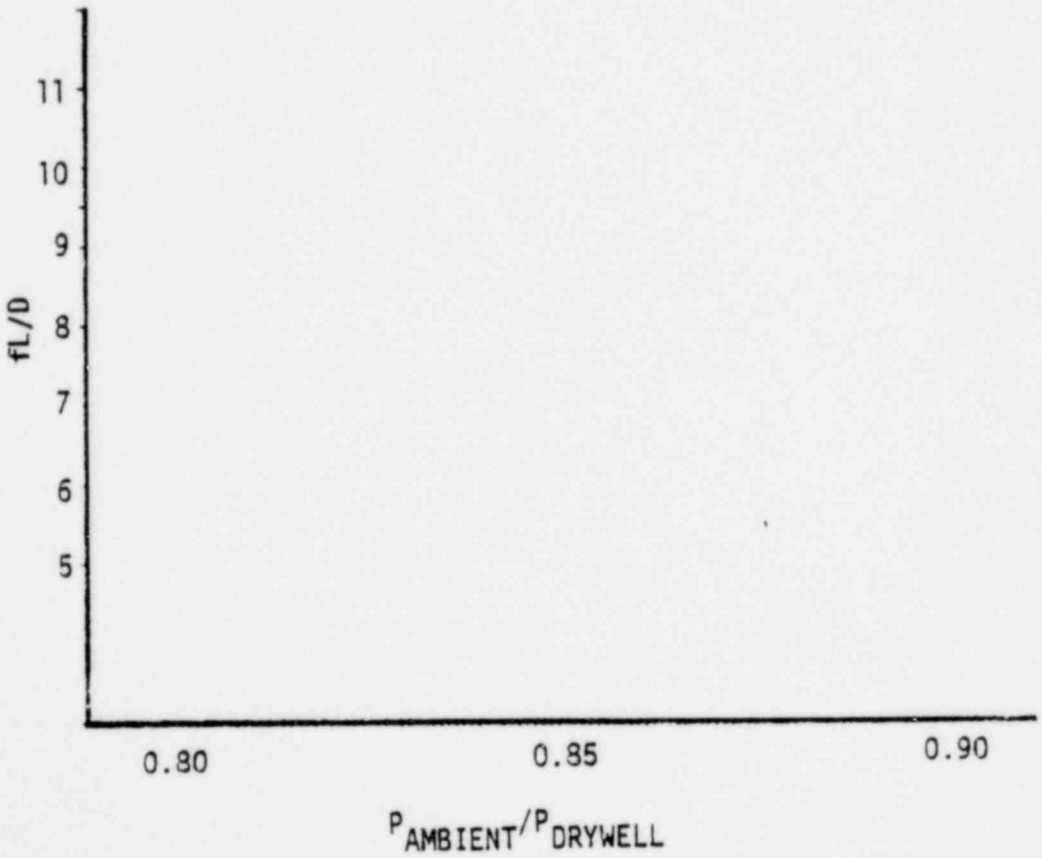

1351 213

FIGURE G-17 CALCULATED VENT RESISTANCE fL/D

COOPER STATION TESTS

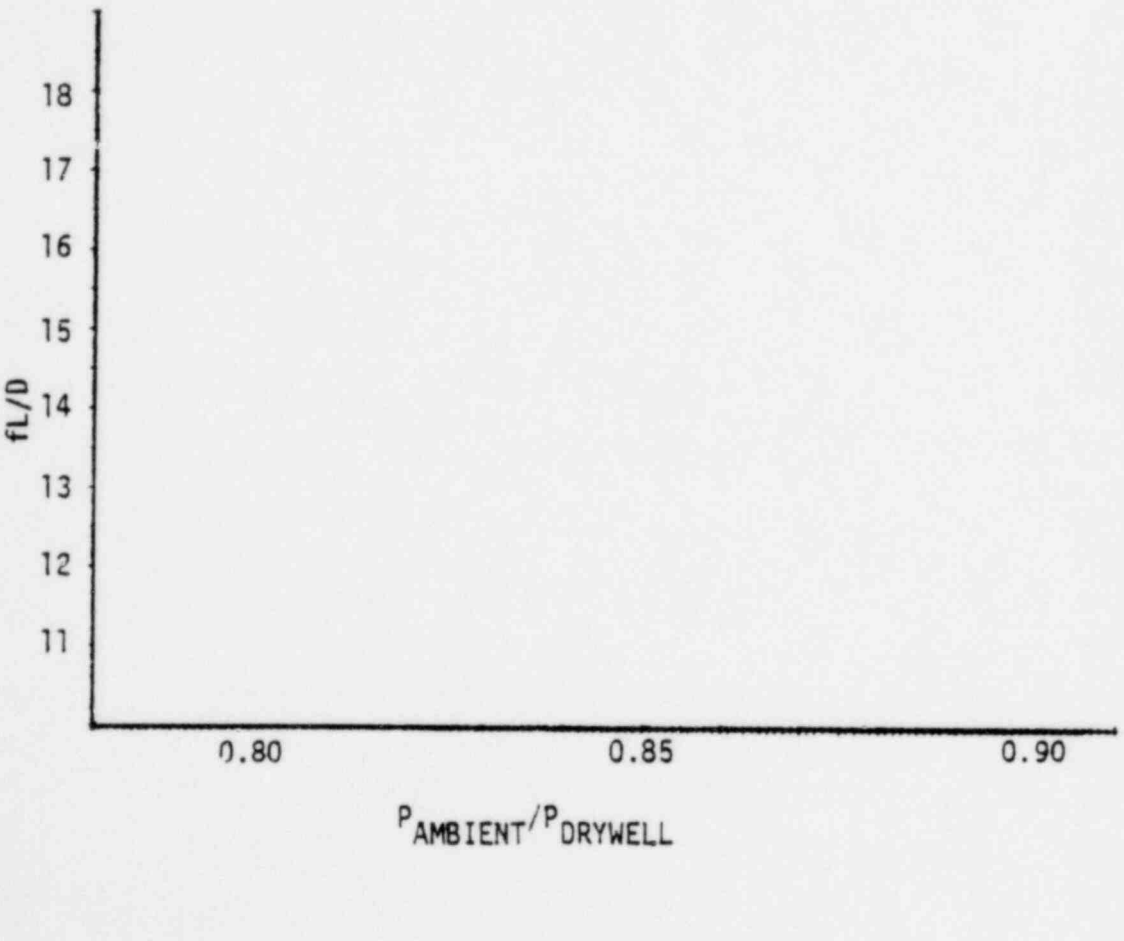

FIGURE G-18 VENT RESISTANCE (fL/D) DISTRIBUTION

COOPER STATION TESTS

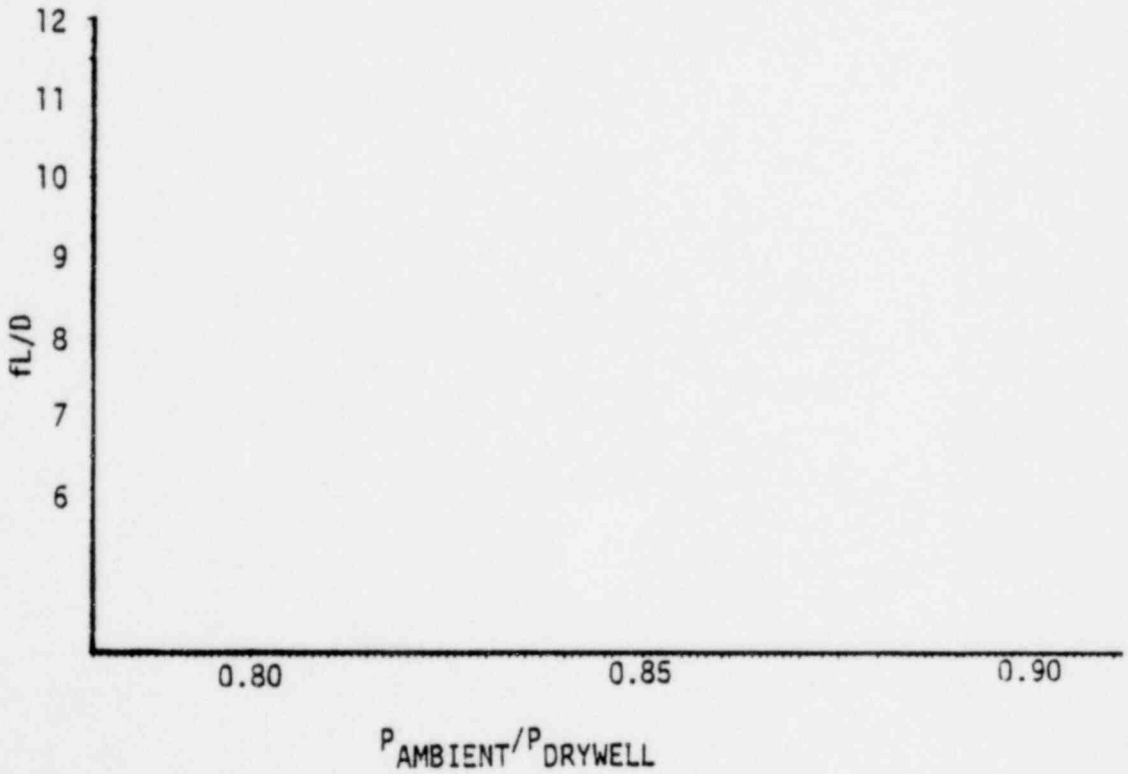

1351 215

FIGURE G-19 CALCULATED VENT RESISTANCE fL/D

DRESDEN TESTS

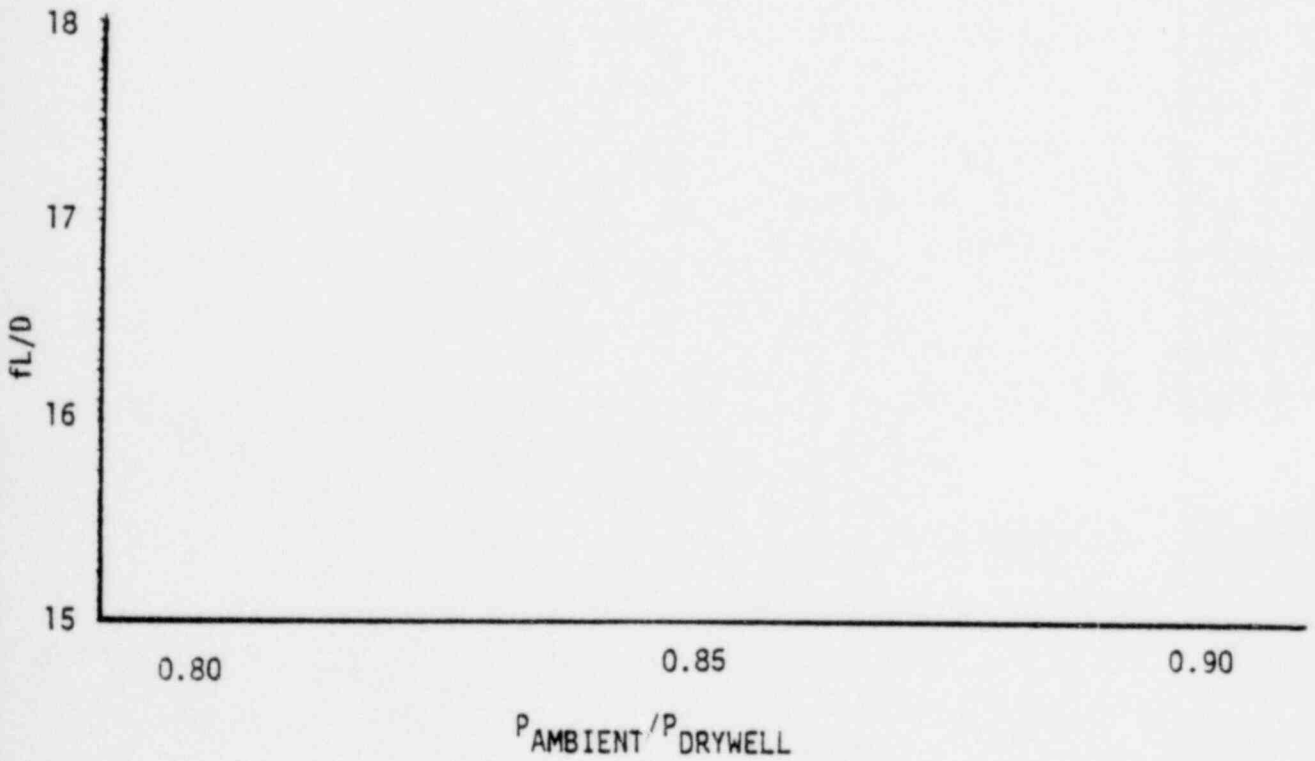

1351 216

FIGURE G-20 VENT RESISTANCE (fL/D) DISTRIBUTION

DRESDEN TESTS

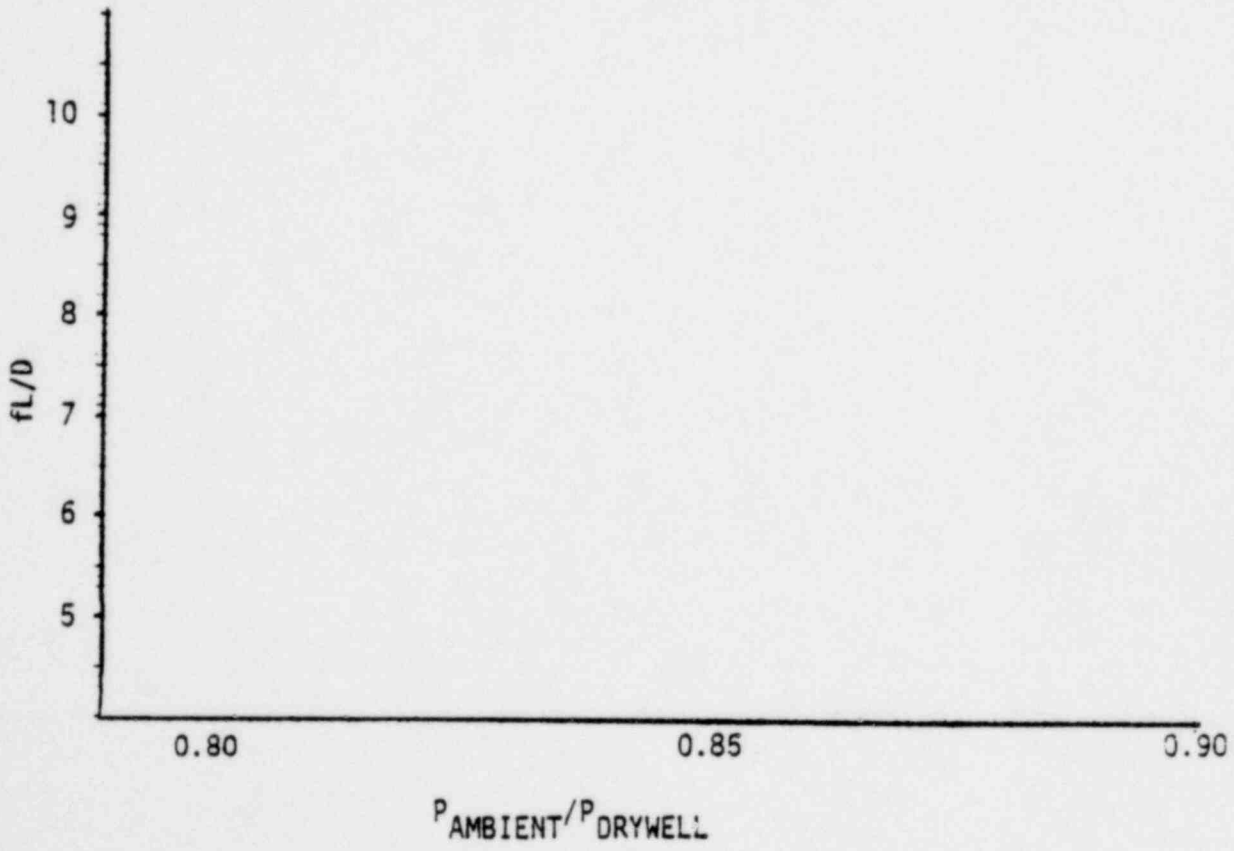

1351 217

FIGURE G-21 CALCULATED VENT RESISTANCE fL/D

BROWNS FERRY TESTS

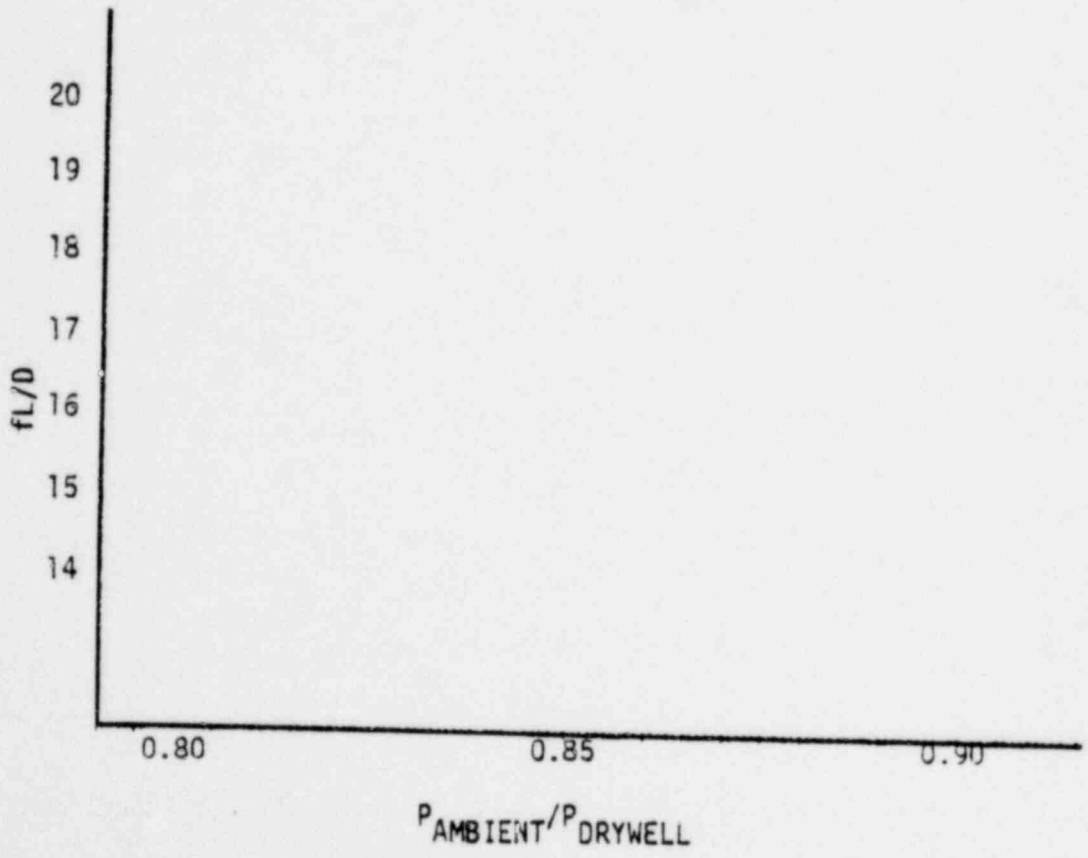

FIGURE G-22 VENT RESISTANCE (fL/D) DISTRIBUTION

BROWNS FERRY TESTS

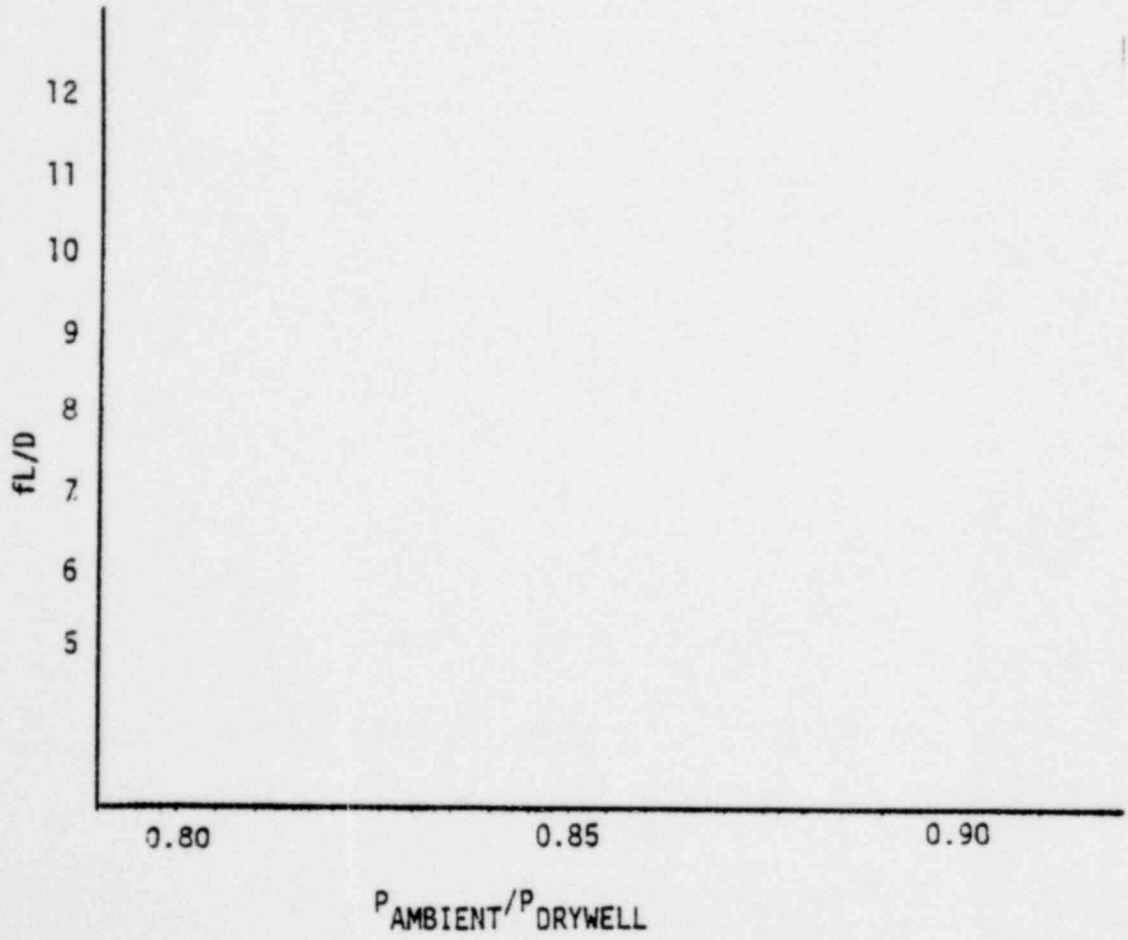

1351 219

FIGURE G-23 CALCULATED VENT RESISTANCE fL/D

PEACH BOTTOM TESTS

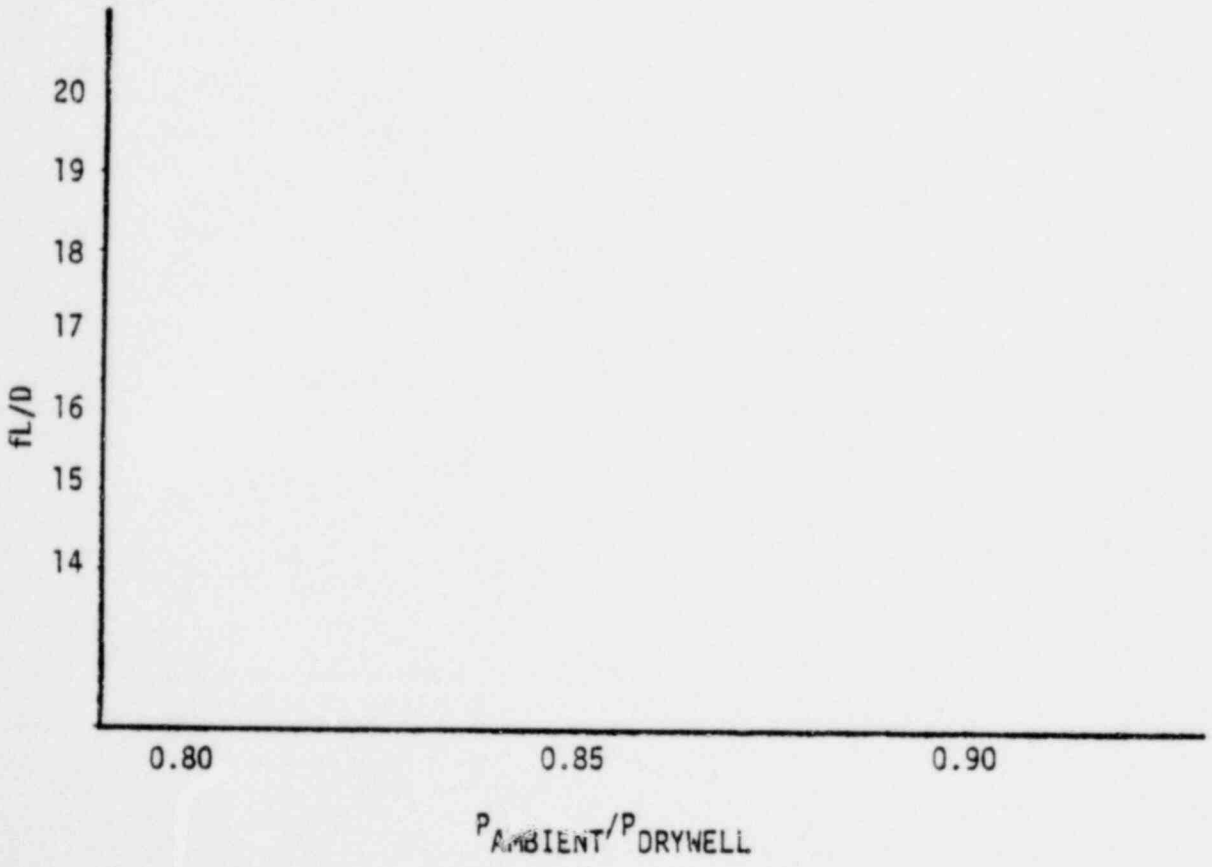

FIGURE G-24 VENT RESISTANCE (fL/D) DISTRIBUTION

PEACH BOTTOM TESTS

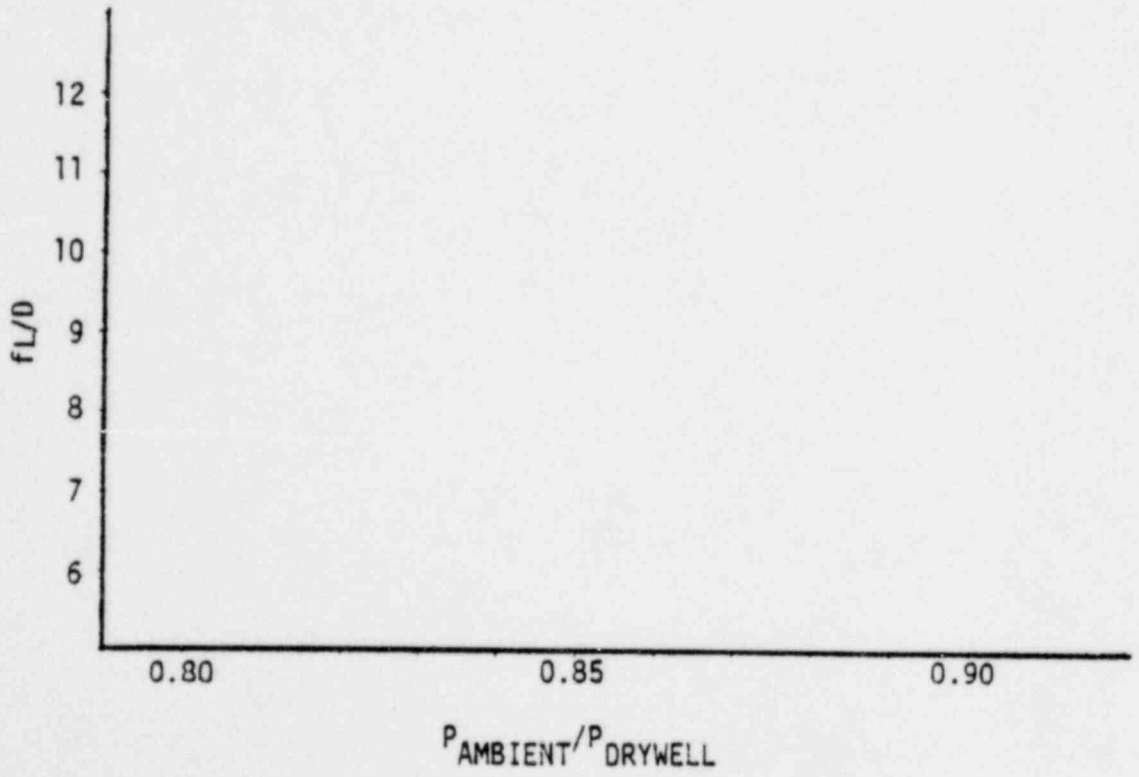

1351 221

FIGURE G-25

CALCULATED VENT RESISTANCE fL/D

MILLSTONE TESTS

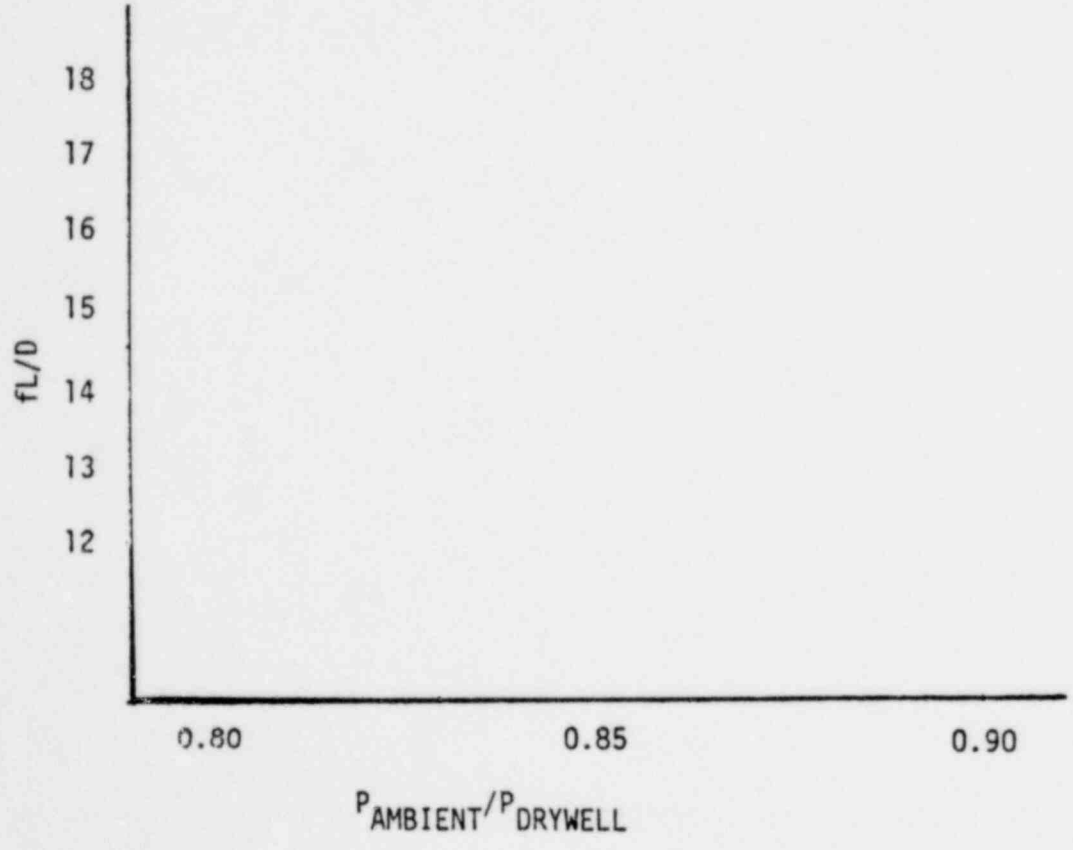

1351 222

FIGURE G-26

VENT RESISTANCE (fL/D) DISTRIBUTION

MILLSTONE TESTS

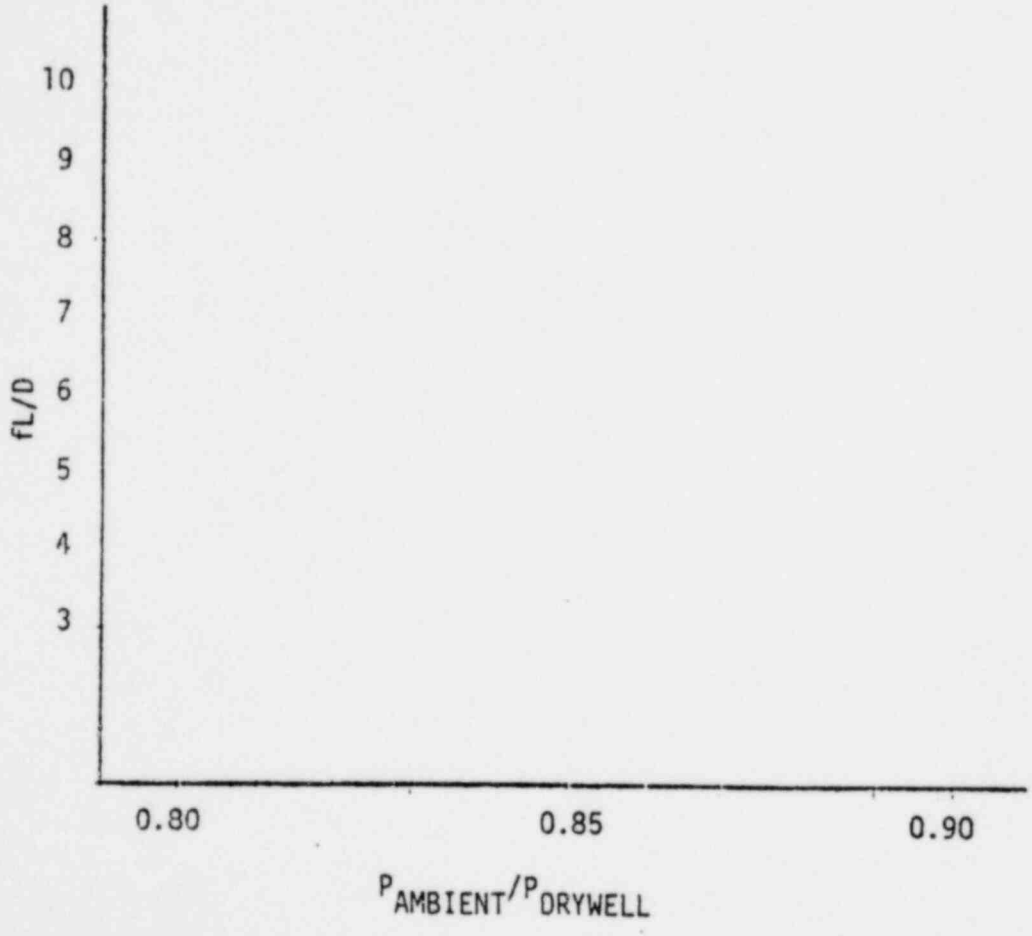

1351 223

FIGURE G-27

CALCULATED VENT RESISTANCE fL/D

OYSTER CREEK TESTS

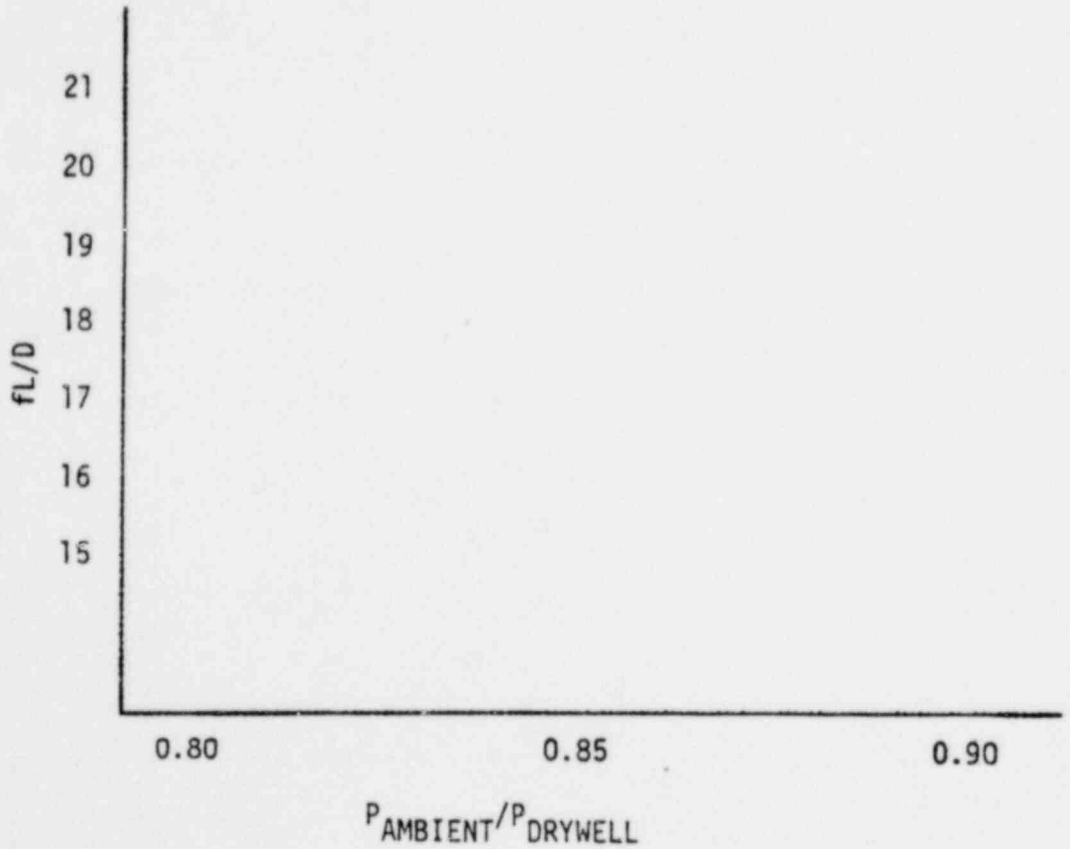

1351 224

FIGURE G-28

VENT RESISTANCE (fL/D) DISTRIBUTION

OYSTER CREEK TESTS

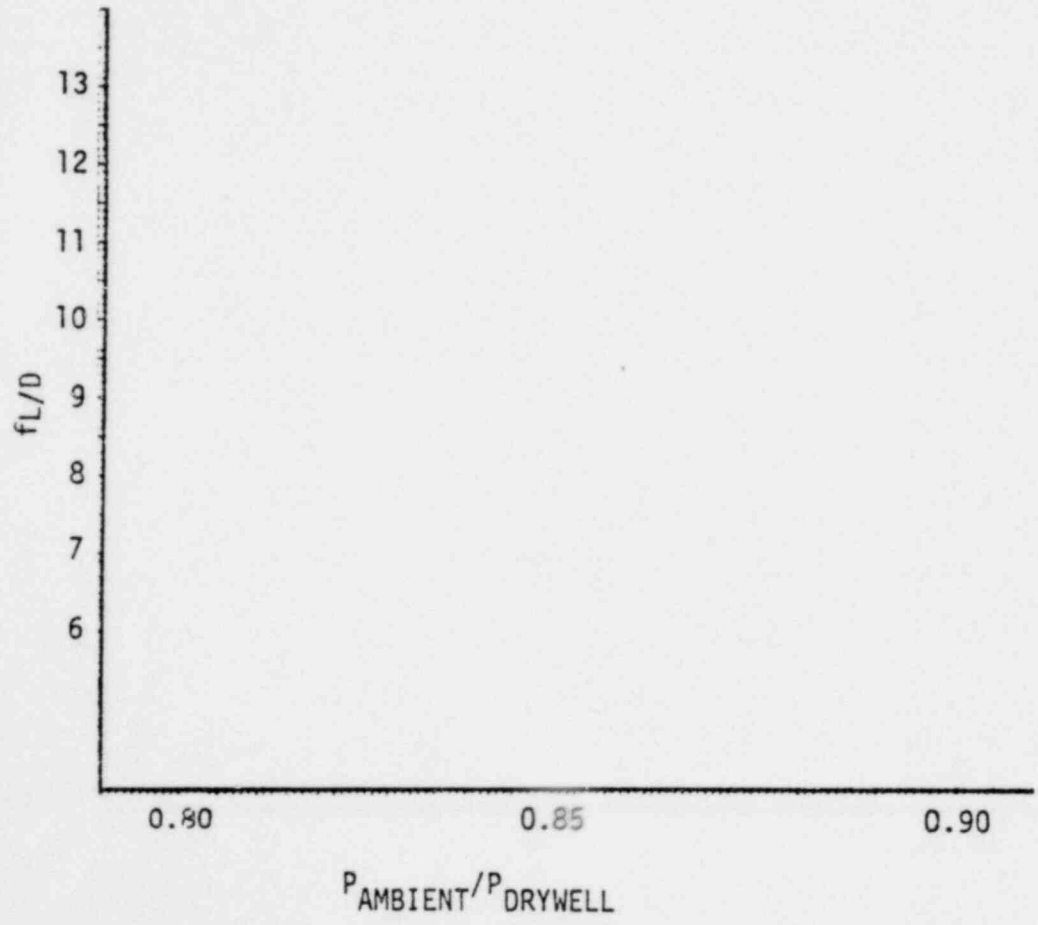

FIGURE G-29

CALCULATED VENT RESISTANCE fL/D

HATCH 1 TESTS

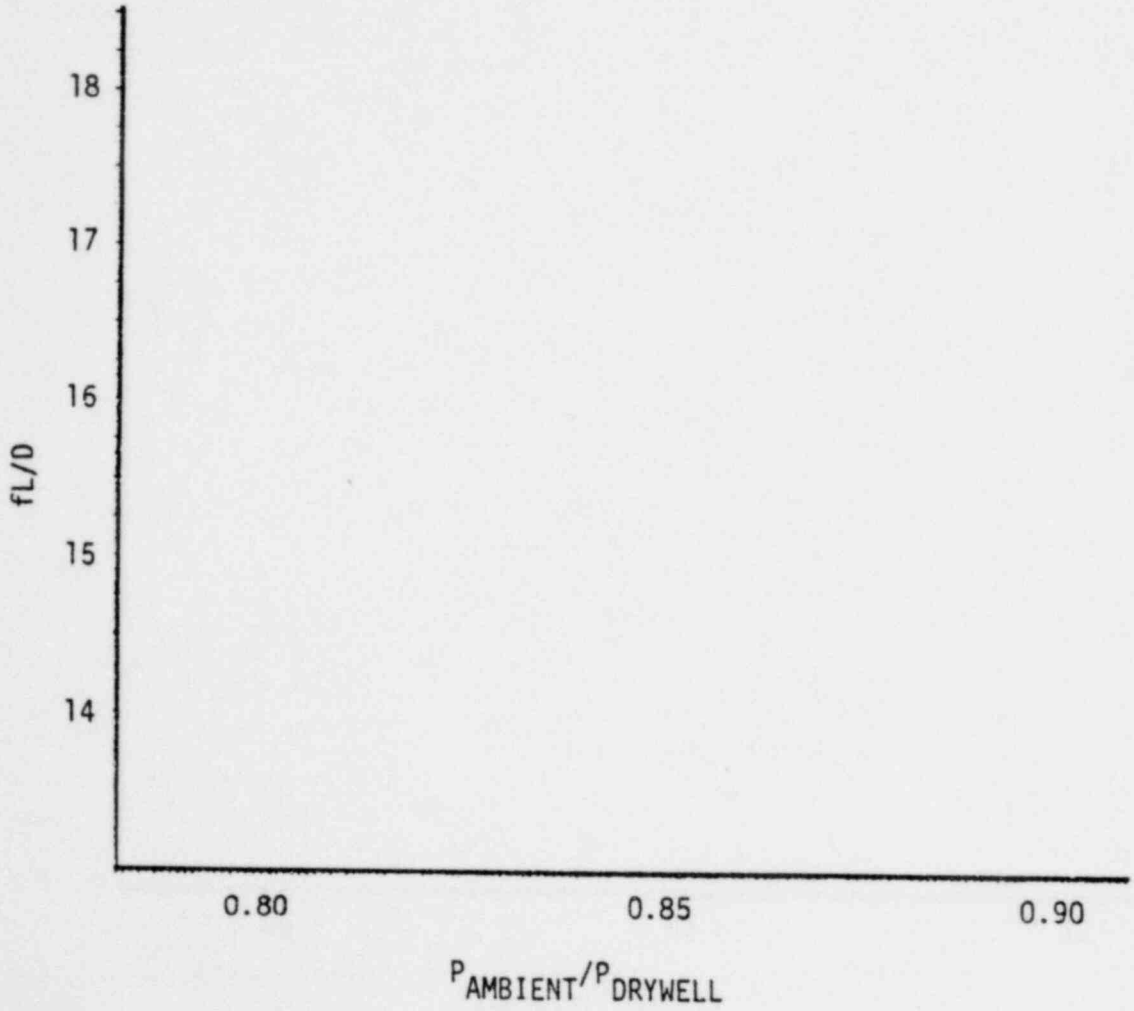

FIGURE G-30

VENT RESISTANCE (fL/D) DISTRIBUTION

HATCH 1 TESTS

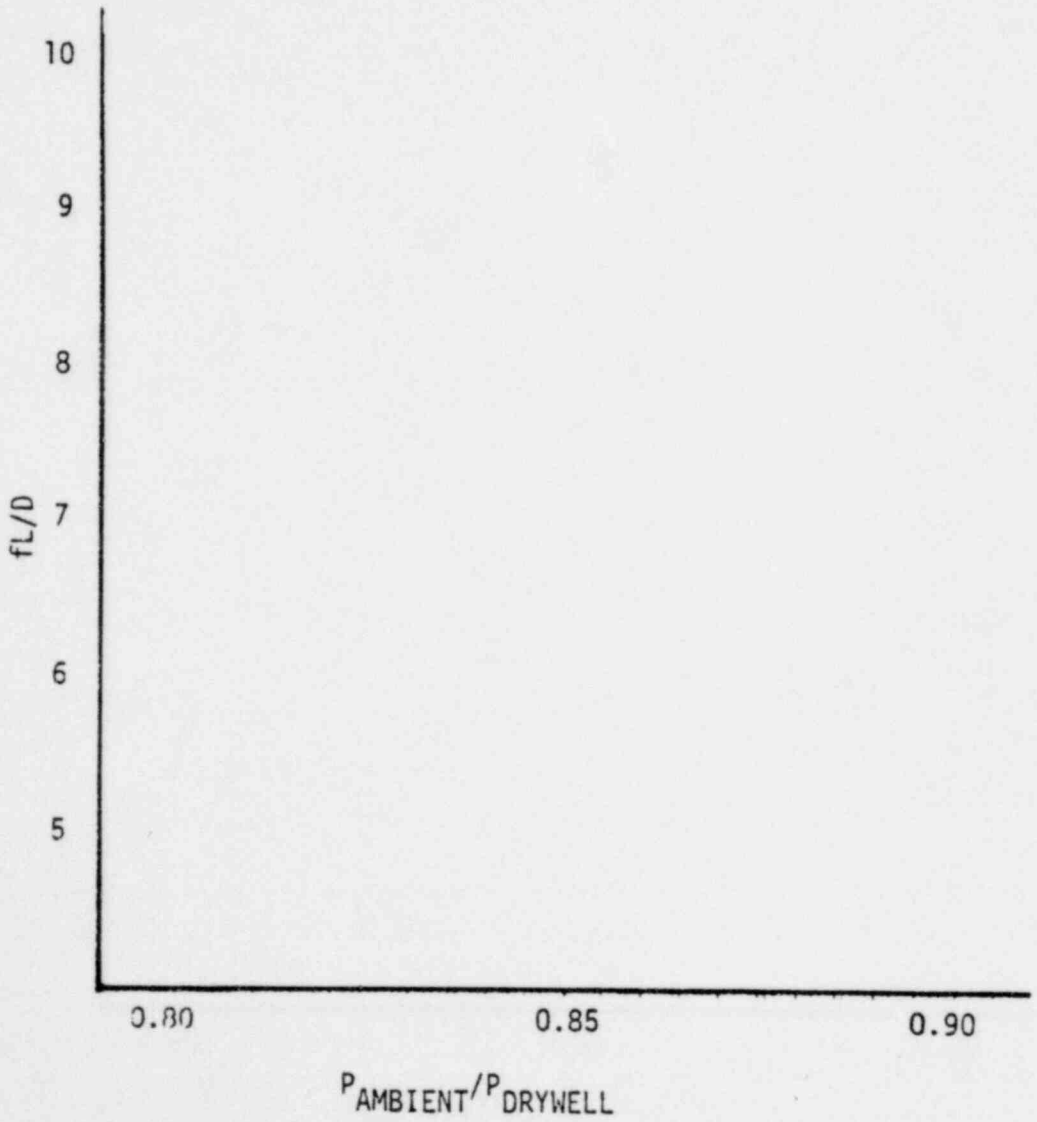

1351 227

FIGURE G-31

CALCULATED VENT RESISTANCE fL/D

VERMONT YANKEE TESTS

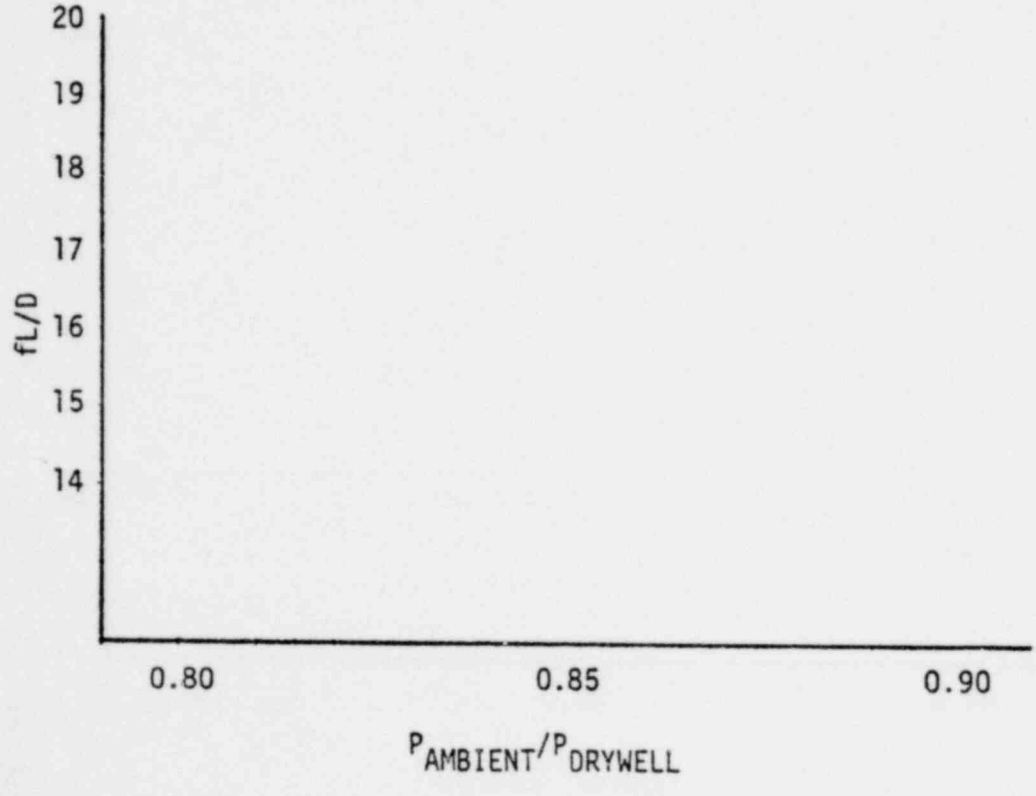

FIGURE G-32

VENT RESISTANCE (fL/D) DISTRIBUTION

VERMONT YANKEE TESTS

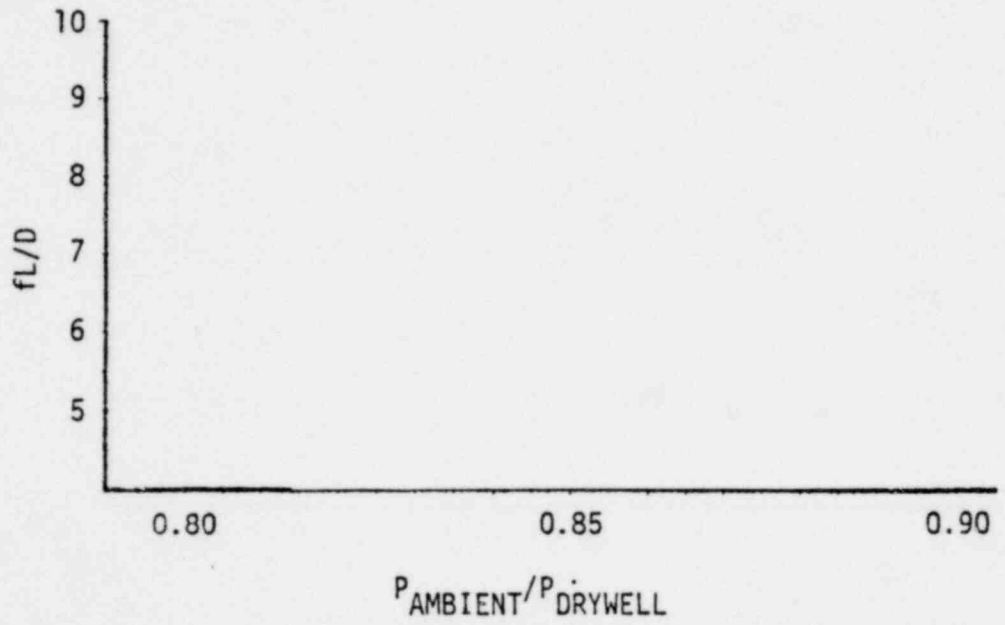

1351 229

FIGURE G-33

CALCULATED VENT RESISTANCE fL/D

FITZPATRICK TESTS

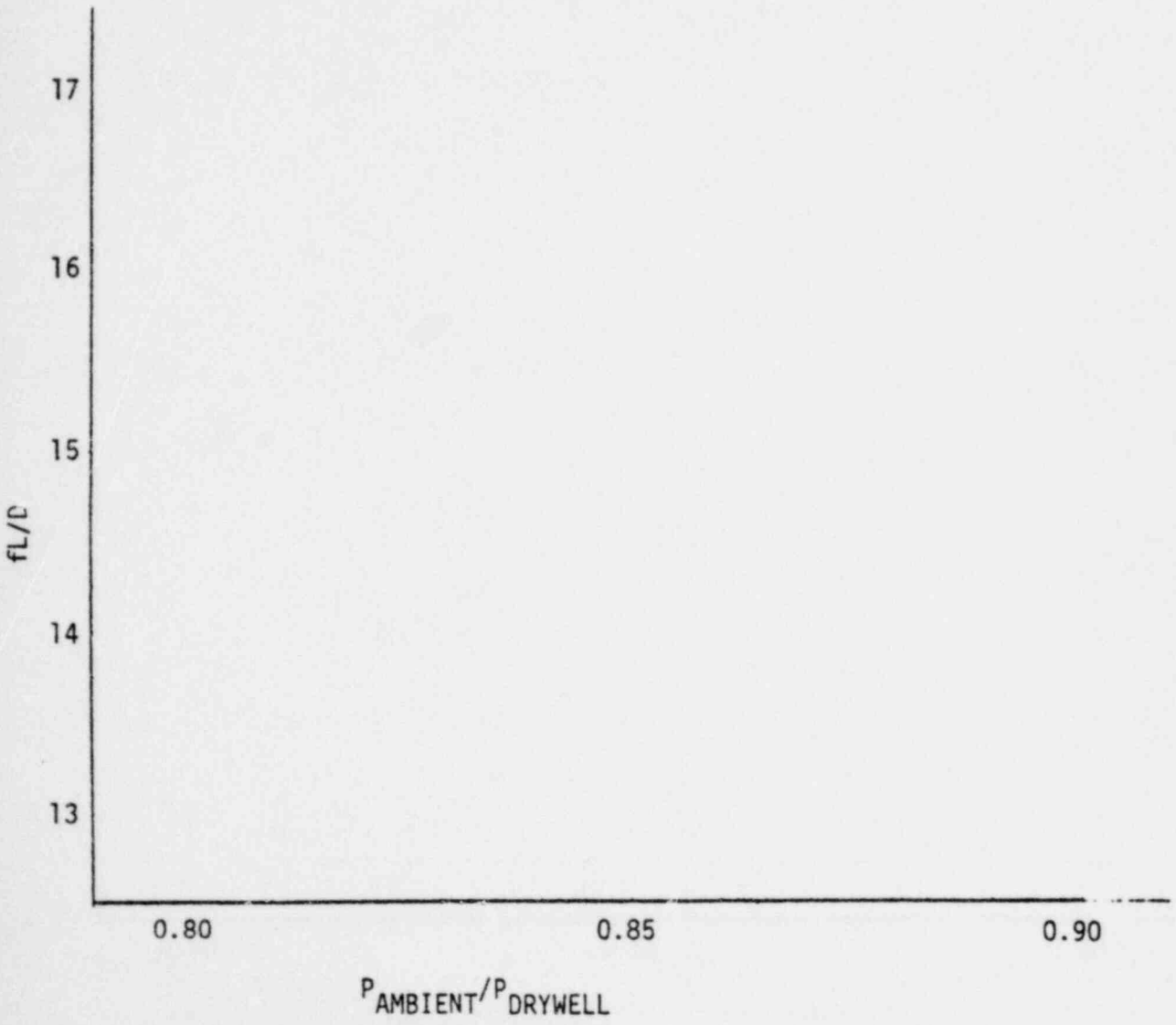

1351 230

FIGURE G-34

VENT RESISTANCE (fL/D) DISTRIBUTION

FITZPATRICK TESTS

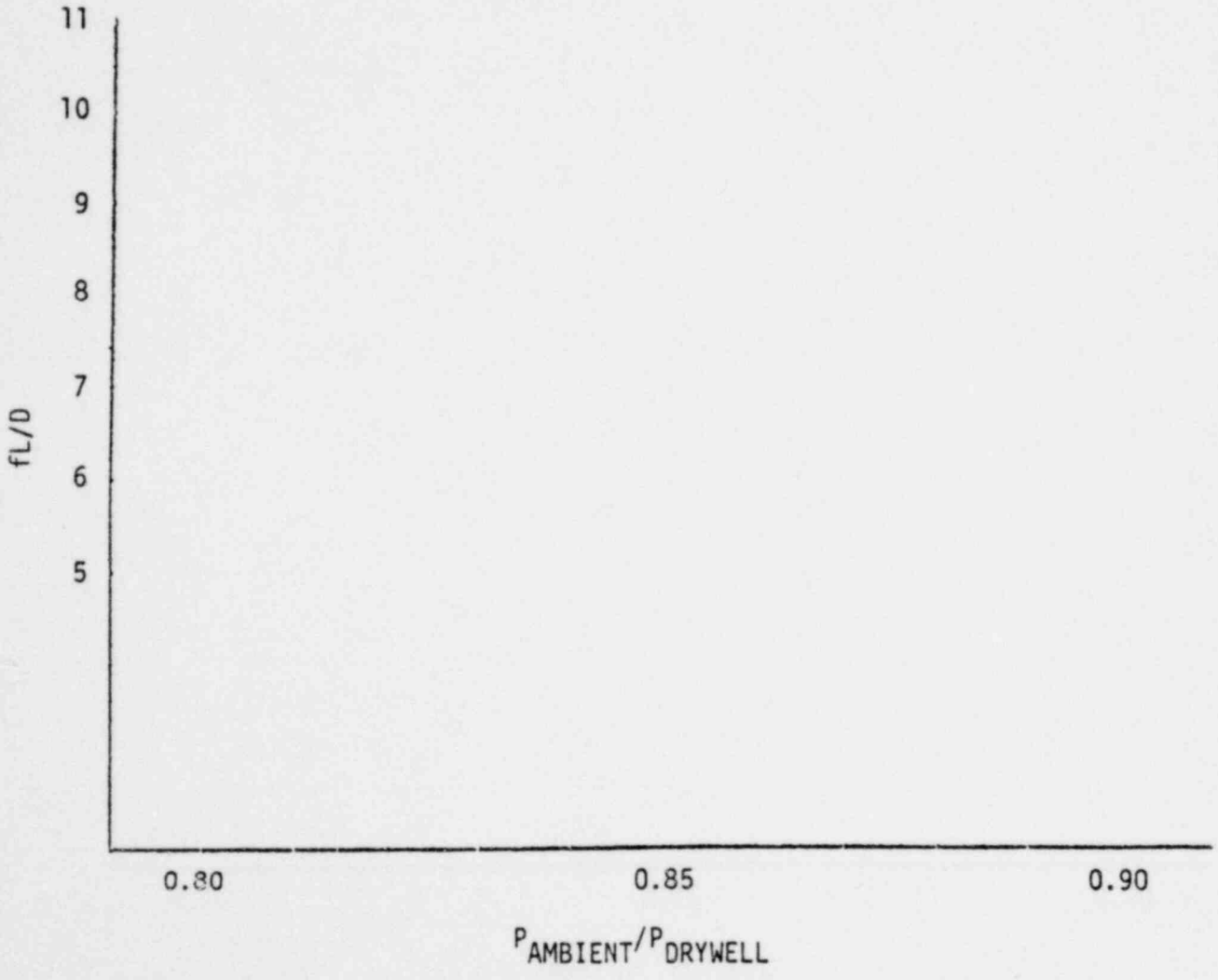

*40% to 60% of actual total fL/D

FIGURE G-35

CALCULATED VENT RESISTANCE fL/D

HOPE CREEK TESTS

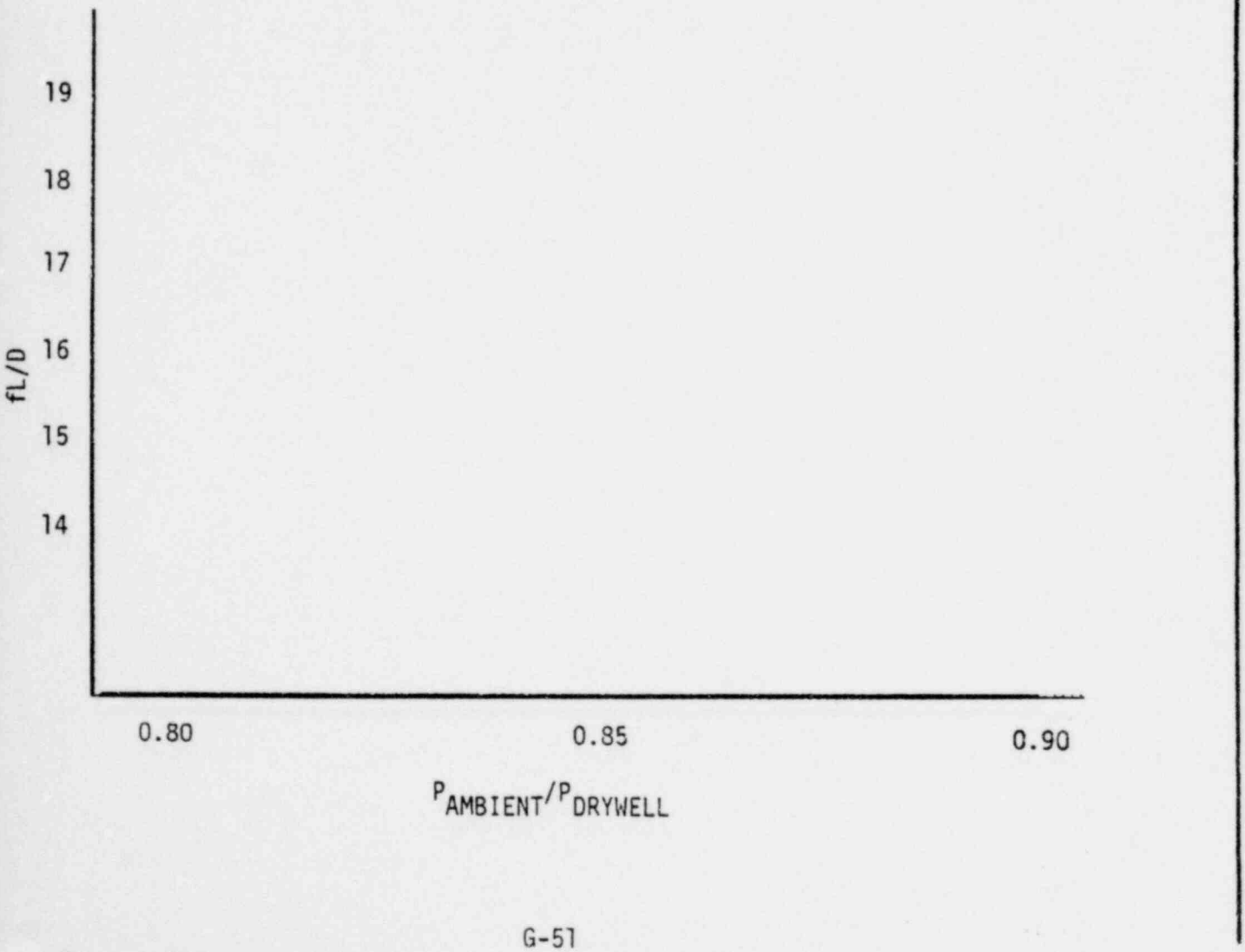

FIGURE G-36

VENT RESISTANCE (fL/D) DISTRIBUTION

HOPE CREEK TESTS

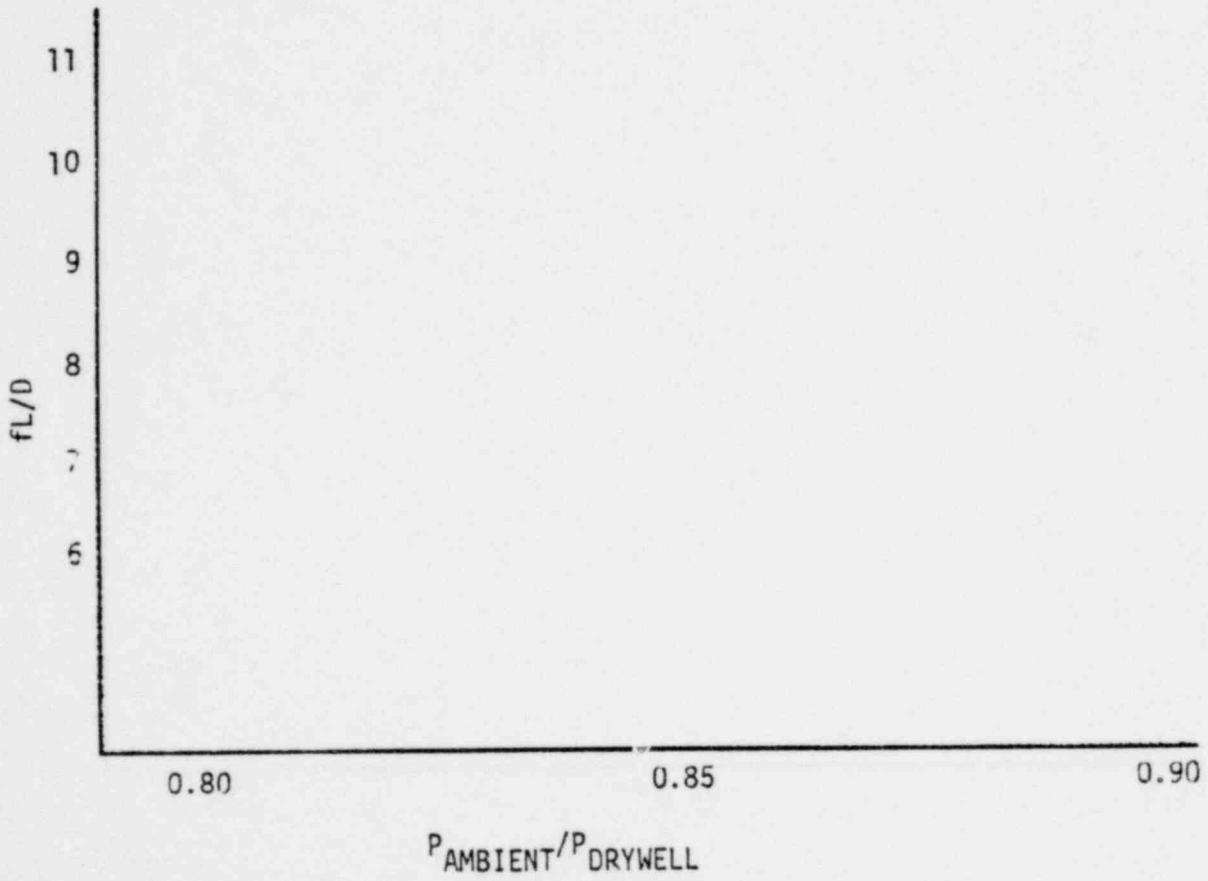

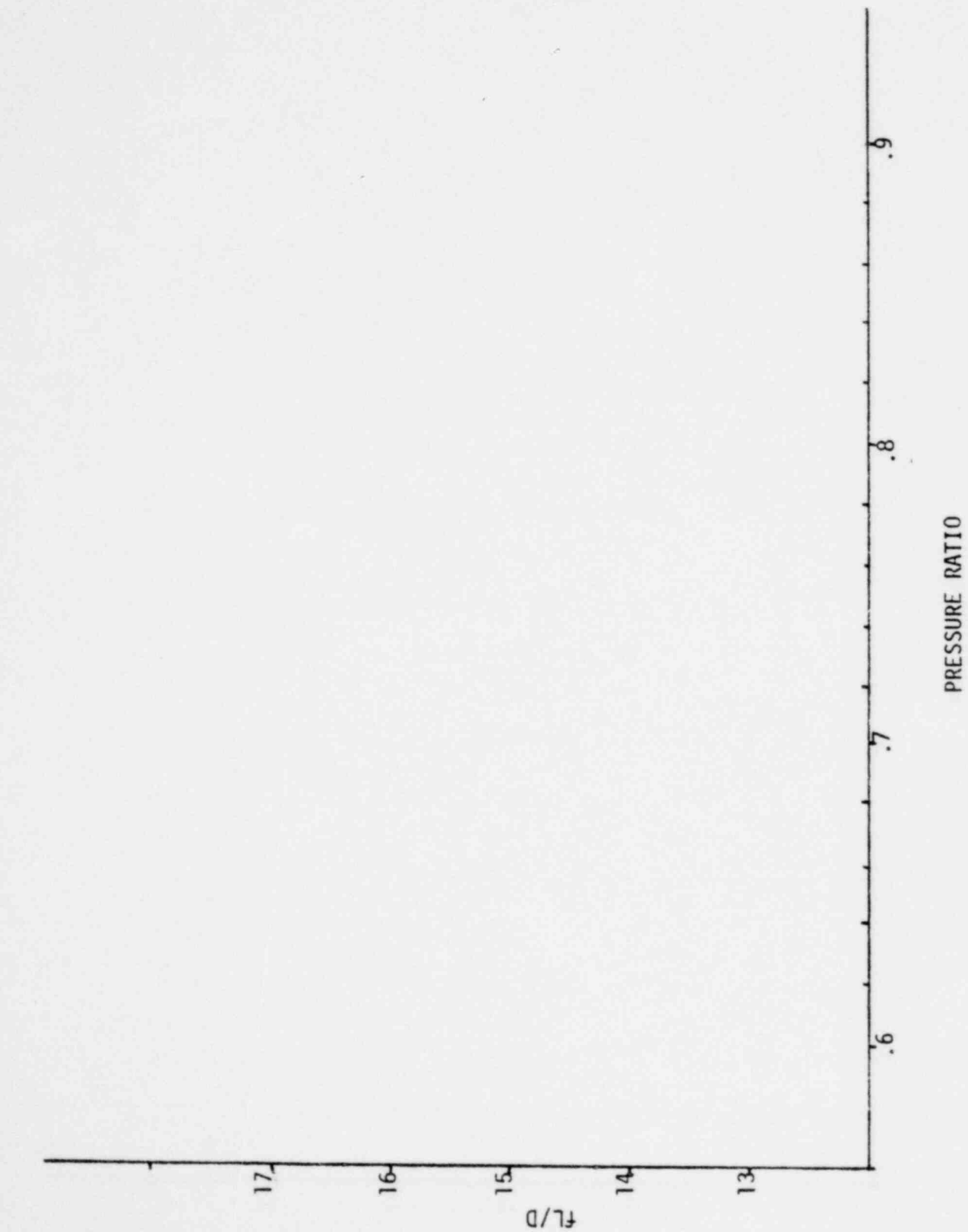

FIGURE G-38

BRUNSWICK 3 - AVERAGE RATE

DRYWELL MASS BALANCE - OPTION 2

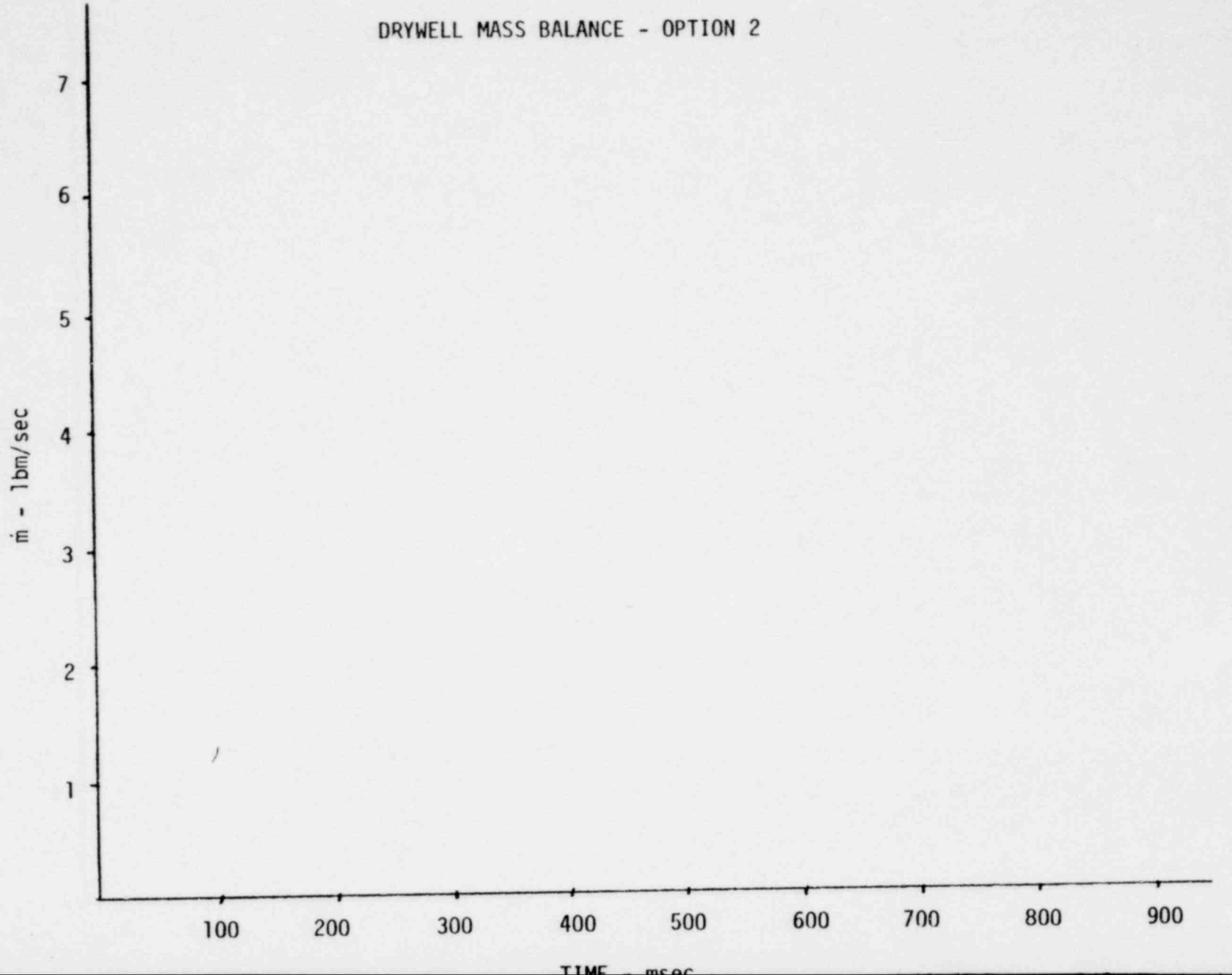

FIGURE G-39

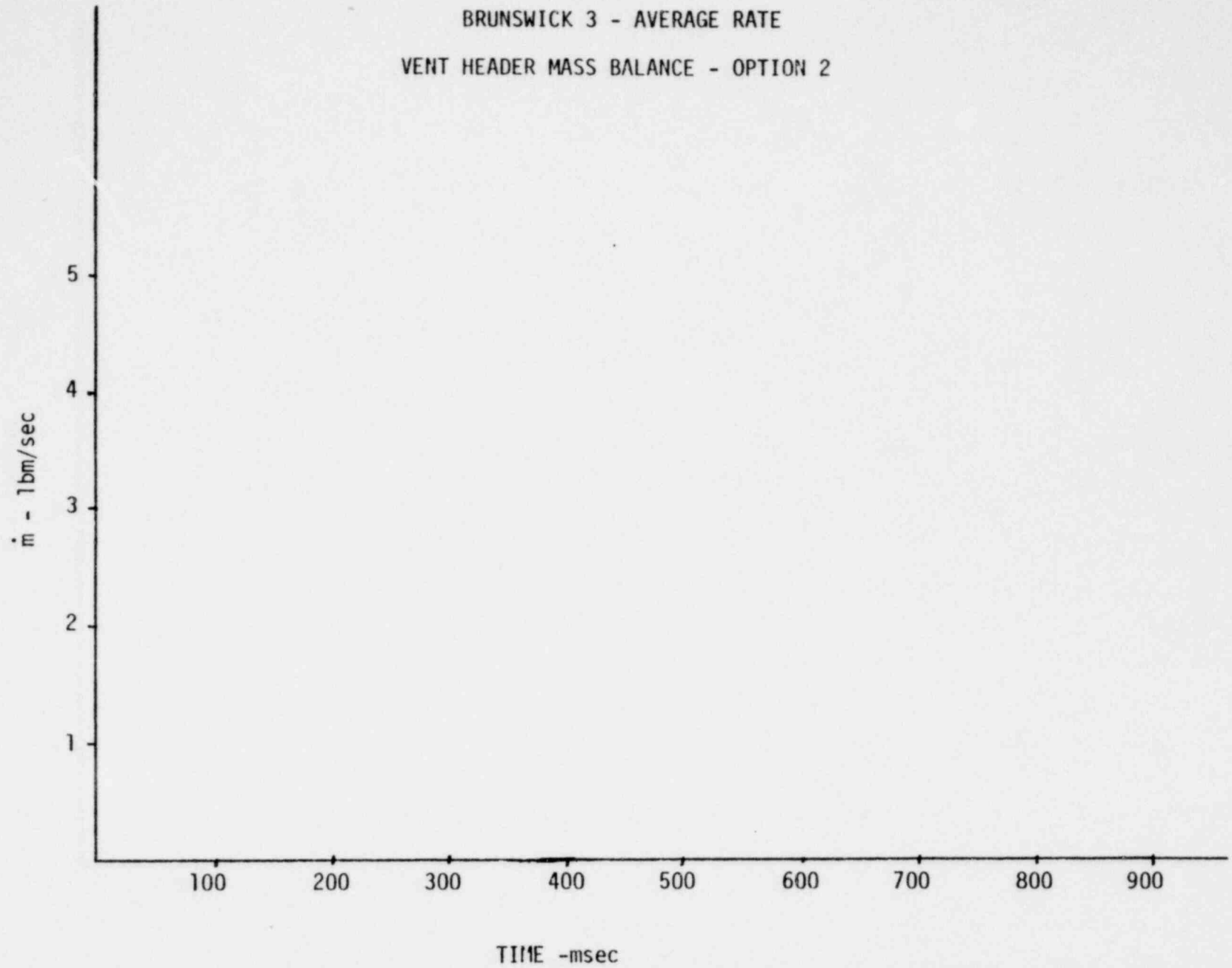

FIGURE G-40

BRUNSWICK 3 - AVERAGE RATE

DRYWELL MASS OUT - COMPARISON OF OPTION 1 - OPTION 2

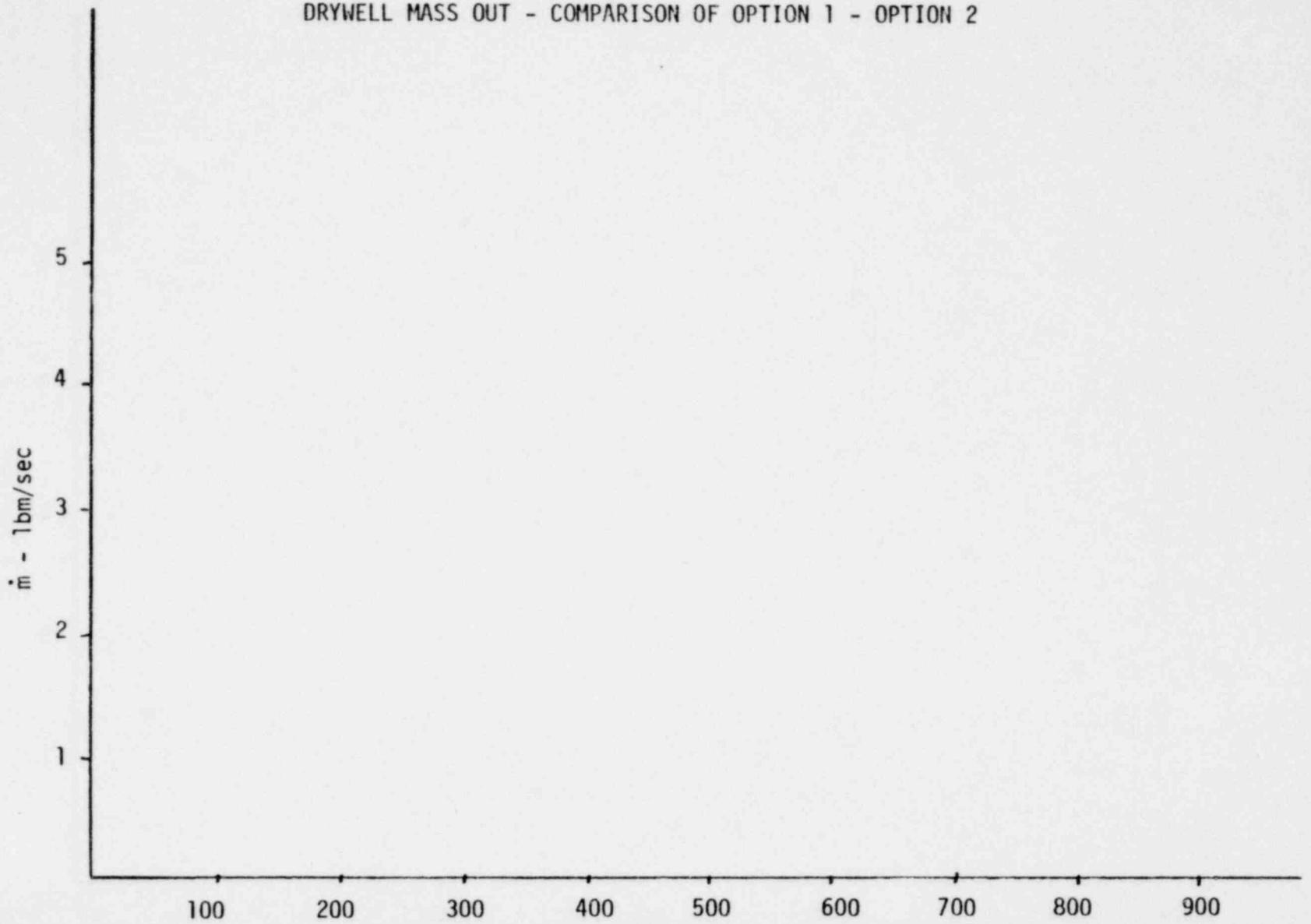

FIGURE G-41

DOWNCOMER AIR TEMPERATURE

Millstone Test 1

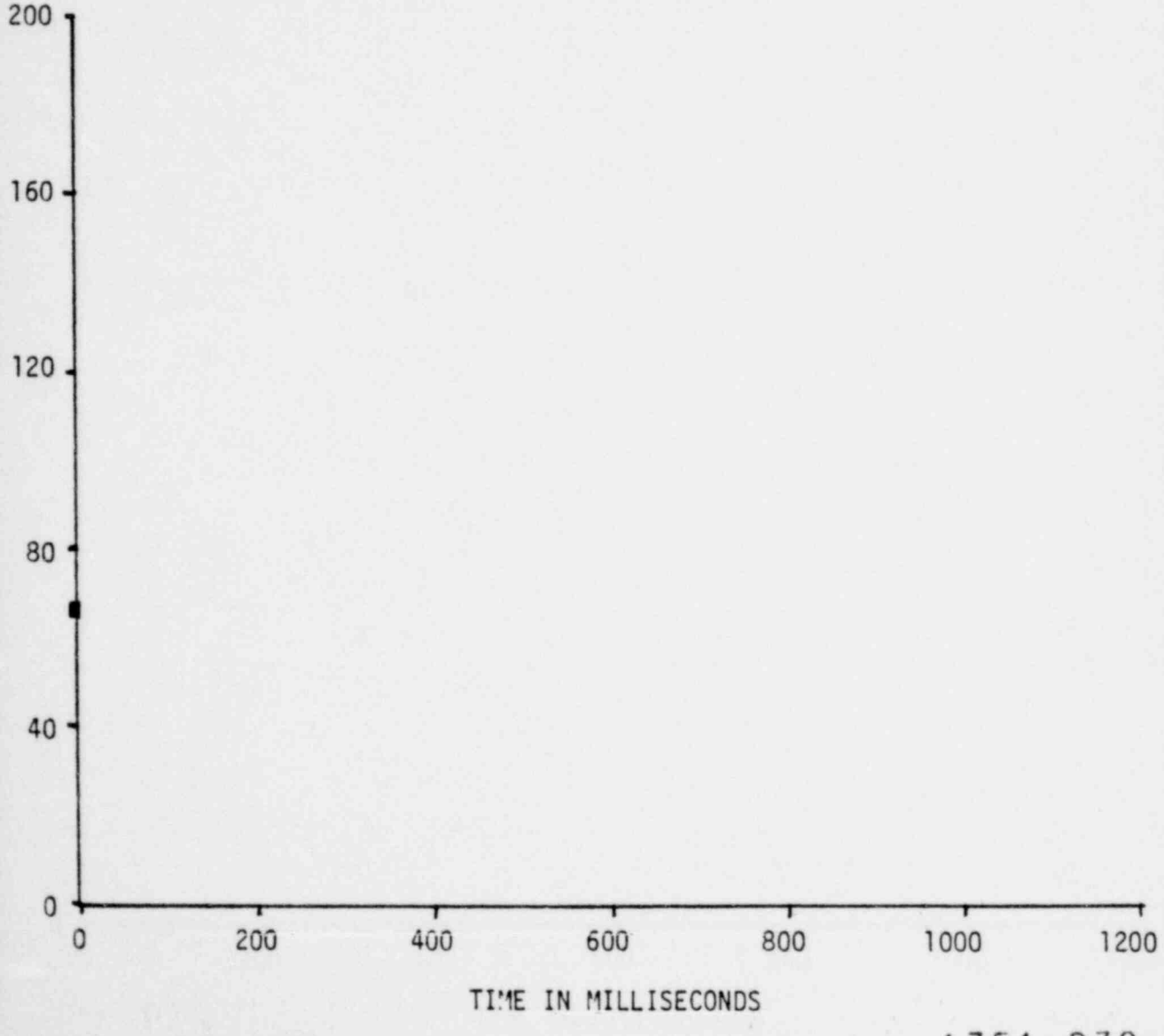

1351 238

FIGURE G-42

BRUNSWICK - DOWNCOMER fL/D FRACTION

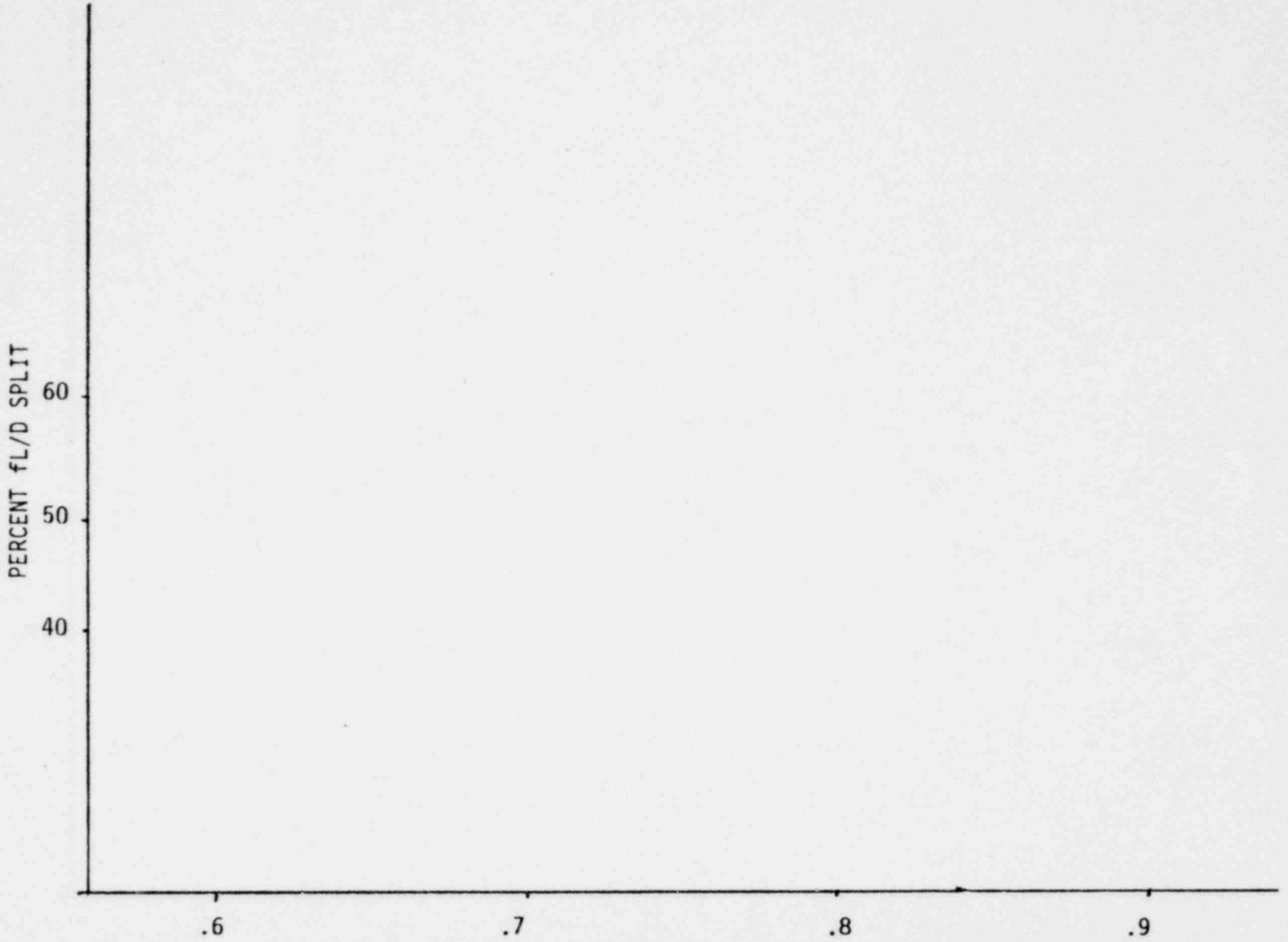

TABLE G-1

SUMMARY OF VENT RESISTANCE

Plant	Total fL/D			fL/D Split		
	Maximum Allowable	Actual	Actual/Maximum	Vent Orifice	Downcomer Orifice	Split*
Hatch 2	17.8	16.4	0.921	7.05	9.35	43/57
Monticello	16.04	14.5	0.904	7.25	7.25	50/50
Pilgrim	17.68	15.5	0.877	8.53	6.97	55/45
Fermi	19.32	17.2	0.890	8.6	8.6	50/50
Duane Arnold	13.38	12.6	0.942	6.43	6.17	51/49
Nine Mile Point	16.85	15.2	0.902	8.06	7.14	53/47
Brunswick	16.81	16.3	0.970	7.5	8.8	46/54
Cooper Station	17.76	17.4	0.980	7.48	9.92	43/57
Dresden	17.45	16.3	0.934	7.99	8.31	49/51
Browns Ferry	18.49	18.3	0.990	7.9	10.4	43/57
Peach Bottom	18.42	17.5	0.950	8.58	8.92	49/51
Millstone	16.05	14.6	0.910	8.61	5.99	59/41
Oyster Creek	19.88	18.8	0.946	10.2	8.6	54/46
Hatch 1	17.64	16.3	0.924	6.85	9.45	42/58
Vermont Yankee	16.04	14.5	0.904	7.4	7.1	51/49
Fitzpatrick	17.1	15.7	0.918	7.54	8.16	48/52
Hope Creek	18.94	17.2	0.908	9.46	7.74	55/45

$$\text{Split} = \left(\frac{\text{Vent Orifice fL/D}}{\text{Actual fL/D}}\ \%\right) \Big/ \left(\frac{\text{Downcomer Orifice fL/D}}{\text{Actual fL/D}}\ \%\right)$$

APPENDIX H

EVALUATION OF TORUS END WINDOW RELATED DOWNLOAD OSCILLATIONS

The use of only three torus window stiffening struts (four for Duane Arnold) for the Plant Unique Tests was overall a good choice to achieve window stiffening consistent with minimum pool interference. However many plants exhibited small oscillations in the downloads at the torus end window frequency. The amplitude of these oscillations was sensitive to the strut location. Three plants exhibited window related download oscillations of sufficient magnitude to warrant filtering. This appendix describes the role of window vibrations in QSTF download oscillations and describes the techniques used to remove these non-prototypical oscillations from the loads.

H.1 Selection of Window Strut Configuration

In the earlier 1/4-scale tests (Tasks 5.5.1 and 5.5.2-1) and 1/12-scale tests, the downforce exerted on the torus has been observed to be oscillatory in nature when no initial drywell/wetwell differential pressure (ΔP) was present. To better understand the cause of downforce oscillations, tests and analysis were conducted in Task 5.5.2 (Reference 3). The test results indicated that downforce oscillations are primarily the result of two effects: (1) fluid-structure interaction due to the window/frame vibration, and (2) the presence of air bubbles most probably on the submerged facility surfaces. When the above two effects were removed with 10 window/frame struts and surfactant addition into the pool, a relatively smooth downforce was obtained.

A downforce trace free of structural oscillations is prototypical for load definition and thus desirable for the plant unique load definition tests. A tradeoff was required between the number of struts and the potential for hydrodynamic interference. During this test series, except for Duane Arnold tests, a three strut design (Figure H-1) was used with one strut on the centerline near the elevation of the downcomer exit and two struts installed above the pool and above the bottom of the header. This design was previously used in Generic Sensitivity Pool Swell Tests, Task 5.5.3-1 (Reference 1) and proved to be a suitable configuration. For the single downcomer Duane Arnold tests, a four strut design (Figure H-2) was used with two struts in the pool near the elevation of the downcomer exit but far enough away from the exit to avoid bubble interference, and two struts installed above the pool and above the bottom of the header.

The results of Generic Sensitivity Pool Swell Tests showed no downforce oscillations (with a standard 3 strut pattern) at full ΔP but indicated a potential for oscillations at partial ΔP.

Evaluation of different torus freespace strut placements showed that download oscillations can be sensitive to this parameter. Tests for Hatch 2, Monticello and Pilgrim using the standard three strut placement all exhibited relatively smooth download traces. However, evaluation of a slightly narrower (19") upper strut placement for Fermi 2 (Figure H-3) caused a marked increase in download oscillations. A return to the standard strut placement reduced but did not eliminate the oscillations. The download trace still exhibited 100 Hz oscillations (Figure H-4) which later analysis showed was the first mode frequency of the window. These test results indicated that both the placement of the torus end window struts which control the stiffness of the window and plant unique test parameters such as the frequency content of the initial download affect the degree of download oscillation observed in the test data.

H.2 Evaluation of Plant Unique Download Oscillations

As the Plant Unique Tests progressed the download oscillations observed for several plants were of a sufficient magnitude to warrant further investigation. In an effort to determine why downforce oscillations appeared in some of the plant tests and not in others, an examination was made of the physical dimensions of the test facilities for all plants (see Figure H-5). The only dimensions which appeared to vary significantly for the tests which produced oscillations were the "Header Centerline to Downcomer Discharge" length (abnormally low for Fermi, Peach Bottom, and Millstone) and the "Header Centerline to Torus Centerline" length (abnormally high for Dresden and Browns Ferry). The effect of both types of variance was to place the downcomer exit at a higher elevation than was normal for the other tests. In order to examine the variation of exit position more closely, the "Torus Centerline to Discharge" length was computed (see Figure H-6). Also examined at this time were the hydrodynamic parameters of "Drywell Pressurization Rate" and "Submergence". No direct correlation between pressurization rate and downforce oscillations was evident. Although low submergence generally correlated with oscillations, the range of variation was quite

small. In addition, the use of submergence as the principal cause of oscillations would result in predicting downforce oscillations in Duane Arnold, Oyster Creek, Hatch 1, and (possibly) Brunswick data. None of those plants exhibited the oscillation phenomenon.

In addition, the three plant configurations demonstrating the most pronounced oscillations (Dresden, Browns Ferry, and Peach Bottom) all had the same test facility width. However, Nine Mile Point was tested with the same width without significant oscillations. Thus, torus width (and its effect on facility resonant frequency) is only a partial factor in downforce oscillations.

A definite correlation seems to be evident between the "Torus Centerline to Discharge" length and downforce oscillations. Since the window is most susceptible to initiation of the first bending mode at its center, more window vibration would be expected as the horizontal bubble force is directed nearer to the window centerline. This criterion would predict oscillatory problems with Hope Creek, and possibly, Fitzpatrick downforce data. Some oscilation was present in the Fitzpatrick downforce trace, but it was not severe. The Hope Creek data indicated no unusual degree of oscillation. But since the Hope Creek tests were performed with a larger than usual test facility width and with a low pressurization rate, the bubble force against the window would not be expected to be as large as for a test with average facility width and pressurization rate.

It would therefore appear that downcomer exit height within the torus is the primary cause of window vibration induced downforce oscillation. Extreme variations in test facility width and pressurizaton rate appear to be capable of mitigating (and possibly compounding) the oscillation which would be expected from downcomer exit location.

H.3 Downforce Smoothing Techniques

When it was apparent that the source of the downforce oscillations was window vibration, two different methods of data treatment were examined in an attempt to eliminate the oscillations. The first method was to apply a correction to the load data based upon window acceleration; the second method was the use of a digital filter.

H.3.1 Window Acceleration Correction

Let the window motion be given by

$$X = \frac{W}{2} + C_1 \sin \omega t, \qquad \text{Equation (1)}$$

where

X = window displacement from vertical (outward is positive)
W = mean torus width
C_1 = constant
ω = frequency
t = time

When $X = \frac{W}{2} - C_1$, that is when $(\omega t) = \frac{3\Pi}{2}, \frac{7\Pi}{2}$, etc.,

the window is at its innermost position and the torus' water height has been displaced to its maximum height. Let the water motion be given by

$$h = h_m - C_2 \sin \omega t \qquad \text{Equation (2)}$$

Where

h = displacement of water surface (upward is positive)
h_m = mean height of water surface
C_2 = constant
ω = frequency
t = time

1351 245

Then when $h = h_m + C_2$, that is when $(\omega t) = \frac{3\Pi}{2}, \frac{7\Pi}{2}$, etc., the water height is at its maximum. At these conditions (window at its inner most position and water height at its maximum),

$$a_{window} = \frac{d^2x}{dt^2} = -C_1 W^2 \sin \omega t \qquad \text{Equation (3)}$$

and $$a_{water} = \frac{d^2h}{dt^2} = C_2 W^2 \sin \omega t \qquad \text{Equation (4)}$$

where

a_{window} = acceleration of window
a_{water} = acceleration of water

When $\frac{d^2h}{dt^2}$ is positive (water mass is accelerating upward), a negative force will be sensed by the torus load cell and reflected in the pressure integral.

$$F_R = -C_3 W^2 \sin \omega t \qquad \text{Equation (5)}$$

Where

F_R = load cell force due to oscillating water motion
C_3 = constant
W = mean torus width
ω = frequency
t = time

From Equations (3) and (5) it can be seen that window acceleration (positive outward) and torus load oscillations (positive upward) are in phase.

The height of the pool's center of gravity at any moment is proportional to the window displacement. The vertical acceleration of

the pool's center of gravity (the ultimate cause of downforce oscillations) is, therefore, proportional to window acceleration.

$$a_{water} = C_4 \, a_{window}$$

The oscillating downforce due to water acceleration is then proportional to the window acceleration.

$$F_R = ma_{water} = m_{eff} \, a_{window} \qquad \text{Equation (6)}$$

where

F_R = load cell force due to oscillating water motion
m = mass of water displaced
a_{water} = acceleration of water
m_{eff} = an "effective" mass of water
a_{window} = acceleration of window

In order to cancel out the oscillating portion of the total load cell force, the force due to window acceleration must be subtracted from it.

$$F = F_T - F_R = F_T - m_{eff} \, a_{window} \qquad \text{Equation (7)}$$

where

F = true downforce
F_T = total downforce, including oscillation

The "effective" mass, m_{eff}, is an artificial quantity which depends upon location of the reference point of window acceleration, pool geometry, window vibration pattern and bubble-window interaction. Although this proportionality constant (m_{eff}) could, in principle, be calculated analytically, it was found easier to determine it empirically by plotting the quantity $F = F_T - m_{eff} \, a_{window}$ for

several values of m_{eff}. This procedure was applied to the Dresden "burp" test data. The uncorrected load trace is quite oscillatory (Figure H-7). Figures H-8 through H-10 show the results of correcting this measured force by using m_{eff} = 1500, 2000, and 2500 lb_m. A mass of 2500 lb_m appeared to give a plot which represented the true torus force more accurately than the unsmoothed data.

Although selection of an effective mass is empirical, this method has a sound physical basis. The fact that window oscillations and downforce oscillations are in phase implies that the windows are driving the pool.

Although this method takes a direct approach for removing the downforce oscillations, it could not be used for the majority of tests, due to the lack of window accelerometer data. In many cases, the window acceleration data was available for only the "burp" test of each plant.

H.3.2 Power Spectral Density Analysis and Data Filtering

Fourier showed that any periodic motion, however complicated, can be reduced to an equation which sums the separate sinusoidal components. The equation, Fourier's Series, may be written

$$y = a \sin 2\Pi nt + b \cos 2\Pi nt + c \sin 4\Pi nt + d \cos 4\Pi nt + e \sin 6\Pi nt + f \cos 6\Pi nt + \ldots$$

in which y is the displacement of the vibration and t is the time.

The power of a vibrating system (the rate of doing work) is proportional to the square of the amplitude of the vibration. But, at any frequency, the mean square value of the complex wave, F(t), is simply the sum of the mean square values of each component present

at that frequency (from Fourier's analysis). The result is a discrete frequency spectrum, as shown below.

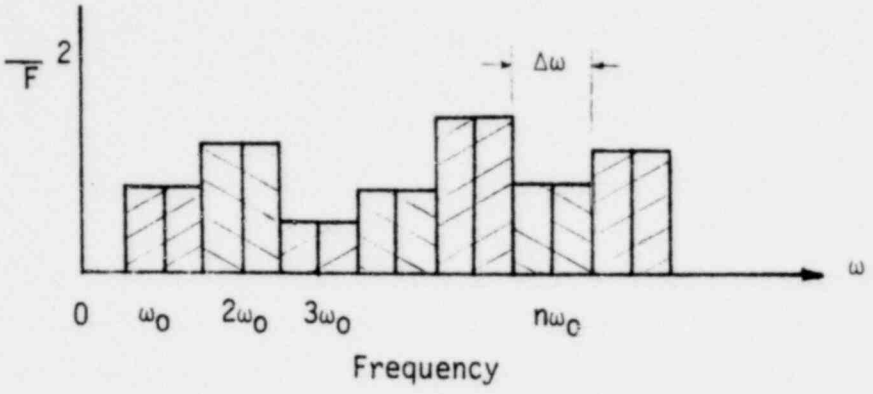

The density of the mean square value in the interval $\Delta\omega$ at the frequency $n\omega_o$ is represented by $S(n\omega_o)$,

where $S(n\,\omega_o) = \frac{\bar{F}^2}{\Delta\omega}$

or $\Delta\omega \;\; S(n\,\omega_o) = \bar{F}^2$

The Power Spectral Density (PSD) is the limiting mean square value (of acceleration, velocity, displacement, stress, or other random variable) per unit bandwidth. That is, PSD is the limit of the mean-square value in a given rectangluar bandwidth as the bandwidth approaches zero. Power Spectral Density is a generic term used regardless of the physical quantity represented by F(t).

A plot of the PSD indicates the variation of vibration magnitude with frequency. The PSD of a random time function may be determined by feeding the function F(t) into a spectrum analyzer that transmits only those frequency components within the bandpass of the analyzer, $\bar{\omega} \pm 1/2(\Delta\omega)$. The average value of F within the bandpass is then computed and squared, resulting in $\bar{F}^2$. The mean Power Spectral Density over the bandpass at $\bar{\omega}$, $S(\bar{\omega})$, is determined by dividing the $\bar{F}^2$ by $\Delta\omega$. The data is then fed back through the analyzer for

another PSD determination at a slightly different frequency. To obtain the complete spectrum, the process is repeated at enough frequencies to give a plot of PSD magnitude versus frequency.

If vibration with a broad spectral density is applied to a lightly damped system, the PSD response of the system will peak at the system's resonant frequency. PSD plots of the test facility window accelerometer and torus load data should, therefore, show peaks at the resonance frequency of the window. The window resonance frequency was independently determined in earlier testing (Reference 3). Figure H-11 shows the PSD of the window accelerometer for the Dresden "burp" test and Figure H-12 shows the PSD of the load data from the same test. Both plots show peaks corresponding to window resonance in the frequency range of 65 to 95 hz. Based on these spectral analyses, a 65 to 95 Hz notch filter was applied to the digital load data.

Filtering is a method of data-smoothing where the data is first reduced to its Fourier equational form. The notch filter is then applied by setting certain of the Fourier coefficients equal to zero and performing the inverse Fourier transform on the remaining data. The resulting filtered data (Figure H-13) is considerably smoother than the unfiltered trace. An overlay of the filtered and unfiltered data (Figure H-14) shows that the general character of the trace has been maintained, while the downforce oscillations have been removed. Furthermore, an overlay of the filtered data on the accelerometer-corrected data (Figure H-15) indicates good agreement between the two downforce smoothing methods.

H.3.3 Finite Element Analysis

A dynamic structural analysis of the plexiglas window was performed in an effort to understand the nature of the oscillations. The analysis included the three stiffening struts used during actual

testing and calculated relative window displacement for the first and second modes. The results (Figure H-16) show that the first mode displacements at 95.7 Hz are in phase over a large part of the window. This "drum" mode is quite effective in displacing water and is the primary source of download oscillations.

The second mode (at 133.5 Hz) allows the submerged part of the window to rock about an axis through the position of the lower strut. This out-of-phase motion results in little vertical water movement and, consequently, is ineffective in producing load oscillations.

That these modes are indeed present can be seen by examining the output of an accelerometer placed on the window during a test. The accelerometer was located near the center of the lower left quadrant of the window and its output is shown in Figure H-17. A power spectral density (PSD) analysis of that data is shown in Figure H-17.

A significant amount of energy is seen to be located under the two peaks centered near 95 and 120 Hz. These, then, are the normal window modes. Further, comparison of 95 Hz window accelerometer data to downforce oscillations measured during a typical test show the two to be in phase thus implying a coupling between downforce oscillations and window movement.

H.4 Specific Downforce Smoothing for Each Plant

The methods described in the previous section were applied to the torus load data for Dresden, Browns Ferry, and Peach Bottom to remove window related downforce oscillatons. The procedure for each test was as follows:

1) Perform a PSD of the window accelerometer data and load data on the Pre-test (Burp) shot.

2) Determine window frequency from (1) and filter load data (Burp) accordingly.
3) Compare filtered data of (2) to a load trace corrected with window accelerometer (m_{eff} optimized).
4) Perform PSD of load data from each test.
5) Determine window frequencies.
6) Filter test data accordingly.

Figures H-18 to H-32 document the filtered downforce traces for Dresden, Browns Ferry, and Peach Bottom.

H.5 Conclusions

1) Most of the downforce oscillations in the burp shots for Dresden, Browns Ferry, and Peach Bottom are in a narrow frequency range clearly evident in the window accelerometer and can be removed by either window acceleration correction or by notch filtering these frequencies.

2) The oscillation frequency seems to increase from the burp to the first or second tests and then stabilize. This stiffening may be due to the removal of residual trapped air (which is one of the reasons for the burp test).

3) Although window accelerometers were not added to the regular tests until the last six plant tests, there is no reason to doubt that the window frequency would not also increase as indicated in (2) above.

4) Data from the last six plant tests indicates that strong torus downforce oscillations are due to the first window mode and that second mode oscillations tend to cancel.

5) The agreement of filtered and corrected loads provide high confidence in the appropriateness of the filtered loads.

6) The filtered data often leaves a first oscillation (see Figures H-18 and H-19) which is at a lower frequency and does not appear to be related to window acceleration.

FIGURE H-1 THREE STRUT PLACEMENT

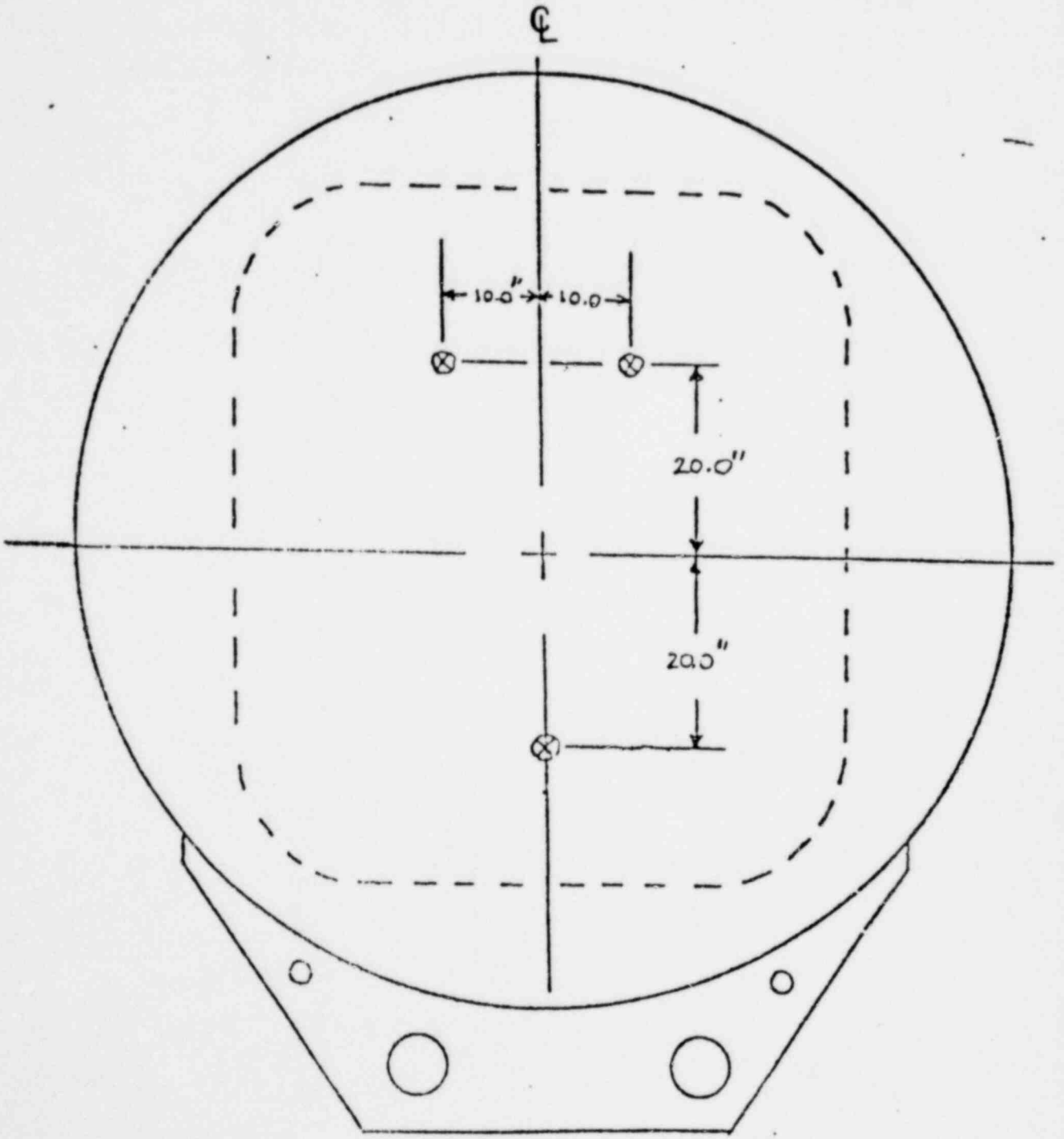

FIGURE H-2 FOUR STRUT PLACEMENT FOR DUANE ARNOLD TESTS

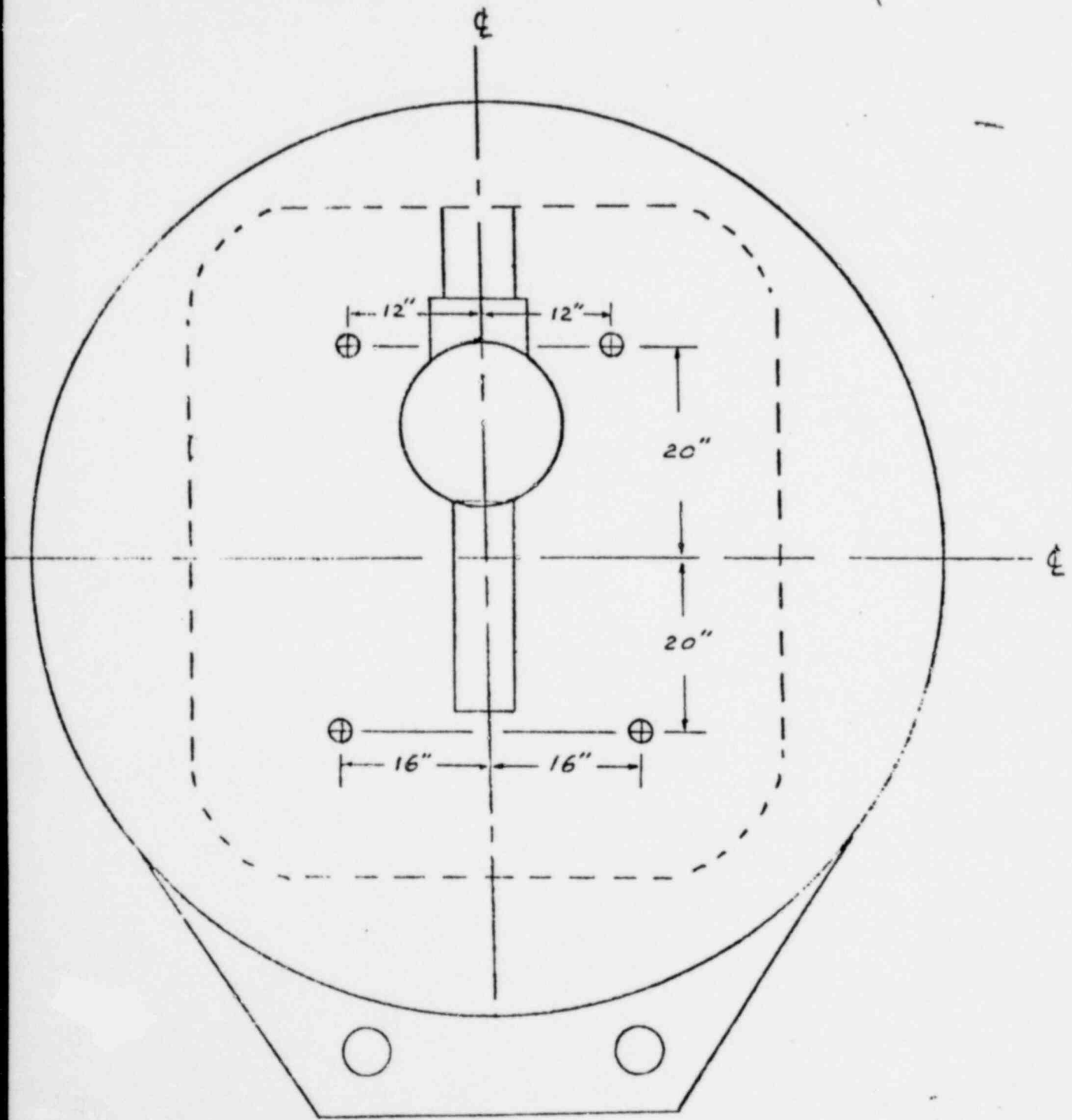

FIGURE H-3

STANDARD AND NARROW UPPER STRUT PLACEMENTS

FOR FERMI 2 TESTS

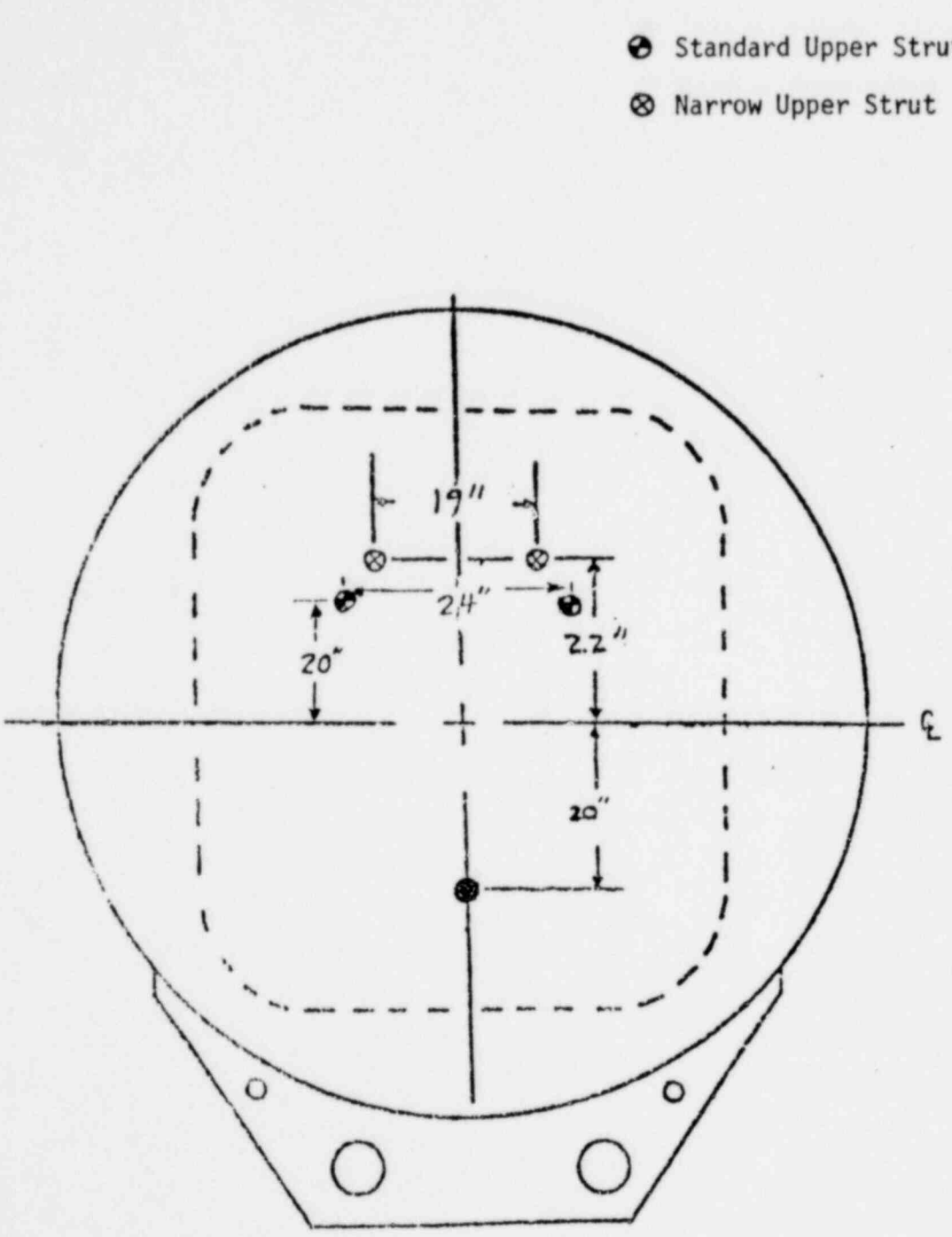

1351 256

FIGURE H-4

NET TORUS FORCE FROM PRESSURE INTEGRAL, CORRECTED FOR WATER INERTIA

Task 5.5.3-2 Fermi 2 Test 3

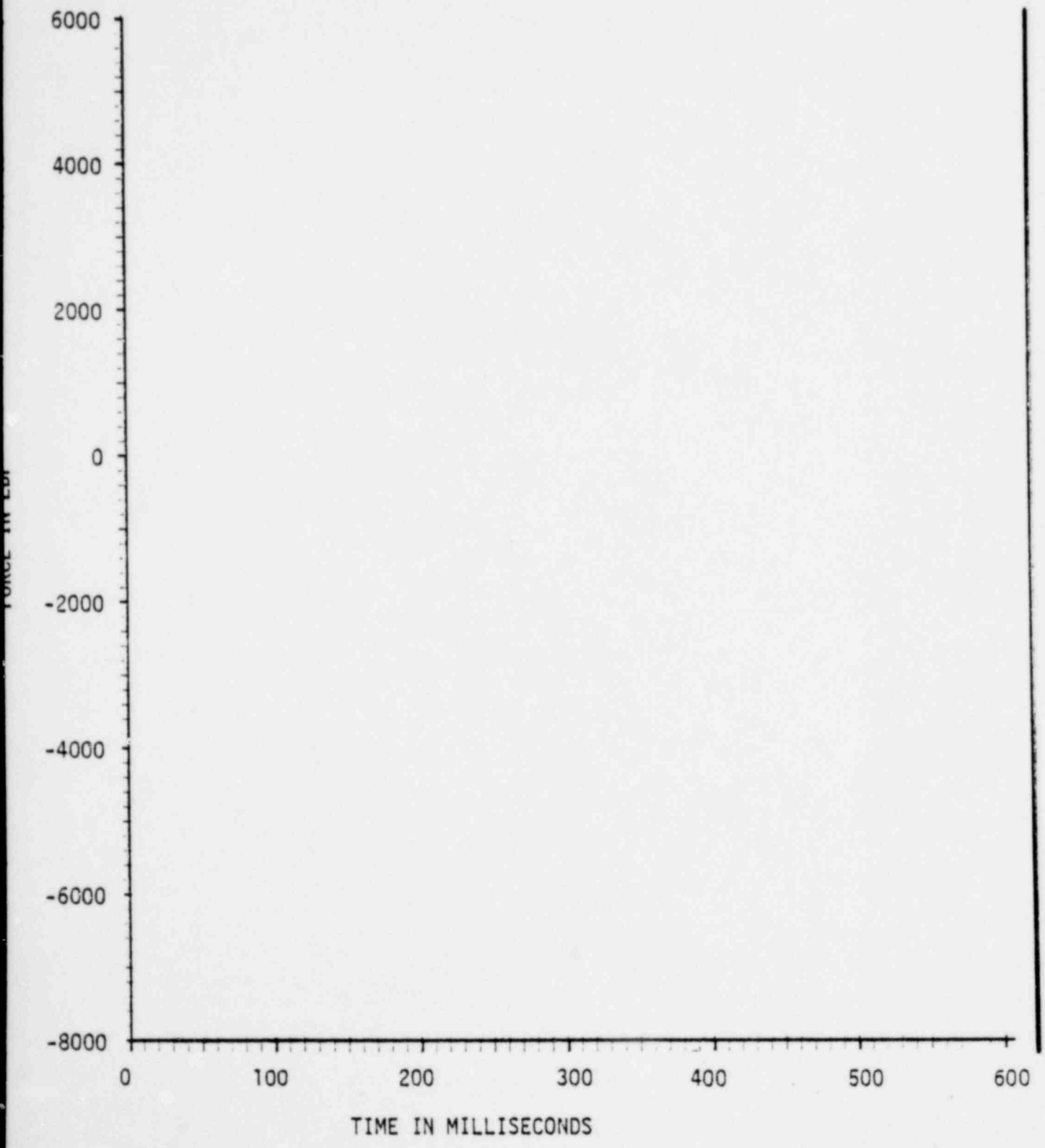

1351 257

FIGURE H-5

PLOT OF TEST FACILITY DIMENSIONS VS. PLANTS

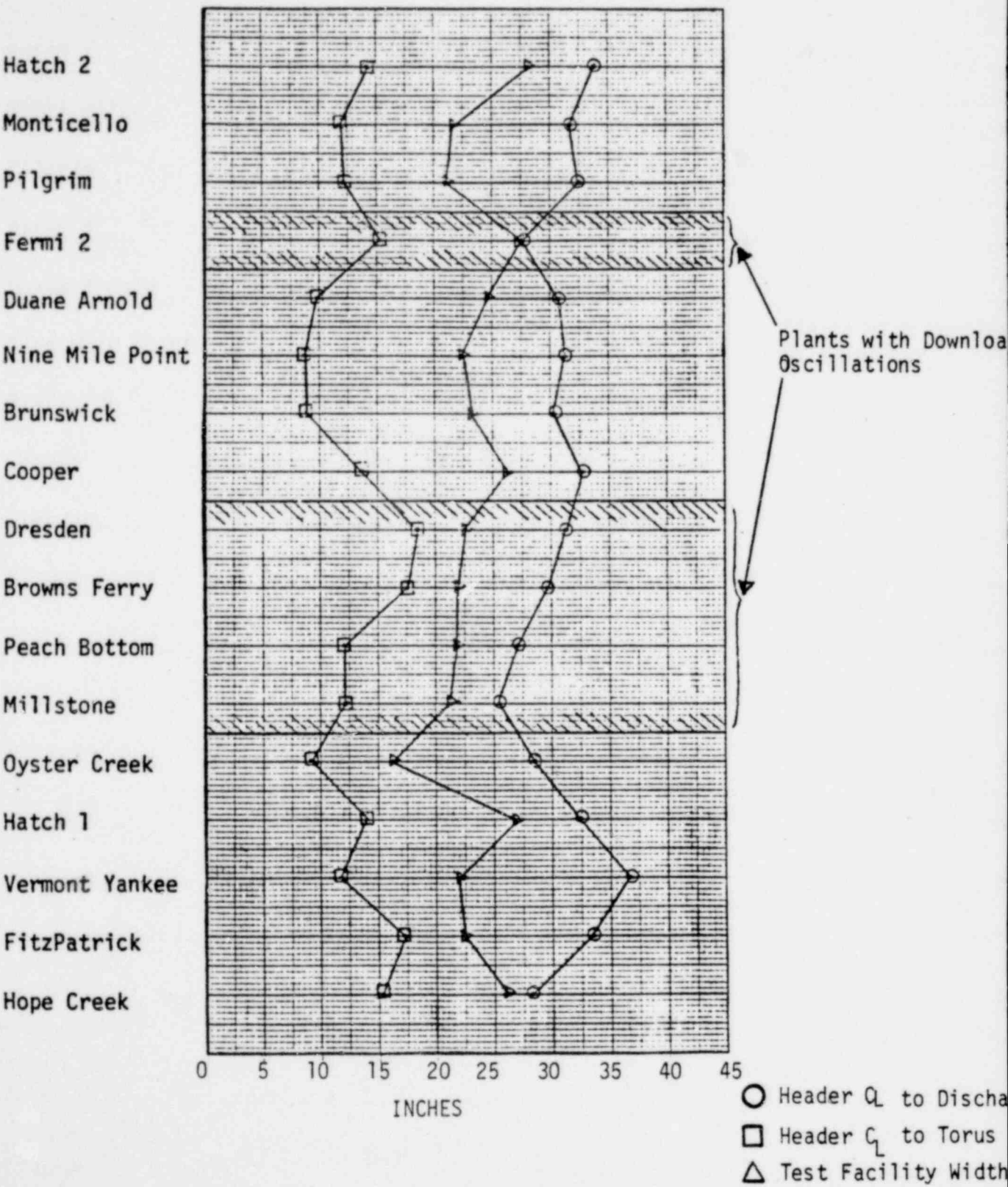

1351 258

FIGURE H-6

PLOT OF TEST FACILITY PARAMETER VS. PLANTS

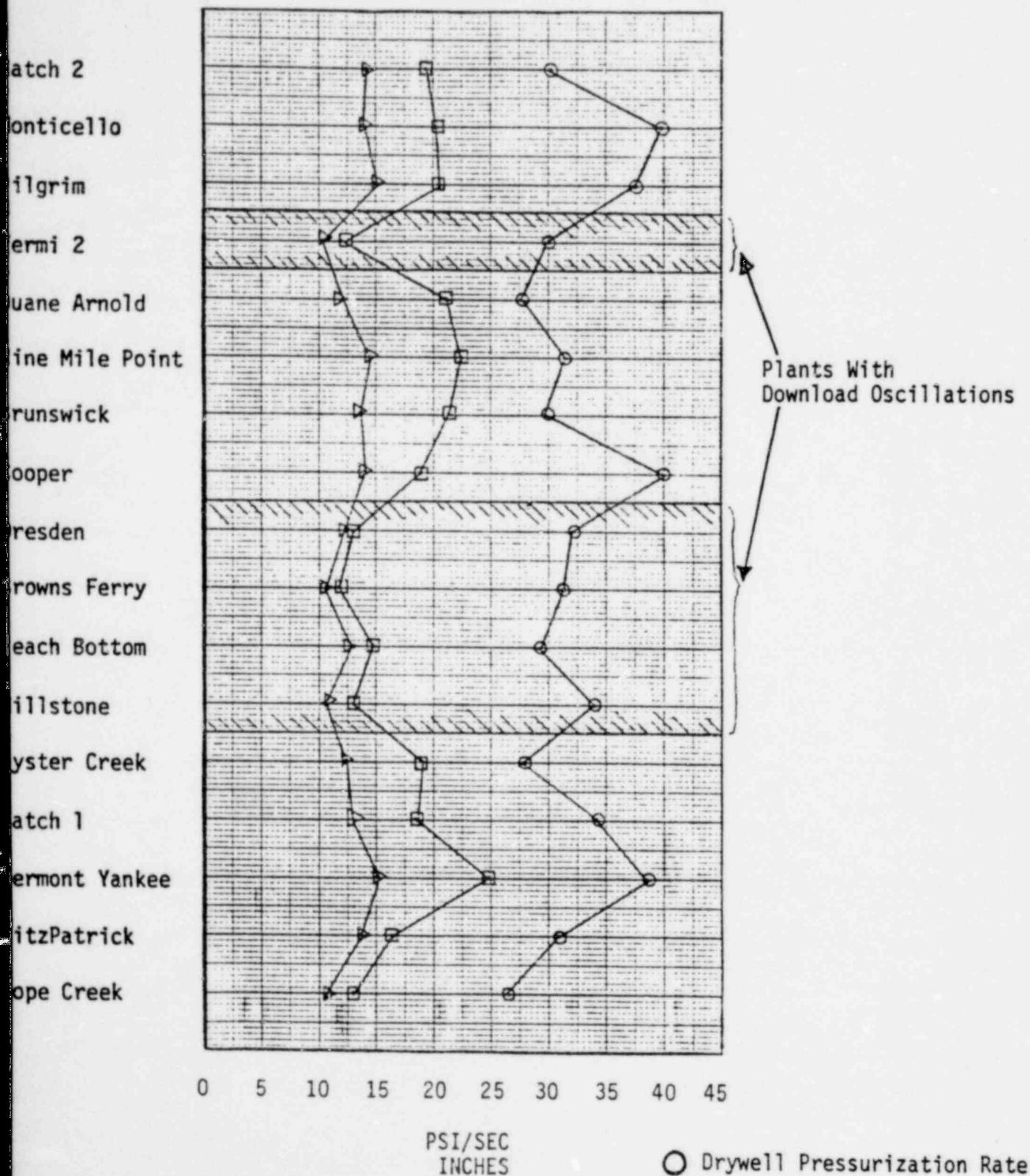

FIGURE H-7

DRESDEN TORUS LOADS (BURP TEST)

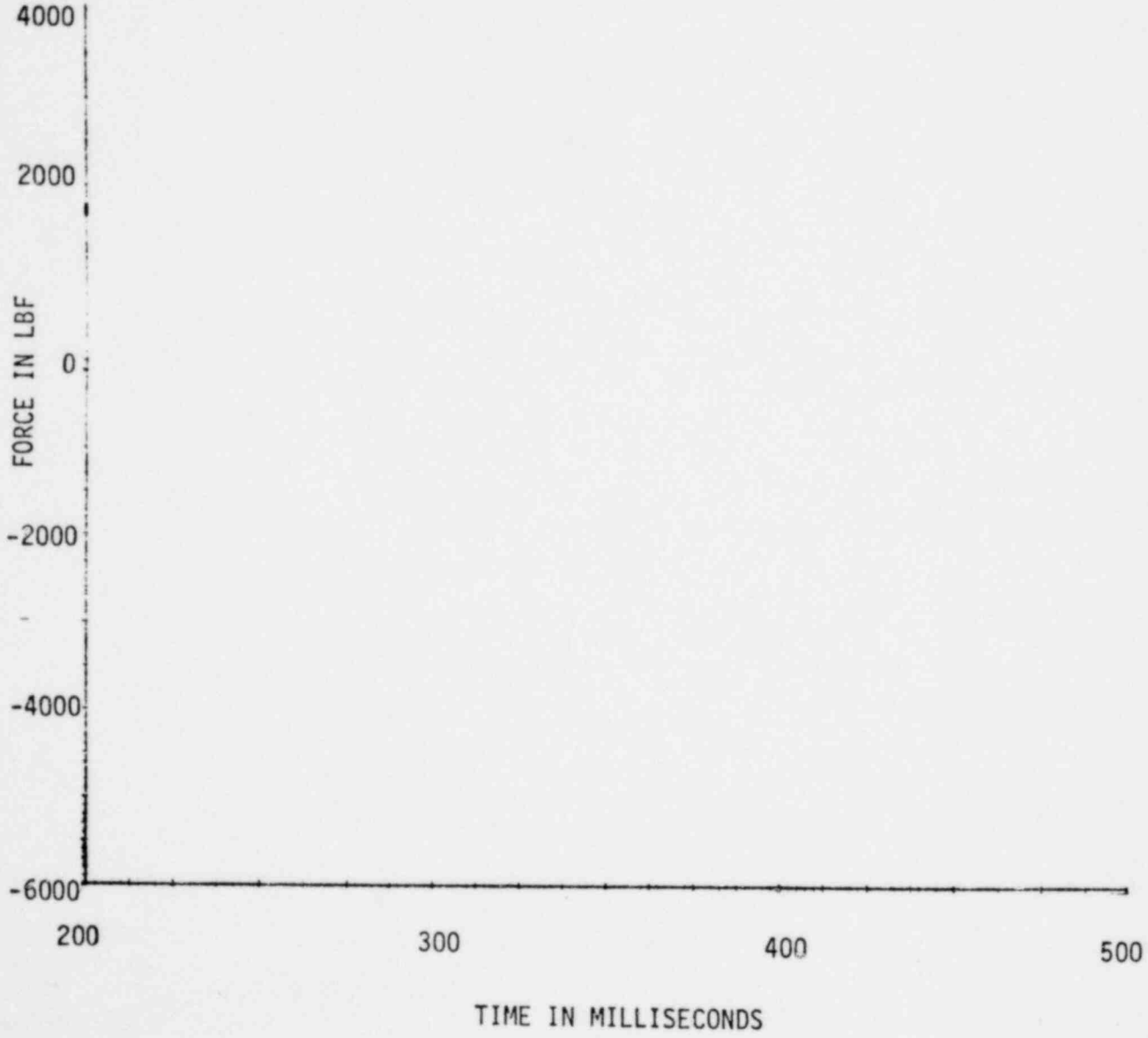

FIGURE H-8

DRESDEN TORUS LOADS (BURP TEST) , CORRECTED

Acceleration Corrected m_{eff} = 1500

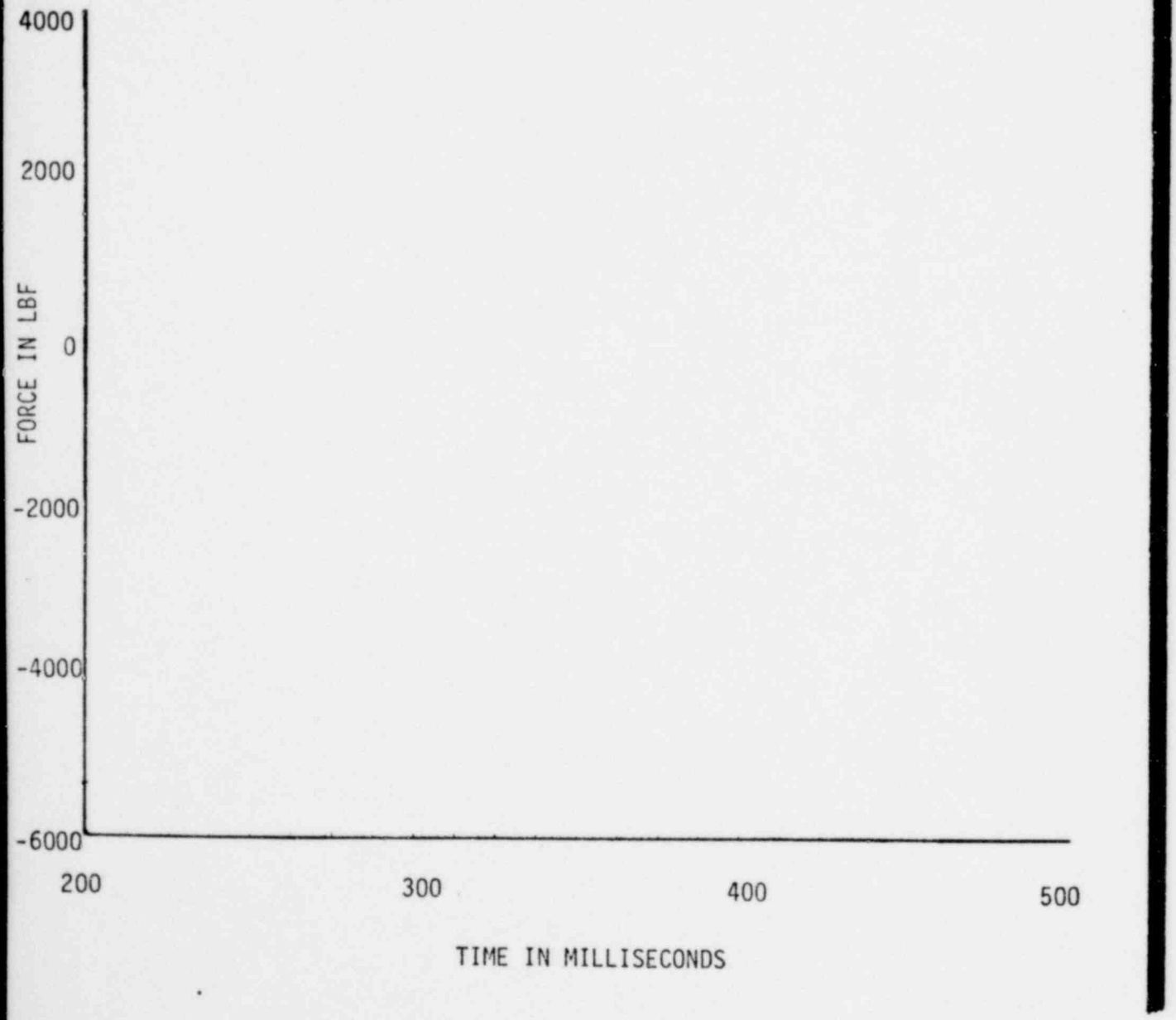

FIGURE H-9

DRESDEN TORUS LOADS (BURP TEST), CORRECTED

Acceleration Corrected m_{eff} = 2000

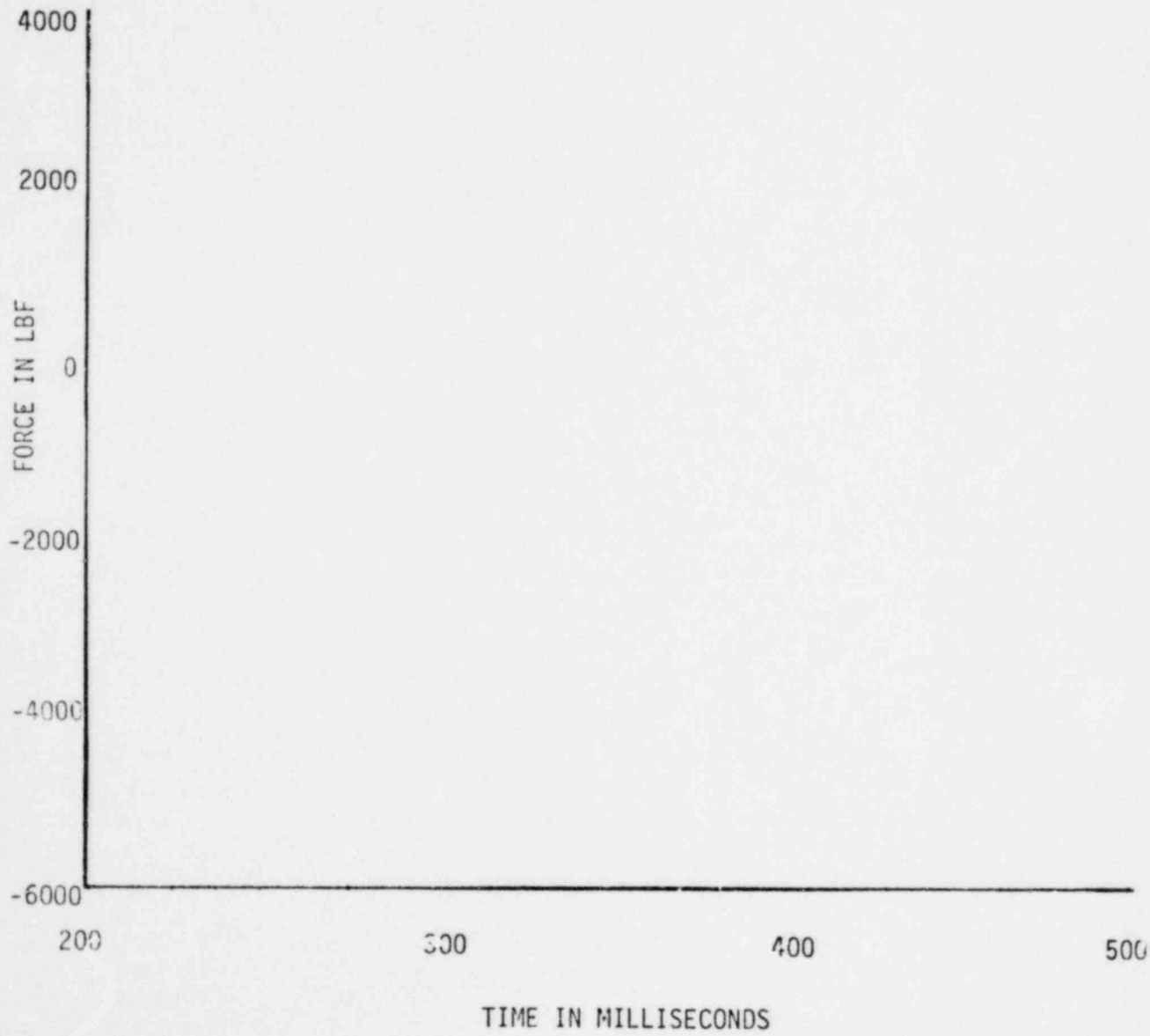

FIGURE H-10

DRESDEN TORUS LOADS (BURP TEST), CORRECTED

Acceleration Corrected m_{eff} = 2500

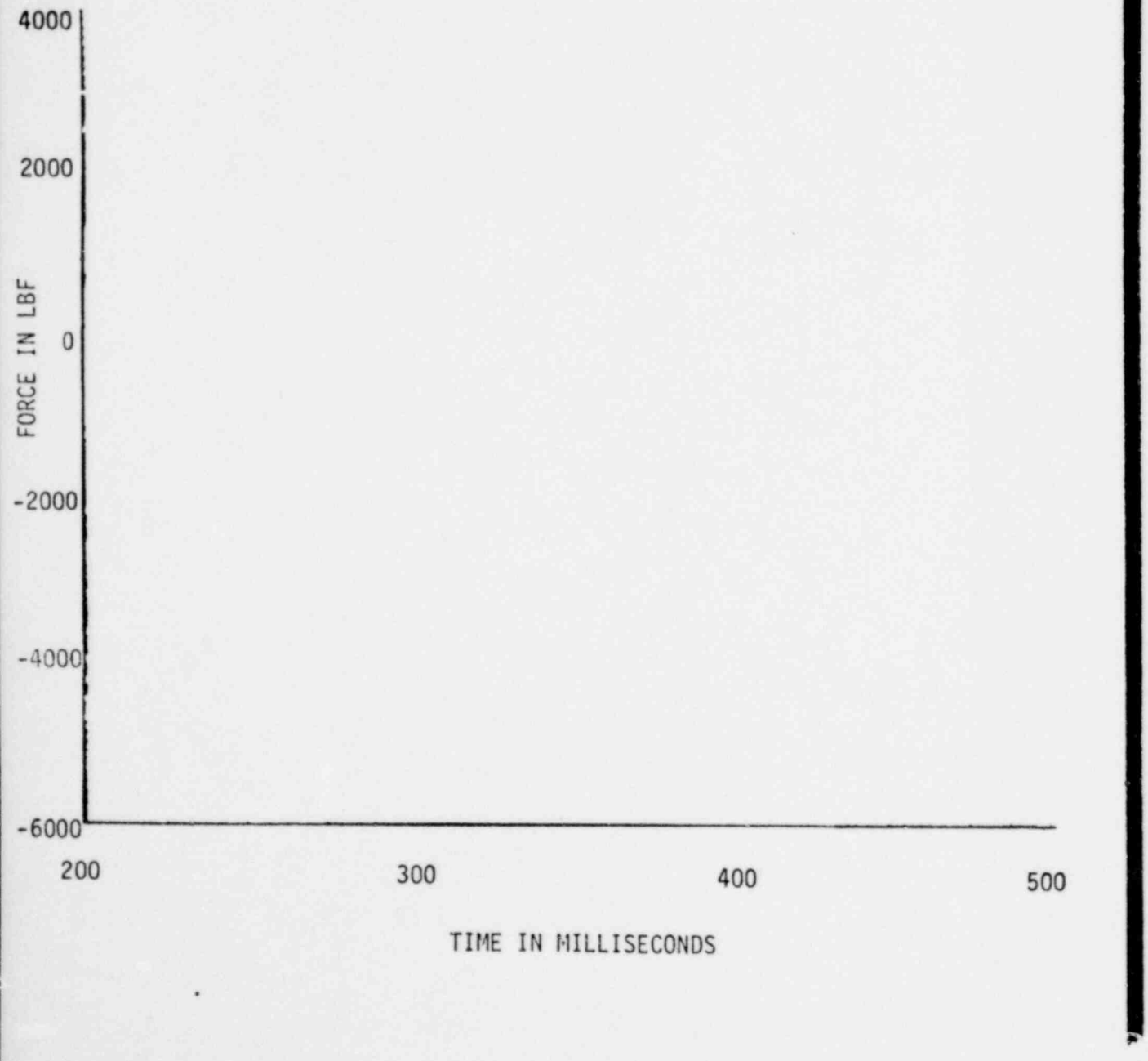

FIGURE H-11

POWER SPECTRAL DENSITY OF
WINDOW ACCELEROMETER
(DRESDEN - BURP TEST)

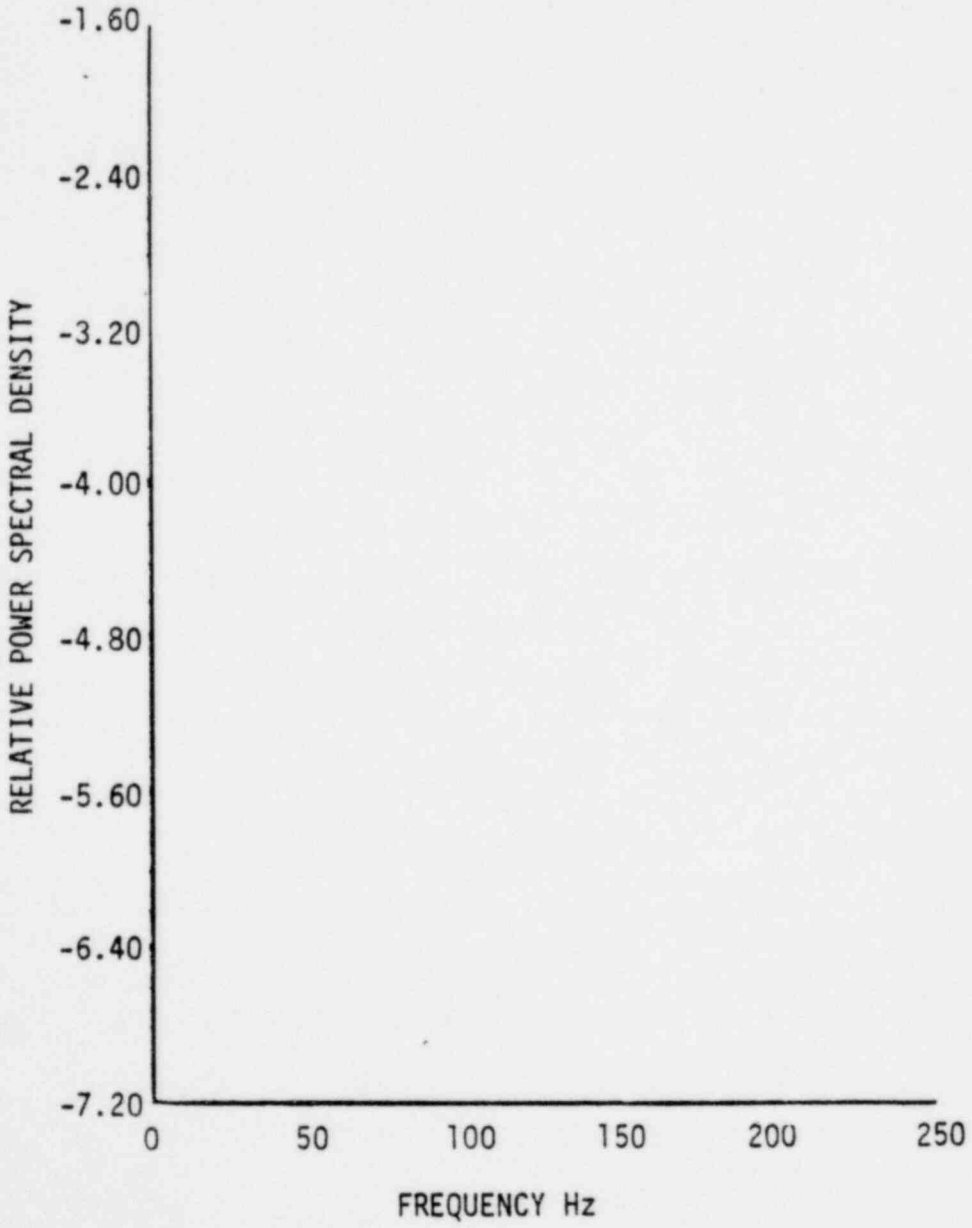

FIGURE H-12

DRESDEN TORUS LOADS (BURP TEST)

POWER SPECTRAL DENSITY

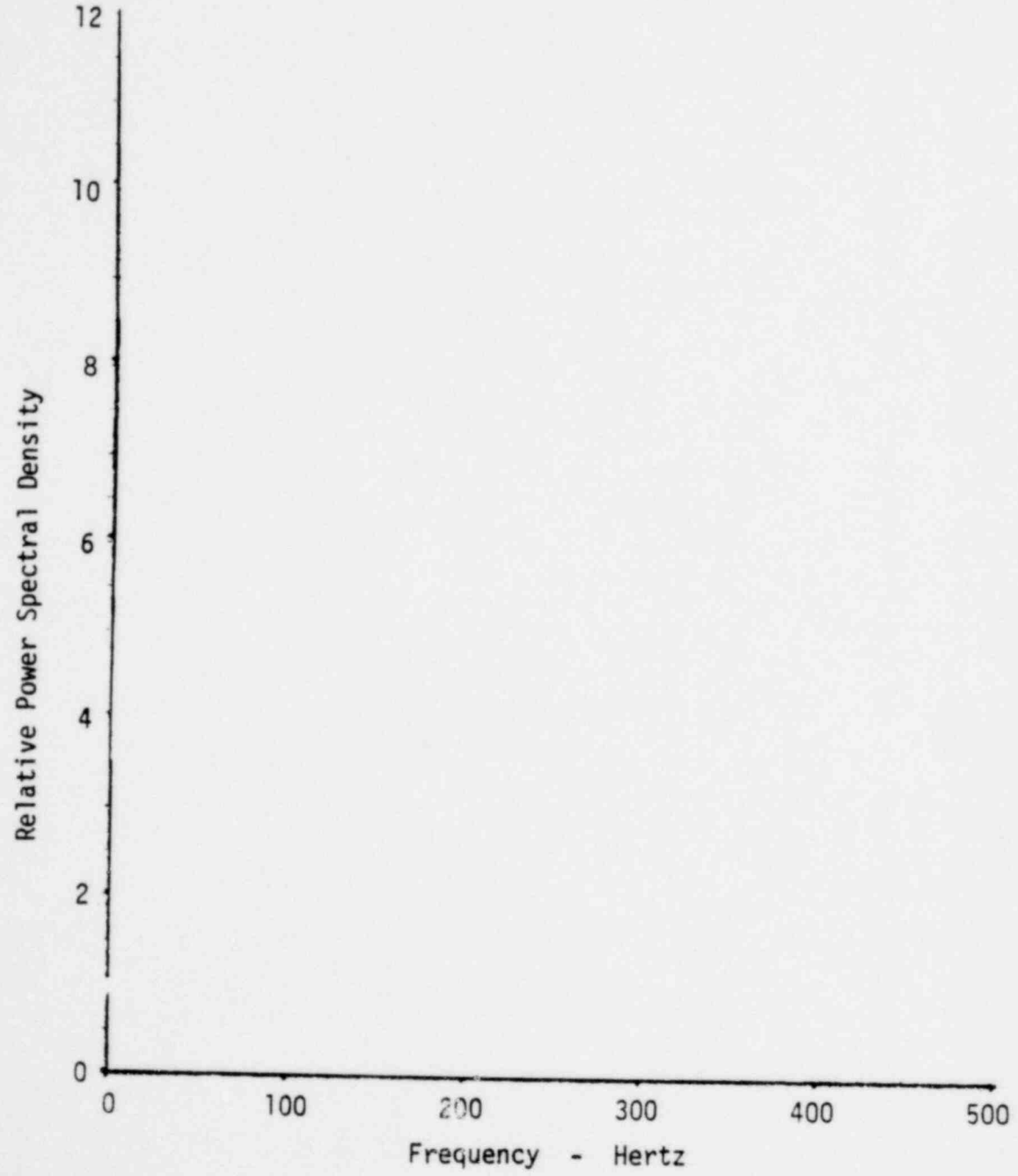

FIGURE H-13

DRESDEN TORUS LOADS (BURP TEST)

Filtered 80 - 120 Hz

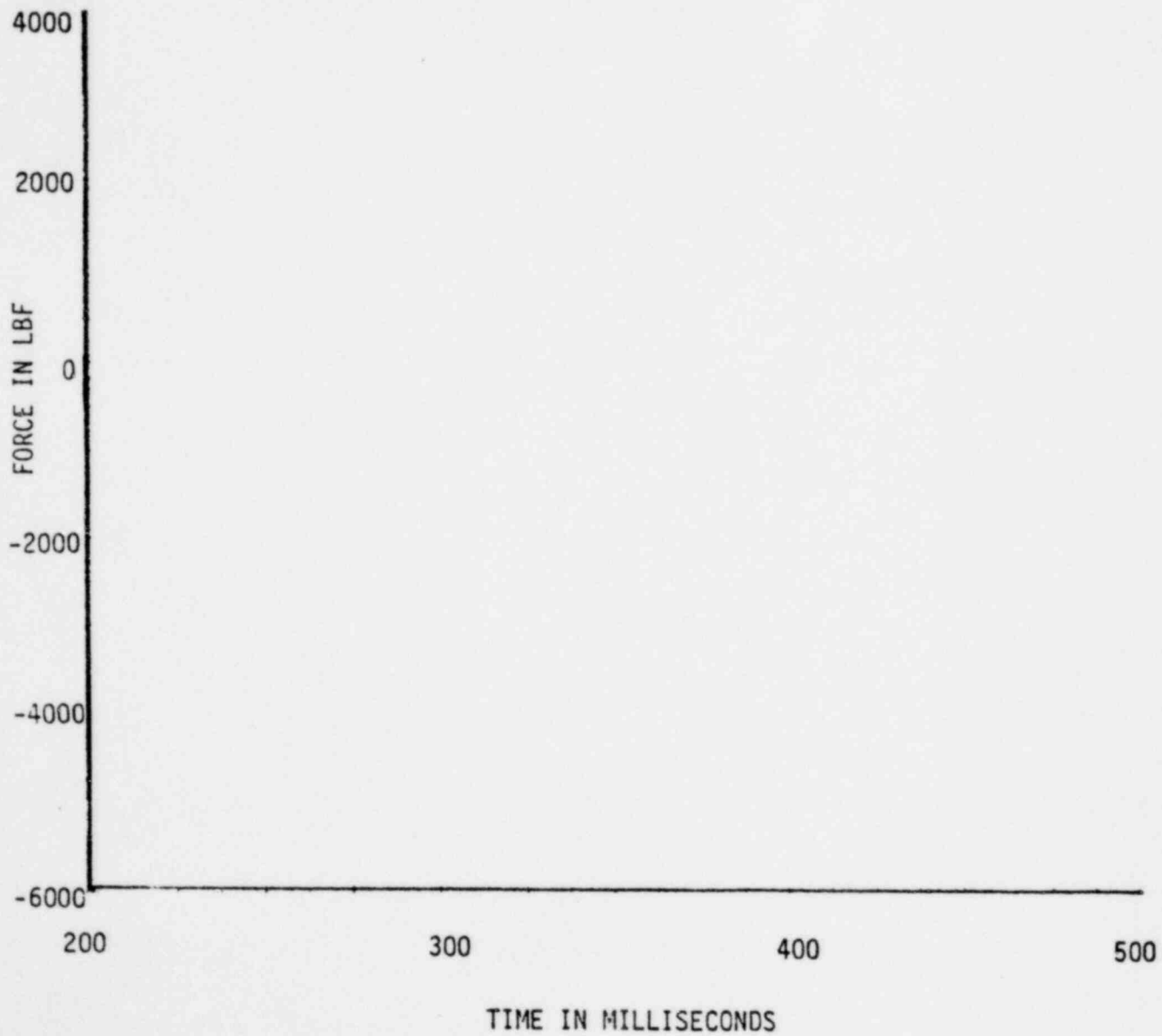

FIGURE H-14

COMPARISON OF FILTERED & UNFILTERED LOADS

DRESDEN (BURP TEST)

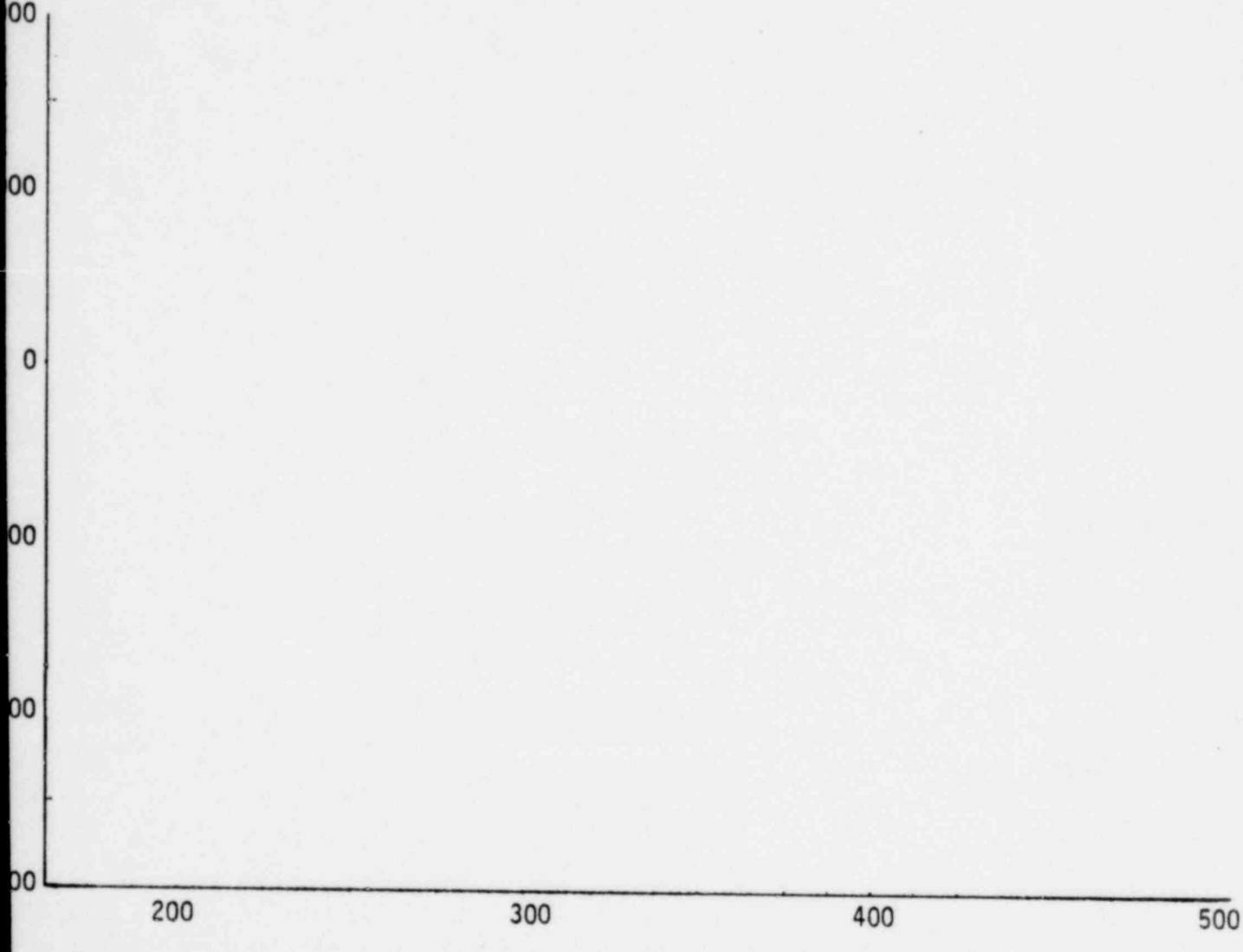

1351 267

FIGURE H-15

Comparison of Filtered and Acceleration Corrected

Dresden Torus Loads (Burp Test)

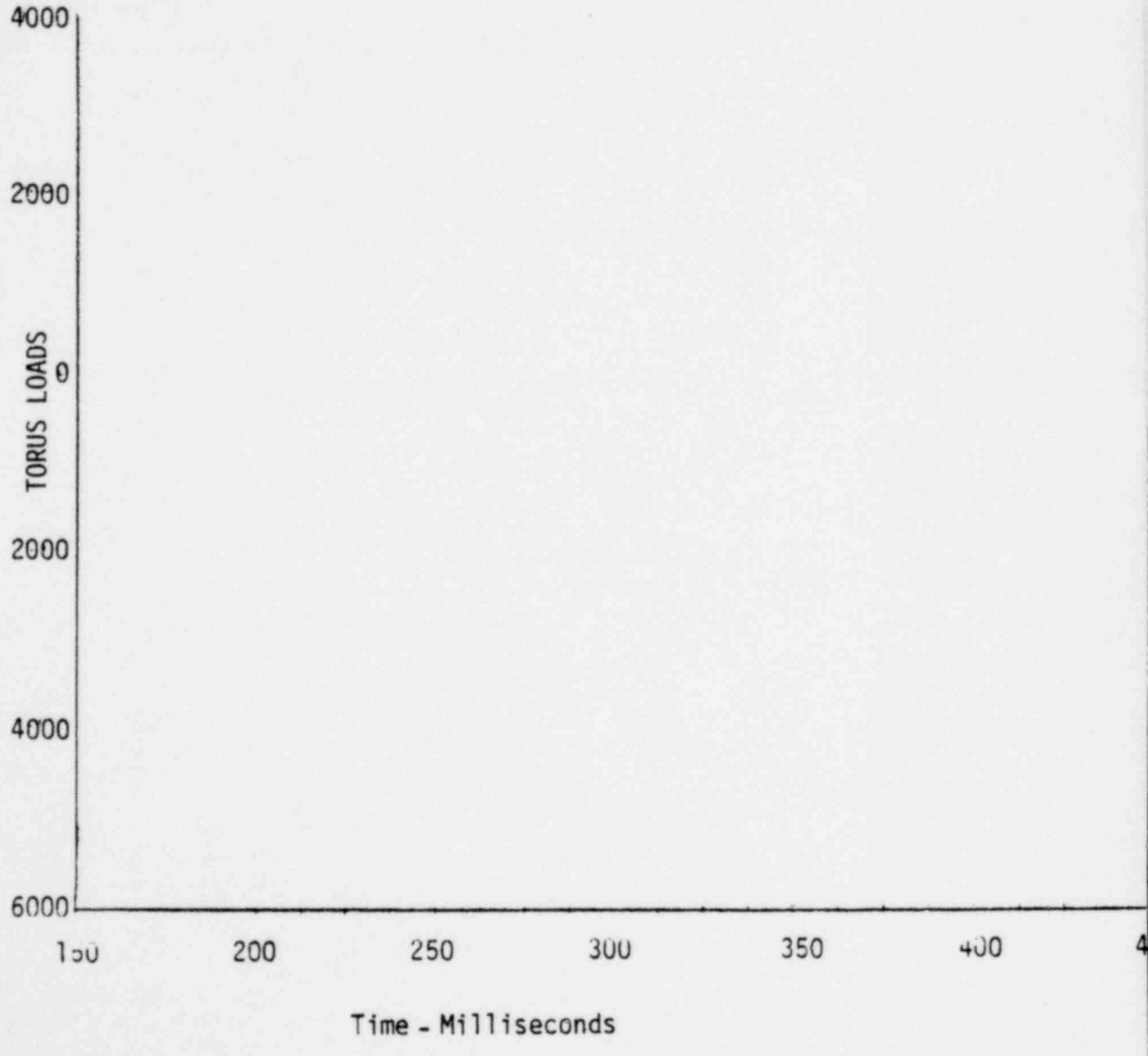

FIGURE H-16

TORUS BENDING MODES

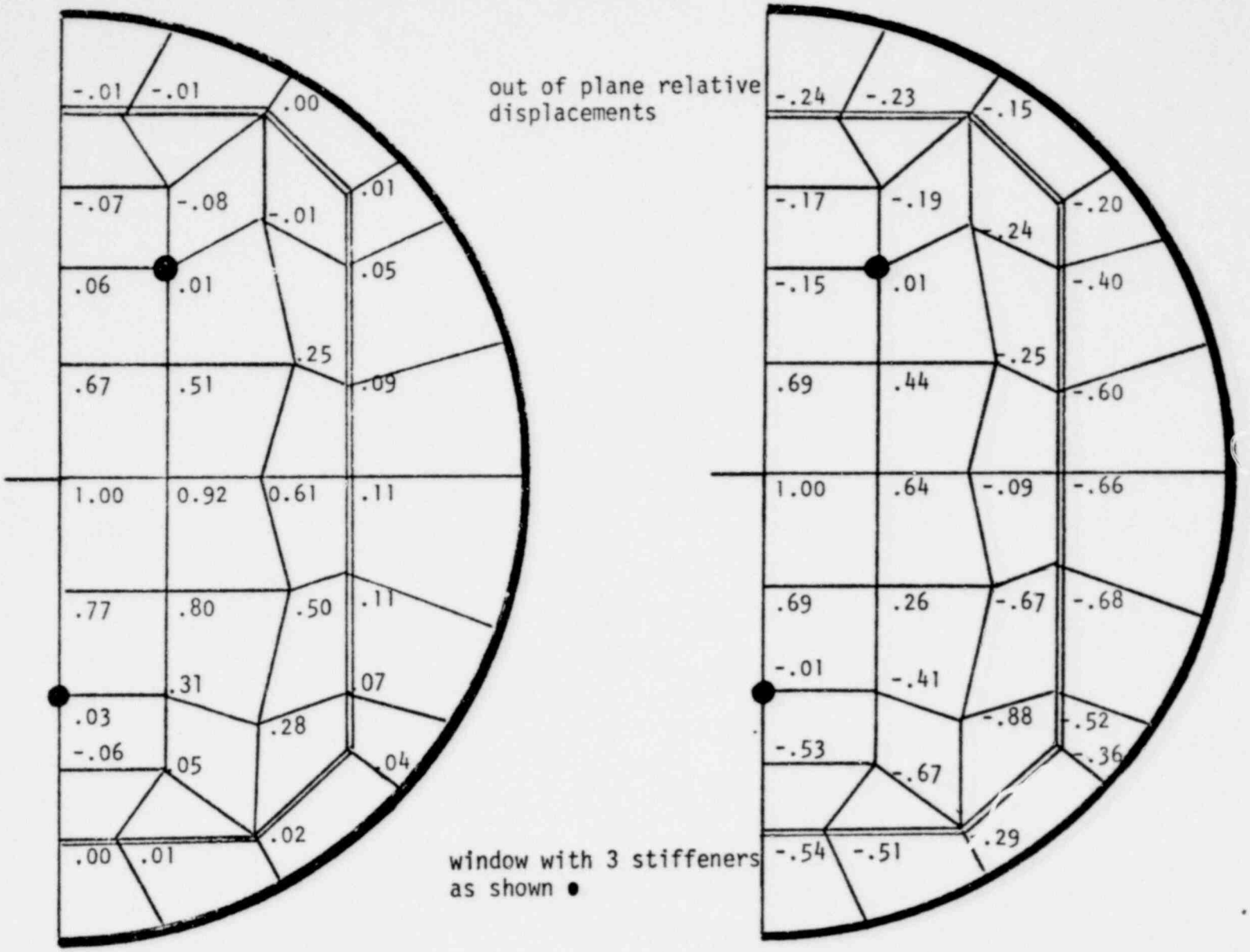

FIRST MODE
FREQUENCY = 96 Hz

SECOND MODE
FREQUENCY = 134 Hz

FIGURE H-17 NEDO-21944

Window Acceleration Analysis

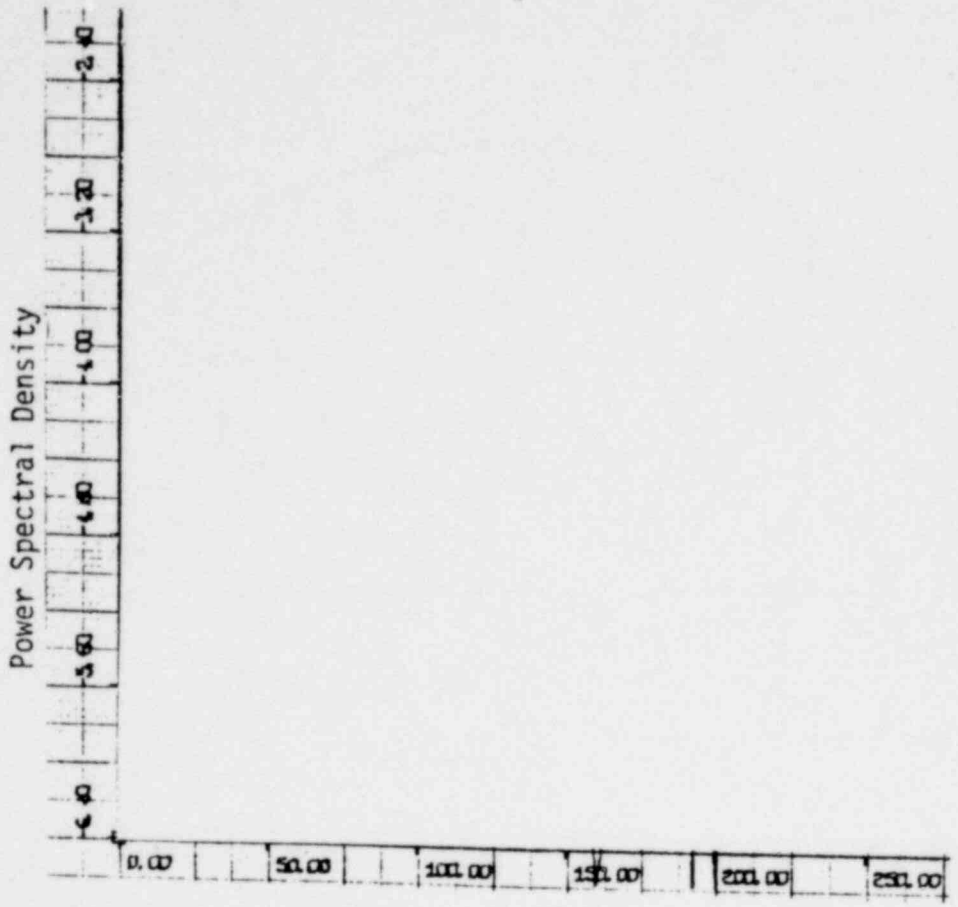

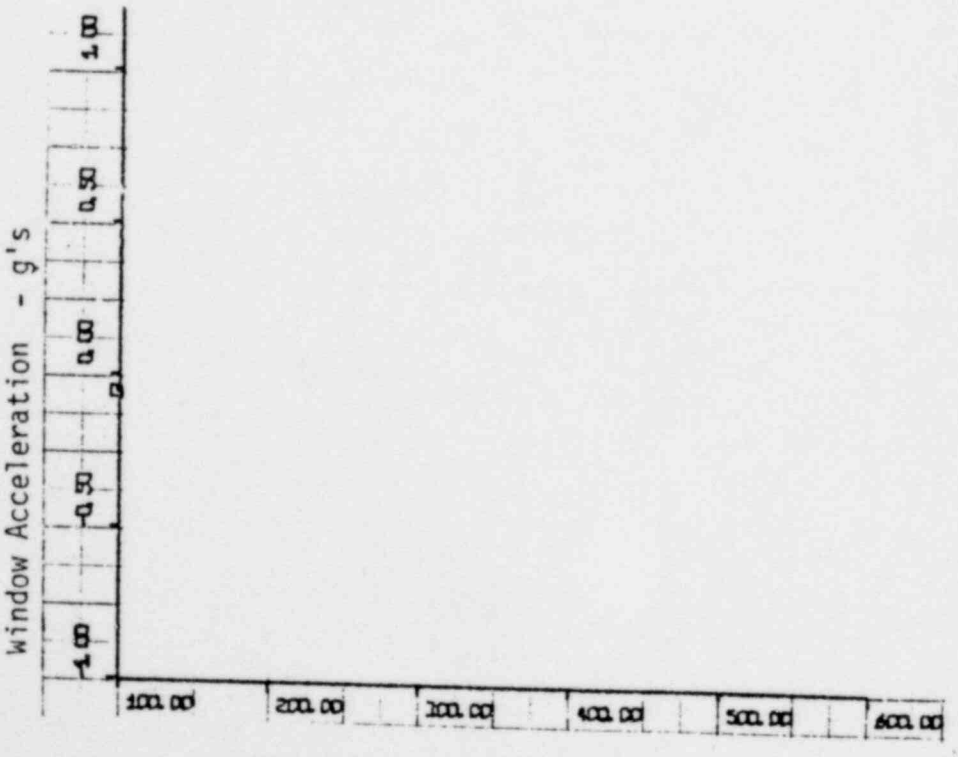

1351 270

FIGURE H-18

FILTERED NET TORUS FORCE,
CORRECTED FOR WATER INERTIA

DRESDEN TEST 1

FILTER : 80-120 HZ

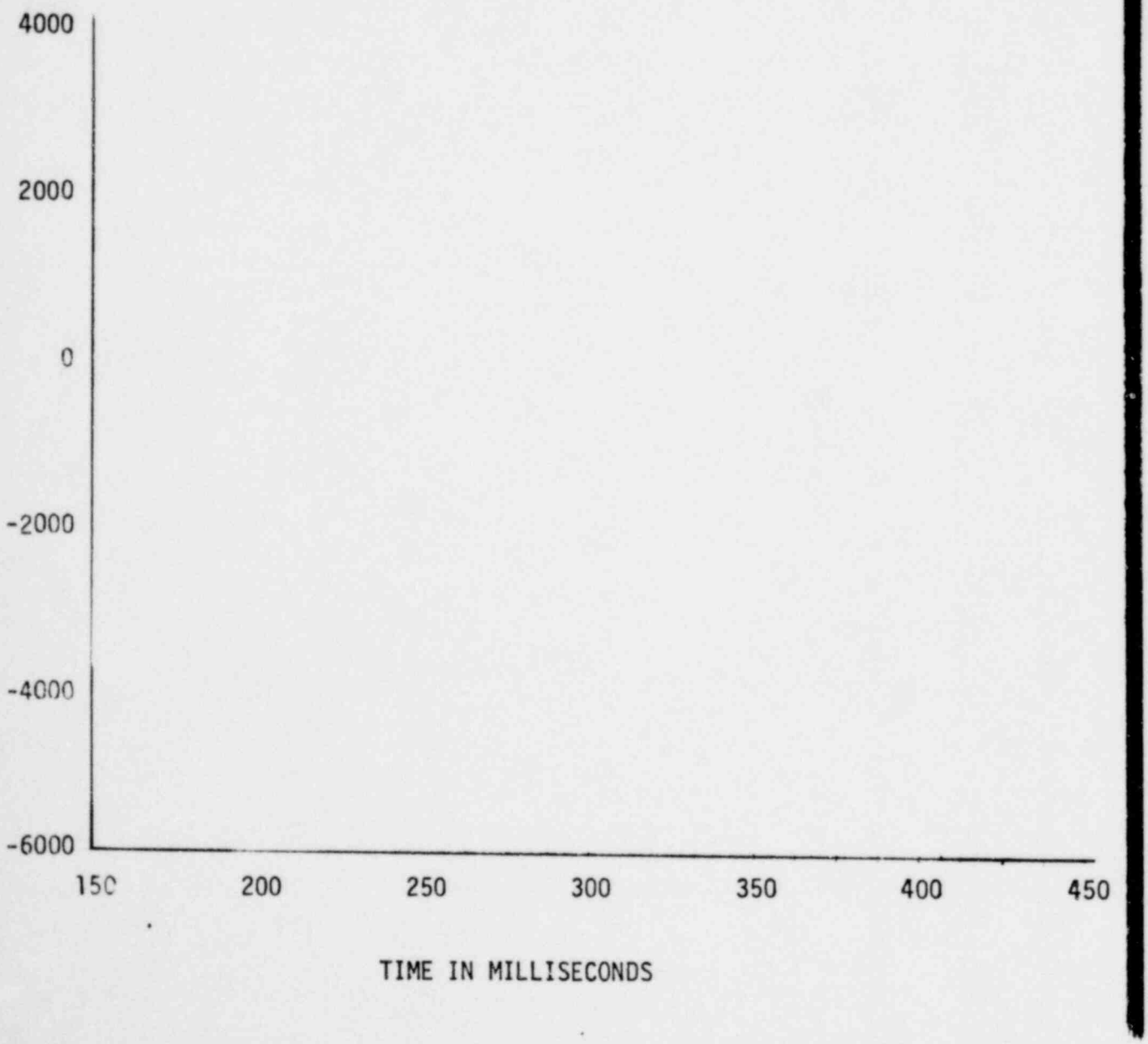

1351 271

FIGURE H-19

FILTERED NET TORUS FORCE,
CORRECTED FOR WATER INERTIA

DRESDEN TEST 2

FILTER : 80-120 HZ

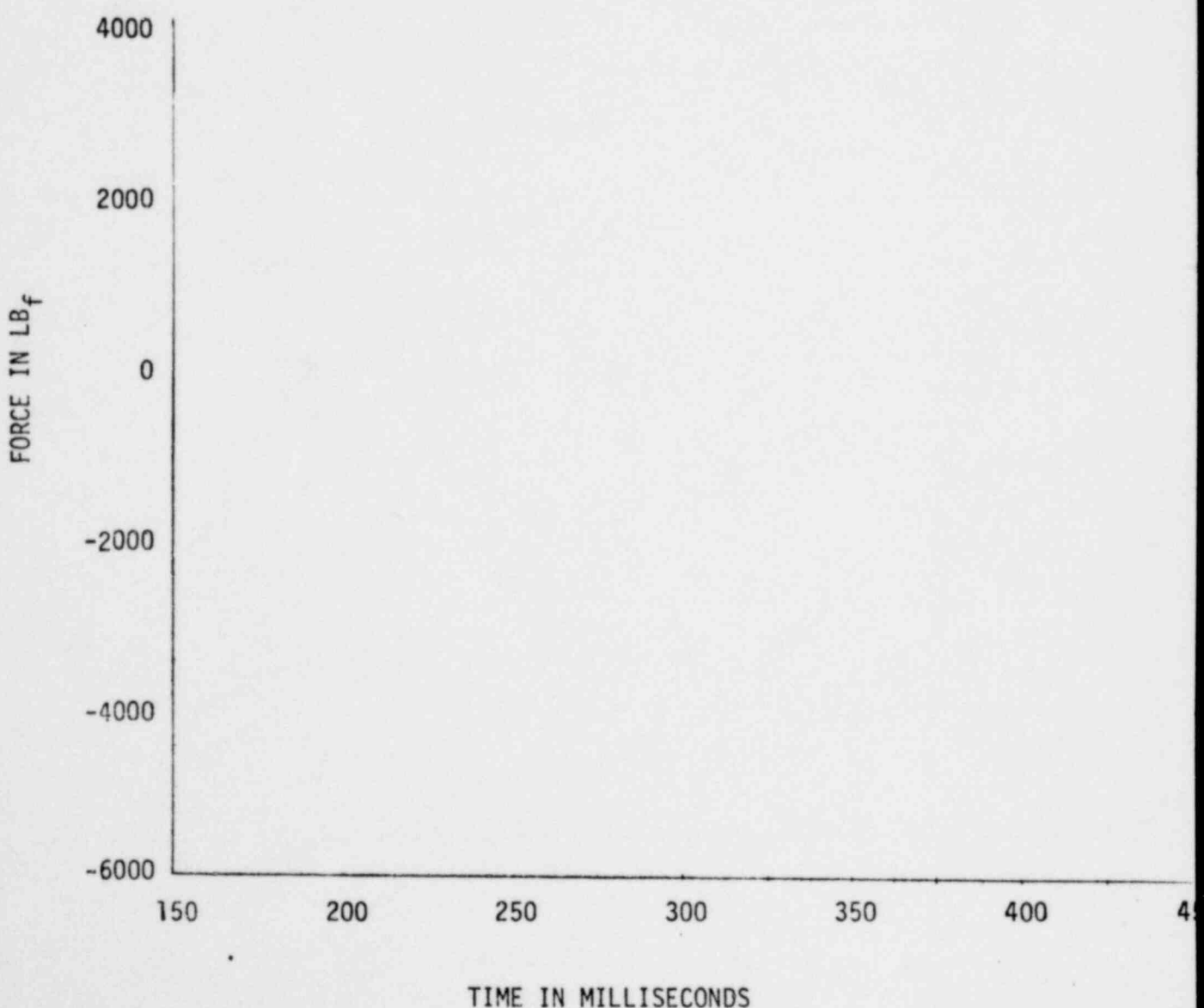

1351 272

FIGURE H-20

FILTERED NET TORUS FORCE,
CORRECTED FOR WATER INERTIA

DRESDEN TEST 3

FILTER : 80-120 HZ

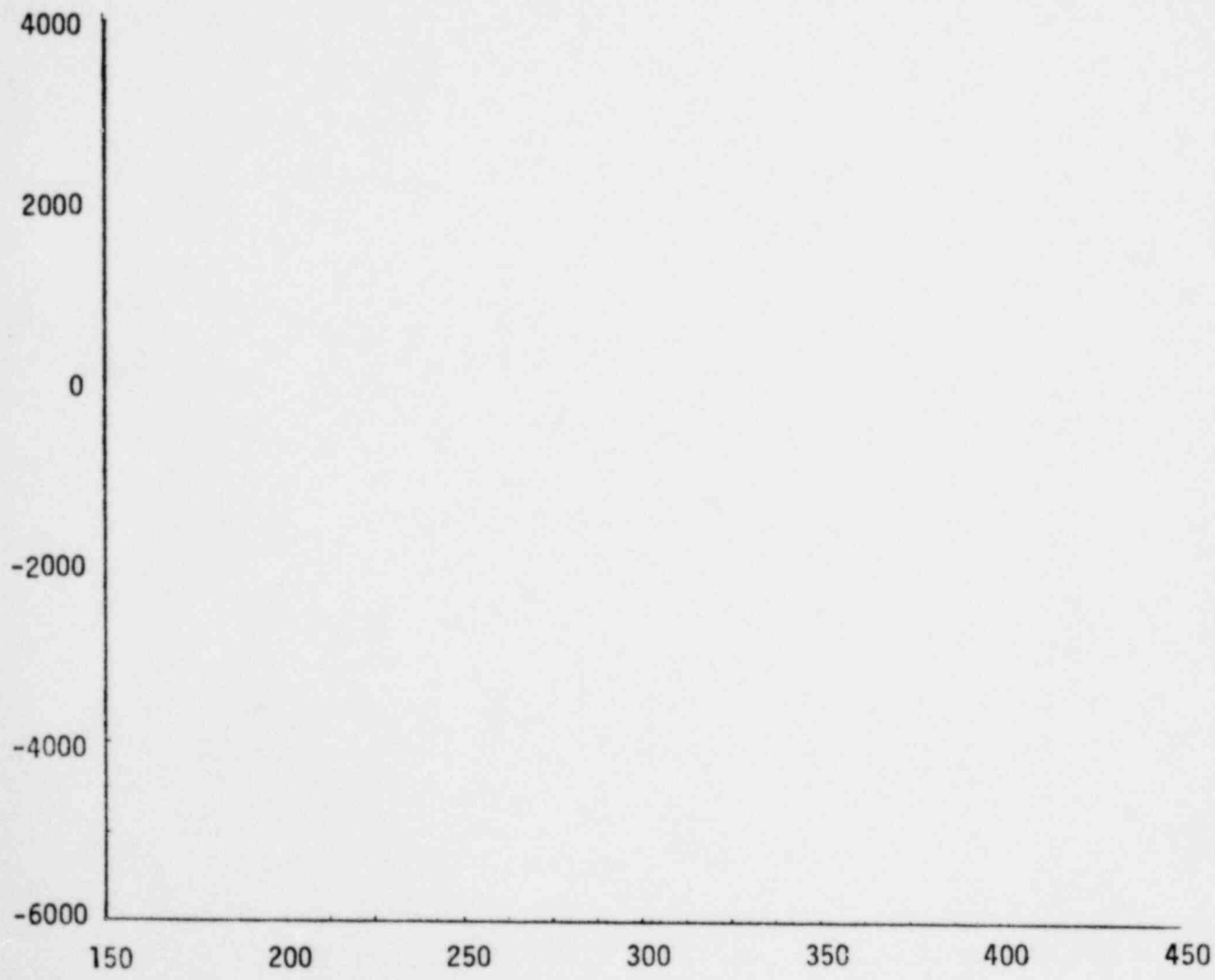

FIGURE H-21

FILTERED NET TORUS FORCE,
CORRECTED FOR WATER INERTIA

DRESDEN TEST 4

FILTER : 80-120 HZ

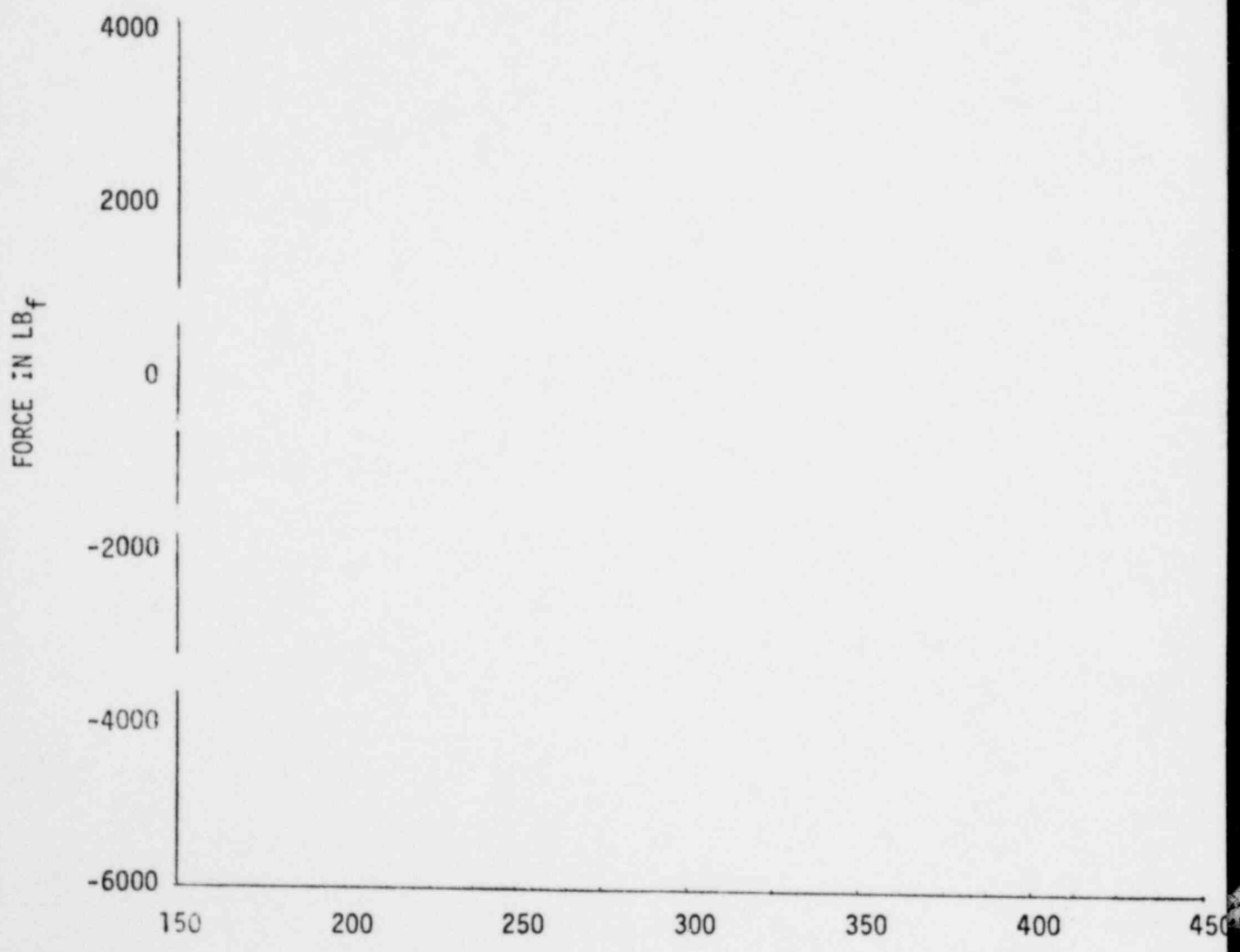

1351 274

FIGURE H-22

FILTERED NET TORUS FORCE,
CORRECTED FOR WATER INERTIA

DRESDEN TEST 5

FILTER : 80-120 HZ

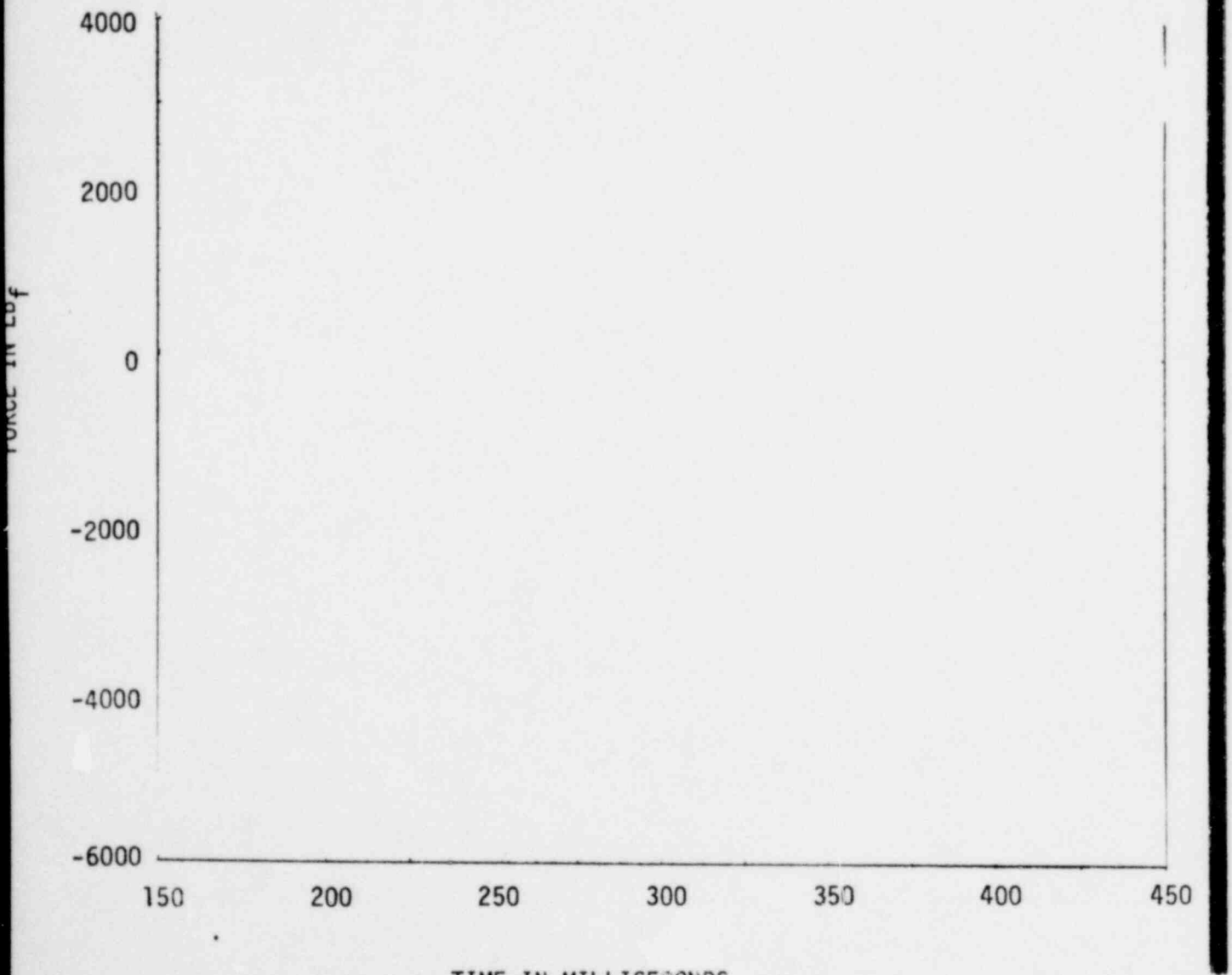

FIGURE H-23

FILTERED NET TORUS FORCE,
CORRECTED FOR WATER INERTIA

BROWNS FERRY TEST 1

FILTER : 65-105 HZ

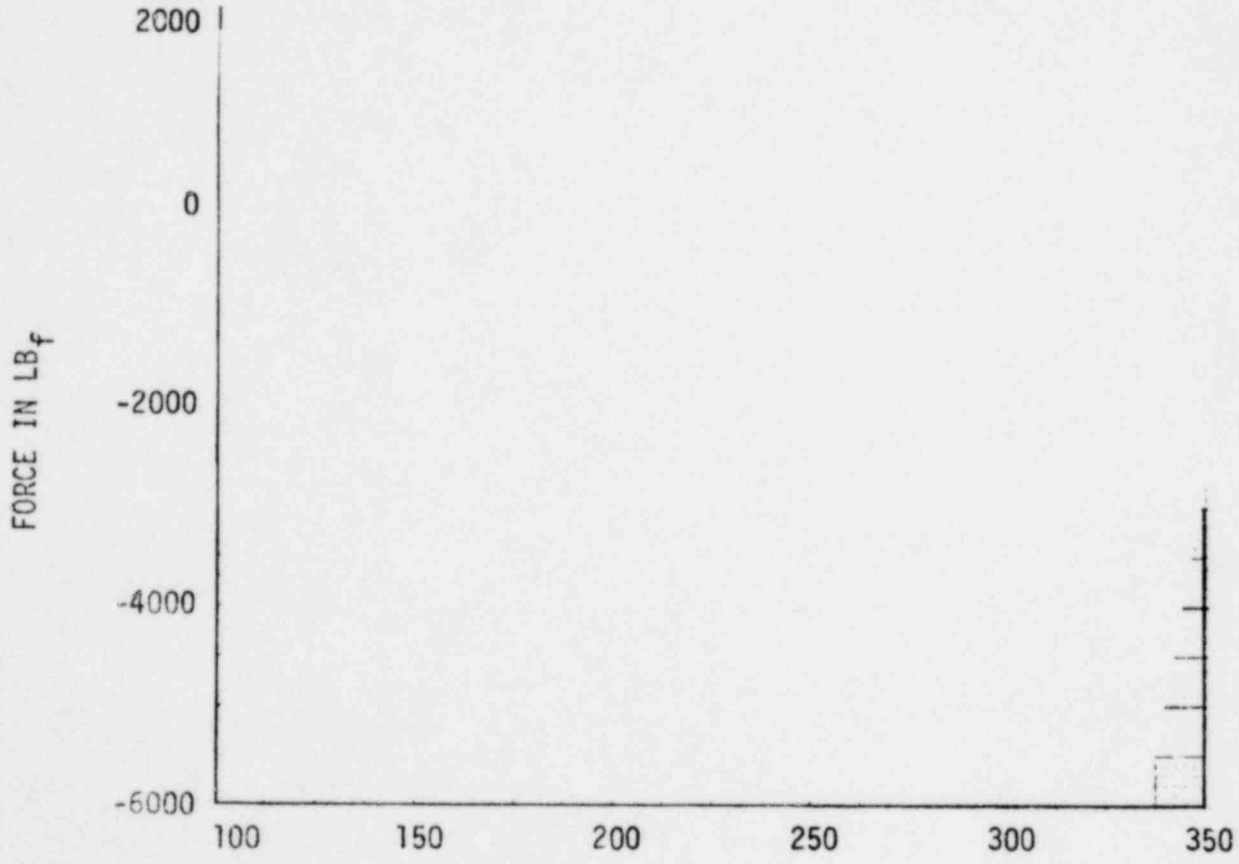

1351 276

FIGURE H-24

FILTERED NET TORUS FORCE,
CORRECTED FOR WATER INERTIA

BROWNS FERRY TEST 2

FILTER : 65-105 HZ

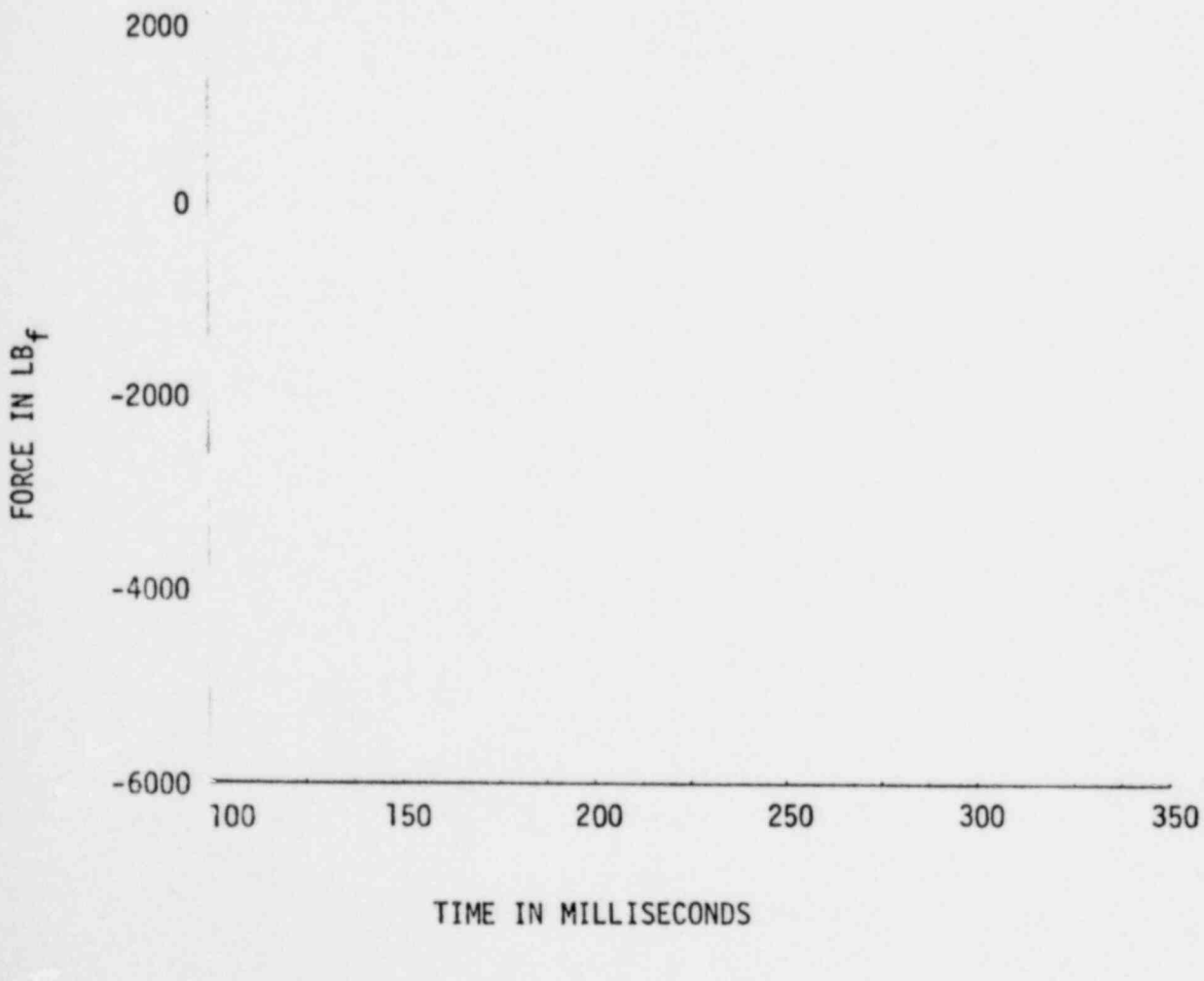

1351 277

FIGURE H-25

FILTERED NET TORUS FORCE,
CORRECTED FOR WATER INERTIA

BROWNS FERRY TEST 3

FILTER : 65-105 HZ

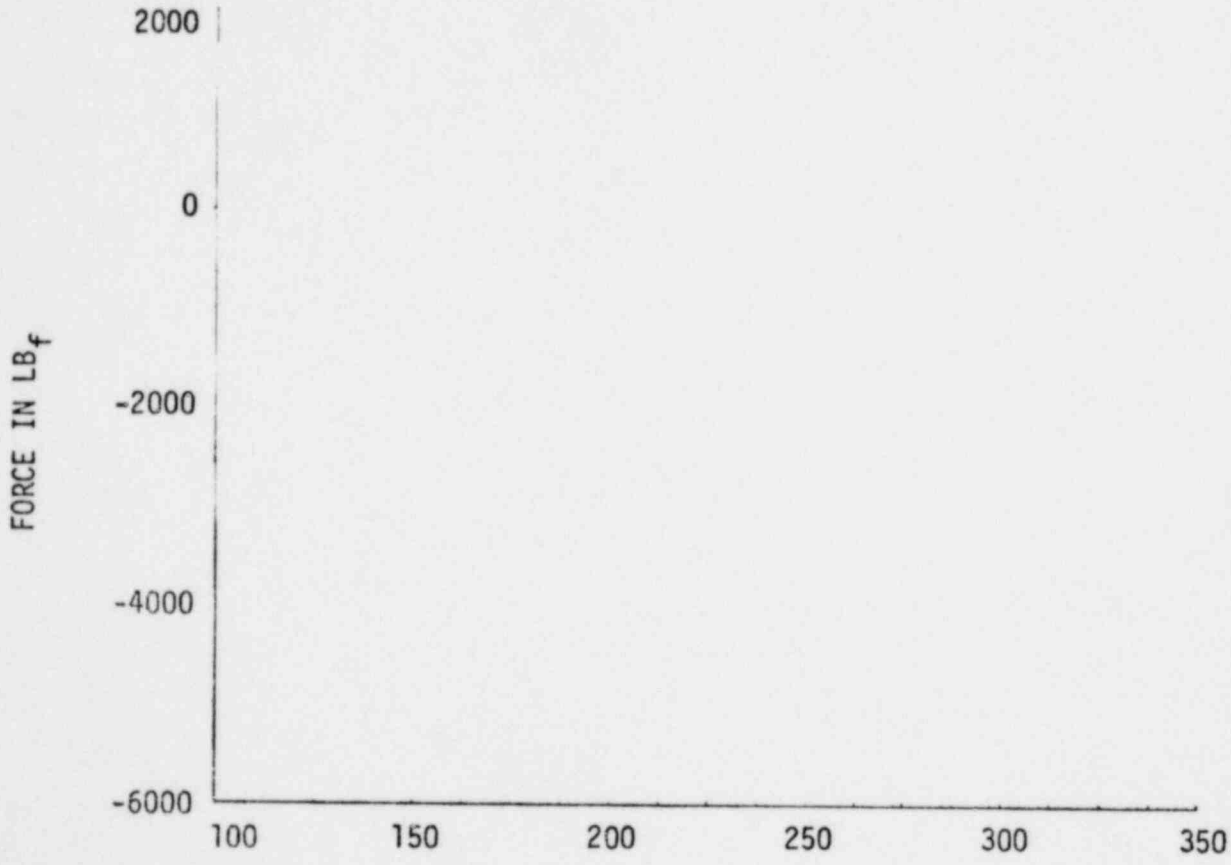

FIGURE H-26

FILTERED NET TORUS FORCE,
CORRECTED FOR WATER INERTIA

BROWNS FERRY TEST 4

FILTER : 65-105 HZ

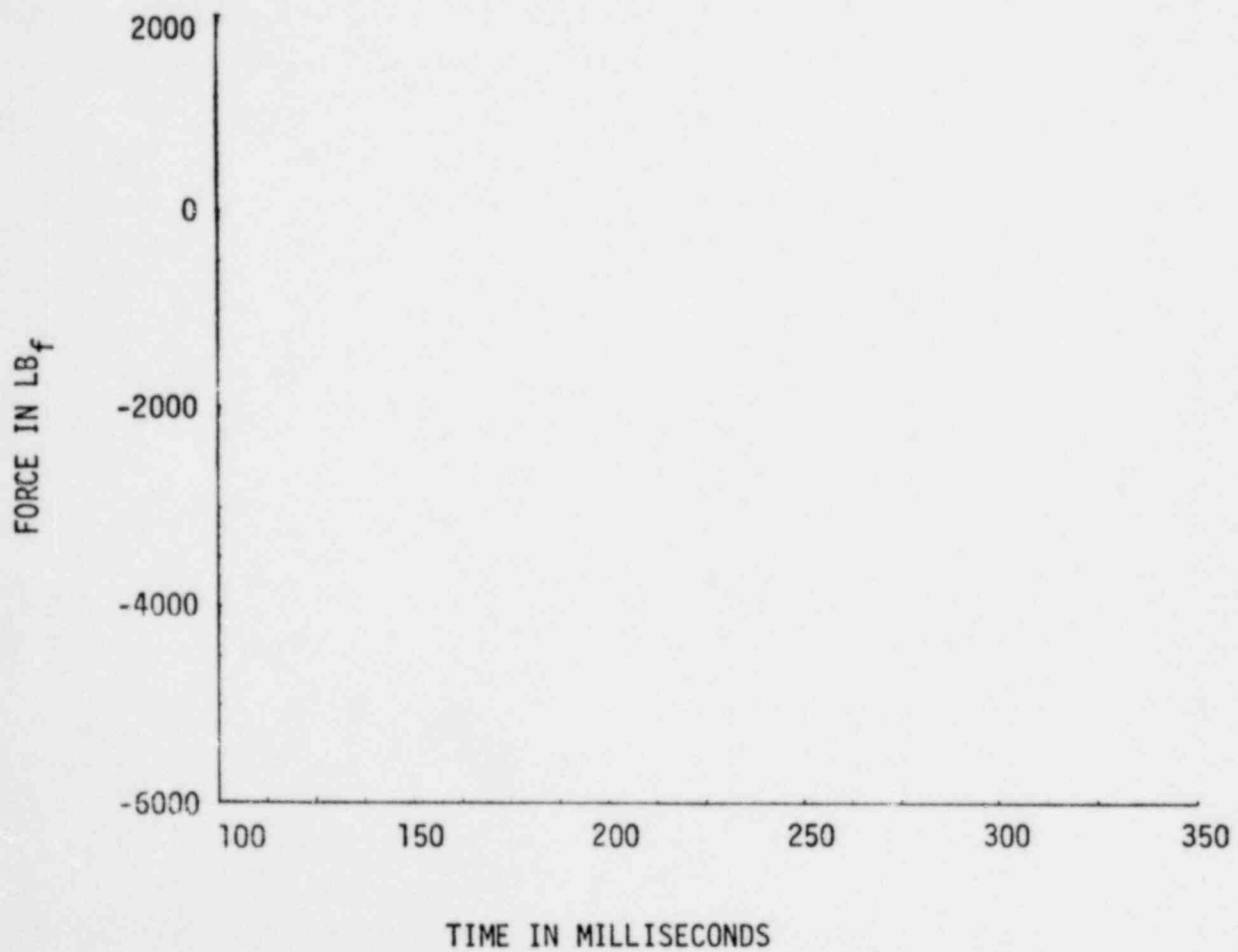

FIGURE H-27

FILTERED NET TORUS FORCE,
CORRECTED FOR WATER INERTIA

BROWNS FERRY TEST 5

FILTER : 65-105 HZ

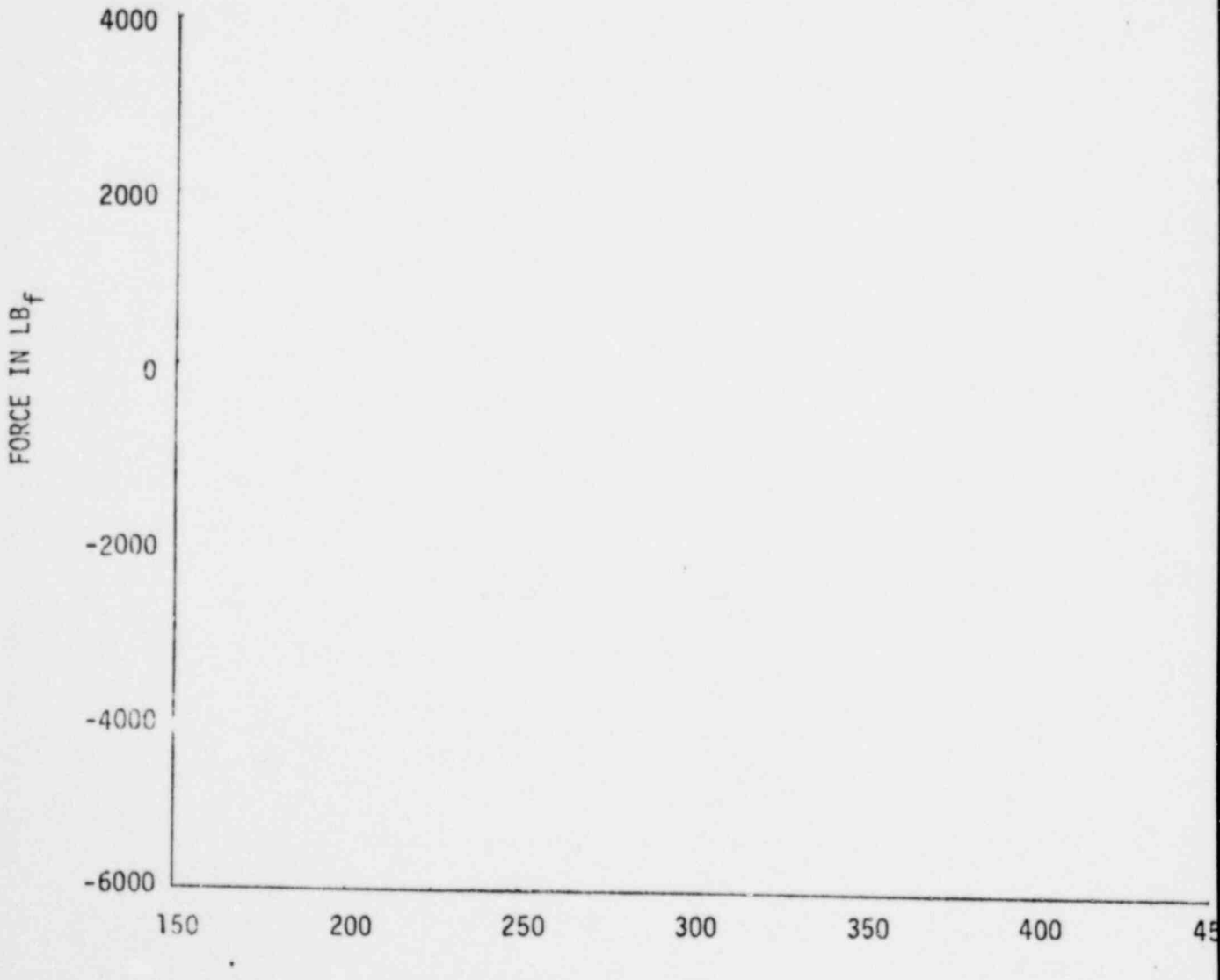

FIGURE H-28

FILTERED NET TORUS FORCE,
CORRECTED FOR WATER INERTIA

PEACH BOTTOM TEST 1

FILTER : 80-120 HZ

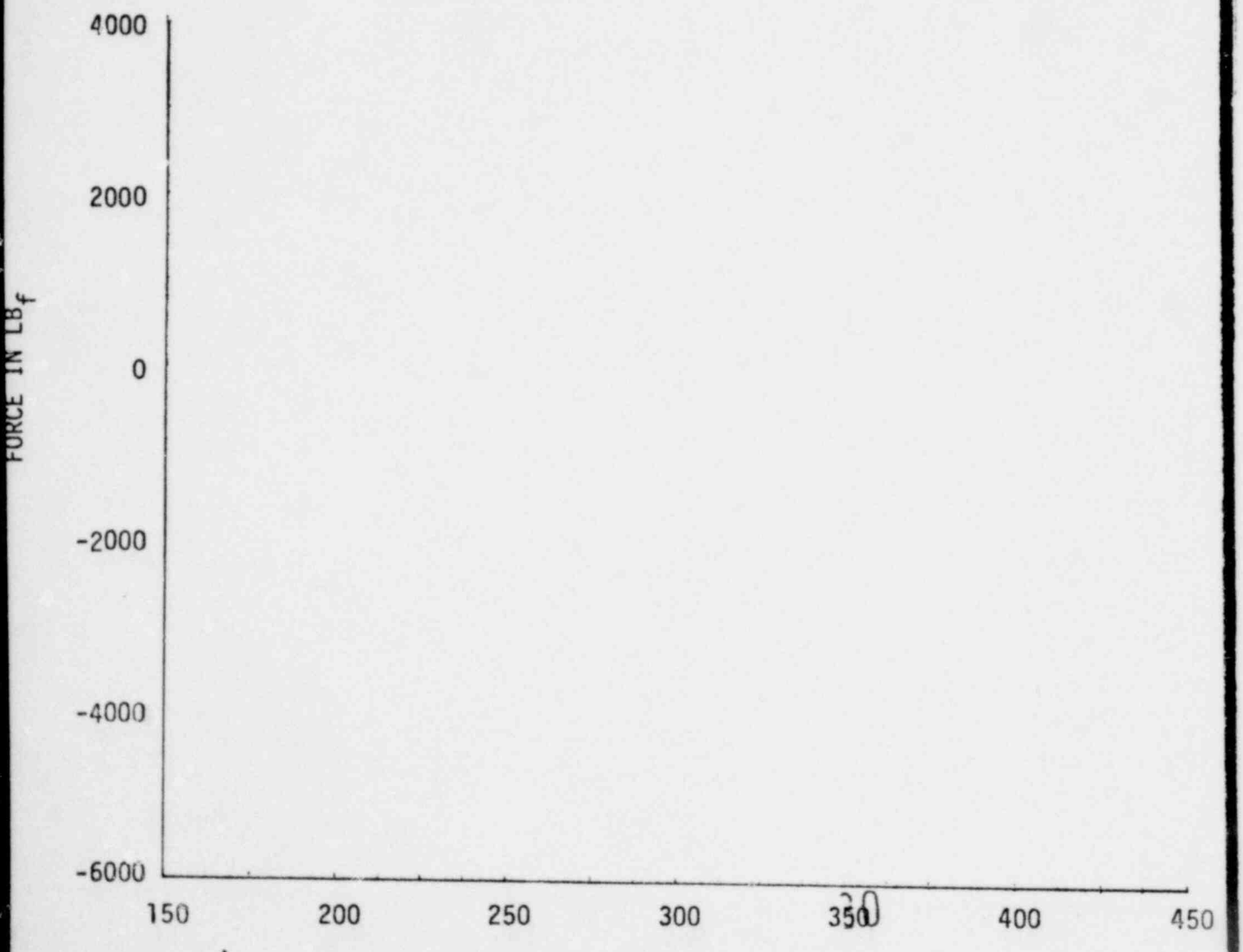

1351 281

FIGURE H-29

FILTERED NET TORUS FORCE,
CORRECTED FOR WATER INERTIA

PEACH BOTTOM TEST 2

FILTER : 80-120 HZ

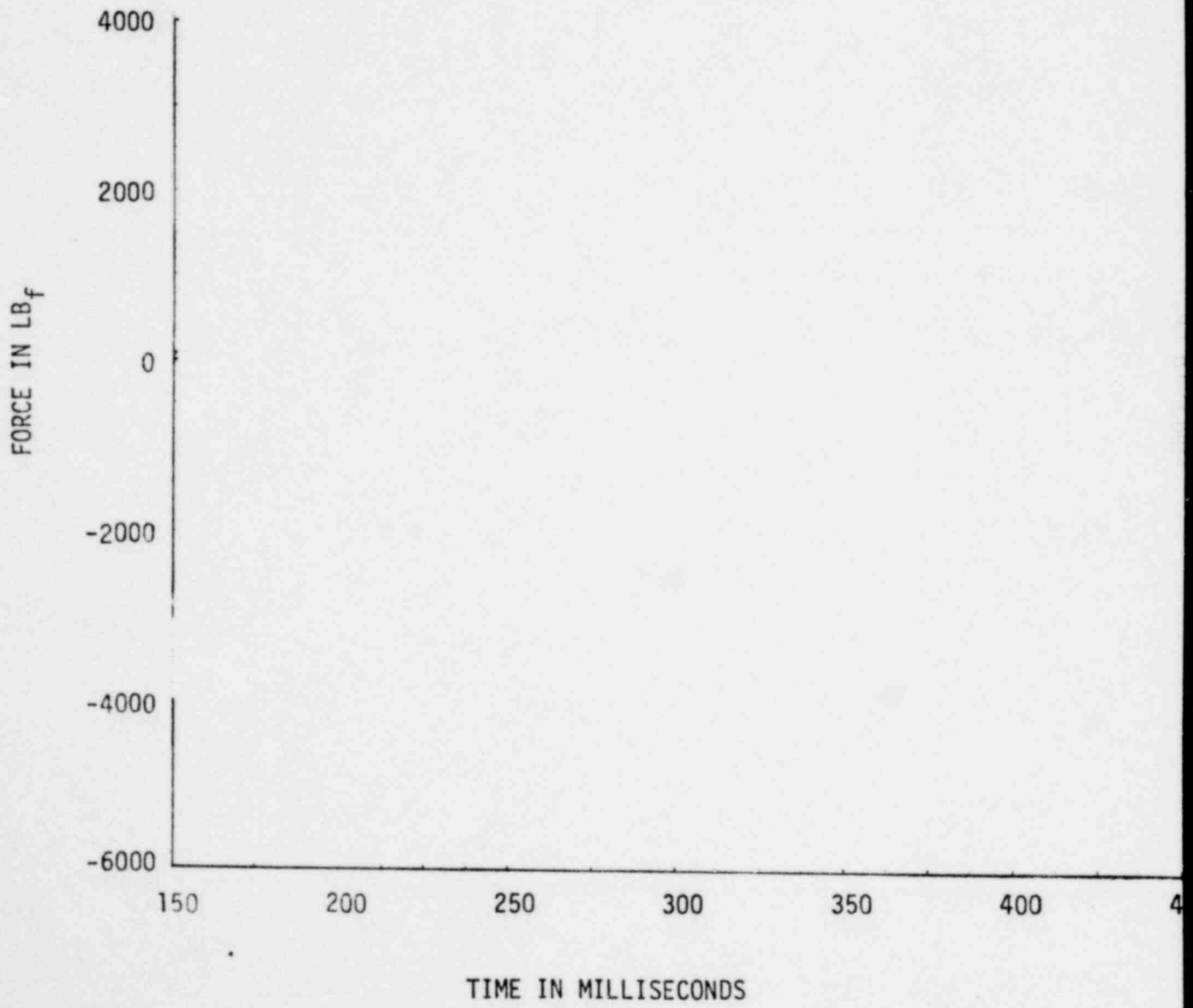

FIGURE H-30

FILTERED NET TORUS FORCE,
CORRECTED FOR WATER INERTIA

PEACH BOTTOM TEST 3

FILTER : 80-120 HZ

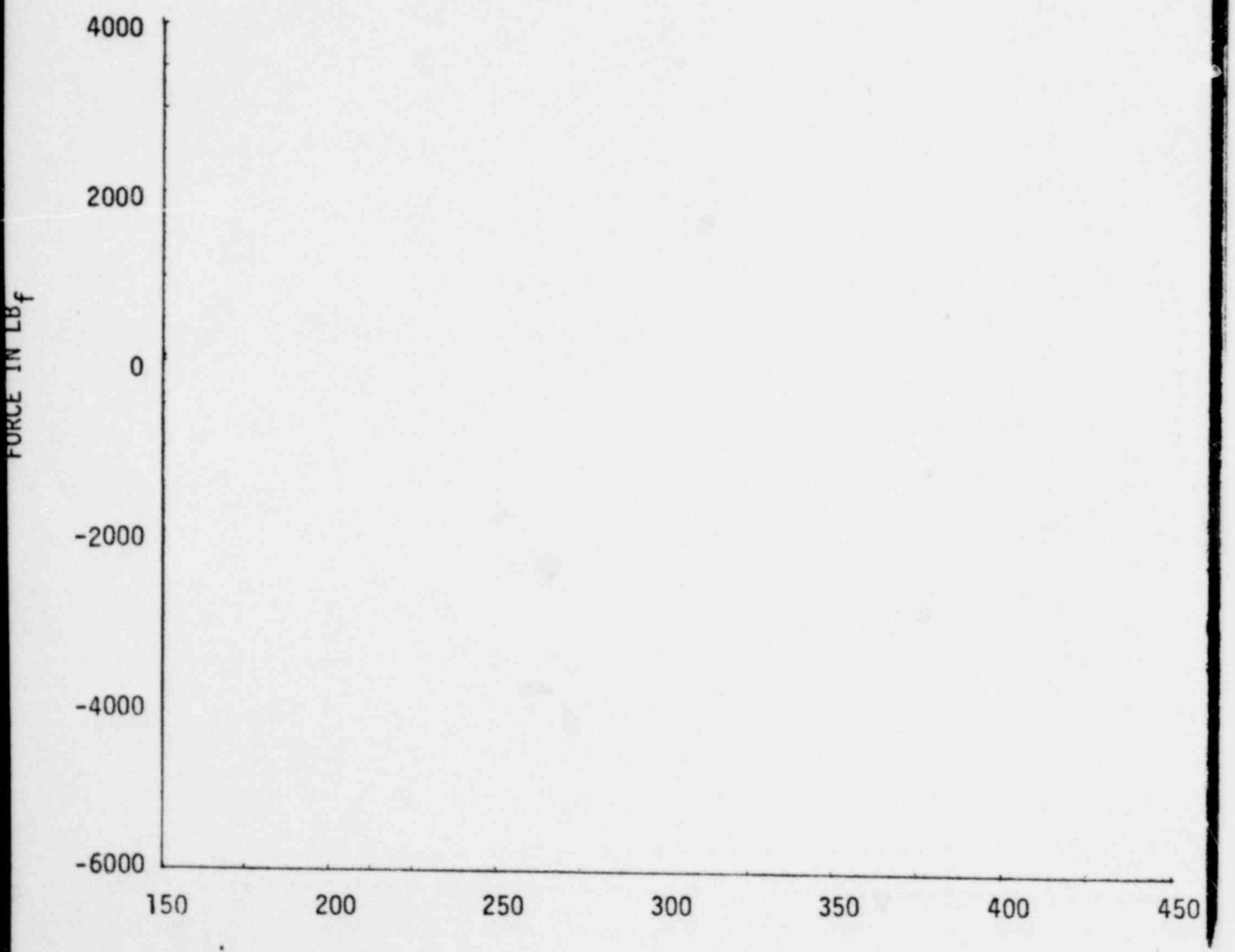

1351 283

FIGURE H-31

FILTERED NET TORUS FORCE,
CORRECTED FOR WATER INERTIA

PEACH BOTTOM TEST 4

FILTER : 80-120 HZ

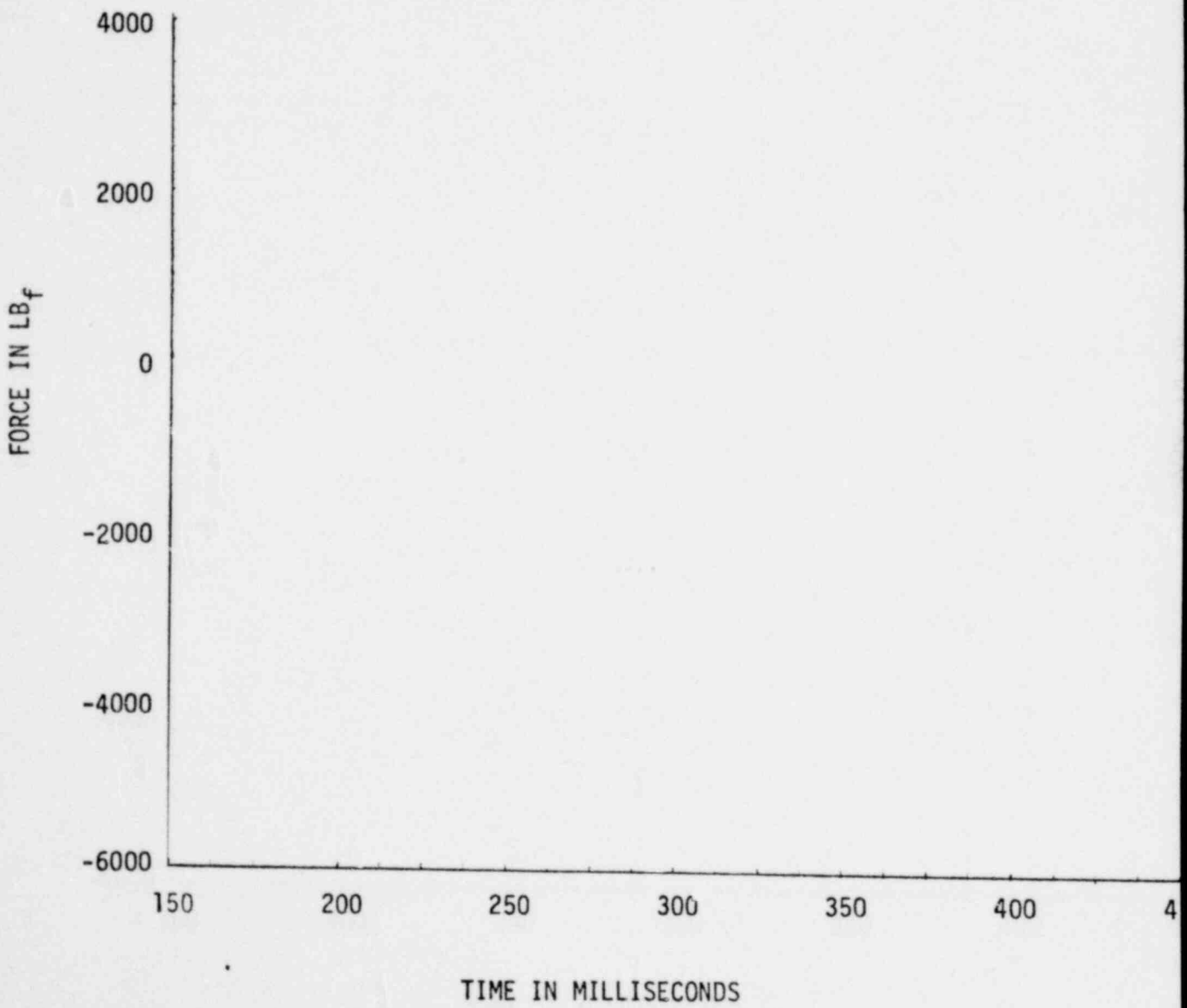

FIGURE H-32

FILTERED NET TORUS FORCE,
CORRECTED FOR WATER INERTIA

PEACH BOTTOM TEST 5

FILTER : 80-120 HZ

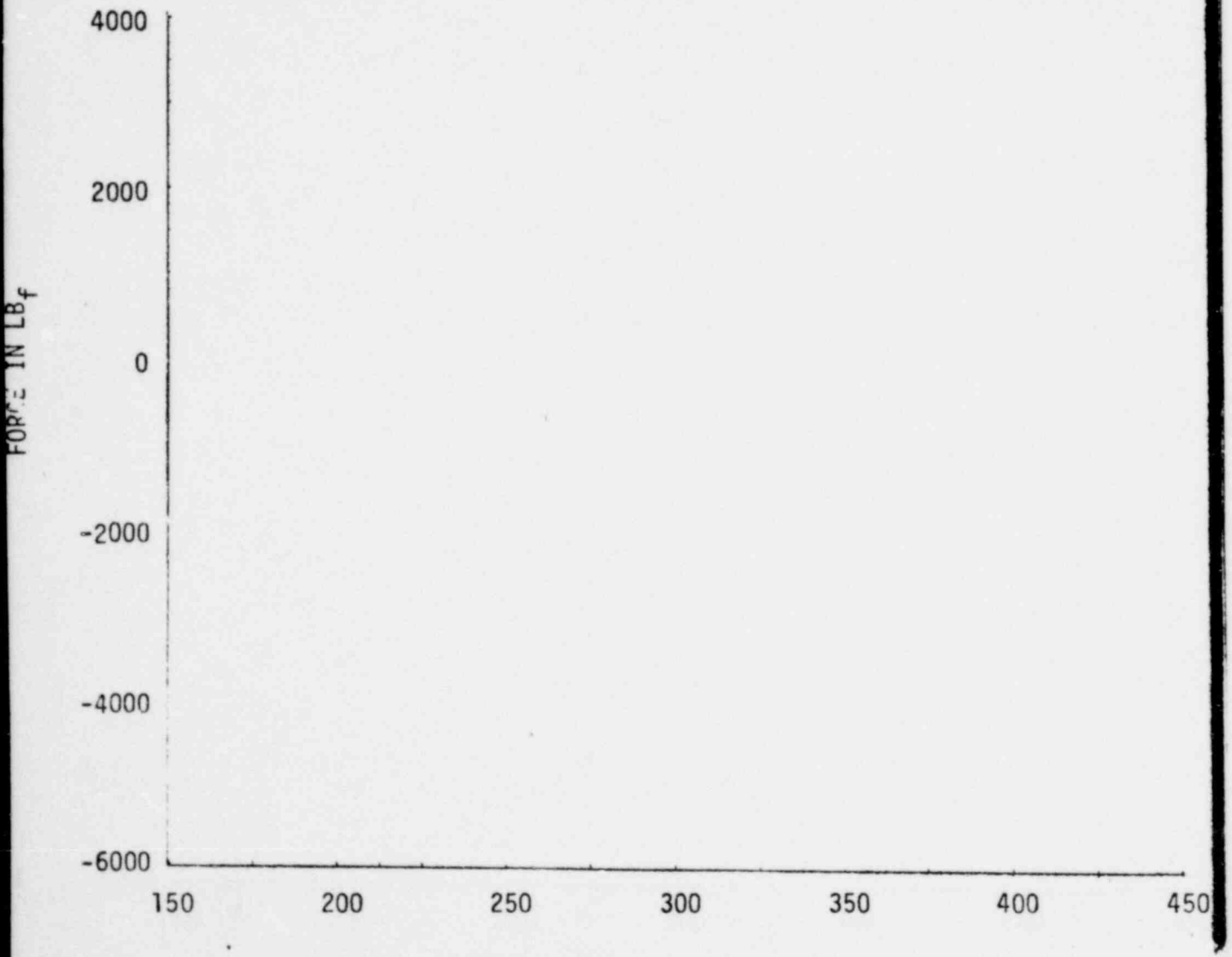

1351 285

NUCLEAR ENERGY DIVISIONS • GENERAL ELECTRIC COMPANY
SAN JOSE, CALIFORNIA 95125

GENERAL ELECTRIC

TECHNICAL INFORMATION EXCHANGE

TITLE PAGE

AUTHOR	SUBJECT	TIE NUMBER
	730	79NED81
		DATE June 1979
TITLE Mark I Containment Program 1/4 Scale Pressure Suppression Pool Swell Test Program: Plant Unique Tests, Task 5.5.3		GE CLASS I
		GOVERNMENT CLASS --
REPRODUCIBLE COPY FILED AT TECHNICAL SUPPORT SERVICES, R&UO, SAN JOSE, CALIFORNIA 95125 (Mail Code 211)		NUMBER OF PAGES 1361

SUMMARY

This report presents the results of the Plant Unique Tests (Mark I Long Term Program Task 5.5.3-2) that were conducted in the Mark I Quarter Scale Test Facility (QSTF) to obtain subscale two-dimensional net vertical torus forces, vent header, impact pressures, and pool surface displacement and velocity transients for 17 Mark I plants.

The work was performed with the support of Quadrex Corporation Nuclear Services Division, and Aerotherm Division of Acurex Corporation under contract to General Electric.

By cutting out this rectangle and folding in half, the above information can be fitted into a standard card file.

DOCUMENT NUMBER NEDO-21944

INFORMATION PREPARED FOR Nuclear Energy Projects Division

SECTION Containment Improvement Programs

BUILDING AND ROOM NUMBER PYD 402 MAIL CODE 904

914 (6/77)